frontiers | Research Topics

Sustainable road infrastructure: Technologies and assessments

Edited by
Meng Jia, Di Wang, Yangming Gao, Jianmin Ma and Dongdong Yuan

Published in
Frontiers in Energy Research

ISSN 1664-8714
ISBN 978-2-8325-4943-8
DOI 10.3389/978-2-8325-4943-8

About Frontiers

Frontiers is more than just an open access publisher of scholarly articles: it is a pioneering approach to the world of academia, radically improving the way scholarly research is managed. The grand vision of Frontiers is a world where all people have an equal opportunity to seek, share and generate knowledge. Frontiers provides immediate and permanent online open access to all its publications, but this alone is not enough to realize our grand goals.

Frontiers journal series

The Frontiers journal series is a multi-tier and interdisciplinary set of open-access, online journals, promising a paradigm shift from the current review, selection and dissemination processes in academic publishing. All Frontiers journals are driven by researchers for researchers; therefore, they constitute a service to the scholarly community. At the same time, the *Frontiers journal series* operates on a revolutionary invention, the tiered publishing system, initially addressing specific communities of scholars, and gradually climbing up to broader public understanding, thus serving the interests of the lay society, too.

Dedication to quality

Each Frontiers article is a landmark of the highest quality, thanks to genuinely collaborative interactions between authors and review editors, who include some of the world's best academicians. Research must be certified by peers before entering a stream of knowledge that may eventually reach the public - and shape society; therefore, Frontiers only applies the most rigorous and unbiased reviews. Frontiers revolutionizes research publishing by freely delivering the most outstanding research, evaluated with no bias from both the academic and social point of view. By applying the most advanced information technologies, Frontiers is catapulting scholarly publishing into a new generation.

What are Frontiers Research Topics?

Frontiers Research Topics are very popular trademarks of the *Frontiers journals series*: they are collections of at least ten articles, all centered on a particular subject. With their unique mix of varied contributions from Original Research to Review Articles, Frontiers Research Topics unify the most influential researchers, the latest key findings and historical advances in a hot research area.

Find out more on how to host your own Frontiers Research Topic or contribute to one as an author by contacting the Frontiers editorial office: frontiersin.org/about/contact

Sustainable road infrastructure: Technologies and assessments

Topic editors

Meng Jia — Shandong University of Science and Technology, China
Di Wang — University of Ottawa, Canada
Yangming Gao — Liverpool John Moores University, United Kingdom
Jianmin Ma — Queen's University, Canada
Dongdong Yuan — Chang'an University, China

Citation

Jia, M., Wang, D., Gao, Y., Ma, J., Yuan, D., eds. (2024). *Sustainable road infrastructure: Technologies and assessments*. Lausanne: Frontiers Media SA. doi: 10.3389/978-2-8325-4943-8

Table of contents

frontiers | Frontiers in Energy Research

TYPE Editorial
PUBLISHED 15 May 2024
DOI 10.3389/fenrg.2024.1418757

OPEN ACCESS

EDITED AND REVIEWED BY
Michael Carbajales-Dale,
Clemson University, United States

*CORRESPONDENCE
Meng Jia,
1656377@qq.com

RECEIVED 17 April 2024
ACCEPTED 03 May 2024
PUBLISHED 15 May 2024

CITATION
Jia M, Wang D, Gao Y, Ma J and Yuan D (2024), Editorial: Sustainable road infrastructure: technologies and assessments.
Front. Energy Res. 12:1418757.
doi: 10.3389/fenrg.2024.1418757

Editorial: Sustainable road infrastructure: technologies and assessments

Meng Jia[1]*, Di Wang[2], Yangming Gao[3], Jianmin Ma[4] and Dongdong Yuan[5]

[1]College of Transportation, Shandong University of Science and Technology, Qingdao, China, [2]Department of Civil Engineering, University of Ottawa, Ottawa, ON, Canada, [3]Faculty of Engineering and Technology, Liverpool John Moores University, Liverpool, United Kingdom, [4]Department of Chemistry, Queen's University, Kingston, ON, Canada, [5]School of Highway, Chang'an University, Xi'an, China

KEYWORDS

sustainable road infrastructure, renewable resources, clean energy, carbon emission, sustainable transportations

Editorial on the Research Topic
Sustainable road infrastructure: technologies and assessments

1 Introduction

The construction of sustainable road infrastructures has become an issue of concern to the international community. This Research Topic on "*Sustainable Road Infrastructure: Technologies and Assessments*" mainly focuses on upgrading the construction and maintenance levels of road infrastructure, improving the recycling level of infrastructure materials, and efficiently harvesting and utilizing clean energy from sustainable road infrastructures. Moreover, the sustainable transportation systems like transportation tools, transportation planning and organization are also included in the Research Topic. There are 69 authors and 13 papers that are contributed to this Research Topic. These papers are classified according to the following sections

1.1 Technologies for sustainable road infrastructures

Tu et al. replaced a limestone filler with a Prestressed High-Strength Concrete Pile Waste Concrete (PPWC) to prepare asphalt concrete. The results indicated that the PPWC filler effectively improved the mechanical properties, high-temperature rutting resistance and low-temperature crack resistance, but reduced the low-temperature fatigue resistance of asphalt concrete. Overall, the use of PPWC as a filler in asphalt mixtures provides a reliable solution for the sustainable development of road.

Chang et al. studied the effects of a warm mix agent (Evotherm M1) on asphalt binders from different oil sources. The results revealed that the addition of warm mix agent could slow down the decrease of asphalt viscosity during the aging process and the aging of asphalt. The warm mixing agents could also make the chemical components in asphalt relatively stable and less prone to further pyrolysis or cracking reactions.

Li et al. aimed to improve the performance of thin overlayers in pavement surface by adding a basalt fiber to two types of thin overlayer asphalt mixtures. The results indicated that adding basalt fiber could enhance the high temperature deformation resistance, low temperature cracking resistance, intermediate temperature cracking resistance and stripping resistance of the thin overlayer, but had no significant impact on skid resistance.

Chu et al. prepared a solid waste–based cementitious material (SWCM) using slag, fly ash, desulfurization gypsum, and gangue, to improve the high-value utilization of industrial solid waste materials. The mechanical strength and hydration process of the SWCM and an ordinary Portland cement (OPC) were studied. The results showed that the induction period of the SWCM was five times that of OPC, and the total 4 days exothermic amount of OPC was 1.7 times that of the SWCM. The unconfined compressive strength of the SWCM-stabilized macadam was comparable to that of the OPC-stabilized macadam.

Wang et al. explored the utilization of natural resources (i.e., solar energy and wind energy) along desert highways in northern Xinjiang, China, to establish hybrid energy generation systems for service areas. The application of these hybrid energy generation systems across the three service areas could provide 3,349,557 kWh of electrical energy annually for the desert highway. The Net Present Cost (NPC) and Cost of Energy (COE) values decreased with increasing radiation levels, while NPC showed an increasing trend with a growing load demand, and COE exhibited a decreasing trend.

Liao et al. constructed a renewable hybrid energy system for the highway tunnel with using a highway in southern China as an example. The research results indicated the feasibility of constructing a highway tunnel renewable hybrid energy system by utilizing natural resources (i.e., solar energy and wind energy) within the road area. The hybrid energy system could reduce greenhouse gas emissions, contributing to the sustainable development of the project.

1.2 Assessment methods for sustainable road infrastructures

Zhang et al. developed a rapid evaluation method of stacking peak ratio(SPR) for assessing the interlayer condition of asphalt pavements. The results indicated that the SPR method could be compatible with various bonding materials and pollution layers, and could identify insufficient layer bonding and predict potential flaws in advance. This method provides theoretical support for promptly evaluating the bonding status, which is also of great significance for improving the durability of asphalt pavements.

Ding et al. explored the correlations between pavement structure combinations and pavement performances to promoting the longevity development of asphalt pavements. The results showed that the seasonal factors significantly affected the deflection values of pavement structures, and that increasing the thickness of the asphalt surface was beneficial for reducing the area of defects, while laying the semi-rigid base layer was beneficial for maintaining the deflection value and rut depth at a lower level.

Ma et al. improved the assessment accuracy of pavement assets by introducing the replacement cost and condition-based valuation methods. The results demonstrated that the condition-based pavement asset valuation method comprehensively considered each stage of pavement operation and could serve as an effective tool for evaluating pavement asset depreciation. This research finding can promote the sustainable development of road infrastructure.

Bi et al. developed an advanced data processing and mathematical model to compare the comprehensive performance of asphalt concretes with replacing different amounts of mineral powder by an activated carbon powder (ACP). The results indicated that the larger the replacement amount of ACP, the better was the comprehensive performance of asphalt concrete, which could improve the microwave heating efficiency of asphalt concrete.

1.3 Sustainable transportation systems

Yang et al. investigated the traffic applicability of five expressway entrance forms: conventional interchange entrance ramp (CI), passenger vehicles and trucks separation (PVTS), lanes separation around interchange (LSI), both left-side and right-side entrance ramp (LRER) and the stacked composite cross-section expressway (CCE). It was demonstrated that the strengths and applicability of PVTS, LSI, and CCE could guide the choice of entrance forms for ten-lane expressways.

Zhang et al. conducted research on the traffic safety of new energy vehicles by using three sampling methods. Studies have found that people using less protective means of transportation (bicycles, motorcycles) and vulnerable groups such as pedestrians were susceptible to serious injury and death.

Dong et al. constructed a carbon emission prediction model applicable to road sections with different planar geometries, which could realize the carbon emission quantification of vehicles on the road sections. The model revealed that the geometric parameters of horizontal curves that affect carbon emissions were the radius of the circular curve, the superelevation, and the length of the gentle curve. The root causes of high carbon emissions on horizontal curve road sections were curve driving resistance and speed fluctuations.

Author contributions

MJ: Writing–original draft, Writing–review and editing. DW: Writing–review and editing. YG: Writing–review and editing. JM: Writing–review and editing. DY: Writing–review and editing.

Funding

The author(s) declare that no financial support was received for the research, authorship, and/or publication of this article.

Conflict of interest

The authors declare that the research was conducted in the absence of any commercial or financial relationships that could be construed as a potential conflict of interest.

Publisher's note

frontiers | Frontiers in Energy Research

TYPE Methods
PUBLISHED 31 October 2023
DOI 10.3389/fenrg.2023.1277817

OPEN ACCESS

EDITED BY
Meng Jia,
Shandong University of Science and Technology, China

REVIEWED BY
Wangjie Wu,
Chang'an University, China
Jiasheng Dai,
University of Bologna, Italy
Shihao Dong,
Shandong University of Science and Technology, China

*CORRESPONDENCE
Longting Ding,
dltphd2018@163.com

RECEIVED 15 August 2023
ACCEPTED 11 September 2023
PUBLISHED 31 October 2023

CITATION
Zhang W, Niu L, Wang S, Han W and Ding L (2023), Study on the interlayer bonding state of an asphalt pavement based on the stacking peak ratio method. *Front. Energy Res.* 11:1277817. doi: 10.3389/fenrg.2023.1277817

Study on the interlayer bonding state of an asphalt pavement based on the stacking peak ratio method

Wenwu Zhang[1], Lei Niu[2], Shanshan Wang[1], Wenyang Han[2] and Longting Ding[1]*

[1]Shandong Hi-Speed Group Co., Ltd., Jinan, China, [2]Shandong Transportation Institute, Jinan, China

The interlayer bonding of an asphalt pavement significantly influences the mechanical properties and long-term durability of the pavement structure. In order to develop a rapid and comprehensive evaluation method for assessing the interlayer condition of asphalt pavements using 3D GPR, we propose the stacking peak ratio (SPR) method. This method involves stacking the ratio between the amplitude peak of the interlayer and that of surface reflection to evaluate the interlayer state. Comparative analysis with direct shear tests and field measurements leads us to draw several conclusions: the optimal test parameters for the SPR method are a stacking peak ratio at 35 ns with a residence time of 1 us; the SPR method is compatible with various bonding materials and pollution layers, demonstrating its ability to effectively assess the bonding state of asphalt pavements; field tests further validate that the SPR approach can identify insufficient layer bonding and predict potential flaws in advance. Through our test findings and data analysis, it is evident that this SPR approach provides theoretical support and technological assistance for promptly evaluating the bonding status in asphalt pavements.

KEYWORDS

ground-penetrating radar, bonding between asphalt pavement, non-destructive rapid detection, reflection amplitude, road engineering

1 Introduction

As transportation power is consistently promoted, China's transportation industry is rapidly expanding. Currently, China has 5.28 million kilometers of roadways, making it the largest country in the world in terms of its road network size (Yuan et al., 2023). The overall length of expressways among them is the longest in worldwide. Asphalt pavement is the primary component of China's expressways. The interlayer interface is the part of the asphalt pavement's upper, middle, and bottom layers that interact with one another (Zhang et al., 2018). Engineers utilize adhesive material between neighboring layers to enable perfect bonding between the layers during construction to ensure that each layer of the asphalt pavement can reach the ideal completely continuous state (Dawei et al., 2022). By minimizing the reflection crack caused by the subgrade, halting water erosion, and achieving good durability and structure-bearing capacity, a good bonding state can ultimately lengthen the life of the road (Cao and Al-Qadi, 2021). Traffic volume, especially heavy traffic, is outpacing the economic growth in China. Stripping damage, which is brought on by the interlayer bonding condition of the asphalt pavement, is prone to

adverse stress conditions, resulting in an interlayer shear slip of asphalt pavement, and even pushing cracks, leading to pavement damage, which has a serious impact on the performance of roads in high-temperature summer weather and heavy traffic (Mohammad et al., 2002). Therefore, studying the bonding states between pavement structures is of great significance.

The cause of insufficient bonding between asphalt pavements may come from internal reasons such as the quality of asphalt or the aggregate, the mismatch between design structure parameters and engineering characteristics, or external causes such as interlayer adhesive pollution and dosage deviation of sticky material (Tashman et al., 2008). Under the cyclic loading of temperature and humidity changes, and heavy traffic repeatedly, the stripping damage occurred, which affected the performance of the pavement (Raouf and Williams, 2010).

In "Specifications for Design of Highway Asphalt Pavement" of China, only simple provisions are made on interlayer adhesive materials and related construction technologies. In contrast, the evaluation methodologies and indexes for the bonding state between asphalt surface layers are relatively poor. The typical evaluation method of the bonding state between pavement layers is the shear test, pulling test, torsion shear test, and other indoor tests (Jiang et al., 2020). Meanwhile, the test method of stretching and the torsion shear test of bonding strength between layers is stipulated in the field test methods of highway subgrade and pavement. Leng et al. designed a piece of new direct shear and oblique shear equipment, considering the test temperature and loading speed between the direct shear test method, and proposed shear strength and unit shear strength to verify each other to determine the asphalt pavement interlayer shear strength test technical parameters and the standard test method, by using the corresponding test method (Leng et al., 2011). To determine the indexes affecting the bonding condition of asphalt pavement, Mohamed et al. set different test temperatures, loading speed, bonding material, sprinkling amount, and other indexes with a direct shear equipment, which showed that the test temperature affected the most. When 70 # asphalt binder is used as a bonding material, the bonding strength is better than that of emulsified asphalt (Mohammad et al., 2002). To determine the optimal sprinkling amount of the adhesive layer material between asphalt pavement layers, Zhang et al. used interlayer shear equipment to test the interlayer shear strength of the asphalt pavement. The results show that when the adhesive layer material is SBS-modified emulsified asphalt, the optimal spreading amount is 0.6–1.0 L/m^2, and the optimal content of SBS was 2.5% (Zhang, 2017). Wang et al. used a direct shear test to analyze the properties, sprinkling amount, load, and aging of the adhesive layer material of an asphalt pavement; the results show that the shear strength of the asphalt pavement is related to the contact area of the upper and the lower layers. After the external load and aging effect, the bonding strength between the layers and the shear strength of the whole road surface can be improved (Wang et al., 2017).

In recent years, ground-penetrating radar (GPR) technology has witnessed significant advancements and breakthroughs in radar hardware equipment, underground target identification,

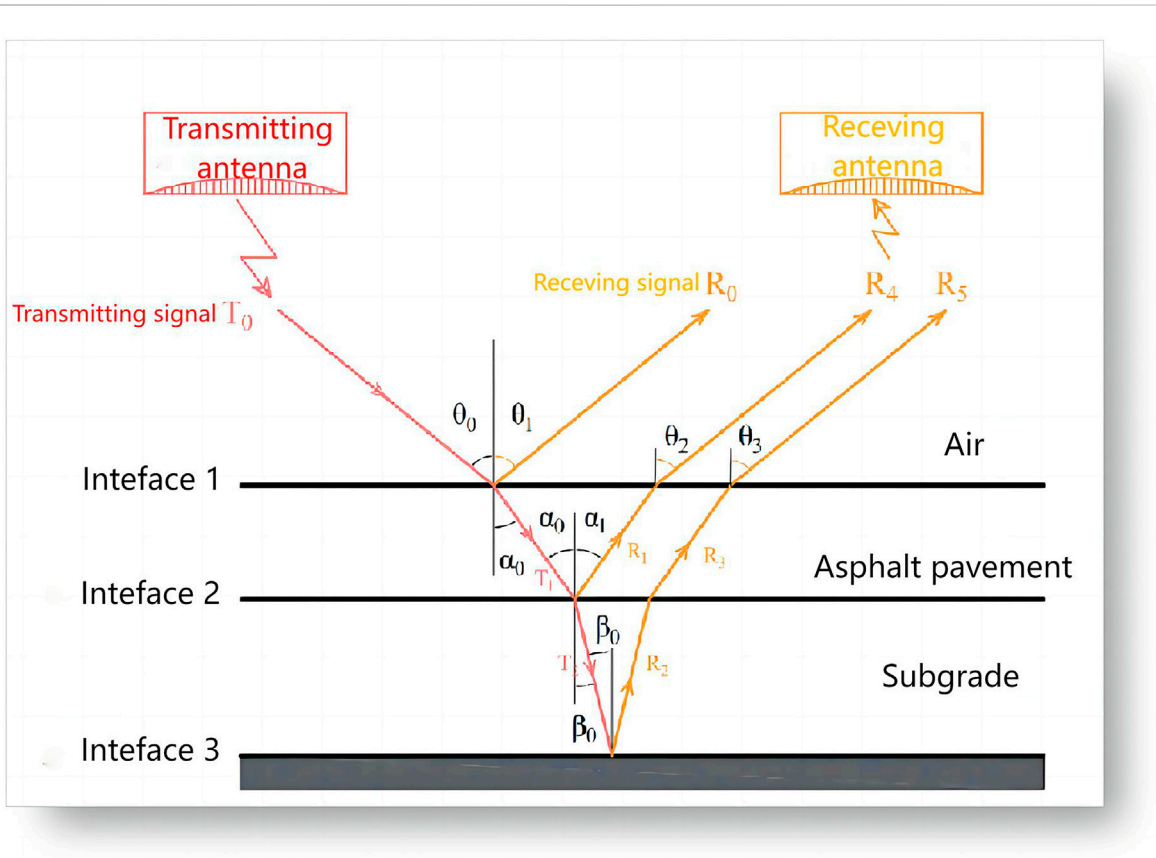

FIGURE 1
Working principle of 3D GPR.

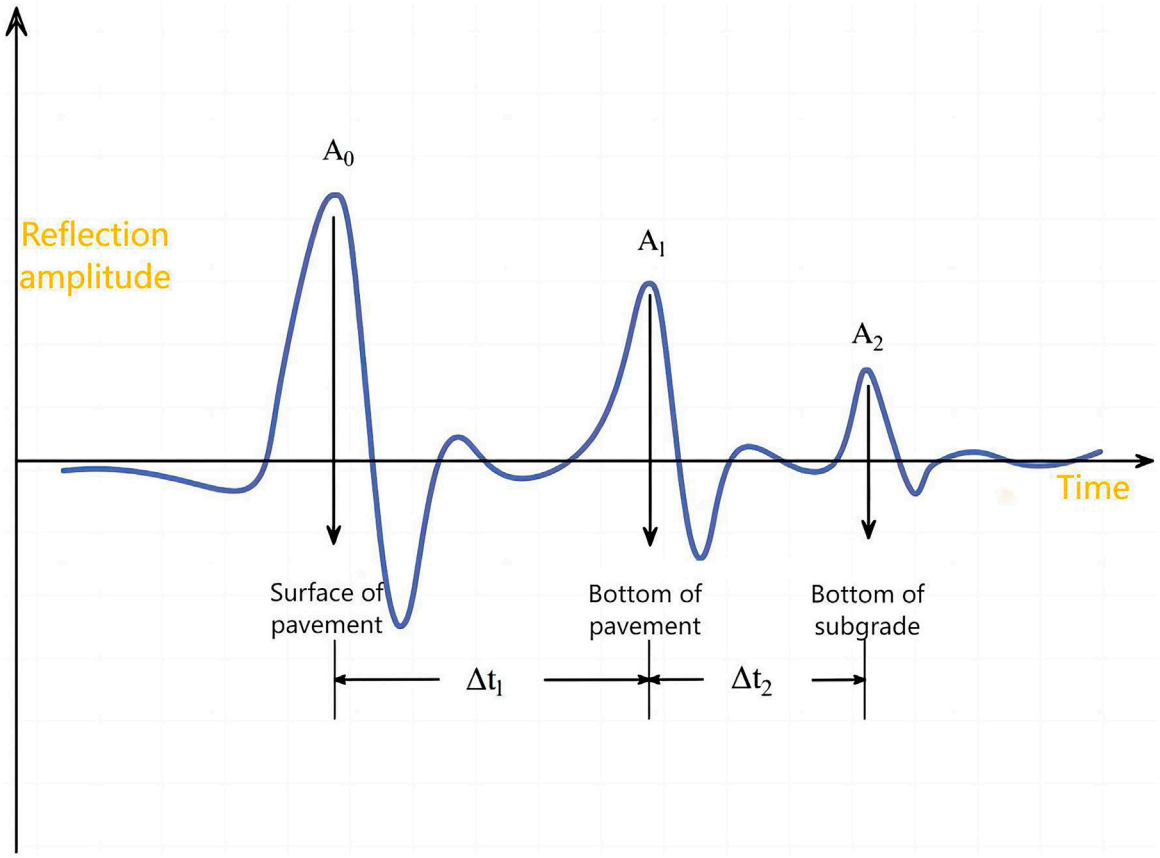

FIGURE 2
Typical map of the electromagnetic wave transferred from the surface to the base.

underground target imaging, and other related aspects as a rapidly evolving non-destructive testing technique. It finds extensive applications in thickness detection and underground disease detection among various fields. Sudyka et al., while evaluating the interlayer bonding state of the asphalt pavement, successfully employed air composite radar to detect horizontal cracks with widths of several millimeters under both dry and wet conditions. This study demonstrates the feasibility of utilizing GPR technology for assessing the bonding state of an asphalt pavement. By employing high-frequency radar coupled with a high-pass filter and Fourier filter techniques, potential invisible diseases within the asphalt pavement, such as gaps, interlayer bonding issues, or looseness, can be effectively eliminated from noise interference. Consequently, an evaluation index termed the "pavement internal damage condition index" is determined to assess the internal health status of asphalt pavements. Furthermore, it was observed that traffic directly influences the probability of interlayer bonding (Sudyka and Krysiński, 2011). The bonding state of an asphalt pavement was investigated by Wang Dawei et al. using three-dimensional ground exploration radar technology. It was observed that the peak amplitude of electromagnetic waves varied across different layers, enabling the evaluation of the asphalt pavement combination state based on reflection amplitudes less than 1.0 mm, indicating a reasonable combination, whereas reflection amplitudes exceeding 2.0 mm indicated weak interlayer bonding (Dawei et al., 2022).

In conclusion, the GPR detection method based on electromagnetic wave transmission–reception technology offers a rapid and convenient non-destructive approach for investigating the interlayer contact conditions in structural analysis, exhibiting distinct advantages over traditional field and laboratory tests (Ma et al., 2021). However, the existing form fails to effectively and promptly assess the overall condition of the layers (Dong et al., 2016). In a comprehensive investigation of indoor shear tests and field tests, we propose the stacking peak ratio approach using 3D GPR based on intrinsic analysis of an asphalt pavement's amplitude characteristics. This article provides a theoretical framework for evaluating pavement bonding conditions, optimizing bonding materials, and improving interlayer operations.

2 Stacking peak ratio theory of 3D GPR

2.1 Three-dimensional GPR system and its working principle

The 3D GPR system utilizes an antenna to transmit electromagnetic waves for the detection of dielectric materials in underground objects. Its theoretical foundation is based on

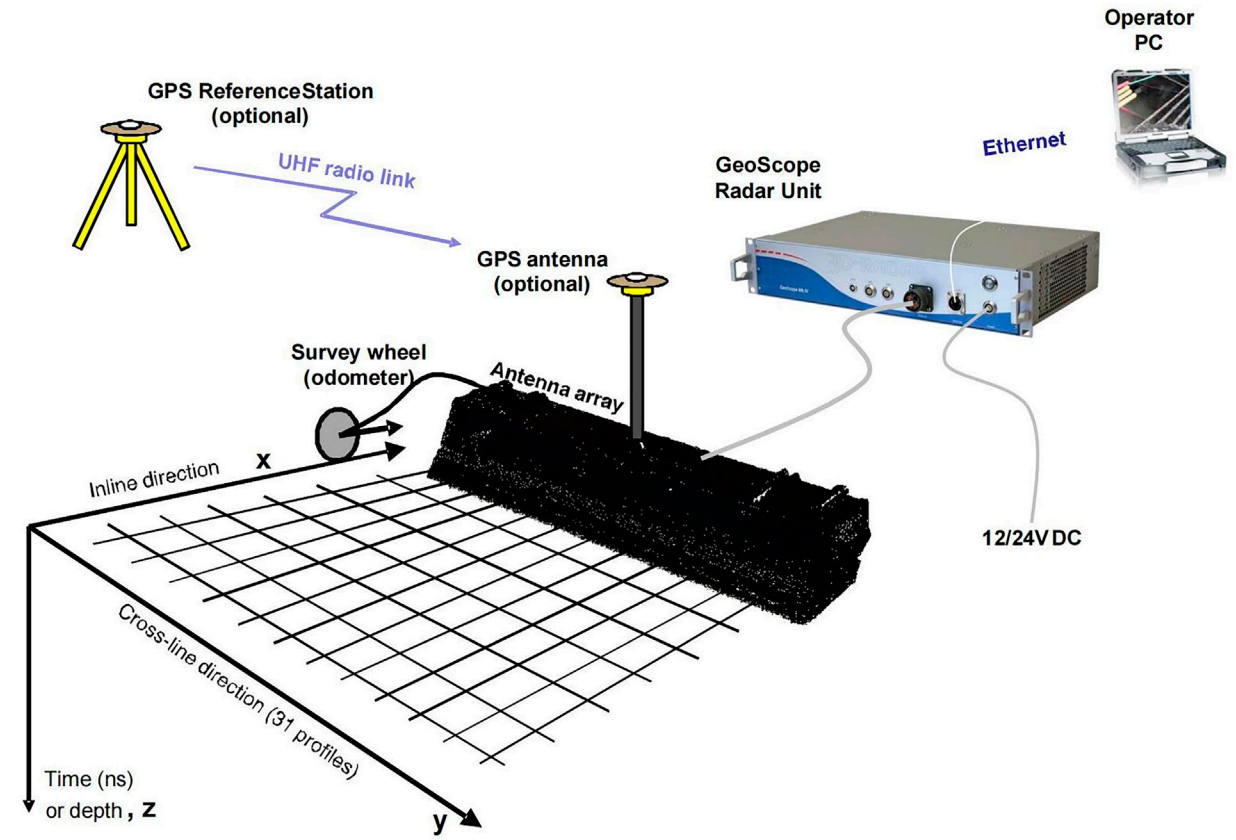

FIGURE 3
Three-dimensional GPR system.

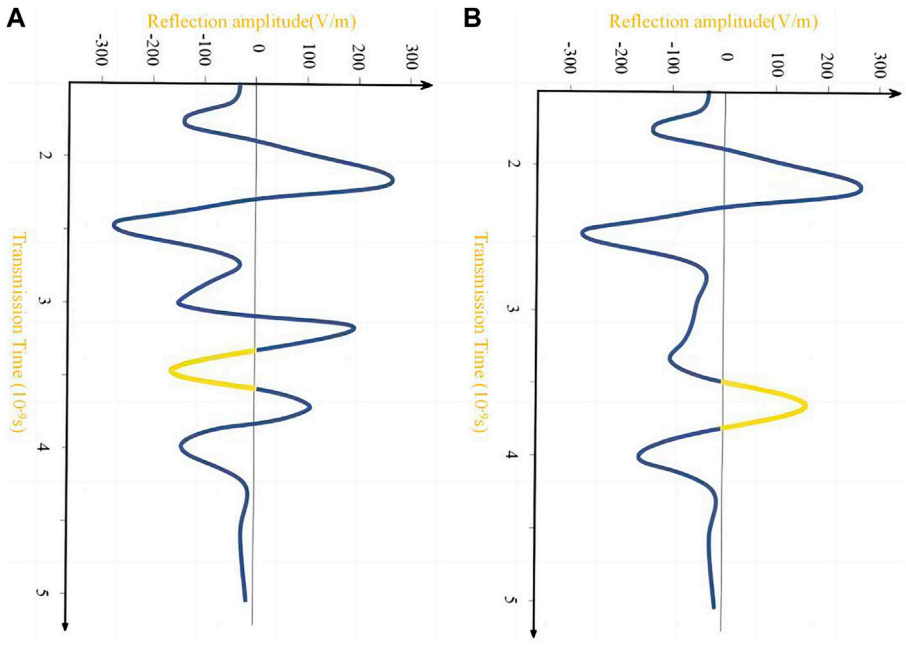

FIGURE 4
A-scan of electromagnetic waves propagated by different media. **(A)** Low dielectric constant to high dielectric constant. **(B)** High dielectric constant to low dielectric constant.

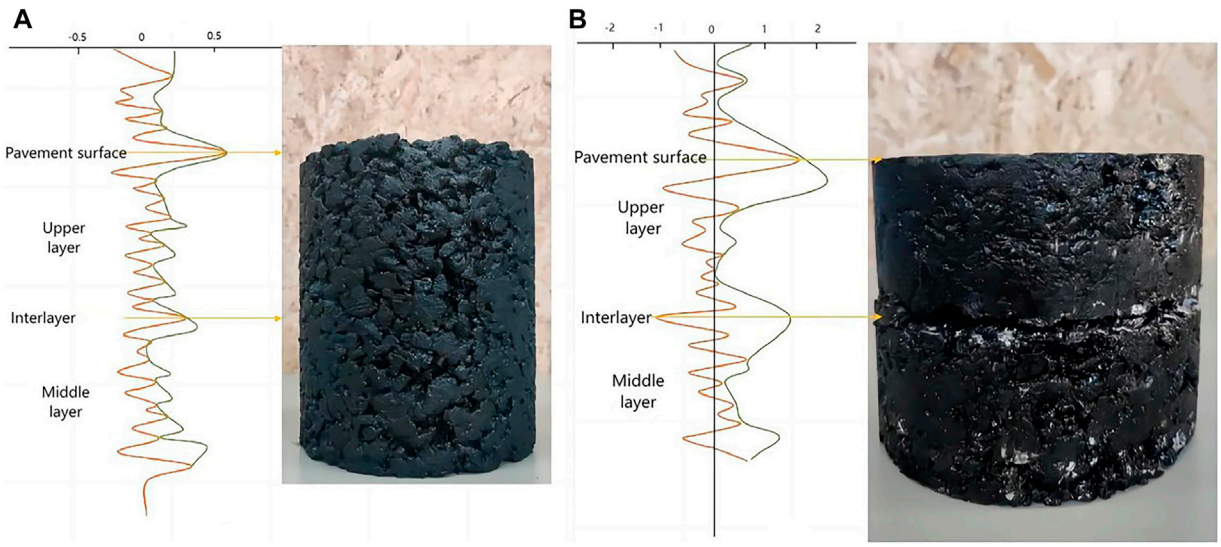

FIGURE 5
Typical radar map of specimens of different interlayer states. **(A)** Good bonding between layers and **(B)** poor bonding between layers.

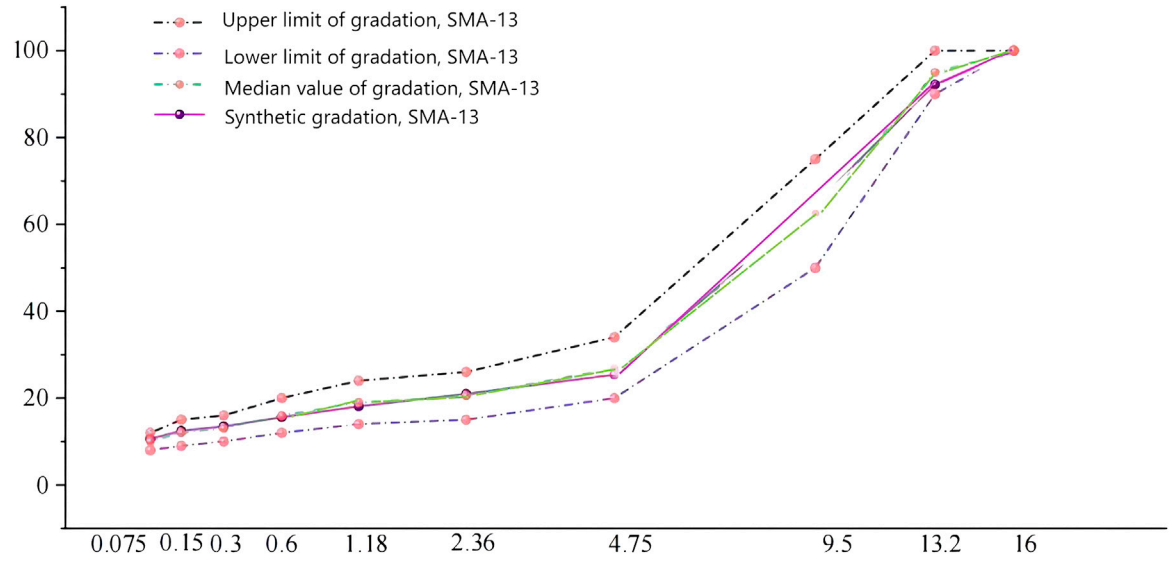

FIGURE 6
Gradation curve of SMA-13.

Maxwell's equations, which study the propagation process of electromagnetic waves through reflection, scattering, and diffraction in various mediums to obtain relevant data about the measured object. The propagation process is significantly influenced by the material property known as the dielectric constant. Variations in the dielectric constant of different materials cause changes in the phase and amplitude of the passing electromagnetic wave, enabling identification of information about observed targets using the 3D GPR system. These changes are governed by a formula for obtaining reflection coefficient that depends on differences in relative dielectric constants among various materials, determining the amplitude of reflected waves when there is a polarity alignment between the reflected and incident waves.

$$R = \frac{\sqrt{\varepsilon_1} - \sqrt{\varepsilon_2}}{\sqrt{\varepsilon_1} + \sqrt{\varepsilon_2}}.$$

The working principle of 3D GPR for detecting typical road structures is shown in Figure 1. The 3D ground exploration radar emits a high-frequency electromagnetic wave signal T, according to the corresponding reflection angle through the antenna$_0$, and an electromagnetic wave emission signal T$_0$. The component is reflected through the interface, where the reflection angle is θ_0 =

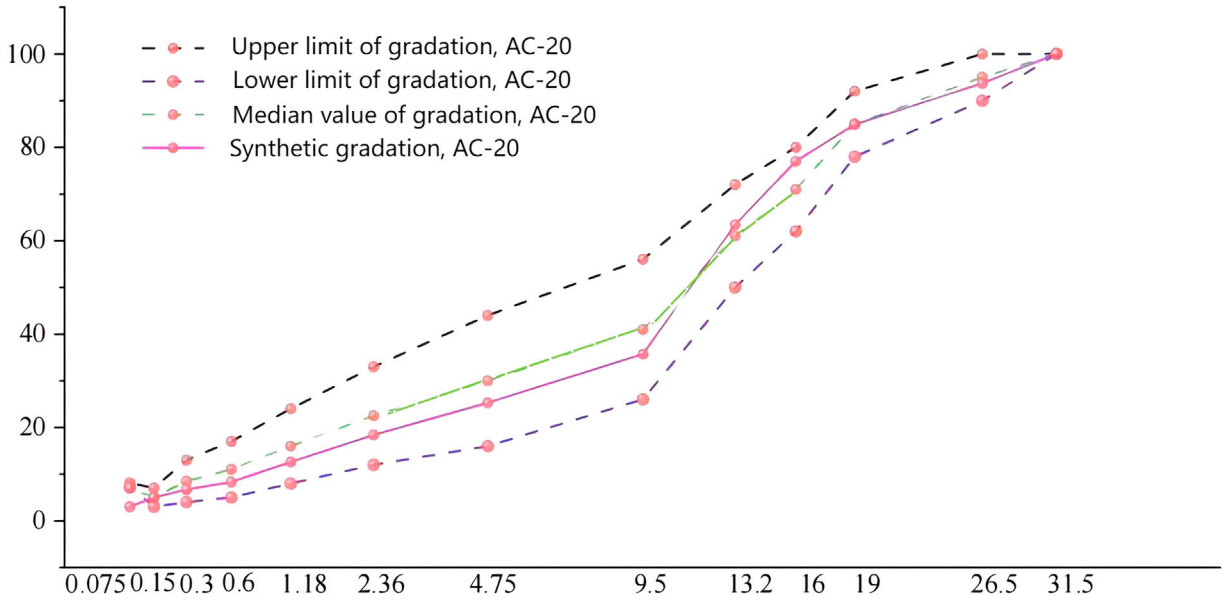

FIGURE 7
Gradation curve of AC-20.

θ_1. The amount of electromagnetic wave reflection received by the receiving antenna is R_0. Because the dielectric constant of the pavement material is much greater than that of the air, a part of the unreflected electromagnetic wave signal energy is lost; only T_1—the electromagnetic wave of the component—penetrates interface 1, and the refraction angle $\alpha_0<\theta_0$. The electromagnetic wave emission amount (T_1) is reflected through interface 2, with R_1—the electromagnetic wave of the reflected amount—being reflected at the interface. The reflected amount accepted by the receiving antenna is R_4, where the electromagnetic wave reflection amount is $T_1<T_0$, $R_1<T_1$, $R_1<R_4$, an angle of refraction $\alpha_0 = \alpha_1$, and $\alpha_1<\theta_2$. Another T_1—the electromagnetic wave of the component—penetrates through interface 2, and the base medium reaches interface 3. This process continues to lose part of the energy; T_1—the electromagnetic wave for the element—is reflected by interface 3, passes through interface 2 and interface 1, and the reflection amount received by the radar antenna is R_5, among $R_5<R_3<R_2$, $\beta_0<\alpha_1<\theta_3$, which completes an electromagnetic wave propagation cycle. In principle, if the medium between the interface is uniform and infinite and there is no foreign matter, the energy loss of the transmitted electromagnetic wave signal through the medium is equal to the transmitted amount, and the receiving antenna does not reflect the movement. Because the road is through a mixture of layered paving, the dielectric constant of different structure layers is another form of the reflection angle, and the reflection amount is also different; 3D ground exploration radar, according to the received reflection signal (electromagnetic waves in the layers of medium reflection signal accumulation), describes the reflection in the form of peak-trough (Figure 2) for electromagnetic wave routing table to the base of the typical map. With the increase in the detection depth, the loss of electromagnetic wave energy in different media also increases. The reflection peak also decreases, and the decay phenomenon of electromagnetic wave propagation in the medium is reflected (Soldovieri et al., 2011).

The 3D penetrating radar GeoScope MKIV 3D, manufactured by the Norwegian company 3D-Radar, is employed in this study and equipped with the DX1821 air coupling antenna, as illustrated in Figure 3. The utilized radar system utilizes the digital stepping frequency technology to precisely emit sine wave signals within controlled frequency steps in the frequency domain, effectively mitigating irrelevant noise through system optimization (Sala et al., 2012). The DX1821 air-coupled antenna comprises 21 channels, with each channel housing two scanning arrays. The standard spacing between each pair of antenna arrays is set at 75 mm, while the effective detection width measures 1.8 m, effectively addressing the issue of low detection efficiency. Composed of a butterfly unipolar antenna boasting a wide bandwidth, the coupled antenna can cover frequencies ranging from 100 MHz to 3,000 MHz, thereby significantly enhancing the detection efficiency (Khamzin et al., 2017).

2.2 Stacking peak ratio method to evaluate the bonding state of an asphalt pavement

The A-scan diagram represents the amplitude curve of the reflected electromagnetic wave signal captured by the air-coupled antenna at a specific location. It is generated when an electromagnetic wave transitions from a structural layer with a lower dielectric constant to one with a higher dielectric constant. As shown in Figure 4A, there is a negative peak surrounded by two sporadic positive peaks. Figure 4B shows the A-scan diagram for the transmission of electromagnetic waves from a high-dielectric constant structural layer to a persistent low-dielectric constant

structure layer, exhibiting a positive peak flanked by two intermittent negative peaks.

For a properly bonded asphalt pavement as the detection area, the A-scan diagram displays two distinct positive peaks. The first peak corresponds to reflections from the road surface and air, while the second peak corresponds to reflections from internal layers at a high frequency. Under typical interlayer bonding conditions (as depicted in Figure 5A), a direct contact between the road table and air leads to a noticeable increase in the reflection amplitude due to a greater difference in relative dielectric constants. As electromagnetic waves interact with the asphalt pavement surface, tighter bonding between layers results in only marginal increases in peak amplitude propagation within upper layers as penetration depth increases. Consequently, there is a decrease in the peak reflection amplitude as electromagnetic wave attenuation gradually occurs within the material. In contrast, poor pavement bonding (as shown in Figure 5B) allows air to reach interfaces, significantly reducing the interlayer material's dielectric constant; weak layer bonding is directly proportional to the interface gap width and consequently leads to an increased positive reflection amplitude as the interface gap widens. To investigate the effects of asphalt layer bonding on reflection amplitude, we utilized 3D GPR on defective specimens and well-adhered specimens for confirmation purposes. By employing techniques such as surface position adjustment, time-zero correction, infinite pulse response filtering, and finite pulse response filtering for noise removal at both high-frequency and low-frequency ranges from obtained characteristic maps distinguishing well-bonded samples from stripping-damaged samples (Soldovieri et al., 2011; Dong et al., 2016).

The peak of the amplitude slightly rises in comparison with the propagation between the higher layers because of the strong connection between the two layers. The loss of electromagnetic waves in the material gradually rises with an increased penetration depth, and the peak of the reflection amplitude gradually declines. The propagation of electromagnetic waves through the road surface to the upper layer is identical (Khamzin et al., 2017). The bonding between the upper and middle layers in the upper and center portions is still penetrated by air and water, which significantly interferes with electromagnetic wave transmission. The peak amplitude increased noticeably, mostly in the direction of the positive axis.

On the basis of this, we developed a novel technique known as the stacking peak ratio (SPR) approach, which compares the interlayer amplitude peak to the asphalt pavement's surface reflection amplitude peak to assess the bonding status between the two surfaces.

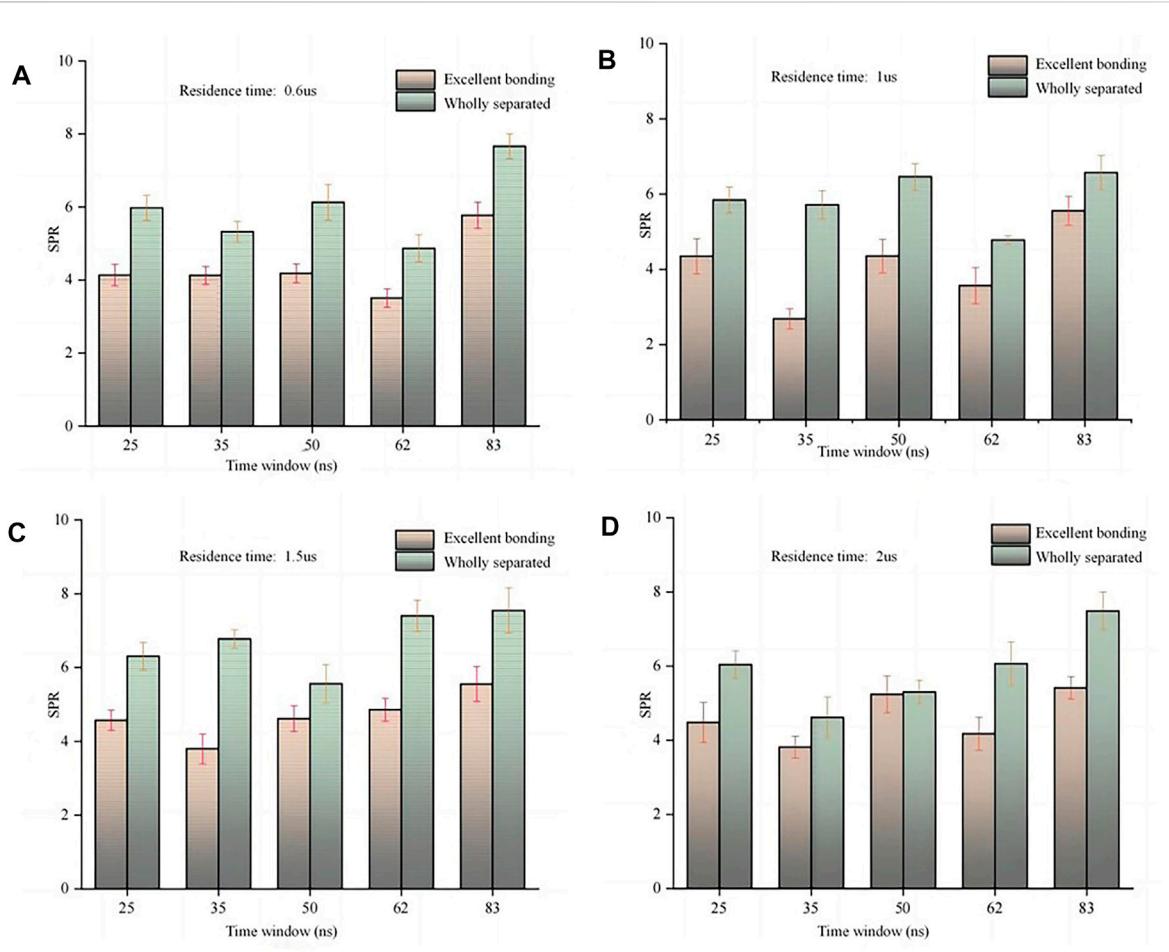

FIGURE 8
SPR under different time windows. Residence time: **(A)** 0.6us; **(B)** 1us; **(C)** 1.5us; **(D)** 2us.

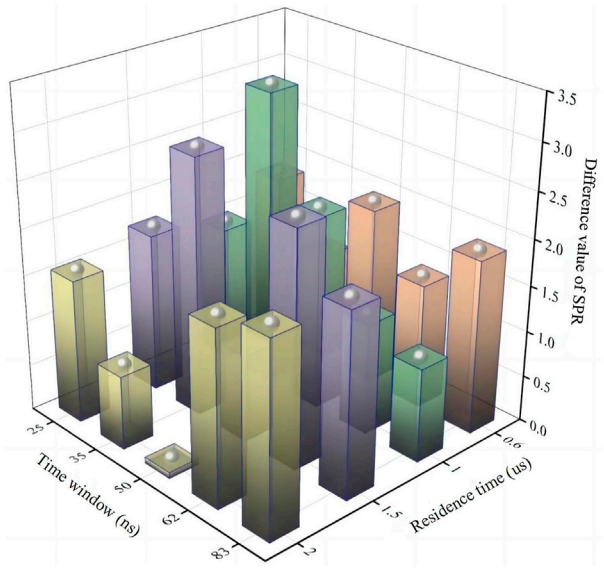

FIGURE 9
Different values of SPR under different parameters.

TABLE 1 Different spraying amounts of adhesive materials.

Level	1	2	3	4	5	6
Adhesive material	Sprinkling amount (kg/m²)					
70 # matrix asphalt binder	0.2	0.4	0.6	0.8	1.0	1.2
SBS-modified asphalt binder	0.2	0.4	0.6	0.8	1.0	1.2
Modified emulsified asphalt binder	0.2	0.4	0.6	0.8	1.0	1.2
Rubber asphalt binder	0.8	1.0	1.2	1.4	1.6	1.8
Pollution	0.1	0.3	0.5	0.7	0.9	1.1

$$SPR = \sum_{i=1}^{n} A_i / A_0.$$

Among them, A_i is the positive amplitude of electromagnetic waves in the range of the asphalt surface, A_0 is the surface reflection amplitude of the asphalt pavement, and n is the number of positive peaks in the surface. For the same radar parameter, its value increases with the increase in surface layer thickness. This method addresses the issue that it is challenging to determine the peak depth and offers a rapid form to assess the bonding condition of the asphalt surface.

3 Study on optimal parameters of 3D GPR based on the SPR method

3.1 Investigated subject

For the DX1821 air-coupled stepping frequency antenna, the early acquisition parameters of 3D GPR are the sampling interval, sampling time window, and residence time (Sala et al., 2012).

The 3D radar's sampling interval reflects the air coupling antenna's sampling density (Ma et al., 2021). The sampling interval for the pulse radar is inversely related to the central frequency and inversely proportional to the sampling rate. The sampling interval must be appropriate for the tested object's size. Neither very large nor very small sampling interval will prevent data overflow from happening. Since the test's specimen is small, a very small sampling interval, like 1 cm, is employed. The sampling interval can be changed to 5 cm–7.5 cm if a wide detection range is conducted on expressways, national, or provincial roadways.

The sampling time window represents the duration required for the electromagnetic wave signal to propagate through the target medium and be transmitted and received by the 3D GPR. This characteristic is determined by the speed of electromagnetic waves and the detection depth of the 3D GPR system. The central frequency and relative permittivity exert significant influence on the residence time of the 3D GPR, which defines the total emission time of each step frequency's electromagnetic wave signal. It plays a crucial role in acquiring internal data from objects, affecting both detection procedures and outcomes, making them essential research objectives for optimizing the 3D GPR parameters.

3.2 Testing program

We constructed two distinct types of asphalt mixture specimens in accordance with the technical requirements for highway asphalt pavement construction, aiming to investigate the optimal acquisition parameters for an asphalt pavement. The first type, completely bonded sample: AC-20 asphalt mixture compacted 75 times, serves as an exemplary interlayer condition. For the top layer, the SMA-13 asphalt mixture underwent 100 rounds of rotary compaction. As recommended by interlayer construction guidelines, the ideal amount of emulsified asphalt to be sprinkled on the surface is 0.6 kg/m². The second type consists of completely segregated layers: the SMA-13 asphalt mixture was subjected to 100 rounds of rotary compaction, followed by a natural cooling period of 48 h; the AC-20 asphalt mixture experienced 75 repetitions of rotary compaction and then remained inactive for another 48 h without any intermediate processing before being directly stacked on top material, facilitating easy separation. Figure 6 and Figure 7 illustrate the gradation curves for SMA-13 and AC-20, respectively. To ensure optimum measurement height at all times, we adjusted the height of the 3D radar antenna accordingly. Each type of sample was tested five times in total, from which mean values and standard deviations were computed. Acquisition parameters used to evaluate bonding in the asphalt pavement are more discernible when there is a greater difference between them; thus, we selected these differences as optimal acquisition parameters along with regular residency times (0.6, 1, 1.5, and 2 us) and standard time window values (25, 35, 50, 62, and 83 ns).

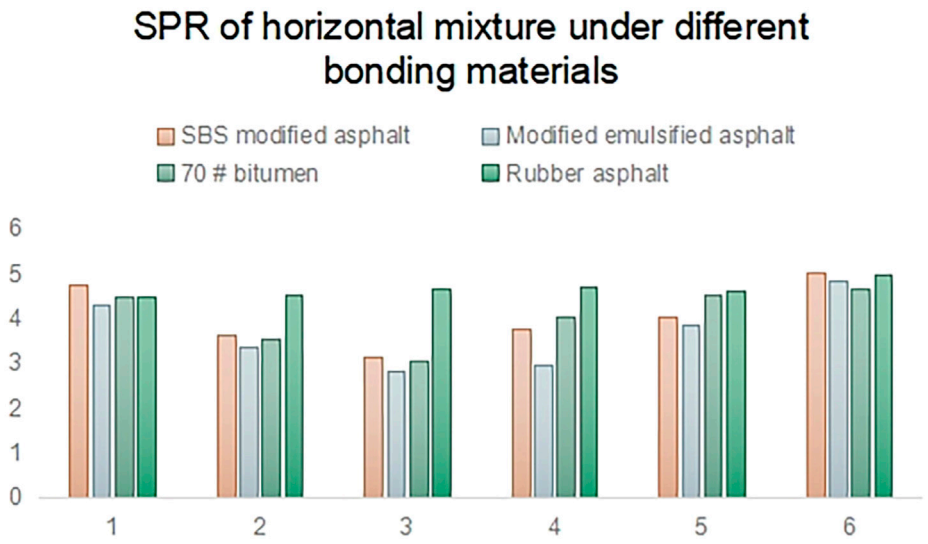

FIGURE 10
SPR under different materials.

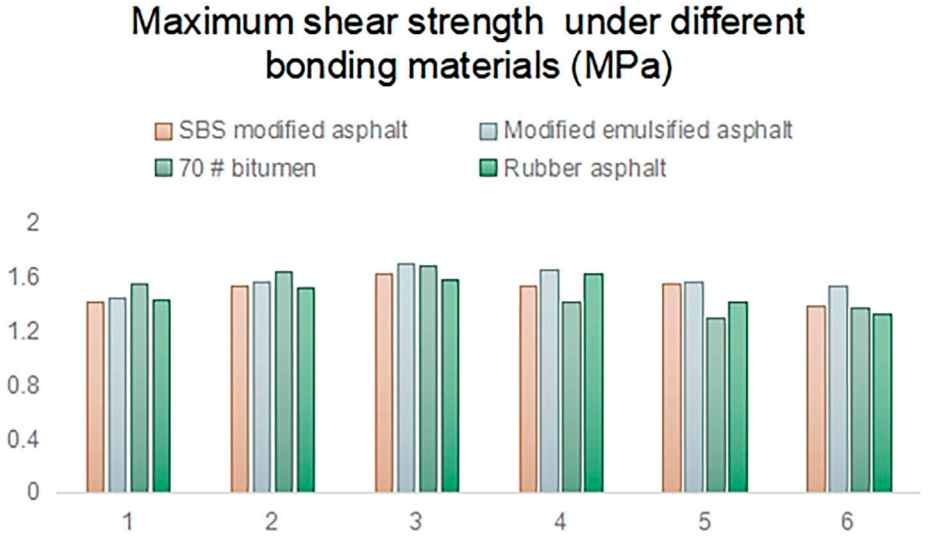

FIGURE 11
Maximum shear strength under different materials.

3.3 Analysis of results

As shown in Figure 8, the investigation found that, with a difference of 38.8%, the average peak value of well-bonding layers was 4.41 and that of separated layers was 6.12. Additionally, the SPR of the isolated samples from each data group was higher than that of the samples with a good interlayer state, indicating that this method can be used to assess the interlayer bonding state with regular parameters. Furthermore, the residence time of 1 μs and the time window of 35 ns were chosen as the optimal parameters for measuring the interlayer state using the stacking peak ratio approach since these values coincided with the appearance of the highest difference value, in Figure 9.

4 Comparison of the stacking peak ratio method and direct shear test

4.1 Testing program

To better understand the assessment impact of the SPR technique, we set up controllable tests contrasting the SPR method and the straight shear method in an effort to recreate

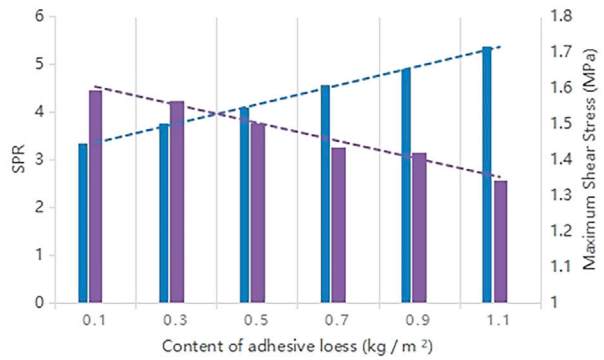

FIGURE 12
SPR and maximum shear strength under different material pollution.

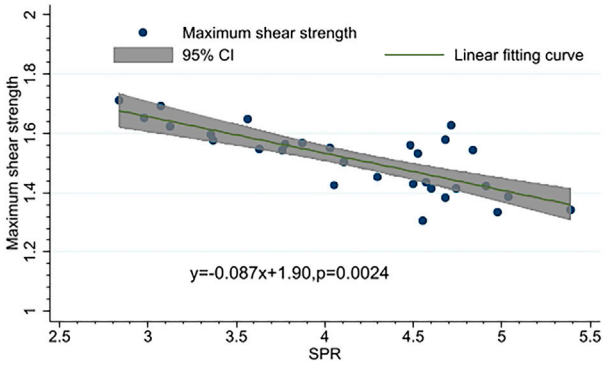

FIGURE 13
Linear fitting curve of SPR and maximum shear strength.

diverse real-world interlayer bonding situations for the asphalt pavement. We used four distinct adhesive materials, each with six gradients of sprinkling amount and six further gradients of interlayer pollution to match existing criteria as much as possible, and we compared the test results under various circumstances.

The forming method of the test specimen was combined with rotary compaction, the upper layer of the sample is SMA-13 asphalt mixture, and the lower layer is the AC-20 asphalt mixture (Zhang et al., 2018). The specific technical indexes are the same as in the previous section. First, a 60-mm-thick AC-20 asphalt mixture was used as the lower layer of the specimen. The compaction was 75 times and stands for 48 h under natural conditions. Then, we mixed the SMA-13 asphalt mixture and placed the heated material into the rotary compaction test mold after insulation so that the compaction hammer can fall ten times 20 cm from the surface of the SMA-13 mixture to form a foundation plane. The preparation process of different bonding materials was as follows: the adhesive layer materials were heated to the flow state; SBS-modified asphalt binder, 70 # matrix asphalt binder, and rubber asphalt binder were sprinkled to the upper surface of the AC-20 mixture. In addition, the modified emulsified asphalt needs to wait for an emulsion breaking before operation. The specific amount of spraying and level is shown in Table 1. The preparation process of test pieces with different pollution degrees is as follows: first, apply 0.6 kg/m^2 emulsified asphalt, and then, sprinkle six different amounts of loess particles, such as 0.1 kg/m^2–1.1 kg/m^2 on the emulsified asphalt to simulate the interlayer pollution caused by the dust on the adhesive layer (Tashman et al., 2008).

GeoScope MKIV 3D GPR and DX1821 air coupling antenna are adopted in the test. The acquisition parameters are as follows: a sampling interval of 1 cm, 35 ns at sampling time, 1 μs at residence time, and a driving speed was less than 20 km/h. The specimens were arranged in a straight line during the test, and each sample was 1 m apart. Iron plates were placed between models with different adhesive materials to distinguish. We controlled the antenna to ensure that 6–16 channels crossed the center of the specimen and collected the data three times for the average result. The direct shear test used a UTM-30 multi-function material testing machine with a direct shear module. After measuring the height and diameter, we put the specimen into a 25°C incubator for 4 hours. Then, the sample was put into the straight shear module, ensured that the lower layer of the selection was fixed to the whole circle, and the interlayer position was located between the upper half ring and the entire ring. Then, the height of the upper ring and the surface of the specimen were adjusted to make contact. The loading rate was 50 mm/min, and the test procedure will show the specimen's real-time shear stress and deformation displacement. The test was stopped when the displacement–stress curve peak drops.

4.2 Test results and analysis

The peak and maximum shear strengths of the same specimen exhibit an inverse relationship, as shown in Figure 10 and Figure 11, while Figure 13 demonstrates a satisfactory fitting effect. This substantiates the effectiveness and feasibility of the stacking peak ratio method for assessing interlayer bonding in the asphalt pavement. Moreover, when comparing three types of asphalt binders at equal quantities, the bonding effect between the modified emulsified asphalt binder and 70# asphalt binder surpasses that of the SBS-modified asphalt binder. Notably, employing 0.6 kg/m^2 as the interlayer bonding material is recommended due to its superior bonding effect ratio. Conversely, the rubber asphalt binder yields inferior results compared to the other three materials; however, it remains challenging to discern changes in its content lawfully. Figure 12 reveals an inverse relationship between SPR (shear resistance parameter) values for polluted samples and pollution levels. Similarly, maximum shear strength exhibits an inverse correlation with the pollution level and displays a linear connection with excellent fit, thereby demonstrating that SPR can effectively assess interlayer pollution levels as well. Figure 13 shows both the SPR method and shear strength test on various specimens demonstrate a significant correlation between these two methods; additionally, distinct variations in bonding materials with additional contents or varying pollution levels were highlighted while maintaining consistent regularity throughout observations. These findings underscore how the SPR method consistently aligns with direct shear tests and can be employed for the rapid assessment of interlayer bond conditions in asphalt pavements.

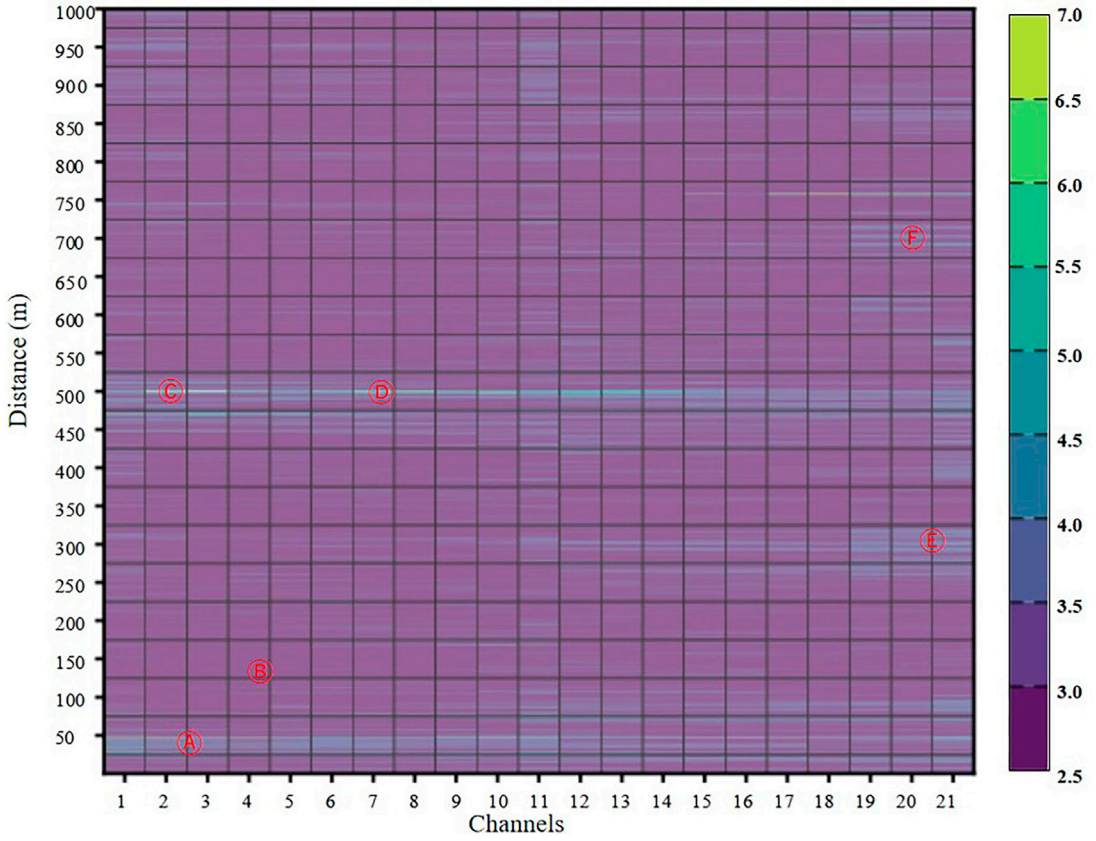

FIGURE 14
Distribution map of SPR and the core of the detected road.

5 Field test

5.1 Test scheme

To further verify the effect of the SPR method, this paper relied on a highway reconstruction construction project in Linyi City, Shandong province, for a field test. The highway has been serviced for more than 10 years, with the asphalt pavement surface thickness of 6 cm AC-20 asphalt mixture and an upper layer of 4-cm-thick SMA-13 asphalt mixture. The effective detection width of the empty coupling antenna used in this detection is 1.5 m. The leading equipment of GPR included the following: a driving computer, GPS, RTK, ranging wheel, radar host, and DX1821 air coupling antenna. For emergency lane detection, we collected the data by a 3D radar into 3DR-Examiner software for pretreatment, and then, we used MATLAB to extract the depth of the amplitude data. We calculated the global stacking peak ratio and its distribution, selected abnormal SPR areas for GPS coordinates, and determined the specific location using RTK for accurate positioning of abnormal areas with core verification. The acquisition parameters were as follows: sampling interval 1 cm, 35 ns at sampling, 1 μs at residence, and driving speed less than 20 km/h. The total length of the test is 1 km, and the test line was located in the left half of the emergency lane of the expressway, which is close to the white solid line of the right road. The core samples were subjected to a direct shear test if necessary.

5.2 Interpretation of results

The SPR macro-distribution map, Figure 14, generated by the SPR method, is utilized for core validation in regions with multiple SPRs, and the illustration of pavement cores is shown in Figure 15. It can be observed that at core sample position A, the average SPR value of 4.873 indicates inadequate interlayer bonding potential. Conversely, at core sample position B, an average SPR value of 2.825 suggests an excellent interlayer bonding performance. In the region surrounding core-sample C, an average SPR value of 5.981 implies poor interlayer adhesion and a likelihood of interlayer separation; this has been confirmed through subsequent core verification procedures. Similarly, near to core sample D, an average SPR value of 5.749 indicates poor interlayer bonding and an actual occurrence of interlayer separation in drilled cores. The mean SPR values around cores E and F are measured as 3.983 and 4.112, respectively; these signify potential stripping defect sites due to inadequate interlayer bonding. Furthermore, the maximum shear strength recorded for samples A, B, E, and F are measured as l.21, 1.65, 1.40, and l.36 MPa, respectively. These field results demonstrate

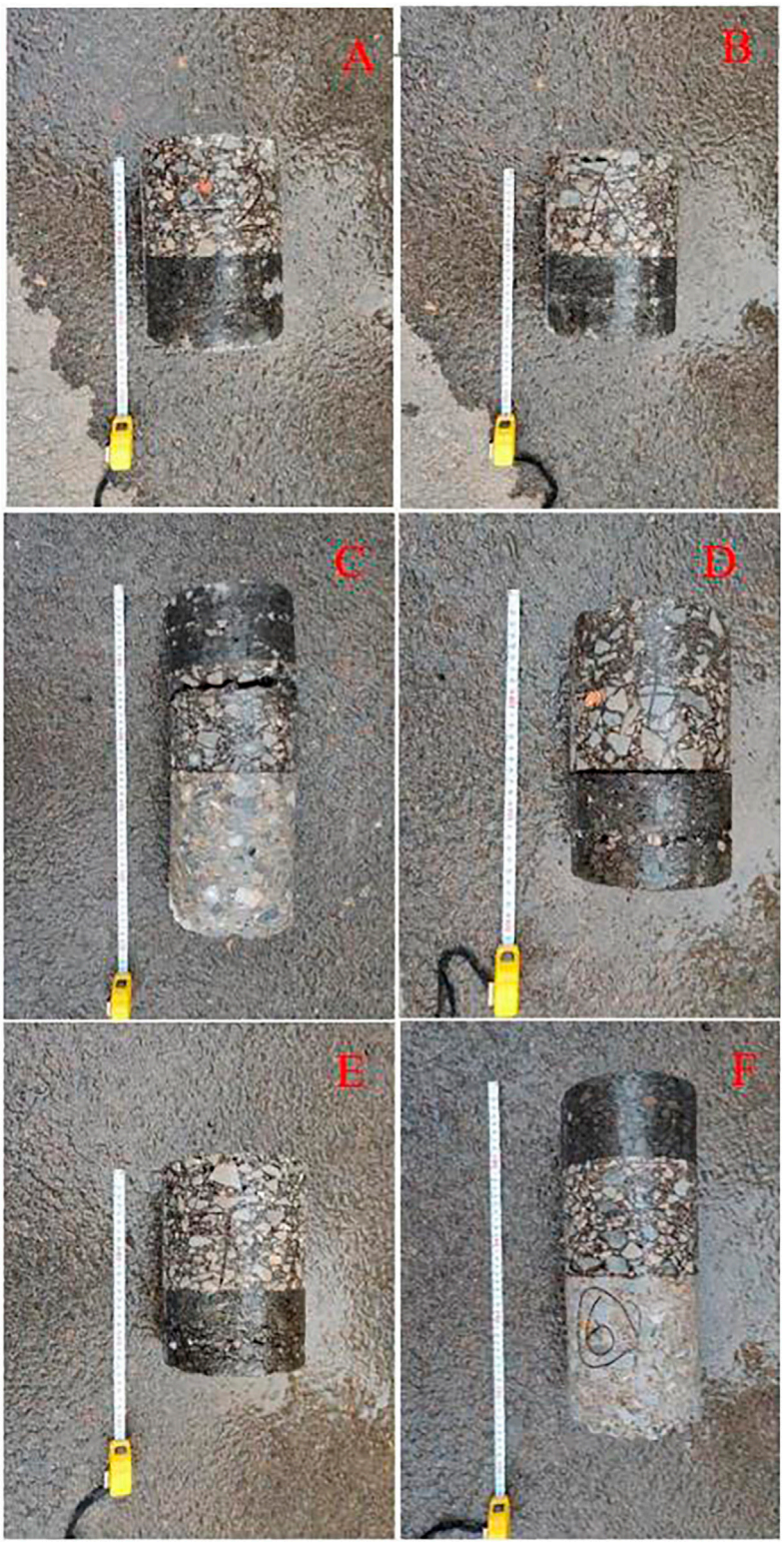

FIGURE 15
Illustration of pavement cores with varying SPR. SPR of cores: **(A)** 4.873; **(B)** 2.825; **(C)** 5.981; **(D)** 5.749; **(E)** 3.983; **(F)** 4.112.

that the use of the SPR method effectively identifies existing defects while also predicting possible future issues related to asphalt pavement evaluation. The SPR method requires a rapid and comprehensive evaluation approach for pavement bonding during road maintenance and repair, thus establishing a basis for precise and environmental friendly maintenance.

6 Conclusion

This paper introduces the method of the principle of the stacking peak ratio method, studies the best parameters of this method, compares the results with the direct shear test, finally analyzes the existing interlayer bonding state, and obtains the following conclusions eventually:

(1) The interlayer bonding state of the asphalt pavement can be determined by superimposing the ratio of the peak interlayer amplitude and the peak surface reflection amplitude as the radar wave reflection image at the poor interlayer bonding of the asphalt pavement will significantly enhance the amplitude of the positive axis direction.
(2) The best test parameter for the SPR method is found to be the time window of 35 ns and the residence time of 1 μs through comparison testing of specimens with various bonding states.
(3) It is demonstrated that the SPR method of the same specimen is inversely proportional to the maximum shear strength and that the regularity of diverse specimens of the two ways is consistent by comparing the SPR method and direct shear test of different bonding materials and different contamination layers.
(4) The outcomes of field tests demonstrate that the SPR approach performs well in assessing the current bad bonding and anticipating the inadequacies of possible bonding defects, offering a practical tool for quickly assessing the bonding state of the asphalt pavement.

Data availability statement

The datasets presented in this article are not readily available due to commercial restrictions, as the raw data was generated at Shandong Hi-Speed Group Co. Derived data supporting the findings of this study are available from the corresponding author Longting Ding on request.

Author contributions

WZ: conceptualization, methodology, and writing—original draft. LN: formal analysis and writing—original draft. SW: investigation, software, and writing—review and editing. HW: project administration, resources, and writing—original draft. LD: writing—review and editing.

Funding

The authors declare that no financial support was received for the research, authorship, and/or publication of this article.

Conflict of interest

Authors WZ, SW, and LD were employed by Shandong Hi-Speed Group Co, Ltd.

The remaining authors declare that the research was conducted in the absence of any commercial or financial relationships that could be construed as a potential conflict of interest.

Publisher's note

All claims expressed in this article are solely those of the authors and do not necessarily represent those of their affiliated organizations, or those of the publisher, the editors, and the reviewers. Any product that may be evaluated in this article, or claim that may be made by its manufacturer, is not guaranteed or endorsed by the publisher.

References

Cao, Q., and Al-Qadi, I. L. (2021). Effect of moisture content on calculated dielectric properties of asphalt concrete pavements from ground-penetrating radar measurements. *Remote Sens. (Basel)* 14, 34. doi:10.3390/rs14010034

Dawei, W., Haotian, L., Fujiao, T., Chengsen, Y., and Pengfei, L. (2022). Intelligent detection technology of contact state between asphalt pavement layers based on 3D ground penetrating radar technology. *J. Beijing Univ. Technol.* 2022, 48. doi:10.11936/bjutxb2021110016

Dong, Z., Ye, S., Gao, Y., Fang, G., Zhang, X., Xue, Z., et al. (2016). Rapid detection methods for asphalt pavement thicknesses and defects by a vehicle-mounted ground penetrating radar (GPR) system. *Sensors (Basel)* 16, 2067. doi:10.3390/s16122067

Jiang, W., Yuan, D., Shan, J., Ye, W., Lu, H., and Sha, A. (2020). Experimental study of the performance of porous ultra-thin asphalt overlay. *Int. J. Pavement Eng.* 23, 2049–2061. doi:10.1080/10298436.2020.1837826

Khamzin, A. K., Varnavina, A. V., Torgashov, E. V., Anderson, N. L., and Sneed, L. H. (2017). Utilization of air-launched ground penetrating radar (GPR) for pavement condition assessment. *Constr. Build. Mater* 141, 130–139. doi:10.1016/j.conbuildmat.2017.02.105

Leng, Z., Al-Qadi, I. L., and Lahouar, S. (2011). Development and validation for *in situ* asphalt mixture density prediction models. *NDT E Int.* 44, 369–375. doi:10.1016/j.ndteint.2011.03.002

Ma, Y., Elseifi, M. A., Dhakal, N., Bashar, M. Z., and Zhang, Z. (2021). Non-destructive detection of asphalt concrete stripping damage using ground penetrating radar. *J. Transp. Res. Board* 2675, 938–947. doi:10.1177/03611981211014199

Mohammad, L. N., Raqib, M., and Huang, B. (2002). Influence of asphalt tack coat materials on interface shear strength. *J. Transp. Res. Board* 1789, 56–65. doi:10.3141/1789-06

Raouf, M. A., and Williams, R. C. (2010). Temperature and shear susceptibility of a nonpetroleum binder as a pavement material. *J. Transp. Res. Board* 2180, 9–18. doi:10.3141/2180-02

Sala, J., Penne, H., and Eide, E. (2012). "Time-frequency dependent filtering of step-frequency ground penetrating radar data," in 2012 14th International Conference on Ground Penetrating Radar (GPR), Shanghai, China, 04-08 June 2012 (IEEE).

Soldovieri, F., Solimene, R., Lo Monte, L., Bavusi, M., and Loperte, A. (2011). Sparse reconstruction from GPR data with applications to rebar detection. *IEEE Trans. Instrum. Meas.* 60, 1070–1079. doi:10.1109/tim.2010.2078310

Sudyka, J., and Krysiński, L. (2011). Radar technique application in structural analysis and identification of interlayer bonding. *Int. J. Pavement Res. Technol.* 4, 176–184. doi:10.1046/j.1365-313X.1994.6020225.x

Tashman, L., Nam, K., Papagiannakis, T., Willoughby, K., Pierce, L., and Baker, T. (2008). Evaluation of construction practices that influence the bond strength at the interface between pavement layers. *J. Perform. Constr. Facil.* 22, 154–161. doi:10.1061/(asce)0887-3828(2008)22:3(154)

Wang, X., Su, Z., Xu, A., Zhou, A., and Zhang, H. (2017). Shear fatigue between asphalt pavement layers and its application in design. *Constr. Build. Mater* 135, 297–305. doi:10.1016/j.conbuildmat.2016.12.151

Yuan, D., Jiang, W., Sha, A., Xiao, J., Wu, W., and Wang, T. (2023). Technology method and functional characteristics of road thermoelectric generator system based on Seebeck effect. *Appl. Energy* 331, 120459. doi:10.1016/j.apenergy.2022.120459

Zhang, K., Zhang, Z., and Luo, Y. (2018). Inspection method and evaluation standard based on cylindrical core sample for rutting resistance of asphalt pavement. *Meas. (Lond)* 117, 241–251. doi:10.1016/j.measurement.2017.12.002

Zhang, W. (2017). Effect of tack coat application on interlayer shear strength of asphalt pavement: A state-of-the-art review based on application in the United States. *Int. J. Pavement Res. Technol.* 10, 434–445. doi:10.1016/j.ijprt.2017.07.003

frontiers | Frontiers in Energy Research

TYPE Original Research
PUBLISHED 10 November 2023
DOI 10.3389/fenrg.2023.1314242

OPEN ACCESS

EDITED BY
Meng Jia,
Shandong University of Science and Technology, China

REVIEWED BY
Fan Zhang,
Aalto University, Finland
Wentong Wang,
Shandong University of Science and Technology, China

*CORRESPONDENCE
Xinkui Yang,
yangxk@whut.edu.cn

RECEIVED 10 October 2023
ACCEPTED 31 October 2023
PUBLISHED 10 November 2023

CITATION
Tu B, Yang X, Xu S, Zhao Z, Zhou Y, Jiang J, Fan L and Tu L (2023), Road performance evaluation of prestressed high-strength concrete pile waste powder as alternative filler in asphalt concrete.
Front. Energy Res. 11:1314242.
doi: 10.3389/fenrg.2023.1314242

Road performance evaluation of prestressed high-strength concrete pile waste powder as alternative filler in asphalt concrete

Botao Tu[1], Xinkui Yang[2]*, Shi Xu[3,4], Zenggang Zhao[2], Yuheng Zhou[2], Jian Jiang[5], Lulu Fan[5] and Liangliang Tu[5]

[1]Guangdong Hongye Building Materials Technology Co., Ltd., Yunfu, Guangdong, China, [2]State Key Laboratory of Silicate Materials for Architectures, Wuhan University of Technology, Wuhan, China, [3]School of Civil Engineering and Architecture, Wuhan University of Technology, Wuhan, China, [4]Faculty of Civil Engineering and Geosciences, Delft University of Technology, Delft, Netherlands, [5]Shenzhen Sez Construction Group Co., Ltd., Shenzhen, Guangdong, China

As a kind of solid waste, using Prestressed High-Strength Concrete Pile Waste Concrete (PPWC) as the replacement for limestone filler in asphalt concrete can not only reduce the accumulation of PPWC and increase its utilization but also avoid the increased road construction costs and environmental degradation associated with limestone mining. This study aims to investigate the effect of using PPWC filler to replace limestone filler on the road performance of asphalt concrete. Firstly, PPWC was ground into filler particles with a diameter less than 0.075 mm. The particle characteristics such as surface morphology, particle size distribution and chemical composition of PPWC filler and limestone filler were compared. Then, PPWC filler was used to replace limestone filler with different volume fractions to prepare asphalt concrete, and the water damage resistance, high-temperature rutting resistance, low-temperature crack resistance, fatigue resistance and adhesion performance of asphalt concrete were tested. The results showed that PPWC filler has a smaller particle size and rougher surface than limestone filler, and it contains $Ca(OH)_2$ produced by hydration. The addition of PPWC filler can effectively improve the mechanical properties of asphalt concrete without reducing its water damage resistance. PPWC filler can improve the high-temperature rutting resistance and low-temperature crack resistance of asphalt concrete, but reduce its low-temperature fatigue resistance. The low content of PPWC filler will enhance the adhesion between asphalt mortar and aggregate. However, when the content of PPWC filler exceeds 50%, Ca $(OH)_2$ in PPWC will reduce the adhesion between acid asphalt mortar and alkaline basalt aggregate. Therefore, the use of PPWC as filler in asphalt mixtures provides a reliable solution for the sustainable development of road materials.

KEYWORDS

PHC pile waste concrete, filler, particle characteristics, asphalt concrete, road performance

1 Introduction

Prestressed High-Strength Concrete Pile (PHC pile), as a type of hollow cylindrical precast concrete pile, is widely used in foundation engineering of bridges, tunnels and other buildings to improve the stability of buildings (Liu et al., 2019; Li et al., 2021; Li et al., 2023). China is the world's largest producer of PHC pile, with a production volume reaching 486.28 million meters in 2022 (Chen et al., 2019). However, for two main reasons, China generates a significant amount of waste PHC pile each year. On the one hand, during the manufacturing process, PHC pile may develop defects, such as cracks or non-compliance with specifications. These defects can render PHC pile unusable for construction, thus becoming waste materials. On the other hand, aging buildings or structures may require maintenance, renovation, or demolition. In such cases, PHC pile may need to be removed and replaced, resulting in the generation of a significant amount of waste pile (Yu et al., 2021). Sua-iam and Makul (2023) used PHC pile waste concrete (PPWC) to replace natural aggregates to prepare green self-compacting concrete. The results show that PPWC can improve the compressive strength of concrete and can significantly reduce the production cost of high-performance concrete. However, there are still few studies on the recycling of PPWC in roads and construction engineering, and a large amount of PPWC is accumulated in factories and cannot be treated. Therefore, the utilization of PPWC has emerged as an essential issue that requires attention.

China's road infrastructure construction has experienced rapid development. In 2022, the total length of China's road network reached 5.3548 million kilometers, and the total length of expressways reached 177,300 km (Yang et al., 2023). Among these roads, asphalt concrete pavement, known for its advantages of low noise, high comfort, and easy construction, is the primary road surface material (Yang et al., 2022; Gong et al., 2023; Lv et al., 2023; Xie et al., 2023). Especially in the construction of expressways in China, the proportion of asphalt concrete pavement exceeds 90% (Cui et al., 2021; Li et al., 2022b; Osuolale et al., 2023). Typically, asphalt concrete is composed of asphalt, aggregates, and mineral fillers (Taherkhani and Vahabi Kamsari, 2020; Jia et al., 2022). The shape and size of mineral fillers can impact asphalt's flowability, consequently influencing the construction performance of asphalt concrete (Xing et al., 2019; Zhang et al., 2020; Belayali et al., 2023). Moreover, mineral fillers can fill the voids in asphalt concrete, enhancing its strength and thus improving the durability of road structures (Amirbayev et al., 2022; Russo et al., 2022; Wei et al., 2022). Limestone filler is the most commonly used mineral filler. However, mineral resources are being depleted due to the rapid development of the road industry, resulting in increased costs and environmental degradation associated with limestone extraction (Liu N. et al., 2023; Ou et al., 2023). Therefore, the adoption of more sustainable materials as alternatives to limestone fillers to reduce mineral resource consumption and mitigate environmental impacts is crucial (Liu et al., 2018; Liu J. et al., 2023). Which is also consistent with the goal of sustainable development, prompting the road industry to pay more attention to environmental protection and resource conservation (Yang et al., 2021; Sun et al., 2023).

There have been studies reporting solid waste can be used in place of mineral filler in asphalt concrete (Habibnejad Korayem et al., 2020; Das and Singh, 2021; Liu N. et al., 2023). Paul et al. (2021) used fly ash (FA) and glass powder (GP) to replace limestone filler in steel slag asphalt mixture, and investigated the water damage resistance and rutting resistance of asphalt concrete. The findings indicate that FA and GP greatly increased the stiffness of steel slag asphalt concrete, resulting in enhanced anti-rutting performance, but slightly reduced the water damage resistance of asphalt concrete. Osuolale et al. (2023) used bamboo leaf ash (BLA) as filler in asphalt mixture and investigated the road performance of asphalt concrete. They found that in addition to enhancing asphalt concrete's volume stability, rutting resistance, and low-temperature cracking resistance, BLA filler can also strengthen the adhesion between asphalt mortar and aggregate, but the fatigue life and anti-skid performance of asphalt concrete were reduced. Yang et al. (2021) used diatomite and bauxite residues to replace the traditional mineral fillers in asphalt concrete and studied the mechanical properties, anti-aging properties and leaching characteristics of porous asphalt mixtures. They found that asphalt concrete's aging and raveling resistance can be improved by using diatomite and bauxite residue fillers, but the leaching concentration of heavy metals in asphalt concrete also increased, which may be raise the risk of environmental pollution. Zhang et al. (2018) used red mud in place of limestone fillers to prepare asphalt concrete, and systematically studied its anti-rutting performance. The results show that red mud filler can increase the complex modulus and phase angle of asphalt mortar, enhance the elastic behavior of asphalt mortar, and lead to the significant improvement of rutting resistance of asphalt concrete at high-temperature. The influence of coal gangue filler on the road performance and crack healing ability of asphalt concrete were investigated by Li et al. (2022a). The findings indicate that coal gangue filler was beneficial to enhance asphalt concrete's low-temperature crack resistance. When the content of coal gangue filler was 50%, asphalt concrete showed the best microwave self-healing capacities.

In conclusion, using solid waste materials instead as mineral fillers can maximize the use of waste resources, lower the cost of raw materials, and enhance the working properties of asphalt concrete. However, the research on using PPWC as the filler in asphalt concrete remains limited. The effect of PPWC filler on the asphalt concrete's road performance awaits further investigation.

This study used PPWC as filler to prepare asphalt concrete to evaluate the impact of replacing limestone filler with PPWC filler in asphalt concrete on the road performance of asphalt concrete. Firstly, by using the planetary ball mill, PPWC was crushed into powder with a particle size less than 0.075 mm. Both the PPWC filler and the limestone filler's particle characteristics were investigated. Then, asphalt concrete was prepared by using PPWC filler to replace limestone fillers with different volume ratios (25%, 50%, 75%, and 100%). Then, Standard Marshall tests, immersion Marshall tests, freeze-thaw splitting tests, rutting tests, bending beam tests, indirect tensile fatigue tests and Cantabro tests were conducted to investigate the water damage resistance, high-temperature rutting resistance, low-temperature crack resistance, fatigue resistance and adhesion performance of asphalt concrete with different PPWC filler contents. The study results will provide a theoretical basis for the application of PPWC filler in asphalt concrete. The research process is shown in Figure 1.

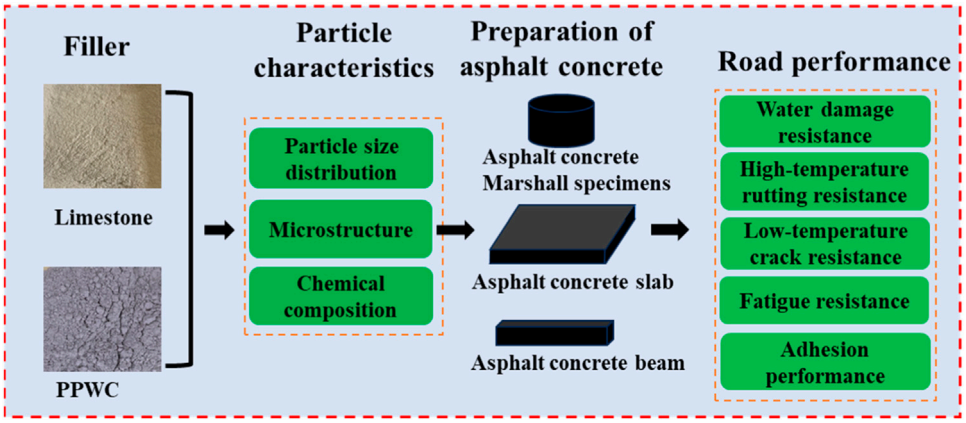

FIGURE 1
Research flow chart.

TABLE 1 Basic properties of SBS modified asphalt.

Properties	Test value
Density/(g/cm^3)	1.033
Penetration (25°C)/0.1 mm	55
Softening point/°C	76
Ductility 5 cm/min (5°C)/cm	29
Dynamic viscosity (135°C)/(Pa·s)	2.25

2 Materials and methods

2.1 Raw materials

SBS-modified asphalt from China's Hebei Province was selected as the basis asphalt. Its basic properties were tested according to the Chinese standard JTG E20-2011 (China, 2011), Table 1 lists the results. The basalt aggregate came from a quarry in the Chinese province of Hubei's Jingshan City. Its basic properties were tested according to the Chinese standard JTG E42-2005 (China, 2005), Table 2 displays the results. The quarry in Wuhan, Hubei Province, China provided the limestone filler, while a PHC pile producer in Yunfu, Guangdong Province, China provided the PPWC. PPWC was ground at 500 rpm for 40 min to a particle diameter of less than 0.075 mm.

The basic properties of PPWC and limestone filler were assessed in accordance with Chinese standard JTG-E42-2005 (China, 2005). Table 3 displays the results. It demonstrated that the density of the PPWC filler was slightly lower than that of the limestone filler. The hydrophilic coefficient, which is used to evaluate the filler's adhesive properties to the asphalt binder, is the ratio of the filler's volume in water to that of the filler's volume in kerosene. According to the results, PPWC filler has a hydrophilic coefficient of 0.78, which means that it has a stronger affinity for asphalt than for water and satisfies the standards' requirements.

2.2 Preparation of asphalt concrete

The SMA-13 gradation was designed and the oil-aggregate ratio was defined as 5.6% based on Marshall design according to the

TABLE 2 Basic properties of basalt aggregate.

Properties		Basalt aggregate	Standard requirements JTG E42-2005
Apparent specific gravity	2.36–4.75 mm	2.903	≥2.6
	4.75–9.5 mm	2.932	≥2.6
	9.5–16 mm	2.915	≥2.6
Water absorption (%)	2.36–4.75 mm	1.05	≤3
	4.75–9.5 mm	0.72	≤3
	9.5–16 mm	0.57	≤3
Los Angeles abrasion (%)		20.7	≤28
Crushed value (%)		16.7	≤26
Polished value (%)		46	≥42
Adhesion level		4	≥4

TABLE 3 Basic properties of limestone filler and PPWC filler.

Properties	Limestone	PPWC	Standard requirement JTG-E42-2005
Density/(g/cm^3)	2.72	2.66	≥2.50
Hydrophilic coefficient	0.75	0.78	≤1.00

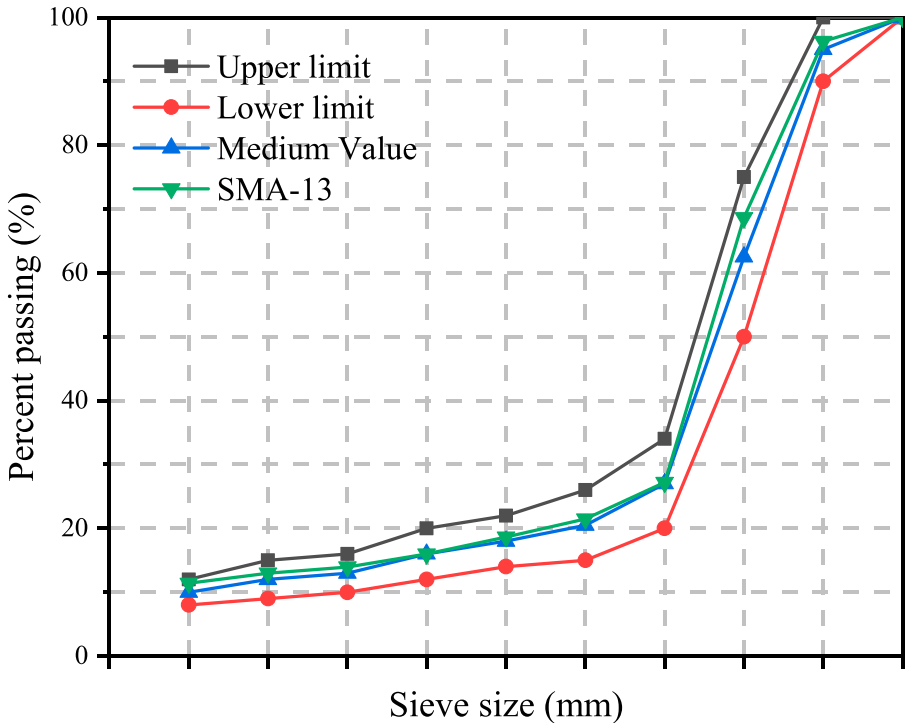

FIGURE 2
Grading curve of SMA-13.

Chinese standard JTG D50-2017 (China, 2017), and five kinds of asphalt concrete were prepared by replacing 25%, 50%, 75%, and 100% volume of limestone filler with PPWC filler. Considering the low content of fillers in asphalt concrete, their influence on aggregate gradation selection was minimal. Therefore, the gradation of the five kinds of asphalt concrete was the same, as shown in Figure 2.

2.3 Experimental methods

2.3.1 Particle characteristics

Scanning electron microscopy (SEM, Zeiss Gemini 300, Carl Zeiss AG, Germany) and laser particle size analyzer (Mastersizer 3,000, Malvern Panalytical, Germany) were used to examine the surface morphology and particle size distribution of PPWC and limestone filler. X-ray fluorescence (XRF) and X-ray diffraction (XRD) tests were used to determine the chemical composition and phase distribution of the two fillers.

2.3.2 Water damage resistance

According to the Chinese standard JTG E20–2011 (China, 2011), standard Marshall test, immersion Marshall test, and freeze-thaw splitting test were conducted, with six parallel samples for each test. The Retained Marshall Stability (RMS) and Tensile Strength Ratio (TSR) were retained to assess the water damage resistance performance of the asphalt concrete.

When testing the RMS, the Marshall specimens with a diameter of 101.6 mm and a thickness of 63.5 mm were immersed in a constant temperature water tank at 60°C for 48 h. The RMS of the asphalt concrete was determined using the following equation:

$$RMS = \frac{MS_n}{MS_0} \times 100\% \quad (1)$$

Where MS_0 is the average Marshall stability of asphalt concrete, kN; MS_n is the average Marshall stability after soaking in a constant temperature water tank at 60°C for 48 h, kN.

In the test of TSR, the Marshall specimen with a diameter of 101.6 mm and a thickness of 63.5 mm was frozen at −18°C for 16 h, and then placed in a constant temperature water tank at 60°C for 24 h. Finally, the Marshall specimen was kept in a constant temperature water tank at 25°C for 2 h to test its splitting tensile strength (STS). The TSR of the asphalt concrete was determined using the following equation:

$$TSR = \frac{STS_n}{STS_0} \times 100\% \quad (2)$$

Where STS_0 is the average STS of asphalt concrete, MPa; STS_n is the average STS of asphalt concrete after freeze-thaw damage, MPa.

2.3.3 High-temperature rutting resistance

According to the Chinese standard JTG E20–2011 (China, 2011), the asphalt concrete slab with a size of 300 × 300 × 50 mm was prepared, and a wheel tracking device was used to conduct the rutting test to evaluate the high-temperature rutting resistance of asphalt concrete. The width of the wheel was 50 mm and the load was 0.7 MPa. At 60°C. The wheel moved back and forth in the central area of the asphalt concrete slab at a speed of 42 times/min for 60 min to obtain dynamic stability and rutting depth.

2.3.4 Low-temperature crack resistance

According to the Chinese standard JTG E20–2011 (China, 2011), asphalt concrete beams with a size of 250 mm × 30 mm × 35 mm were prepared to conduct bending beam test at −10°C to test the low-temperature cracking resistance of asphalt concrete.

2.3.5 Fatigue resistance

The Marshall specimen with a diameter of 101.6 mm and a thickness of 63.5 mm was cut to a thickness of 40 mm, and the fatigue life of five kinds of asphalt concrete was tested by indirect tensile fatigue test. The test temperature was set to 15°C. Before the test, the stress level is determined according to the splitting strength of asphalt concrete.

2.3.6 Adhesion performance

According to the Chinese standard JTG E20–2011 (China, 2011), the impact of PPWC filler on asphalt-aggregate adhesion performance was evaluated by Cantabro test. The Marshall specimen with a diameter of 101.6 mm and a thickness of 63.5 mm was immersed in a constant temperature water tank at 20°C for 20 h and taken out. After being placed at room temperature for 24 h, it was placed in a Los Angeles tester and rotated at the speed of 30 r/min for 300 revolutions. The scattering loss is calculated according to the following equation:

$$\Delta S = \frac{m_0 - m_1}{m_0} \times 100 \quad (3)$$

Where ΔS is the scattering loss of asphalt concrete, m_0 is the mass of Marshall specimen when it is taken out from the water tank, m_1 is the residual mass of Marshall specimen after rotation.

3 Results and discussions

3.1 Particle characteristics of filler

3.1.1 Surface morphology of filler

The micro-morphology of PPWC and limestone filler is depicted in Figures 3A, B after being magnified 10,000 times, respectively. It is clear that the PPWC filler's surface is covered in the gel products created by hydration, and it has a rougher surface than the limestone filler. The study by Zhao et al. (2021) found that filler with rougher surfaces is beneficial for increasing the density, stability and skid resistance of asphalt concrete. The limestone filler, in comparison, has an uneven surface made up of smooth flakes. The abundant angularity on the surface of PPWC fillers can enhance the interaction forces between asphalt and filler particles, thereby improving the mechanical properties of asphalt concrete.

3.1.2 Particle size distribution of filler

Figure 4 displays the particle size distribution curves for the two fillers. The results indicate that PPWC filler has a smaller average particle size (12.53 μm) than limestone filler (15.49 μm) and a larger specific surface area (1.78 m^2/g) than limestone filler (1.45 m^2/g). This may be because in comparison to limestone filler, PPWC filler has a rougher surface as well as smaller particle size and density.

3.1.3 Chemical composition of filler

Figure 5 shows the oxide composition of PPWC and limestone fillers. It can be observed that the main oxides in both PPWC filler and limestone filler are CaO and SiO_2. Since calcium carbonate makes up the majority of limestone filler, its CaO content is larger (58.87%) than that of PPWC (37.17%). However, The SiO_2 content of PPWC filler (34.31%) is larger than that of limestone filler (18.98%), which may be due to the existence of SiO_2-rich aggregates such as sand and crushed stone in PPWC.

Figure 6 shows the XRD curves for PPWC filler and limestone filler. The results show similar mineral compositions between the two fillers, with SiO_2 and $CaCO_3$ as the major crystalline phases. The diffraction peak of Ca $(OH)_2$ is apparent on the PPWC's XRD curve, though. This may be related to the hydration of the cement during the production of PHC piles. As the cementitious material for the preparation of PHC piles, the CaO contained in the cement will react with H_2O to form Ca $(OH)_2$.

3.2 Road performance

3.2.1 Water damage resistance

The RMS results of asphalt concrete are shown in Figure 7. It is evident that the Marshall stability of asphalt concrete increased with the increase of PPWC filler content. Compared with limestone filler asphalt concrete, the Marshall stability of asphalt concrete increased by 4.9%, 10.8%, 16.7%, and 20.6% respectively when PPWC filler was used to replace 25%, 50%, 75%, and 100% volume of limestone filler. The RMS of the five kinds of asphalt concrete had no significant difference, which is about 93%, meeting the requirements of the Chinese standard JTG/T 3350-03-2020 (higher than 85%). According to the results, using PPWC filler can improve asphalt concrete's stability, which may be due to the rougher surface of PPWC filler than limestone filler, so the friction between PPWC filler particles and asphalt is stronger, thereby enhancing the structural stability of asphalt concrete.

The TSR results of asphalt concrete are shown in Figure 8. It is evident that as the content of PPWC filler rose, the splitting strength of asphalt concrete also increased. When the content of PPWC filler increased from 25% to 100%, compared with limestone filler asphalt concrete, the splitting strength of Marshall specimens before freeze-thaw damage increased by 3.2%, 14%, 20.4%, and 25.8%, respectively, which was consistent with the trend of Marshall

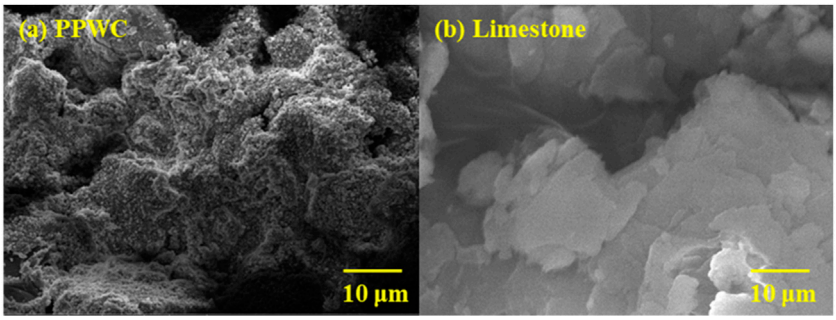

FIGURE 3
SEM images of PPWC filler and limestone filler, **(A)** PPWC filler, **(B)** limestone filler.

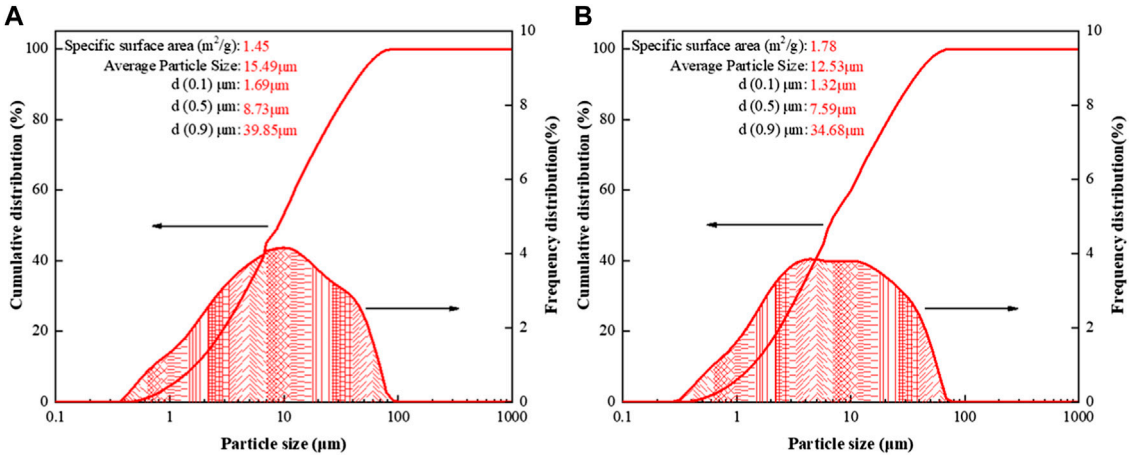

FIGURE 4
Particle size distribution curves of the two fillers, **(A)** limestone filler, **(B)** PPWC filler.

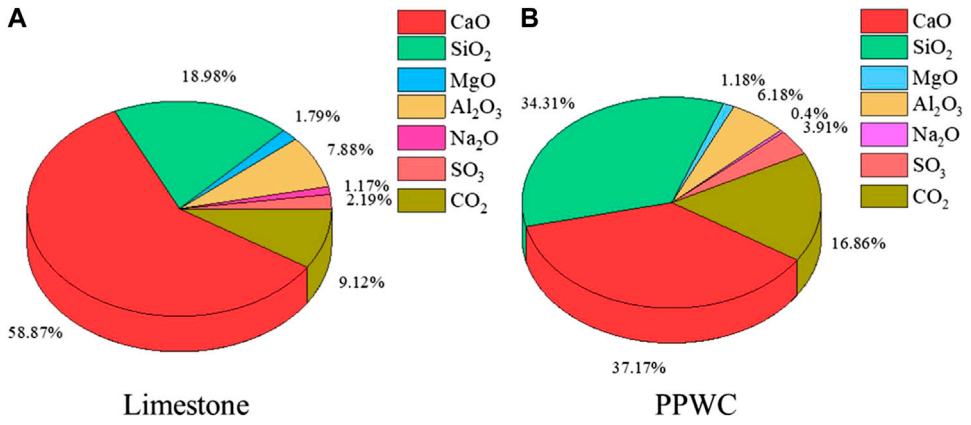

FIGURE 5
The oxide composition of PPWC filler and limestone filler, **(A)** Limestone filler, **(B)** PPWC filler.

stability. The TSR of the five kinds of asphalt concrete is very close, all around 92.5%, which satisfies the requirements of the Chinese standard JTG/T 3350-03-2020 (higher than 80%). Combined with the results of RMS, it is shown that the incorporation of PPWC filler can significantly enhance the mechanical properties of asphalt concrete without reducing its water damage resistance.

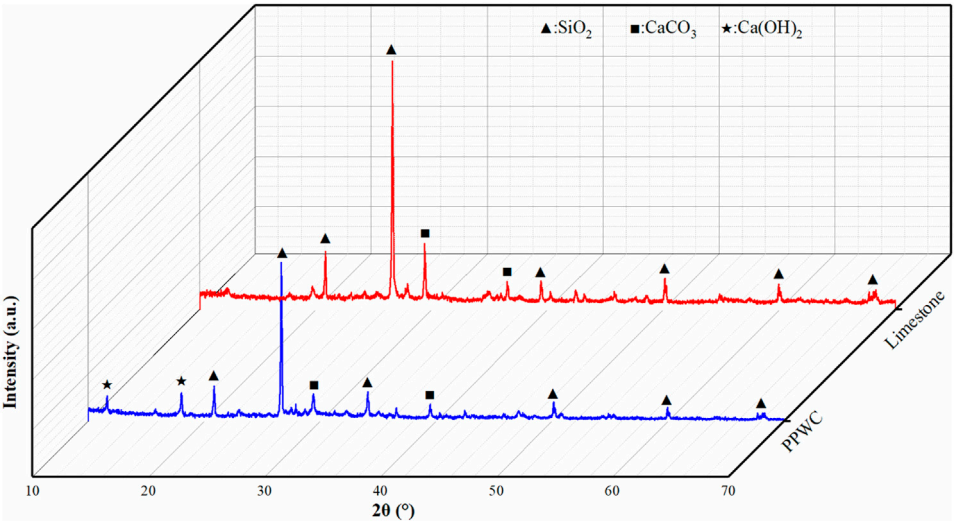

FIGURE 6
XRD curves of PPWC filler and limestone filler.

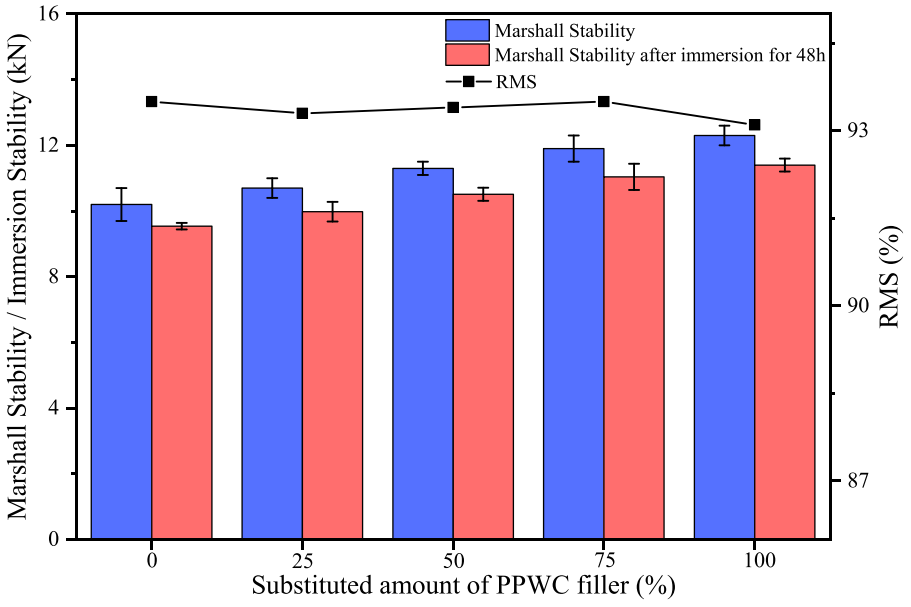

FIGURE 7
The results of Retained Marshall Stability (RMS).

3.2.2 High-temperature rutting resistance

Rutting test can assess the rutting resistance of asphalt concrete at high-temperatures. The dynamic stability and rutting depth of five kinds of asphalt concrete slabs are depicted in Figure 9 based on the results of the rutting test. It can be seen that the dynamic stability of asphalt concrete improved and the depth of rutting decreased with an increase in PPWC filler content. Compared with limestone filler asphalt concrete, when the content of PPWC filler increased from 25% to 100%, the dynamic stability of asphalt concrete increased by 1.2%, 3.7%, 4.8%, and 6.3% respectively, and the rutting depth decreased from 3.32 mm to 3.21 mm, 3.08 mm, 2.93 mm, and 2.81 mm respectively. The dynamic stability of the five kinds of slab specimens is higher than 5,000 times/mm, which is sufficient for engineering application. The modification effect of filler on asphalt can significantly affect the high-temperature stability of asphalt concrete. Compared to limestone filler, PPWC filler has smaller particles, rougher surface and greater specific surface area, so its adsorption capacity for asphalt is stronger than that of limestone filler. The free asphalt in asphalt concrete is transformed into structural asphalt under the adsorption of PPWC filler, thereby enhancing the stiffness of asphalt mortar. Therefore, the use of PPWC filler to replace limestone filler can make asphalt concrete

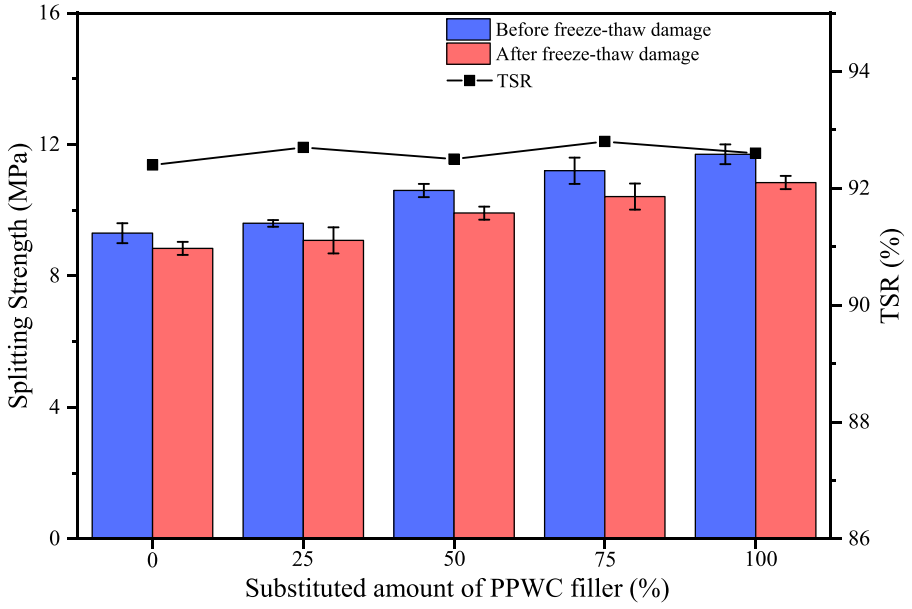

FIGURE 8
The results of Tensile Strength Ratio (TSR).

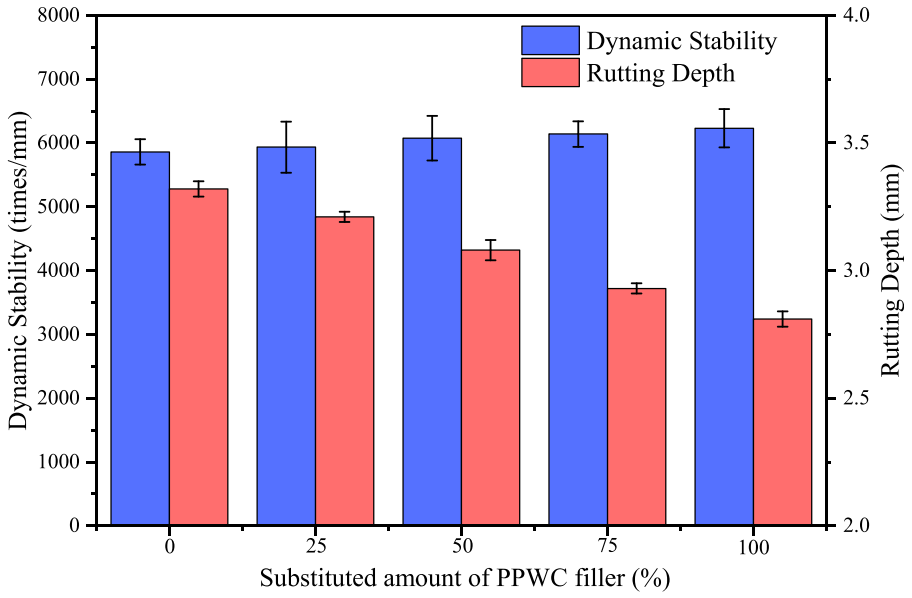

FIGURE 9
The results of high-temperature rutting test.

have stronger deformation resistance at high temperatures, so as to increase asphalt concrete's resistance to rutting at high temperatures and reduce the permanent deformation of asphalt concrete under high temperature rutting.

3.2.3 Low-temperature crack resistance

Table 4 shows the test results of low-temperature crack resistance of five kinds of asphalt concrete. Ultimate flexural tensile strength can represent the mechanical strength of asphalt concrete at low-temperature. Ultimate flexural tensile strain can characterize the deformability of asphalt concrete at low-temperature. The stiffness modulus, which measures the toughness of asphalt concrete, is the ratio of ultimate flexural tensile strength to ultimate flexural strain. It is evident that the influence of PPWC filler on ultimate flexural tensile strength and ultimate flexural tensile strain is inconsistent. With the increase of

TABLE 4 The results of bending tensile strain test.

Types	Ultimate flexural tensile strength (MPa)	Ultimate flexural tensile strain (με)	Stiffness modulus (MPa)
Limestone filler	10.124	3,121.2	3,243.6
25% PPWC filler	10.312	3,041.7	3,390.2
50% PPWC filler	10.428	2,989.7	3,488.0
75% PPWC filler	10.566	2,912.4	3,627.9
100% PPWC filler	10.728	2,853.3	3,759.9

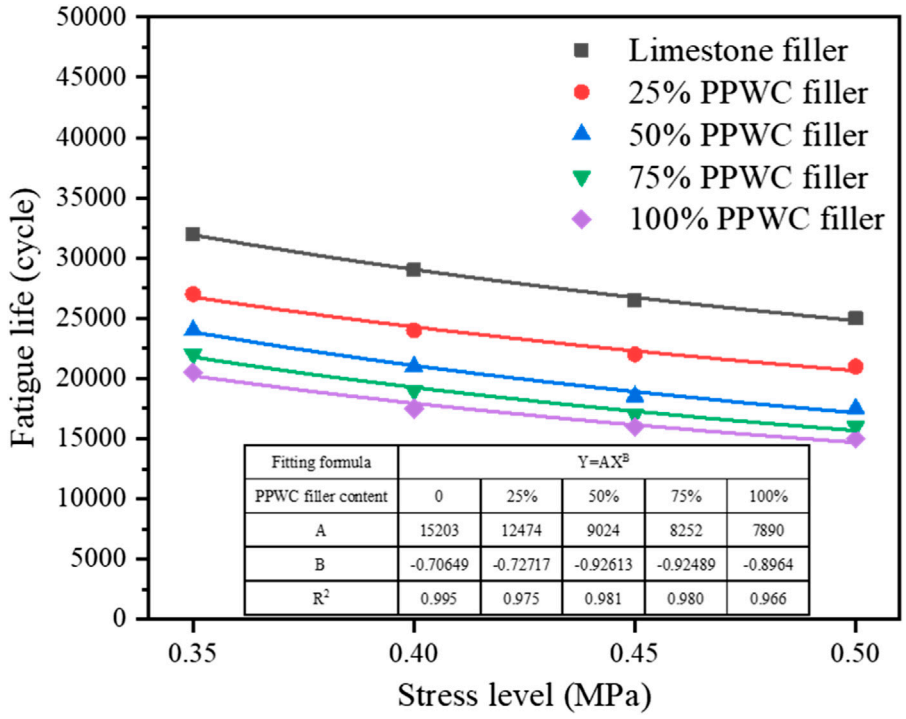

FIGURE 10
The results of fatigue life.

PPWC filler content, the ultimate flexural tensile strength and stiffness modulus of asphalt concrete increased, the ultimate flexural tensile strain of asphalt concrete decreased. This shows that at low-temperature, PPWC filler enhanced the mechanical strength of asphalt concrete, but reduced the toughness of asphalt concrete, resulting in a decrease in its deformability. This may be due to the hardening effect of PPWC filler on asphalt. PPWC filler is a kind of material with large specific surface area and rough surface. Its adsorption on asphalt enhances the stiffness of asphalt mortar, thus enhancing the strength of asphalt concrete. However, the ductility and fluidity of asphalt mortar decrease with the increase of stiffness at low-temperature, making asphalt concrete more prone to brittle failure, thus reducing the ultimate bending tensile strain.

3.2.4 Fatigue resistance

The fatigue life and fitting results of asphalt concrete under different stress levels are shown in Figure 10. As the stress level increased, it can be seen that asphalt concrete's fatigue life decreased. At the same stress level, the fatigue life of asphalt concrete decreased with the increase of PPWC filler content. As a kind of viscoelastic material, asphalt has a certain ability to repair micro-cracks. However, PPWC filler will harden asphalt mortar and reduce the response rate of asphalt concrete to stress, thus weakening the healing ability of asphalt to strain cracks, resulting in more brittle cracks in asphalt concrete under stress, which is in agreement with the findings of the bending strain test. Under the action of cyclic load, the brittle cracks in asphalt concrete continue to develop, which eventually leads to brittle fracture of asphalt concrete. Therefore, the asphalt concrete with higher PPWC filler content exhibits worse fatigue resistance.

3.2.5 Adhesion performance

Figure 11 shows the results of the Cantabro test. ΔS can characterize the adhesive capacity between asphalt mortar and aggregate. The smaller ΔS indicates the stronger adhesive capacity between asphalt mortar and aggregates. It is evident that

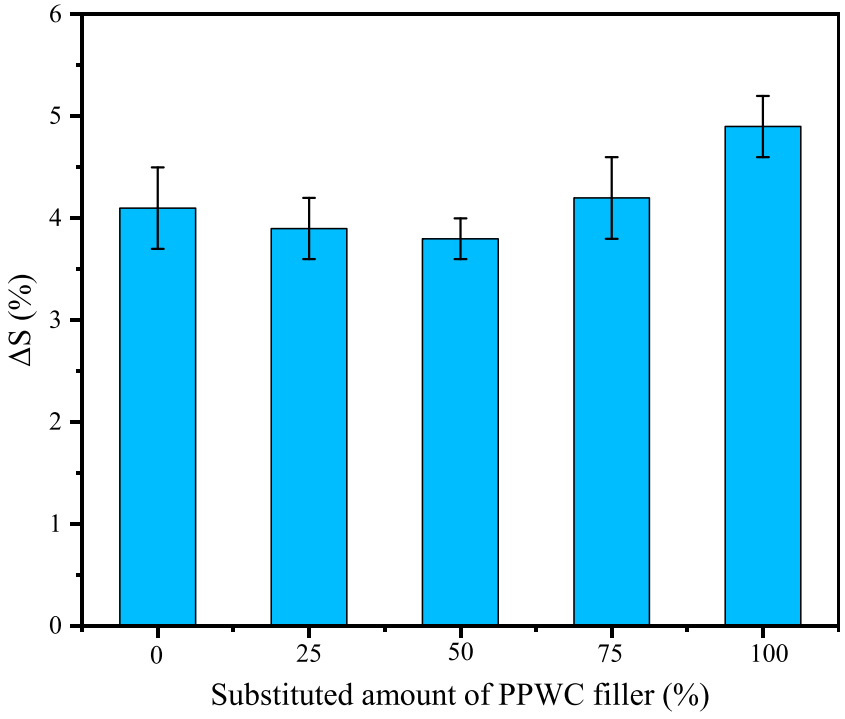

FIGURE 11
The results of Cantabro test.

the ΔS of asphalt concrete decreased first and then increased with the increase of PPWC content. When the content of PPWC filler was less than 50%, the ΔS of asphalt concrete was lower than that of limestone filler asphalt concrete, indicating that the adhesion between basalt aggregate and asphalt mortar was stronger. However, when the content of PPWC filler exceeded 50%, ΔS began to increase, indicating that the adhesion between basalt aggregate and asphalt mortar was weakened. PPWC filler has rough surface and high specific surface area. Therefore, the addition of low content of PPWC filler can improve the adsorption between filler and asphalt, enhance the compactness and cohesion of asphalt mortar, thereby improve the adhesion between asphalt mortar and basalt aggregate and reduce the ΔS of asphalt concrete. However, basalt is the typical alkaline aggregate. When high content of PPWC filler was added to asphalt, the Ca $(OH)_2$ produced by hydration in PPWC will reduce the acidity of asphalt mortar (Meng et al., 2023), thereby reducing the adhesion between asphalt mortar and basalt aggregate, resulting in the increase of ΔS.

4 Conclusion

This study aims to evaluate the effect of using PPWC filler to replace limestone filler in asphalt concrete on its road performance. Firstly, limestone and PPWC fillers' chemical and physical characteristics were examined. Then, five kinds of asphalt concrete were prepared by using PPWC filler to replace different volume of limestone filler (0, 25%, 50%, 75%, and 100%), and their road performance were tested. Based on the test results, the main conclusions are as follows.

(1) PPWC filler has a smaller particle size, lower density and rougher surface when compared to limestone filler. PPWC filler contains Ca $(OH)_2$ from hydration and has a lower CaO content than limestone filler.
(2) The addition of PPWC filler can improve the Marshall stability of asphalt concrete, but there is no significant difference in RMS and TSR of five kinds of asphalt concrete, indicating that the addition of PPWC filler can effectively improve the mechanical properties of asphalt concrete without reducing its water damage resistance.
(3) The use of PPWC filler to replace limestone filler can make asphalt concrete have stronger deformation resistance at high temperatures. The hardening effect of PPWC on asphalt concrete improves the low temperature crack resistance of asphalt concrete, but the fatigue resistance decreases.
(4) The rough surface of PPWC filler will enhance the adhesion between asphalt mortar and basalt aggregate. However, when the content of PPWC filler exceeds 50%, Ca $(OH)_2$ in PPWC will reduce the acidity of asphalt mortar, thus reducing the adhesion between asphalt mortar and the alkaline basalt aggregate.

The above conclusions show that PPWC filler can be used to replace limestone filler in asphalt concrete to maximize resource utilization, reduce raw material costs, and enhance road performance, thereby providing a new solution for the sustainable development of the road industry.

5 Limitations and further study

In this paper, the effect of PPWC filler on the road performance of asphalt concrete is studied. However, the effect of PPWC on the performance of basis asphalt is still unclear, and the performance of PPWC filler asphalt concrete in the service process needs to be further verified. In the future study, the influence of PPWC filler on the performance of asphalt mortar will be further studied, and the PPWC filler concrete will be applied to the pavement engineering to verify its durability.

Data availability statement

The original contributions presented in the study are included in the article/Supplementary material, further inquiries can be directed to the corresponding author.

Author contributions

BT: Conceptualization, Writing–original draft. XY: Conceptualization, Writing–original draft. SX: Methodology, Writing–review and editing. ZZ: Methodology, Writing–review and editing. YZ: Methodology, Writing–review and editing. JJ: Investigation, Writing–review and editing. LF: Investigation, Writing–review and editing. LT: Investigation, Writing–review and editing.

Funding

The author(s) declare financial support was received for the research, authorship, and/or publication of this article. This work was supported by the National Natural Science Foundation of China (52108416), the National Natural Science Foundation of China (No. 52308464), Hubei Science and Technology Innovation Talent and Service Project (No. 2022EHB006).

Conflict of interest

Author BT is employed by Guangdong Hongye Building Materials Technology Co., Ltd. Authors JJ, LF, and LT is employed by Shenzhen Sez Construction Group Co., Ltd.

The remaining authors declare that the research was conducted in the absence of any commercial or financial relationships that could be construed as a potential conflict of interest.

Publisher's note

All claims expressed in this article are solely those of the authors and do not necessarily represent those of their affiliated organizations, or those of the publisher, the editors and the reviewers. Any product that may be evaluated in this article, or claim that may be made by its manufacturer, is not guaranteed or endorsed by the publisher.

References

Amirbayev, Y., Yelshibayev, A., and Nugmanova, A. (2022). Characterization of asphalt bitumens and asphalt concretes modified with carbon powder. *Case Stud. Constr. Mater.* 17, e01554. doi:10.1016/j.cscm.2022.e01554

Belayali, F., Maherzi, W., Benzerzour, M., and Abriak, N.-E. (2023). Influence of the physical and chemical characteristics of sediment fillers on the properties of mastic asphalt. *Powder Technol.* 421, 118393. doi:10.1016/j.powtec.2023.118393

Chen, Z., Xiao-Yu, B., Ming-Yi, Z., and De-Zi, M. (2019). *Study on bearing behavior and Q-s curve model of rock-socketed PHC pipe piles based on ultimate load tests*. Journal of Guangxi University(Natural Science Edition.

China, M.O.T.O.T.P.S.R.O (2005). *Test methods of aggregate for highway engineering: JTG E42-2005*.

China, M.O.T.O.T.P.S.R.O (2011). *Standard test methods of bitumen and bituminous mixtures for highway engineering: JTG E20-2011*.

China, M.O.T.O.T.P.S.R.O (2017). *Specifications for design of highway asphalt pavement*. JTG D50-2017.

Cui, P., Wu, S., Xiao, Y., Hu, R., and Yang, T. (2021). Environmental performance and functional analysis of chip seals with recycled basic oxygen furnace slag as aggregate. *J. Hazard. Mater.* 405, 124441. doi:10.1016/j.jhazmat.2020.124441

Das, A. K., and Singh, D. (2021). Evaluation of fatigue performance of asphalt mastics composed of nano hydrated lime filler. *Constr. Build. Mater.* 269, 121322. doi:10.1016/j.conbuildmat.2020.121322

Gong, X., Liu, Q., Wang, H., Wan, P., Chen, S., Wu, J., et al. (2023). Synthesis of environmental-curable CO2-based polyurethane and its enhancement on properties of asphalt binder. *J. Clean. Prod.* 384, 135576. doi:10.1016/j.jclepro.2022.135576

Habibnejad Korayem, A., Ziari, H., Hajiloo, M., Abarghooie, M., and Karimi, P. (2020). Laboratory evaluation of stone mastic asphalt containing amorphous carbon powder as filler material. *Constr. Build. Mater.* 243, 118280. doi:10.1016/j.conbuildmat.2020.118280

Jia, Y., Yang, Y., Zhou, T., Gao, Y., Wang, S., and Wei, Z. (2022). Stiffening effect of filler on asphalt mastic composite: a new insight based on nearest surface function. *Constr. Build. Mater.* 344, 128177. doi:10.1016/j.conbuildmat.2022.128177

Li, G., Chen, X., Zhang, Y., Zhuang, Z., and Lv, Y. (2023). Studies of nano-SiO2 and subsequent water curing on enhancing the frost resistance of autoclaved PHC pipe pile concrete. *J. Build. Eng.* 69, 106209. doi:10.1016/j.jobe.2023.106209

Li, J., Cao, Y., Sha, A., Song, R., Li, C., and Wang, Z. (2022a). Prospective application of coal gangue as filler in fracture-healing behavior of asphalt mixture. *J. Clean. Prod.* 373, 133738. doi:10.1016/j.jclepro.2022.133738

Li, J., Yu, J., Wu, S., and Xie, J. (2022b). The mechanical resistance of asphalt mixture with steel slag to deformation and skid degradation based on laboratory accelerated heavy loading test. *Mater. Basel* 15. doi:10.3390/ma15030911

Li, L., Yang, C., and Li, J. (2021). Corrosion initiation life of laterally loaded PHC pipe piles served in marine environment: theoretical prediction and analysis. *Constr. Build. Mater.* 293, 123457. doi:10.1016/j.conbuildmat.2021.123457

Liu, J., Wang, Z., Jia, H., Jing, H., Chen, H., Zhou, L., et al. (2023a). Characteristics and properties of asphalt mortar containing FO filler. *Constr. Build. Mater.* 392, 132039. doi:10.1016/j.conbuildmat.2023.132039

Liu, N., Liu, L., Li, M., and Sun, L. (2023b). Effects of zeolite on rheological properties of asphalt materials and asphalt-filler interaction ability. *Constr. Build. Mater.* 382, 131300. doi:10.1016/j.conbuildmat.2023.131300

Liu, X., Zhang, M., Shao, L., and Chen, Z. (2018). Effect of volcanic ash filler on thermal viscoelastic property of SBS modified asphalt mastic. *Constr. Build. Mater.* 190, 495–507. doi:10.1016/j.conbuildmat.2018.09.101

Liu, Z., Bu, L., Wang, Z., and Hu, G. (2019). Durability and microstructure of steam cured and autoclaved PHC pipe piles. *Constr. Build. Mater.* 209, 679–689. doi:10.1016/j.conbuildmat.2019.03.166

Lv, Y., Wu, S., Li, N., Cui, P., Wang, H., Amirkhanian, S., et al. (2023). Performance and VOCs emission inhibition of environmentally friendly rubber modified asphalt with UiO-66 MOFs. *J. Clean. Prod.* 385, 135633. doi:10.1016/j.jclepro.2022.135633

Meng, Y., Lai, J., Mo, S., Fang, G., Deng, S., Wei, X., et al. (2023). Investigating the deterioration mechanism of adhesion between asphalt and aggregate interface under acid rain erosion. *Appl. Surf. Sci.* 639, 158171. doi:10.1016/j.apsusc.2023.158171

Osuolale, O. M., Arinkoola, A. O., and Olawuyi, O. A. (2023). Performance evaluation of bamboo leaf ash and steel slag powder as alternative filler in asphaltic mixes. *J. Eng. Res.*, 100117. doi:10.1016/j.jer.2023.100117

Ou, L., Li, R., Zhu, H., Zhao, H., and Chen, R. (2023). Upcycling waste phosphogypsum as an alternative filler for asphalt pavement. *J. Clean. Prod.* 420, 138332. doi:10.1016/j.jclepro.2023.138332

Paul, D., Suresh, M., and Pal, M. (2021). Utilization of fly ash and glass powder as fillers in steel slag asphalt mixtures. *Case Stud. Constr. Mater.* 15, e00672. doi:10.1016/j.cscm.2021.e00672

Russo, F., Veropalumbo, R., Pontoni, L., Oreto, C., Biancardo, S. A., Viscione, N., et al. (2022). Sustainable asphalt mastics made up recycling waste as filler. *J. Environ. Manag.* 301, 113826. doi:10.1016/j.jenvman.2021.113826

Sua-Iam, G., and Makul, N. (2023). Recycling prestressed concrete pile waste to produce green self-compacting concrete. *J. Mater. Res. Technol.* 24, 4587–4600. doi:10.1016/j.jmrt.2023.04.101

Sun, X., Ou, Z., Zhao, T., Qin, X., Jin, J., Yu, H., et al. (2023). Interaction state and element leaching of waste incineration fly ash-asphalt mortar based on fillerization. *Constr. Build. Mater.* 398, 132463. doi:10.1016/j.conbuildmat.2023.132463

Taherkhani, H., and Vahabi Kamsari, S. (2020). Evaluating the properties of zinc production wastes as filler and their effects on asphalt mastic. *Constr. Build. Mater.* 265, 120748. doi:10.1016/j.conbuildmat.2020.120748

Wei, Z., Jia, Y., Wang, S., Li, Z., Li, Y., Wang, X., et al. (2022). Utilization of iron ore tailing as an alternative mineral filler in asphalt mastic: high-temperature performance and environmental aspects. *J. Clean. Prod.* 335, 130318. doi:10.1016/j.jclepro.2021.130318

Xie, J., Chen, J., Hu, L., Wu, S., Wang, Z., Li, M., et al. (2023). Preparation, thermochromic properties and temperature controlling ability of novel pellets in ultra-thin wearing course. *Constr. Build. Mater.* 389, 131797. doi:10.1016/j.conbuildmat.2023.131797

Xing, B., Fan, W., Zhuang, C., Qian, C., and Lv, X. (2019). Effects of the morphological characteristics of mineral powder fillers on the rheological properties of asphalt mastics at high and medium temperatures. *Powder Technol.* 348, 33–42. doi:10.1016/j.powtec.2019.03.014

Yang, B., Li, H., Zhang, H., Sun, L., Harvey, J., Tian, Y., et al. (2021). Environmental impact of solid waste filler in porous asphalt mixture. *Constr. Build. Mater.* 303, 124447. doi:10.1016/j.conbuildmat.2021.124447

Yang, C., Wu, S., Cui, P., Amirkhanian, S., Zhao, Z., Wang, F., et al. (2022). Performance characterization and enhancement mechanism of recycled asphalt mixtures involving high RAP content and steel slag. *J. Clean. Prod.* 336, 130484. doi:10.1016/j.jclepro.2022.130484

Yang, C., Wu, S., Xie, J., Amirkhanian, S., Zhao, Z., Xu, H., et al. (2023). Development of blending model for RAP and virgin asphalt in recycled asphalt mixtures via a micron-Fe3O4 tracer. *J. Clean. Prod.* 383, 135407. doi:10.1016/j.jclepro.2022.135407

Yu, J.-L., Zhou, J.-J., Gong, X.-N., and Zhang, R.-H. (2021). Shaft capacity of prestressed high strength concrete (PHC) pile-cemented soil column embedded in clayey soil. *Soils Found.* 61, 1086–1098. doi:10.1016/j.sandf.2021.05.006

Zhang, J., Li, P., Liang, M., Jiang, H., Yao, Z., Zhang, X., et al. (2020). Utilization of red mud as an alternative mineral filler in asphalt mastics to replace natural limestone powder. *Constr. Build. Mater.* 237, 117821. doi:10.1016/j.conbuildmat.2019.117821

Zhang, J., Liu, S., Yao, Z., Wu, S., Jiang, H., Liang, M., et al. (2018). Environmental aspects and pavement properties of red mud waste as the replacement of mineral filler in asphalt mixture. *Constr. Build. Mater.* 180, 605–613. doi:10.1016/j.conbuildmat.2018.05.268

Zhao, Z., Wu, S., Liu, Q., Xie, J., Yang, C., Wan, P., et al. (2021). Characteristics of calcareous sand filler and its influence on physical and rheological properties of asphalt mastic. *Constr. Build. Mater.* 301, 124112. doi:10.1016/j.conbuildmat.2021.124112

frontiers | Frontiers in Energy Research

TYPE Original Research
PUBLISHED 20 November 2023
DOI 10.3389/fenrg.2023.1323965

OPEN ACCESS

EDITED BY
Meng Jia,
Shandong University of Science and Technology, China

REVIEWED BY
Yang Shao,
Xi'an University of Post and Telecommunications, China
Xueao Li,
Tongji University, China

*CORRESPONDENCE
Binghong Pan,
panbh@chd.edu.cn

RECEIVED 18 October 2023
ACCEPTED 06 November 2023
PUBLISHED 20 November 2023

CITATION
Yang H, Liu Y, Pan B, Ren X, Zhang J and Yan H (2023), Understanding sustainability effectiveness on design strategy of ten-lane expressway merging areas based on entropy method. *Front. Energy Res.* 11:1323965. doi: 10.3389/fenrg.2023.1323965

Understanding sustainability effectiveness on design strategy of ten-lane expressway merging areas based on entropy method

Hang Yang, Yutong Liu, Binghong Pan*, Xueyuan Ren, Jiale Zhang and Huang Yan

Highway Academy, Chang'an University, Xi'an, China

Due to the rapid growth of traffic volume, some existing expressways are being transformed into two-way ten-lane configurations. The increased lane flexibility of two-way ten-lane expressways implies a more serious mixing of passenger and freight traffic, thus necessitating a focus on traffic organization, especially at bottleneck sections. This study, based on field-measured data and traffic simulation, investigates the traffic applicability of five expressway entrance forms: conventional interchange entrance ramp (CI), passenger vehicles and trucks separation (PVTS), lanes separation around interchange (LSI), both left-side and right-side entrance ramp (LRER) and the stacked composite cross-section expressway (CCE). Using a comprehensive evaluation method, it provides optimal design solutions for varying traffic volumes, truck ratios, and merging ratios. Comprehensive evaluation results indicate that for one-way total traffic volumes exceeding 9,000 veh/h and truck ratios above 25%, the PVTS form should be prioritized. The LSI scheme demonstrates significant advantages when the truck proportion is below 30% and the merging ratio is above 20%. Additionally, due to its relatively low construction cost, it can serve as a good substitute for the PVTS approach. The LRER plan is unsuitable for entrance sections due to poor traffic capacity, increased CO emissions, and foreseeable safety issues. The strengths and applicability of PVTS, LSI, and CCE can guide the choice of entrance forms for ten-lane expressways.

KEYWORDS

ten-lane expressway, expressway entrance, design scheme, comprehensive evaluation, traffic suitability

1 Introduction

Expressways play a central role in transportation as a significant component of modern transportation networks. Developing countries consider the construction of expressways as a national strategy to meet the growing travel demands of the population and promote regional economic development. Research has suggested that the increased travel convenience brought by expressways significantly contributes to urban economic growth (Han and Gao, 2010).

However, the rapid economic development in recent years has also created an imbalance between transportation demand and infrastructure conditions. Particularly, numerous four-lane or six-lane expressways constructed initially have struggled to handle the growing traffic volumes in developing countries such as China, urgently requiring expansion from the

original alignments. Despite the precedents of construction and operation of expressways with more than 10 lanes of cross-section in developed countries, the frequent lane changes and complex interweaving behaviors at diverging and merging areas are still a cause for concern (Golob et al., 2004; Kononov et al., 2008).

Experts in China's transport construction industry have proposed the use of composite sections to deal with complex merging and diverging flows by dividing lanes in the same direction into two levels (Sun et al., 2021; Weibin et al., 2021). Inevitably, this approach suffers from a significant increase in construction costs, making it uneconomical under certain design traffic conditions. Therefore, the exploration of new design and traffic organization strategies for multi-lane expressway interchanges is urgently needed, as well as essential for supporting policy revision and implementation for expressway upgrading and expansion in developing countries.

Despite ten-lane expressways providing more flexibility to drivers changing lanes when they are dissatisfied with driving conditions of the current lane, the lack of appropriate lane restriction management will also create a more severe mixing of different-sized vehicles.

The coexistence of various types of vehicles can lead to non-negligible safety issues. Data from the Federal Motor Carrier Safety Administration (FMCSA) indicates that passenger vehicle occupants accounted for the highest percentage of fatalities in accidents involving large trucks, at 34.1% (FACTS, 2020). This may be attributed to significant differences in outline dimensions, kinetic characteristics, and driver styles among various vehicle types, particularly passenger vehicles that possess a relatively fragile body structure compared to trucks.

Additionally, some industry organizations have conducted in-depth investigations and studies on the safety, economic, social, and environmental effects of lane restriction strategies (Borchardt et al., 2004; Fontaine et al., 2009). By restricting trucks to use only the rightmost lane on the I-10 expressway in Louisiana, United States, traffic safety significantly improved as both the number and severity of accidents reduced, especially those involving trucks (Ishak et al., 2012). Similarly, the I-40 expressway in Tennessee, United States, has also achieved improvements in road safety through enhanced safety measures, including lane restrictions and following distance control (Stammer and Shannon, 2010).

Furthermore, trucks usually operate at lower speeds due to the limitations of their power characteristics and impact on load, further causing lane restriction measures to affect road capacity. Specifically, queuing and deceleration often occur following trucks when various types of vehicles share lanes. In 1992, researchers in the United States noticed this phenomenon and introduced the concept of the "bottleneck effect" (Gazis and Herman, 1992). Researchers have investigated the formation mechanisms, impact effects, and control strategies of moving bottlenecks from the perspectives of traffic waves, numerical methods, and traffic flow models (Daganzo and Laval, 2005b; a; Yamamoto et al., 2006; Singh and Santhakumar, 2022). However, these studies primarily focused on basic road sections and have not considered the impact of bottleneck effects on the merging and diverging areas of interchanges.

When lane separation for trucks and passenger vehicles is implemented in high traffic density conditions, the performance and vehicle types on each lane tend to be consistent, leading to the formation of vehicle platoons with similar speeds and smaller following distances, referred to as homogeneous traffic flow (Kerner and Konhäuser, 1993; Verma, 2016). The short time headways and inhomogeneous traffic flow can make it difficult for other vehicles to merge. Although lane restrictions are usually removed at expressway entrances and exits, the curb lanes remain in a relatively high proportion during such periods, leading to the occurrence of approximate homogeneous traffic flow on the curb lanes. This contributes to the challenge for vehicles on the entrance ramp to merge into the mainline, meanwhile obstructed visibility for passenger vehicles on the fast lanes, resulting in difficulty in reading signs and recognizing exits. Researchers attribute the impact of large vehicles on expressway entrance and exit ramp vehicles to the "barrier effect" of large vehicles and provide a macro-level explanation for this effect (Gan and Jo, 2003; Jo et al., 2003).

Therefore, aiming to reduce the probability of accidents on multi-lane expressways and fully utilize the capacity of multi-lane expressways, appropriate lane management measures should be implemented for multi-lane expressways (El-Tantawy et al., 2009; Davis, 2012). Lane management methods for ten-lane expressways can be divided into several forms, including mixed passenger and freight traffic, lanes designated for passenger vehicles and trucks, hard separation between passenger and freight lanes, and dedicated lanes for passenger and freight vehicles. Furthermore, the adverse effects of large vehicles can also be mitigated through geometric design. Available geometric design strategies include conventional interchange entrance ramp (CI), passenger vehicles and trucks separation (PVTS), lanes separation around interchange (LSI), both left-side and right-side entrance ramps (LRER), and others (Chen et al., 2023b). These design strategies can better separate passenger vehicles and trucks, thereby reducing the impact of trucks. Additionally, as previously stated, to address limited land availability, narrow corridor widths, and excessive lane numbers leading to overly wide cross-sections, the concept of a stacked composite cross-section expressway (CCE) has been proposed.

Apart from considerations of traffic efficiency, the sustainability of road traffic infrastructure has also garnered continuous attention in recent years (Khurshid et al., 2023; Patel and Ruparathna, 2023). Some scholars have attempted to find answers for low-carbon road transportation in the integration of transportation-energy integration (Chen et al., 2023a; Jiang et al., 2023; Yuan et al., 2023). However, the geometric design of roads and traffic organization forms also play a pivotal role in addressing this issue. Different design schemes for expressway entrances and exits can lead to significant changes in traffic flow characteristics, potentially impacting fuel consumption and exhaust emissions of vehicles. Additionally, once the form of expressway entrances and exits is established, it often requires considerable cost to modify. Therefore, determining appropriate designs for expressway entrances and exits could be crucial for the sustainability of road traffic infrastructure.

Traffic simulation technology has experienced rapid development in recent years. Through traffic simulation technology, it is possible to simulate road traffic conditions for construction projects that have not yet been implemented, to assess congestion and safety. Representative software includes CORSIM, VISSIM, INTEGRATION, AIMSUN, SimTraffic (Bloomberg and

Dale, 2000; Moen et al., 2000; Gao, 2008; Shaaban and Kim, 2015). Notably, it is necessary to calibrate and adjust simulation model parameters using real-world data to ensure the accuracy of the simulation (Toledo and Koutsopoulos, 2004; Rrecaj and Bombol, 2015).

The comprehensive evaluation method is a multi-index evaluation approach that comprehensively considers the importance and impact of various indicators, thereby obtaining more objective, scientific results. Commonly used methods include the entropy weight method, analytic hierarchy process, TOPSIS-Entropy method, and others (Vaidya and Kumar, 2006; Ding et al., 2016; Zhao et al., 2017; Shi et al., 2023). The comprehensive evaluation method has been widely applied in fields such as meteorology, architecture, ecology, and transportation (Zhao et al., 2009; Liu et al., 2017; Li et al., 2018; Wu and Hu, 2020; Pan et al., 2021). Compared with various subjective comprehensive evaluation models, the biggest advantage of the entropy weight method is that it avoids the interference of human factors on the weights of indicators, thus improving the objectivity of the comprehensive evaluation results. In the evaluation of schemes in the field of transportation, the entropy weight method can judge the advantages and disadvantages of schemes more objectively and comprehensively, instead of being limited to a single indicator (Liu et al., 2022). However, the entropy weight method also has issues, such as the potential for distortion in standardized results when there are too many zeros in the measured values. It also ignores the rank discrimination degree of the index, among other problems (Zhu et al., 2020).

There is currently no clear conclusion regarding the applicable conditions of various forms at the entrance of the expressway, especially the specific conditions under different proportions of truck and merging ratios. For ten-lane expressways, the "moving bottleneck effect" and "barrier effect" of large vehicles at the entrance need to be considered. The extent of the impact of these two effects at the entrance under various traffic organization methods still requires further research. Furthermore, the applicable boundaries of PVTS and CCE are still not well-defined.

The organization of the rest of this article is as follows: Section 2 primarily introduces data collection methods, the establishment and calibration of simulation models, and evaluation methods. Section 3 presents the situation of collected empirical data and the proposed design schemes for evaluation. Section 4 showcases the results and conducts sensitivity analysis. Section 5 discusses the results in detail, and the conclusion is presented in Section 6.

2 Methodology

In this paper, empirical data are used to calibrate the parameters of the simulation model, followed by verification. Subsequently, the simulation model is employed to conduct a comprehensive evaluation of the entrance design schemes for a ten-lane expressway. The evaluation is based on the entropy method, three indicators are selected for comprehensive evaluation, to determine the optimal solution under different traffic volumes and truck ratios.

2.1 Data collection method

Data collection should be conducted under conditions without traffic accidents and road maintenance. Clear weather without significant crosswinds or severe haze should also be ensured. Additionally, the data collection location should have a favorable terrain and unobstructed line of sight to avoid influencing drivers' behavior (Tian et al., 2023).

Data collection is conducted using roadside laser traffic surveyors (Figure 1). The laser device is set on either the paved or unpaved shoulder during the survey, aligned vertically to the lane and the driving direction of the vehicles. The instrument continuously emits 10 kHz laser pulses at the vehicle's chassis position, measuring the time of the reflected laser pulses. With the accompanying Nano-L software, it can record the driving position, speed, passage time, wheelbase, and other parameters of each vehicle as it passes through the section.

The types of data to be collected include vehicle counts for both passenger vehicles and trucks, as well as traffic volumes and merging speeds for both types of vehicles on the mainline and ramp. The collected data will be used for parameterization and model calibration in traffic simulation.

2.2 Simulation model

2.2.1 Model development

Currently, the number of ten-lane expressways that have been completed and opened to traffic is extremely limited, with the vast majority of ten-lane expressways still in the planning or construction phase in China. Consequently, the evaluation of various design schemes necessitates reliance on VISSIM, a sophisticated traffic flow simulation software. This software is capable of modeling the behaviors and interactions of individual road users and vehicles at a microscopic level, as well as simulating traffic dynamics and network performance at a mesoscopic level.

It is essential to use traffic characteristics and vehicle trajectories consistent with the empirical data and to have the same geometric features as the data collection site to ensure the accuracy of the model.

Additionally, to ensure fairness in comparing different scenarios, when setting up VISSIM nodes, it should be ensured that the nodes cover equal lengths of the mainline and ramps, and they should fully encompass the ramp diverge area and the mainline-ramp merge area.

2.2.2 Model calibration

Initially, the distribution of vehicle speeds and headways, derived from the collected data, are input into the model as critical parameters for calibration. Furthermore, parameters governing vehicle lane-changing behavior are adjusted following prior experience to align them more closely with the observed driving habits on Chinese expressways.

The model calibration process involves calculating the discrepancies between observed values and simulated values for capacity, density, and subsequently, the simulation accuracy of speed. Among these, the mean absolute percentage error (MAPE) is often used as a measure of accuracy in calibration (Bowerman

FIGURE 1
Roadside laser traffic surveyor.

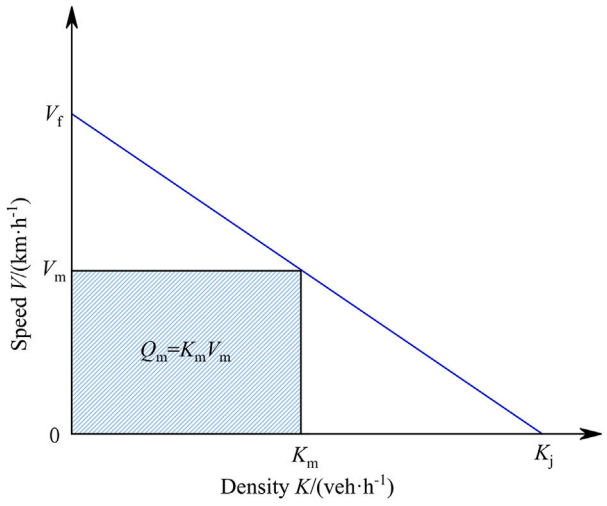

FIGURE 2
K-V relationship based on Greenshields model.

et al., 2004). MAPE can be calculated according to equations Eq. 1 and Eq. 2.

$$MAPE_C = \left(\sum_{i=1}^{n} C_v^i - \sum_{i=1}^{n} C_f^i\right) \Big/ \sum_{i=1}^{n} C_f^i \tag{1}$$

$$MAPE_K = \left(\sum_{i=1}^{n} K_v^i - \sum_{i=1}^{n} K_f^i\right) \Big/ \sum_{i=1}^{n} K_f^i \tag{2}$$

Where C_v^i and K_v^i denote the simulated capacity and density in the VISSIM model, while C_f^i and K_f^i denote the investigated capacity and density, with i denoting traffic flow and n denoting a total of through and merging traffic flows.

For design schemes lacking empirical data, corresponding speed, density, and traffic volume can be calculated based on the simulation results using equations Eqs 3–5. Since multiple simulation segments make up a specific entrance type, the three-parameter average value for the entire segment needs to be derived from the three-parameter data of various local simulation segments.

$$\bar{K} = \frac{\sum_{1}^{i} K_i l_i}{\sum_{1}^{i} l_i} \tag{3}$$

$$\bar{V} = \frac{\sum_{1}^{i} l_i}{\sum_{1}^{i} \frac{l_i}{V_i}} \tag{4}$$

$$\bar{Q} = \frac{1}{i}\sum_{1}^{i} Q_i \tag{5}$$

Where $\bar{K}$, $\bar{Q}$, $\bar{V}$ denote the average density (veh/km), traffic volume (veh/h), and speed (km/h) of the road section or connector (veh/km), while l_i, K_i, Q_i, V_i denote the measurements of length (km), density (veh/km), traffic volume (veh/h) and speed (km/h) of a section or connector.

Considering that measuring road sections shorter than the length of a passenger vehicle is meaningless, the results of road sections with connectors shorter than 6 m should be disregarded.

According to the Greenshields model, there exists a linear relationship between traffic density (K) and speed (V) (Figure 2). The linear relationship of K-V can provide another perspective for the validation and calibration of the model.

The coefficient of determination R^2 represents the percentage of the variance in the data that is explained by the model. Its computation is based on the total sum of squares (TSS), the regression sum of squares (RSS), and the error sum of squares (ESS). R^2 is calculated as shown in equation Eqs 6–9.

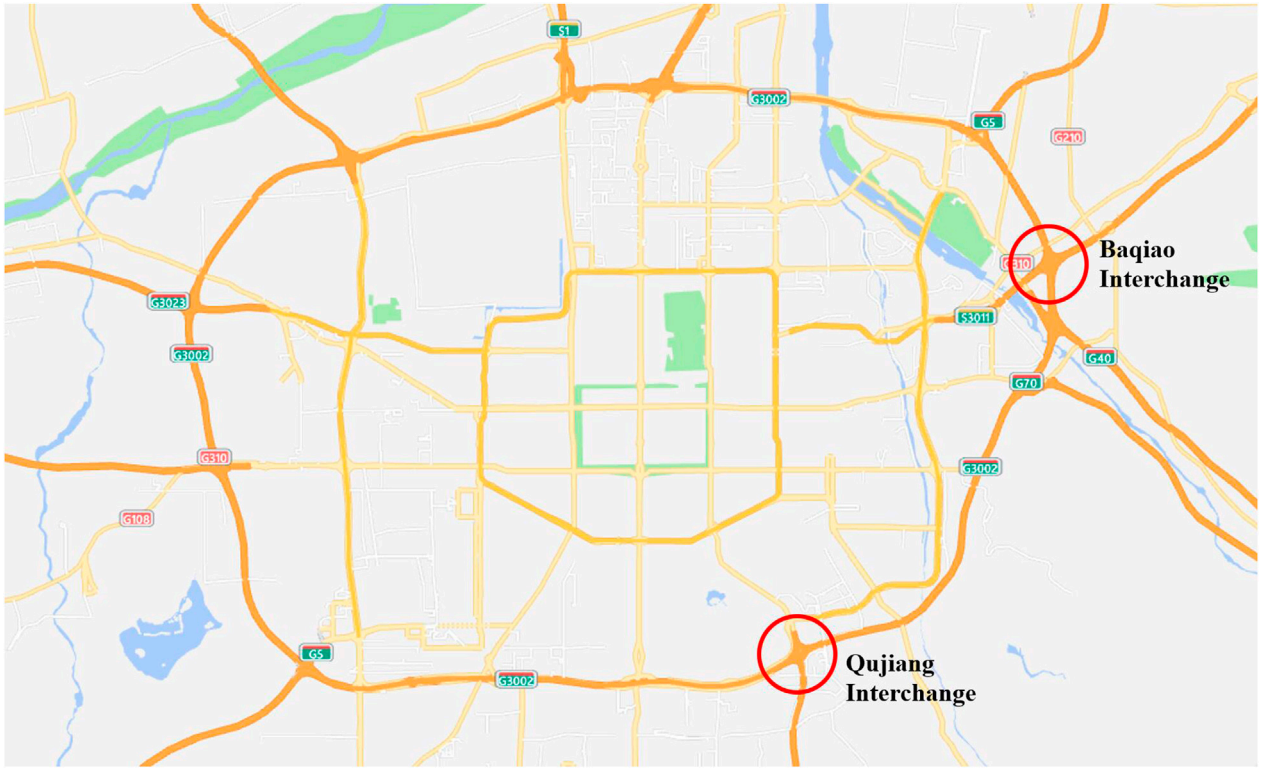

FIGURE 3
Interchange location for data collection.

TABLE 1 Collected vehicle data statistics.

Vehicle type		V_{85} (km/h)
Passenger vehicles (veh)	Trucks (veh)	
1,036	310	114.92

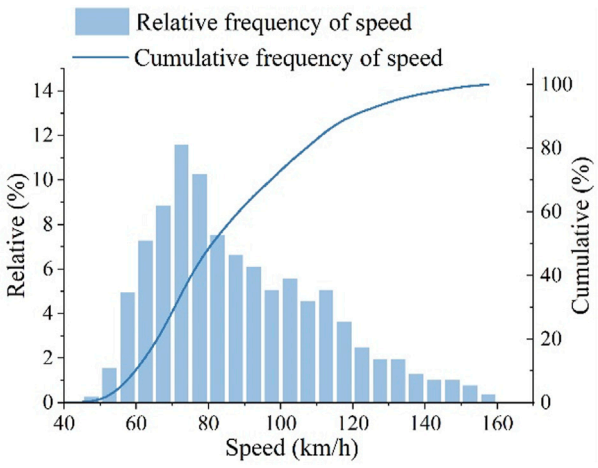

FIGURE 4
Distribution of vehicle speeds.

$$TSS = \sum_{i=1}^{n} (V_i - \bar{V})^2 \tag{6}$$

$$ESS = \sum_{i=1}^{n} (V_i - \hat{V}_I)^2 \tag{7}$$

$$RSS = TSS - ESS \tag{8}$$

$$R^2 = \frac{RSS}{TSS} \tag{9}$$

Where V_i denotes the observed value, $\bar{V}$ denotes the mean of V and $\hat{V}_i$ denotes the value predicted by the linear model.

2.3 Evaluation method

2.3.1 Principle of evaluation method

The entropy method is a comprehensive evaluation approach. It determines the objective weights based on the variability of indicators. If the entropy of a certain indicator is smaller, it indicates that the degree of variation in the indicator values is greater, providing more information

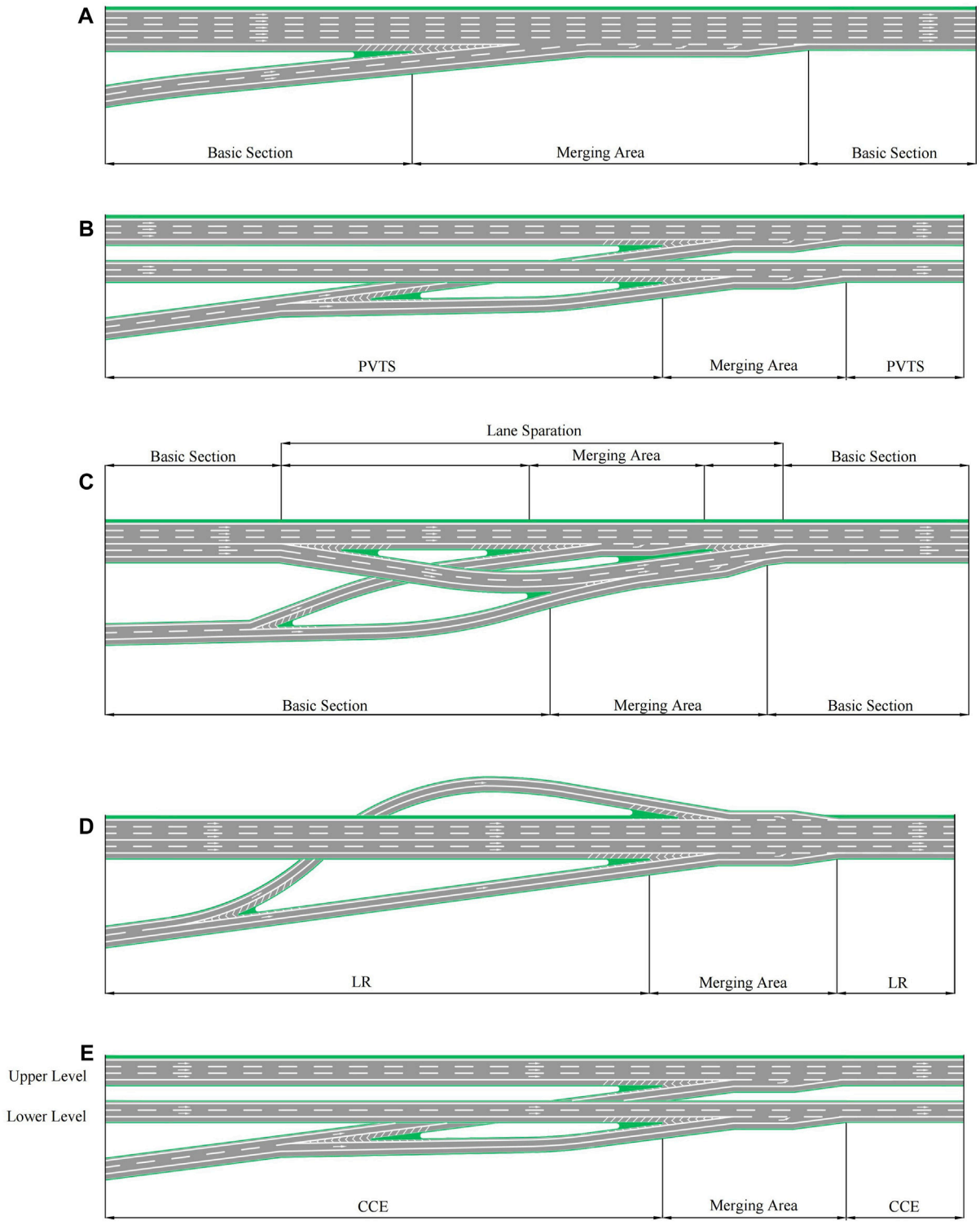

FIGURE 5
Comparative schematic diagrams of various schemes. **(A)** Schematic diagram of CI Scheme. **(B)** Schematic diagram of PVTS Scheme. **(C)** Schematic diagram of LSI Scheme. **(D)** Schematic diagram of LRER Scheme. **(E)** Schematic diagram of CCE Scheme.

and thus having a greater impact on the comprehensive evaluation, resulting in a higher weight. Conversely, if the entropy of a certain indicator is larger, it indicates that the variation in the indicator values is smaller, providing less information and thus having a smaller impact on the comprehensive evaluation, resulting in a lower weight. The specific steps are shown in Eqs 10–17.

1. Data standardization

TABLE 2 MAPE calculation results.

Location	Investigated capacity (veh/h)	Simulated capacity (veh/h)	$MAPE_C$ (%)
Baqiao	764	818	7.07
Qujiang	1,256	1,343	6.93
Location	**Investigated Density (veh/km)**	**Simulated Density (veh/km)**	**$MAPE_K$ (%)**
Baqiao	10.266	9.300	−9.41
Qujiang	14.065	13.564	−3.56

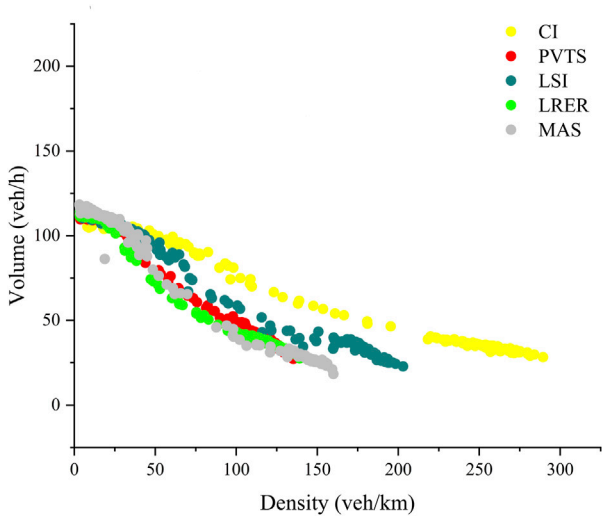

FIGURE 6
K-V scatterplots for the five design schemes.

TABLE 3 Linear fitting of R^2 values for different design schemes.

Scheme	CI	PVTS	LSI	LRER	CCE
R^2	0.98894	0.99193	0.98399	0.98075	0.98267

Suppose we choose k indices X_1, X_2, …, X_k, where

$$X_i = \{x_1, x_2, x_3, \cdots, x_n\}$$

To avoid the impact of non-unification of units of measurement for indicators, the data of each indicator should be standardized first.

Suppose that the values of each indicator data after standardization are Y_1, Y_2, …, Y_m for the positive indicators, there are:

$$Y_{ij} = \frac{X_{ij} - \min(X_i)}{\max(X_i) - \min(X_i)} \tag{10}$$

For negative indicators, there are:

$$Y_{ij} = \frac{\max(X_i) - X_{ij}}{\max(X_i) - \min(X_i)} \tag{11}$$

2. Find the weight of each indicator under each scheme

The proportion of the jth item to the overall index in the ith scheme is calculated as follows:

$$p_{ij} = \frac{Y_{ij}}{\sum_{i=1}^{n} Y_{ij}}, i = 1, \cdots, n, j = 1, \cdots, m \tag{12}$$

3. Find the information entropy of each index

The information entropy of a set of data is:

$$E_j = -\ln(n)^{-1} \sum_{i=1}^{n} p_{ij} \ln p_{ij} \tag{13}$$

In particular, when $p_{ij} = 0$, order

$$p_{ij} \ln p_{ij} = 0 \tag{14}$$

4. Determine the weights of each indicator

First, calculate the redundancy of information D_j,

$$D_j = 1 - E_j \tag{15}$$

Then calculate the index weight value according to this:

$$w_j = \frac{D_j}{\sum_{j=1}^{m} D_j} \tag{16}$$

5. Calculate the comprehensive score of each scheme

$$s_i = \sum_{j=1}^{m} w_j \cdot p_{ij} \tag{17}$$

2.3.2 Evaluation index selection

Factors such as traffic efficiency and environmental pollution, road capacity, delay, and CO emissions have been selected for evaluation, which are related to the sustainability of road infrastructure.

Road capacity is the most critical indicator for assessing whether a road meets its intended design level and fulfills the demand for road use. The differences in traffic capacity between different scenarios will result in their adaptability to varying traffic volumes.

Delay refers to the time lost by vehicles during travel due to interference from other vehicles beyond the driver's control or

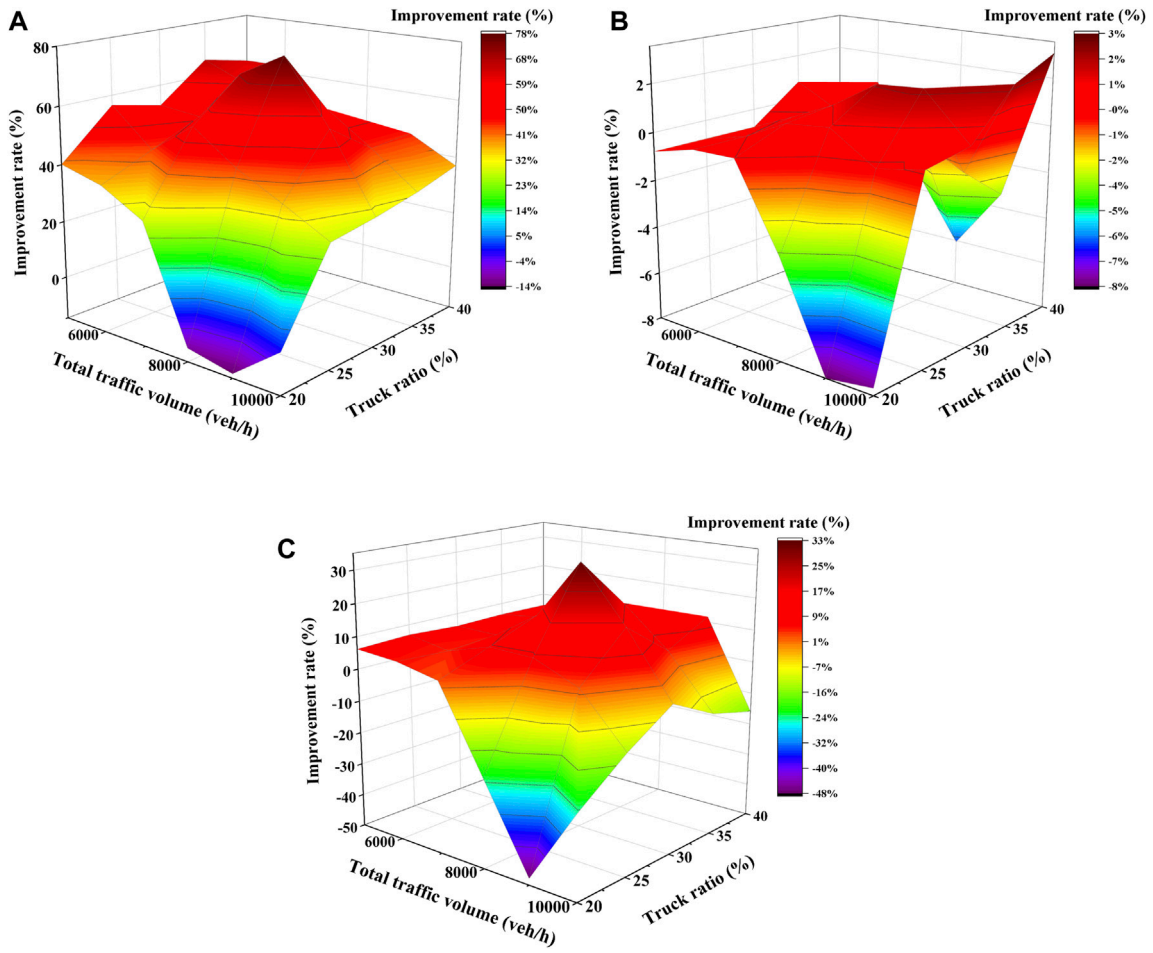

FIGURE 7
PVTS improvement rate of **(A)** delay **(B)** capacity **(C)** CO emission.

unexpected obstacles, including parking delays and delays caused by operating at speeds lower than the ideal speed. It is an important indicator of traffic flow service level.

Carbon monoxide (CO) is generally considered one of the most harmful pollutants to human health in vehicle exhaust emissions (Brugge et al., 2007). Furthermore, CO emissions can also cause damage to the environment, thus affecting the sustainability of road infrastructure.

3 Data and design description

3.1 Case description

For our study, we chose two interchanges to collect traffic flow data. The Baqiao Interchange on the Xi'an Ring Expressway features two lanes in each direction, with a design speed of 120 km/h. On the other hand, the Qujiang Interchange on the Baomao Expressway has four lanes in each direction, also with a design speed of 120 km/h.

3.2 Data collection

Data is collected at merging points at the entrance of the Bao Mao Expressway and Xi'an Ring Expressway. The locations of these two interchanges are shown in Figure 3. Data quantity, vehicle type, and speed are summarized in Table 1. The speed distribution at the merging point of the two interchanges is shown in Figure 4. Based on previous experience, the time of data collection was chosen to be between 11:00 and 16:00 to match the local peak hours in Xi'an.

3.3 Design scheme

3.3.1 CI

The conventional interchange entrance ramp (CI) scheme does not require additional construction work; instead, it only necessitates the addition of specific signs to implement lane restriction measures, making it the most cost-effective option. Lane restriction refers to traffic control measures that restrict specific types of vehicles from traveling in certain lanes. Lane

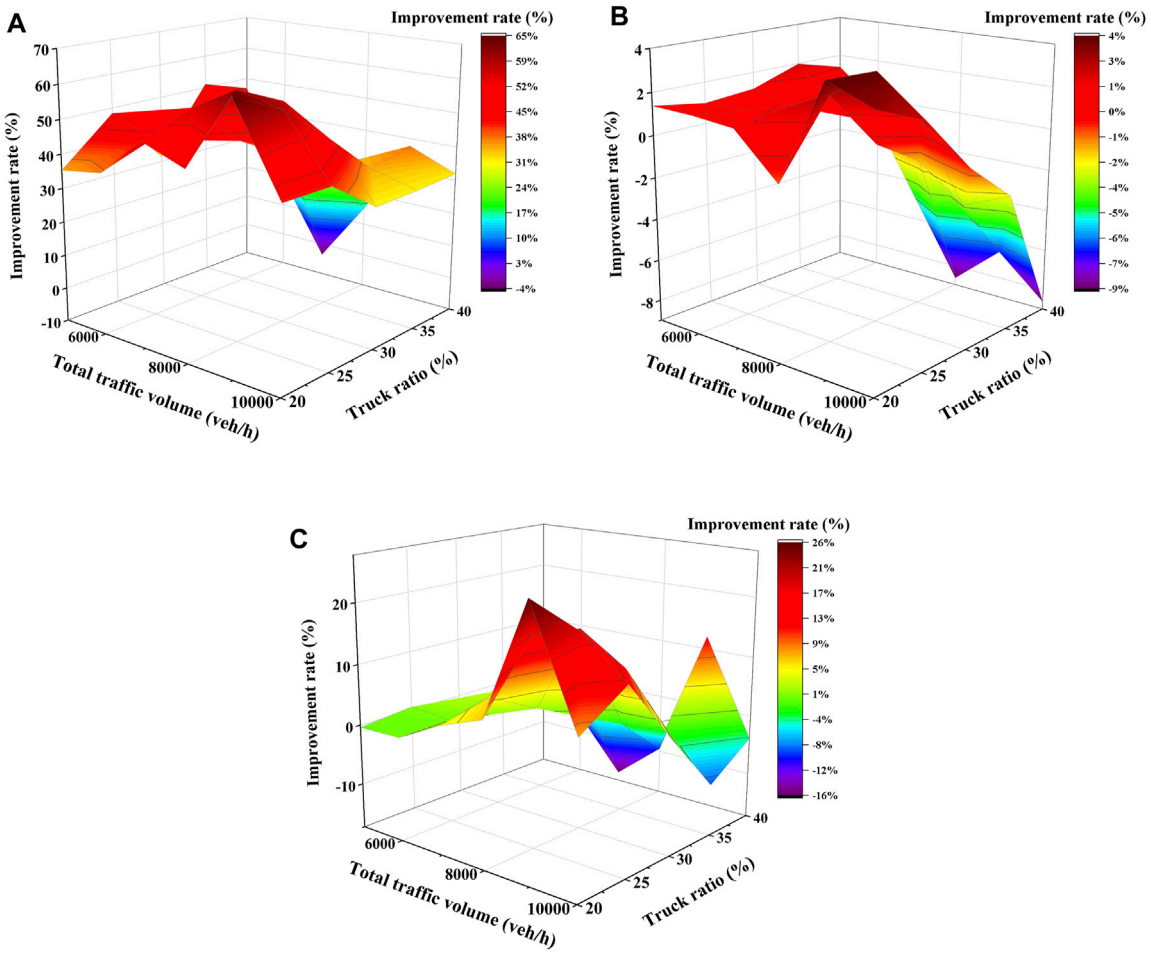

FIGURE 8
LSI improvement rate of **(A)** delay **(B)** capacity **(C)** CO emission.

restriction management is relatively flexible, but the selection of its combination methods can be complex. Moreover, the phenomenon of mixing truck and passenger vehicles still exists at interchange entrances and exits, service areas, and other sections.

There are various ways to implement lane restrictions, but they can generally be divided into two types: one is to separate trucks and passenger vehicles into different lanes, with trucks in the truck lanes and passenger vehicles in the passenger vehicle lanes; the other is to designate certain lanes as exclusive lanes for either trucks or passenger vehicles, while the remaining lanes allow mixed traffic of both trucks and passenger vehicles.

To align with the expressway conditions in China and support rigorous research, this paper adopts a prevalent traffic management strategy in China. In this approach, trucks utilize designated lanes, whereas passenger vehicles face no specific lane restrictions.

Since there is no separate ramp for designated vehicle types, trucks, and passenger vehicles will merge from a single ramp into the mainline.

The scheme is illustrated in Figure 5A.

3.3.2 PVTS

The passenger vehicle and truck separation (PVTS) scheme utilizes physical separation to segregate truck and passenger vehicles, providing both directions with inner and outer lanes that are mutually separated. At the on-ramp, trucks, and passenger vehicles will be separated to enter the mainline through their ramp. This lane management approach physically separates trucks and passenger vehicles, improving the speed of passenger vehicles and reducing accident rates. PVTS can also design road geometry and traffic safety facilities based on the characteristics of truck and passenger vehicles, greatly ensuring the efficiency of large vehicle travel. In complex expressway systems, the PVTS scheme may have broad prospects for application.

In the same direction, there are five lanes, which can be represented as X + Y, where X is the number of lanes dedicated to small vehicles, and Y is the number of lanes dedicated to large vehicles. It is not difficult to understand that under the conditions of $X \geq 1$ and $Y \geq 1$, there are a total of 4 combinations of lanes dedicated to small and large vehicles in the X + Y format. However, to meet the overtaking needs, the “1 + 4”and “4 + 1”schemes

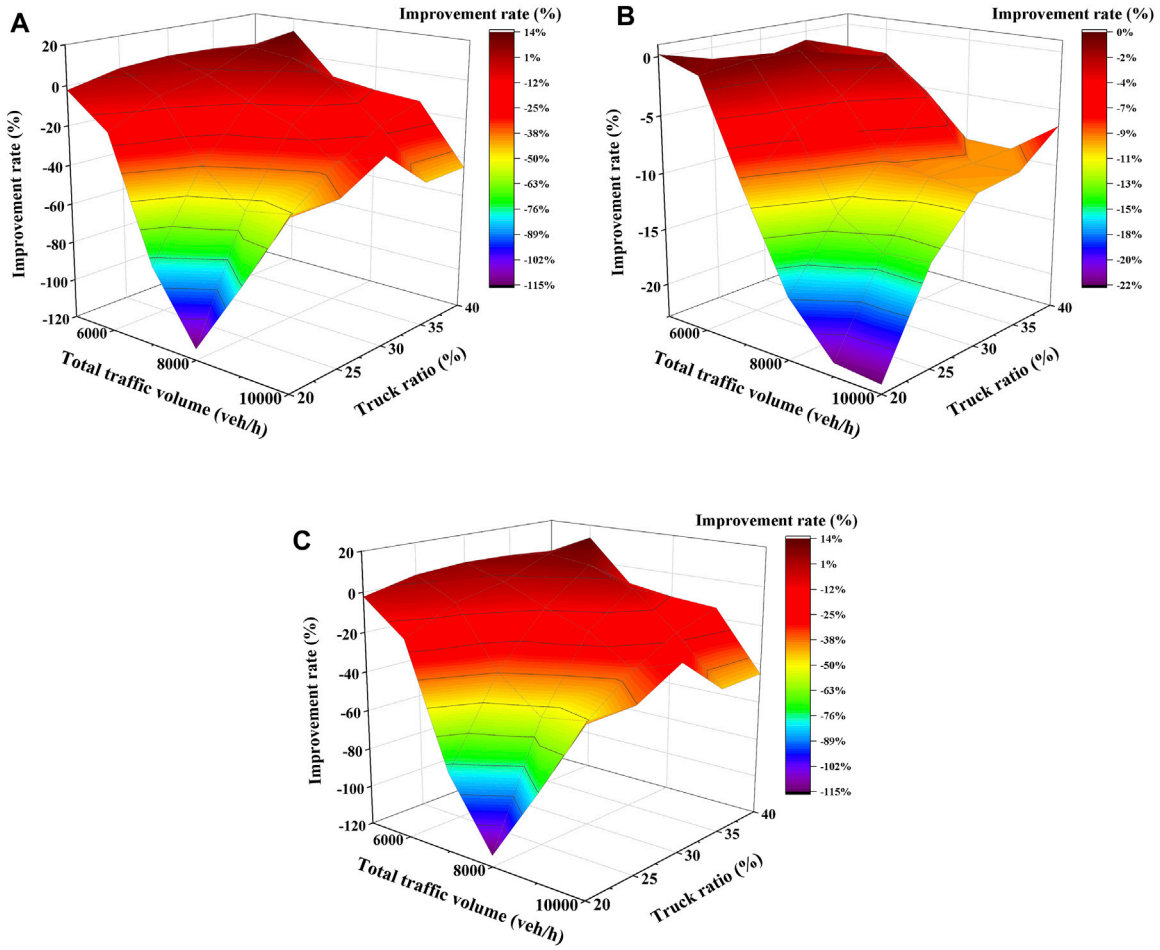

FIGURE 9
LRER improvement rate of **(A)** delay **(B)** capacity **(C)** CO emission.

should be excluded. Additionally, in the vast majority of cases, the number of trucks is always less than passenger vehicles. Therefore, in this study, the PVTS scheme employs a more reasonable traffic organization format of "3 lanes for passenger vehicles +2 lanes for trucks."

It is foreseeable that the scheme will likely be more costly. At the same time, it will likely be less flexible concerning the proportion of trucks, as the physical separation between the passenger vehicle and truck lanes will likely result in some of the five lanes being wasted while others are extremely congested.

The scheme is illustrated in Figure 5B.

3.3.3 LSI

The lanes separation around interchange (LSI) scheme can be considered a cheap alternative to PVTS. The LSI scheme was proposed because of the high cost of the PVTS, which requires the subgrade to be separated or placed in levels above and below. This scheme separates the subgrade only at the exit and entrance sections to place dedicated ramps for passenger vehicles and trucks, while only soft segregation is used on the basic section. This scheme combines the advantages of soft segregation and the PVTS scheme, and the passenger vehicles can also drive in the two lanes on the right side, avoiding the waste of the dedicated lanes for trucks when the percentage of truck traffic is not high and may have better flexibility and adaptability.

The mainline separation position for LSI should match the decision sight distance of 12–14 s at the exit taper start point, which is approximately 1,500 feet (450 m).

The schematic of this scheme is shown in Figure 5C.

3.3.4 LRER

Due to space constraints and other reasons, in some areas where the PVTS scheme is applicable, it is not possible to separate the subgrade to accommodate two right-side entrances. Therefore, both the left-side and right-side entrance ramp (LRER) scheme of allowing passenger vehicles to enter from the left and trucks from the right is adopted. Although LRER occupies less land and has lower construction costs, it should be noted that there may be more serious safety issues associated with this scheme. Under the left-hand driving rules, the left lane is typically used as an overtaking lane, and vehicles on this lane tend to have higher operating speeds. Therefore, entrance vehicles

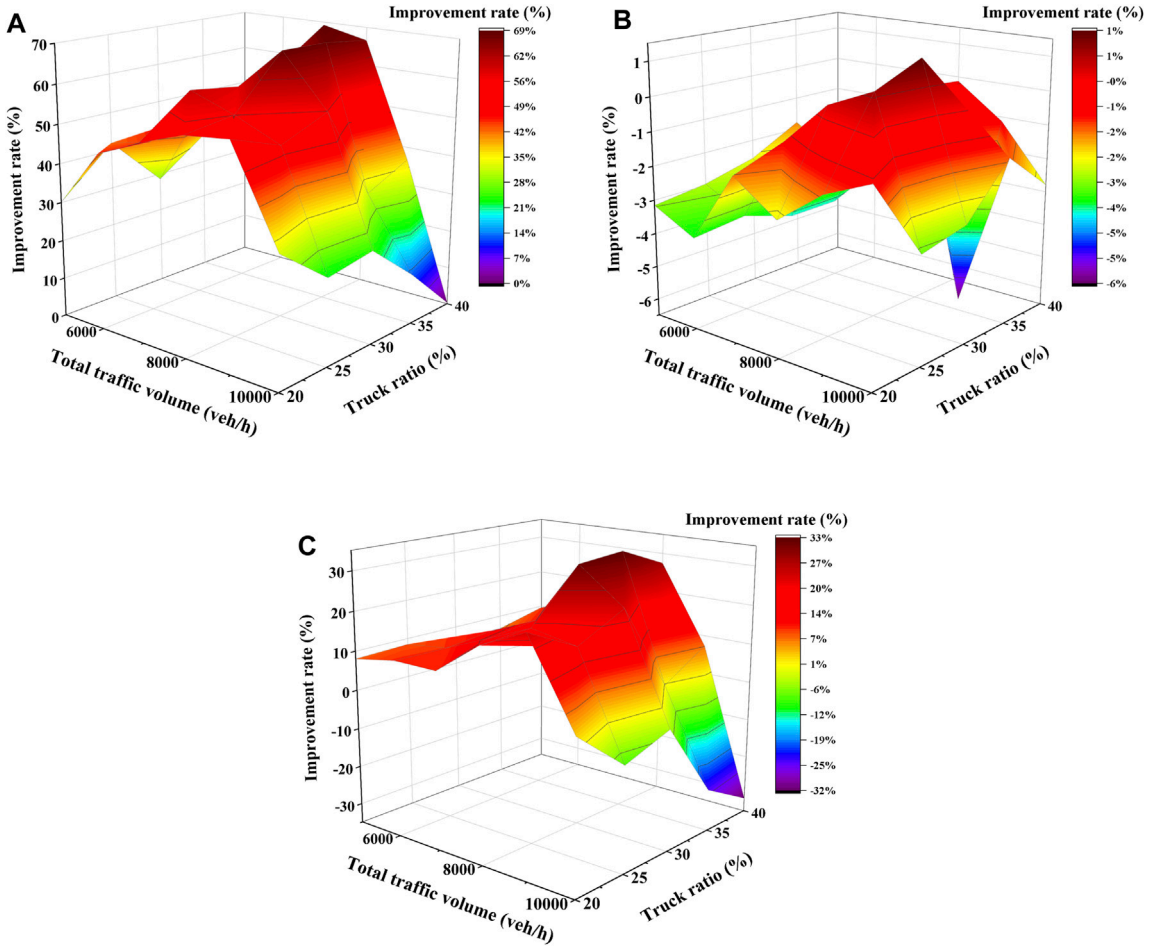

FIGURE 10
CCE improvement rate of **(A)** delay **(B)** capacity **(C)** CO emission.

merging onto the mainline may face greater speed differentials and increased collision risks.

The scheme is illustrated in Figure 5D.

3.3.5 CCE

The stacked composite cross-section expressway (CCE), as illustrated in Figure 5E, represents a commonly employed design within complex expressway systems. Instead of separating passenger vehicles from trucks, this design separates transit traffic from short-distance traffic. In situations where the presence of trucks is not predominant, implementing the PVTS scheme may lead to an excessive allocation of lanes for trucks, potentially resulting in underutilization. However adjusting the number of dedicated truck lanes to just one might curtail the ability of trucks to overtake, thereby impeding traffic flow efficiency. Consequently, in such scenarios, the adoption of the CCE scheme proves to be a more suitable alternative.

In this scheme, two auxiliary lanes are situated on the lower level, while three main lanes with a closely geometric design are positioned on the upper level, all in the same direction. To ensure a smooth transition of traffic and efficient traffic management on both main lanes and auxiliary lanes, distinct entrances should be designated for each category.

3.4 Simulation design

For the five design schemes (CI, PVTS, LSI, LRER, CCE) on a ten-lane expressway entrance, this study considers a total of 450 scenarios by examining six total input traffic volumes (5000veh/h, 6000veh/h, 7000veh/h, 8000veh/h, 9000veh/h, 10000veh/h), five passenger-to-freight ratios (0.8:0.2, 0.75:0.25, 0.7:0.3, 0.65:0.35, 0.6:0.4), and three merge rates (10%, 20%, 30%).

Geometric parameters are taken from the current Chinese expressway route design specifications. The length of acceleration lanes is 230 m for single-lane entrances and 400 m for dual-lane entrances. To meet lane balance requirements, dual-lane entrances require the addition of auxiliary lanes, with a length of 400 m. The length of all taper sections is uniformly set to 90 m.

To ensure the accuracy of simulation results, the simulation time for each scenario is set to 3,600 s.

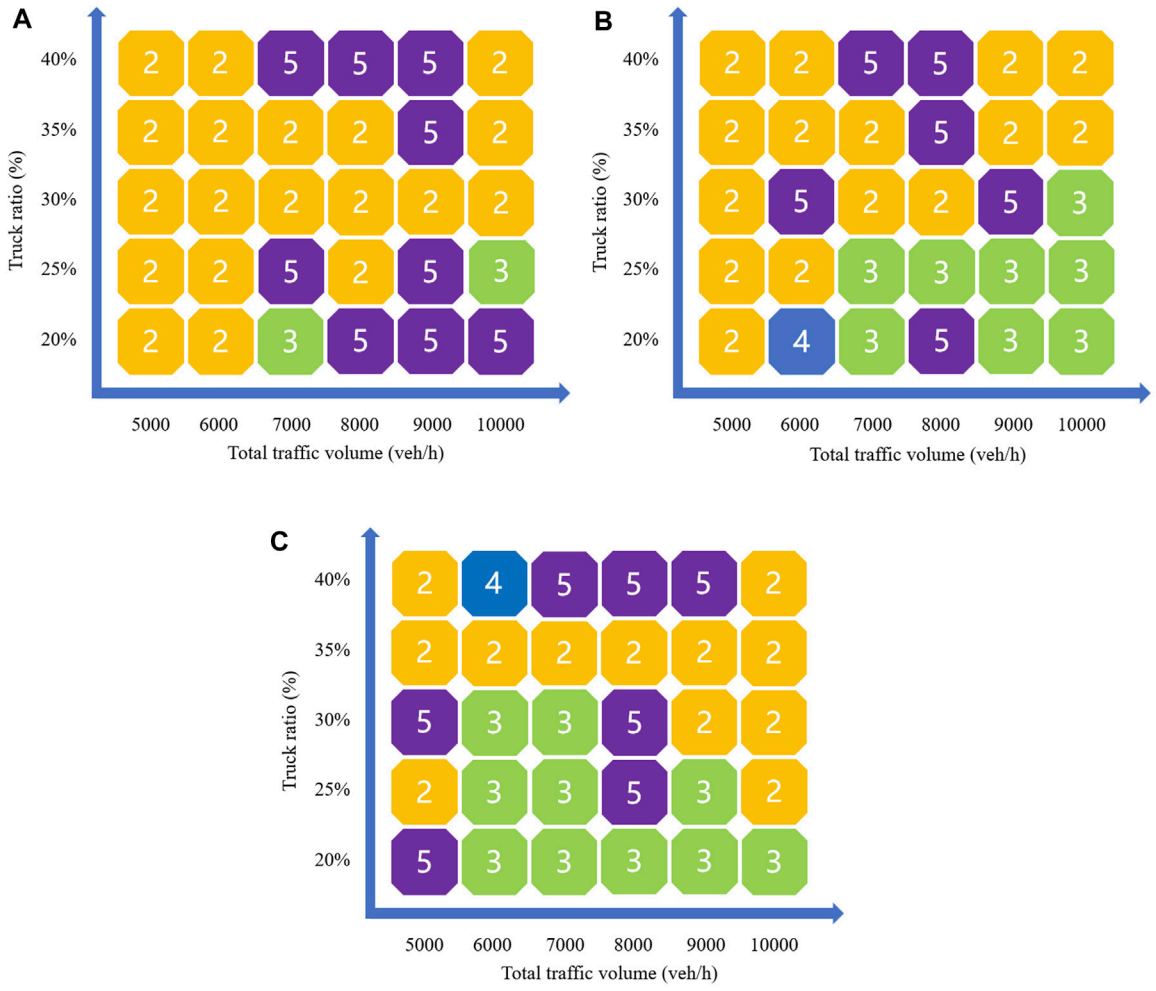

FIGURE 11
The optimal scheme under **(A)** 10% merge ratio **(B)** 20% merge ratio **(C)** 30% merge ratio.

4 Results and analysis

4.1 Calibration result

4.1.1 MAPE results

Both the Baqiao Interchange and the Qujiang Interchange have adopted the CI scheme. Therefore, MAPE values were calculated for this scheme only. The calculation results are shown in Table 2.

This estimation error is acceptable for engineering applications (Xiang et al., 2016).

4.1.2 K-V linear fitting

The input traffic volume for the five schemes is increased from 1000veh/h to 19000veh/h in increments of 1000veh/h, resulting in 19 groups. Each group is simulated 10 times. For each simulation result, density, velocity, and flow are calculated using Eqs 3–5 respectively. The K-V scatterplots for the five design schemes are shown in Figure 6.

Linear fits of the K-V relationships are conducted for each of the five design schemes, and the determination R^2 is shown in Table 3.

The R^2 values for the fits are all greater than 0.98, indicating a significant linear relationship between density and velocity in the simulation results. This suggests that the simulation results are valuable for research purposes.

4.2 Sensitivity analysis

Three key evaluation indexes (delay, capacity, CO emissions) were selected for the commonly used and representative 20% merge rate. Four improvement schemes (PVTS, LSI, LRER, CCE) were applied, and their respective improvements over CI were depicted in Figures 7–10.

In some scenarios, the PVTS scheme shows significant improvements in delay and CO emissions compared to the CI scheme, with maximum improvement rates of approximately 78% and 33%, respectively. The highest improvement rates are observed at around a total traffic volume of 8000 veh/h and a 30% truck ratio. However, there is not much variation in terms of capacity compared to CI. It is also worth noting that although the

PVTS scheme exhibits improvements in delay and capacity to some extent under high traffic volume and a high truck ratio, it has a negative impact on CO emissions. This may indicate that the scheme is not environmentally friendly.

The LSI scheme generally exhibits significant advantages in terms of delay, capacity, and CO emissions compared to CI when the truck ratio is less than 30%. However, when the truck ratio exceeds 30%, the improvement rates for these factors sharply decrease, resulting in negative improvements.

The LRER scheme effectively reduces delay when the truck ratio is high, but it generally has a negative impact on capacity and CO emissions in most scenarios. It should be noted that LRER may have significant safety issues, and even though it improves delay to some extent in scenarios with a high truck ratio, its usage should still be avoided whenever possible.

The CCE scheme shows improvements in delay compared to CI in most scenarios. However, improvement rates for capacity and CO emissions become negative when the traffic volume is greater than 9000veh/h and the truck ratio exceeds 25%. This suggests the applicable conditions for the two common traffic organization forms on a dual-direction ten-lane expressway: for a single-direction traffic volume exceeding 9000veh/h and a truck ratio greater than 25%, it is advisable to prioritize the PVTS scheme.

4.3 Comprehensive evaluation result

CI is labeled as 1, PVTS as 2, LSI as 3, LRER as 4, and CCE as 5. The scheme with the highest overall evaluation score is considered the optimal scheme. Schematic diagrams of the optimal scheme are created for different traffic volumes and truck ratios at three merge rates (10%, 20%, 30%), as shown in Figure 11.

From the figure, it can be observed that PVTS, LSI, and CCE all exhibit a certain degree of competitiveness and often become the optimal solutions. On the other hand, CI and LRER have rarely taken a leading position, especially CI, which is surpassed by other schemes under various conditions.

Under a 10% merge rate, the PVTS scheme exhibits strong competitiveness under both high and low passenger-freight ratios. The remaining positions are predominantly occupied by the CCE scheme, particularly concentrated around 20% and 40% truck ratios.

When the merge rate reaches the more common 20%, the LSI scheme starts to gain an advantage. It partially replaces PVTS and CCE in scenarios with truck ratios between 20% and 30% and traffic volumes exceeding 7000veh/h. It is worth emphasizing once again that LSI, due to its separation of roadbed only at entrance and exit locations and the use of soft barriers elsewhere, has lower costs compared to PVTS and CCE schemes.

Under a 30% merge rate, the traffic volume on ramps increases significantly, and vehicles merging onto the mainline have a greater impact on the mainline traffic flow. In this case, the range of advantages of LSI moves towards lower traffic volumes. That is, when the truck ratio is below 30%, the LSI solution shows more competitiveness. PVTS holds a dominant position under high truck ratios and high traffic volumes.

5 Discussion

Unlike the mandatory lane change at expressway exits, the lane change demand for vehicles at entrances is not as “strong”. Drivers can first merge into the rightmost lane on the mainline and then look for opportunities to merge into the ideal lane. Therefore, the continuous lane-changing behavior at entrances is significantly reduced compared to exits. This can explain to some extent the significant difference in optimal solutions between entrances and exits (Chen et al., 2023b).

From an overall evaluation of various schemes, LSI, with its lower cost and better overall rating at a 30% truck ratio, can be considered a cost-effective alternative to the PVTS scheme. This may be because LSI, with its more relaxed lane restrictions, to some extent, avoids the waste of double truck-exclusive lanes in the PVTS scheme at low truck ratios.

In Figure 11, it can be observed that CCE is not completely overtaken by PVTS at a 40% truck ratio and still maintains a certain advantage. One possible explanation is that at a 40% truck ratio, due to the increased number of trucks, it becomes more difficult for trucks to change lanes and merge into the truck-exclusive lanes at entrance ramps, resulting in more delays, lower traffic capacity, and higher CO emissions at the ramp. In contrast, the CCE scheme, with its mixed traffic organization, allows passenger vehicles and trucks to freely choose between the mainline and auxiliary lanes, reducing lane-changing behavior at the ramps.

It seems that the truck ratio does not have a decisive impact on the superiority of the CCE scheme. This may be because the CCE scheme does not restrict the travel lanes for trucks, resulting in less significant barrier effects from trucks. In contrast, the CI scheme, which imposes lane restrictions on trucks, still results in significantly higher truck ratios in the right lanes, even after removing lane restrictions and adding auxiliary lanes before the entrance. The likely reason is that the left-side passenger vehicle exclusive lane operates at a higher speed, prompting truck drivers to change lanes but still struggling to find suitable merging gaps, leading them to continue in the right lane. This, in turn, hinders the merging of entrance vehicles onto the mainline, causing significant delays and restricting traffic capacity.

The LRER scheme significantly reduces delays when the truck ratio is relatively high. One possible explanation is that the LRER scheme is still based on the PVTS scheme with modifications, and the separation of passenger vehicles and trucks allows for lower delays even at high truck ratios. However, the increase in CO emissions and the decrease in traffic capacity may be due to the significant speed difference between the far-left lane on the passenger vehicle exclusive lane and the entrance ramp, leading to more frequent deceleration and stop-and-go traffic.

Moving on, let’s begin discussing the limitations of this study. The scope and limitations of this research mainly include the following points:

1. Due to the limited availability of fully operational ten-lane highways in China, this study is based on VISSIM traffic simulation, with model calibration and lacking validation from real-world data. Therefore, the simulation results in this study

may have a certain margin of error and cannot be entirely equivalent to real-world data.
2. This study only considers the traffic flow characteristics of various schemes under different traffic volumes, truck ratios, and merge ratios, without fully considering safety aspects such as collision probabilities and the severity of accidents. A comparison of safety among the various schemes remains a subject for further research.

In future research, attention may be focused on the following issues:

1. When allocating dedicated lanes, the sensitivity of lane restrictions to the proportion of trucks necessitates a potential increase in the number of lanes dedicated to trucks and a corresponding decrease in those allocated for passenger vehicles as the proportion of trucks increases.
2. Although serious safety issues are anticipated with the LRER scheme, this study did not specifically evaluate the safety of each scheme. Subsequent research can comprehensively consider factors such as the traffic efficiency, safety, environmental impact, and economic aspects of each scheme.

6 Conclusion

Due to the increasing truck ratio, the barrier effect of trucks has exacerbated congestion at expressway entrances. To address this issue, design schemes such as PVTS, LSI, LRER, and CCE are introduced, and VISSIM simulation is used to compare their capacity, delay, and CO emissions under different traffic volumes, truck ratios, and merge ratios. The aim is to find the optimal solution for different scenarios. This study concludes the following findings, providing data support and references for the construction of ten-lane expressways:

1. PVTS and CCE schemes, as the two most important traffic organization forms for composite expressways, have different suitability conditions. In bidirectional ten-lane expressways, when the total one-way traffic volume exceeds 9,000 veh/h and the truck ratio is above 25%, the passenger and freight separation organization should be prioritized.
2. The LSI scheme shows significant advantages when the truck ratio is below 30% and the merge ratio is above 20%. Additionally, due to its relatively low construction cost, it can serve as a good alternative to the PVTS scheme.
3. The LRER scheme, due to its poor traffic capacity, higher CO emissions, and foreseeable safety issues, is not suitable for entrance sections.

Data availability statement

The raw data supporting the conclusion of this article will be made available by the authors, without undue reservation.

Author contributions

HY: Conceptualization, Writing–original draft, Formal Analysis, Investigation, Methodology, Visualization, Writing–review and editing. YL: Conceptualization, Formal Analysis, Methodology, Visualization, Writing–original draft, Writing–review and editing. BP: Conceptualization, Funding acquisition, Methodology, Project administration, Writing–original draft, Writing–review and editing. XR: Formal Analysis, Writing–original draft. JZ: Formal Analysis, Investigation, Writing–original draft. HY: Investigation, Writing–original draft.

Funding

The author(s) declare financial support was received for the research, authorship, and/or publication of this article. This work was supported by the Natural Science Basic Research Program of Shaanxi Province (Program No. 2023-JC-QN-0560), the Scientific Research Program Funded by Shaanxi Provincial Education Department (Program No. 21JK0908).

Acknowledgments

The authors would like to acknowledge the Department of Science and Technology of Shaanxi Province, Shaanxi Provincial Education Department for partially funding this work.

Conflict of interest

The authors declare that the research was conducted in the absence of any commercial or financial relationships that could be construed as a potential conflict of interest.

Publisher's note

References

Bloomberg, L., and Dale, J. (2000). Comparison of VISSIM and CORSIM traffic simulation models on a congested network. *Transp. Res. Rec.* 1727 (1), 52–60. doi:10.3141/1727-07

Borchardt, D. W., Jasek, D. L., and Ballard, A. J. (2004). *Monitoring of Texas vehicle lane restrictions*. Texas: Texas Transportation Institute.

Bowerman, B., O'Connell, R., and Koehler, A. (2004). *Forecasting: methods and applications*. Belmont, CA: Thomson Brooks/Cole.

Brugge, D., Durant, J. L., and Rioux, C. (2007). Near-highway pollutants in motor vehicle exhaust: a review of epidemiologic evidence of cardiac and pulmonary health risks. *Environ. health* 6 (1), 23–12. doi:10.1186/1476-069x-6-23

Chen, F., Xia, M., Chen, Q., and Yang, L. (2023a). Resilience enhancement method against persistent extreme weather with low temperatures in self-sustained highway transportation energy system. *IEEE Trans. Industry Appl.*, 1–14. doi:10.1109/tia.2023.3290569

Chen, Q., Pan, B., and Liu, Y. (2023b). Understanding the performance of multilane expressway exit design and a traffic organization strategy based on VISSIM micro-simulation and a comprehensive evaluation method. *Appl. Sci.* 13 (12), 7094. doi:10.3390/app13127094

Daganzo, C. F., and Laval, J. A. (2005a). Moving bottlenecks: a numerical method that converges in flows. *Transp. Res. Part B Methodol.* 39 (9), 855–863. doi:10.1016/j.trb.2004.10.004

Daganzo, C. F., and Laval, J. A. (2005b). On the numerical treatment of moving bottlenecks. *Transp. Res. Part B Methodol.* 39 (1), 31–46. doi:10.1016/j.trb.2004.02.003

Davis, L. (2012). Mitigation of congestion at a traffic bottleneck with diversion and lane restrictions. *Phys. A Stat. Mech. its Appl.* 391 (4), 1679–1691. doi:10.1016/j.physa.2011.10.036

Ding, L., Shao, Z., Zhang, H., Xu, C., and Wu, D. (2016). A comprehensive evaluation of urban sustainable development in China based on the TOPSIS-entropy method. *Sustainability* 8 (8), 746. doi:10.3390/su8080746

El-Tantawy, S., Djavadian, S., Roorda, M. J., and Abdulhai, B. (2009). Safety evaluation of truck lane restriction strategies using microsimulation modeling. *Transp. Res. Rec.* 2099 (1), 123–131. doi:10.3141/2099-14

Facts, C. (2020). *Large truck and BUS crash FACTS*.

Fontaine, M. D., Bhamidipati, C. S., and Dougald, L. E. (2009). Safety impact of truck lane restrictions on multilane freeways. *Transp. Res. Rec.* 2096 (1), 25–32. doi:10.3141/2096-04

Gan, A., and Jo, S. (2003). *Operational performance models for freeway truck-lane restrictions*. Florida: Lehman Center for Transportation Research.

Gao, Y. (2008). Calibration and comparison of the VISSIM and INTEGRATION microscopic traffic simulation models. *Va. Tech*. Available at: http://hdl.handle.net/10919/35005.

Gazis, D. C., and Herman, R. (1992). The moving and "phantom" bottlenecks. *Transp. Sci.* 26 (3), 223–229. doi:10.1287/trsc.26.3.223

Golob, T. F., Recker, W. W., and Alvarez, V. M. (2004). Safety aspects of freeway weaving sections. *Transp. Res. Part A Policy Pract.* 38 (1), 35–51. doi:10.1016/j.tra.2003.08.001

Han, Y., and Gao, G. (2010). "Relationship between highway transportation and economy development," in Proceedings of the 2010 International Conference on Mechanic Automation and Control Engineering (MACE), Wuhan, China, July 2010. doi:10.1109/mace.2010.5535461

Ishak, S., Wolshon, B., Sun, X., Korkut, M., and Qi, Y. (2012). *Evaluation of the traffic safety benefits of a lower speed limit and restriction of trucks to use of right lane only on I-10 over the Atchafalaya Basin*. Baton Rouge, Louisiana: Louisiana Transportation Research Center.

Jiang, W., Li, P., Sha, A., Li, Y., Yuan, D., Xiao, J., et al. (2023). Research on pavement traffic load state perception based on the piezoelectric effect. *IEEE Trans. Intelligent Transp. Syst.* 24, 8264–8278. doi:10.1109/tits.2023.3264248

Jo, S., Gan, A., and Bonyani, G. (2003). "Impacts of truck-lane restrictions on freeway traffic operations," in Proceedings of the 82nd annual meeting of the Transportation Research Board, janv), Washington, DC, January 2003.

Kerner, B. S., and Konhäuser, P. (1993). Cluster effect in initially homogeneous traffic flow. *Phys. Rev. E* 48 (4), R2335–R2338. doi:10.1103/physreve.48.r2335

Khurshid, A., Khan, K., and Cifuentes-Faura, J. (2023). 2030 Agenda of sustainable transport: can current progress lead towards carbon neutrality? *Transp. Res. Part D Transp. Environ.* 122, 103869. doi:10.1016/j.trd.2023.103869

Kononov, J., Bailey, B., and Allery, B. K. (2008). Relationships between safety and both congestion and number of lanes on urban freeways. *Transp. Res. Rec.* 2083 (1), 26–39. doi:10.3141/2083-04

Li, Z., Zhou, B., Teng, D., Yang, W., and Qiu, D. (2018). Comprehensive evaluation method of groundwater environment in a mining area based on fuzzy set theory. *Geosystem Eng.* 21 (2), 103–112. doi:10.1080/12269328.2017.1386594

Liu, Y., Huang, X., Duan, J., and Zhang, H. (2017). The assessment of traffic accident risk based on grey relational analysis and fuzzy comprehensive evaluation method. *Nat. hazards* 88, 1409–1422. doi:10.1007/s11069-017-2923-2

Liu, Y., Pan, B., Zhang, Z., Zhang, R., and Shao, Y. (2022). Evaluation of design method for highway adjacent tunnel and exit connection section length based on entropy method. *Entropy* 24 (12), 1794. doi:10.3390/e24121794

Moen, B., Fitts, J., Carter, D., and Ouyang, Y. (2000). *A comparison of the VISSIM model to other widely used traffic simulation and analysis programs*. Washington, DC: Institute of Transportation Engineers.

Pan, B., Ying, J., Luo, S., Shao, Y., Liu, S., Li, X., et al. (2021). Evaluation and analysis model of the length of added displaced left-turn lane based on entropy evaluation method. *J. Adv. Transp.* 2021, 1–22. doi:10.1155/2021/2688788

Patel, K., and Ruparathna, R. (2023). Life cycle sustainability assessment of road infrastructure: a building information modeling-(BIM) based approach. *Int. J. Constr. Manag.* 23 (11), 1837–1846. doi:10.1080/15623599.2021.2017113

Rrecaj, A. A., and Bombol, K. M. (2015). Calibration and validation of the VISSIM parameters-state of the art. *TEM J.* 4 (3).

Shaaban, K., and Kim, I. (2015). Comparison of SimTraffic and VISSIM microscopic traffic simulation tools in modeling roundabouts. *Procedia Comput. Sci.* 52, 43–50. doi:10.1016/j.procs.2015.05.016

Shi, M., Tian, X., Li, X., and Pan, B. (2023). The impact of parallel U-turns on urban intersection: evidence from Chinese cities. *Sustainability* 15 (19), 14356. doi:10.3390/su151914356

Singh, S., and Santhakumar, S. M. (2022). Platoon-based impact assessment of heavy-duty vehicles on traffic stream characteristics of highway lanes under mixed traffic environment. *Int. J. Intelligent Transp. Syst. Res.* 20, 29–45. doi:10.1007/s13177-021-00268-z

Stammer, R. E., and Shannon, K. (2010). *I-40 trucking operations and safety analyses and strategic planning initiatives*.

Sun, C., Dai, X., Luo, J., and Li, C. (2021). "Research on evaluation of construction organization plan of reconstruction and extension of expressway based on fuzzy comprehensive model," in Proceedings of the 2021 4th International Symposium on Traffic Transportation and Civil Architecture (ISTTCA), Suzhou, China, November 2021 (IEEE), 307–311.

Tian, X., Shi, M., Shao, M., and Pan, B. (2023). Calculation method of deceleration lane length and slope based on reliability theory. *Sustainability* 15 (17), 13081. doi:10.3390/su151713081

Toledo, T., and Koutsopoulos, H. N. (2004). Statistical validation of traffic simulation models. *Transp. Res. Rec.* 1876 (1), 142–150. doi:10.3141/1876-15

Vaidya, O. S., and Kumar, S. (2006). Analytic hierarchy process: an overview of applications. *Eur. J. operational Res.* 169 (1), 1–29. doi:10.1016/j.ejor.2004.04.028

Verma, A. (2016). Review of studies on mixed traffic flow: perspective of developing economies. *Transp. Dev. Econ.* 2, 1–16. doi:10.1007/s40890-016-0010-0

Weibin, Z., Jianbei, L., Weiwei, L., and Yuanyuan, J. (2021). Study on the setting conditions of high density and small spacing compound interchange in stereo-compound expressway. *J. Phys. Conf. Ser.* 1972, 012069. doi:10.1088/1742-6596/1972/1/012069

Wu, X., and Hu, F. (2020). Analysis of ecological carrying capacity using a fuzzy comprehensive evaluation method. *Ecol. Indic.* 113, 106243. doi:10.1016/j.ecolind.2020.106243

Xiang, Y., Li, Z., Wang, W., Chen, J., Wang, H., and Li, Y. (2016). Evaluating the operational features of an unconventional dual-bay U-turn design for intersections. *PLoS one* 11 (7), e0158914. doi:10.1371/journal.pone.0158914

Yamamoto, S., Hieida, Y., and Tadaki, S.-i. (2006). Effects of bottlenecks on vehicle traffic. *J. Phys. Soc. Jpn.* 75 (11), 114601. doi:10.1143/jpsj.75.114601

Yuan, D., Jiang, W., Sha, A., Xiao, J., Wu, W., and Wang, T. (2023). Technology method and functional characteristics of road thermoelectric generator system based on Seebeck effect. *Appl. Energy* 331, 120459. doi:10.1016/j.apenergy.2022.120459

Zhao, H., Yao, L., Mei, G., Liu, T., and Ning, Y. (2017). A fuzzy comprehensive evaluation method based on AHP and entropy for a landslide susceptibility map. *Entropy* 19 (8), 396. doi:10.3390/e19080396

Zhao, J., Wu, Y., and Zhu, N. (2009). Check and evaluation system on heat metering and energy efficiency retrofit of existing residential buildings in northern heating areas of China based on multi-index comprehensive evaluation method. *Energy Policy* 37 (6), 2124–2130. doi:10.1016/j.enpol.2008.11.044

Zhu, Y., Tian, D., and Yan, F. (2020). Effectiveness of entropy weight method in decision-making. *Math. Problems Eng.* 2020, 1–5. doi:10.1155/2020/3564835

frontiers | Frontiers in Energy Research

TYPE Original Research
PUBLISHED 28 November 2023
DOI 10.3389/fenrg.2023.1329688

OPEN ACCESS

EDITED BY
Meng Jia,
Shandong University of Science and Technology, China

REVIEWED BY
Jing Xu,
East China Jiaotong University, China
Fucheng Guo,
Lanzhou Jiaotong University, China

*CORRESPONDENCE
Yan Li,
liyan@chd.edu.cn

RECEIVED 29 October 2023
ACCEPTED 14 November 2023
PUBLISHED 28 November 2023

CITATION
Zhang Z, Niu Z, Li Y, Ma X and Sun S (2023), Research on the influence factors of accident severity of new energy vehicles based on ensemble learning. *Front. Energy Res.* 11:1329688. doi: 10.3389/fenrg.2023.1329688

Research on the influence factors of accident severity of new energy vehicles based on ensemble learning

Zixuan Zhang[1], Zhenxing Niu[2], Yan Li[2]*, Xuejun Ma[3] and Shaofeng Sun[1]

[1]School of Transportation Engineering, Chang'an University, Xi'an, Shaanxi, China, [2]Key Laboratory of Highway Engineering in Special Region of Ministry of Education, Chang'an University, Xi'an, Shaanxi, China, [3]Jiaoke Transport Consultants Ltd., Beijing, China

With the deepening of the concept of green, low-carbon, and sustainable development, the continuous growth of the ownership of new energy vehicles has led to increasing public concerns about the traffic safety issues of these vehicles. In order to conduct research on the traffic safety of new energy vehicles, three sampling methods, namely, Synthetic Minority Over-sampling Technique (SMOTE), Edited Nearest Neighbours (ENN), and SMOTE-ENN hybrid sampling, were employed, along with cost-sensitive learning, to address the problem of imbalanced data in the UK road traffic accident dataset. Three algorithms, eXtreme Gradient Boosting (XGBoost), Light Gradient Boosting Machine (LightGBM), and Categorical Boosting (CatBoost), were selected for modeling work. Lastly, the evaluation criteria used for model selection were primarily based on G-mean, with AUC and accuracy as secondary measures. The TreeSHAP method was applied to explain the interaction mechanism between accident severity and its influencing factors in the constructed models. The results showed that LightGBM had a more stable overall performance and higher computational efficiency. XGBoost demonstrated a balanced combination of computational efficiency and model performance. CatBoost, however, was more time-consuming and showed less stability with different datasets. Studies have found that people using fewer protective means of transportation (bicycles, motorcycles) and vulnerable groups such as pedestrians are susceptible to serious injury and death.

KEYWORDS

green transportation, traffic engineering, ensemble learning, traffic accidents, new energy vehicles

1 Introduction

As society continues to develop, people strive to implement the concept of sustainable development and high-level protection of the ecological environment in all aspects. There is a strong push for energy conservation and environmental protection, and a transformation of the economic development model of traditional industries. Therefore, the use of new energy vehicles in daily travel has become a necessary condition for promoting social and environmental development. With the increase in the number of new energy vehicles, there has also been a corresponding rise in the number of accidents involving these vehicles, making the safety of new energy vehicles a focus of concern for scholars. However, currently, there is limited research on the road traffic safety of new energy vehicles, and the existing

studies have certain limitations. There are significant discrepancies among the research findings, making it difficult to reach consistent conclusions.

New energy vehicles primarily use electric motors for power output in most scenarios, resulting in lower vehicle noise compared to internal combustion engine vehicles. This difference in sound may pose a safety threat to drivers or other road users. Wogalter et al. investigated public attitudes and concerns regarding hybrid vehicles, and found that the majority of participants considered the "quietness" of hybrid vehicles to be a safety threat for pedestrians (Wogalter et al., 2014). Goodes et al. conducted perception studies related to electric vehicles specifically targeting visually impaired individuals (Goodes et al., 2009). The research showed that the sound conditions of vehicles significantly affected the perception abilities of visually impaired individuals. It also confirmed that the use of additional sound devices can help visually impaired individuals detect electric vehicles earlier. Similarly, studies conducted by Garay-Vega, Parizet, and Fleury obtained similar conclusions (Garay-Vega et al., 2010; Wall Emerson et al., 2011; Parizet et al., 2014; Fleury et al., 2016). Chen et al. proposed an improved, contextually-coordinated approach to enhance traffic safety measures by utilizing drivers' inherent visual perceptual characteristics, further improving the overall safety of the roadway environment (Chen Yunteng et al., 2023). Cocron et al. conducted a study on the issue of low noise in electric vehicles from the driver's perspective (Cocron and Krems, 2013). The research indicated that severe incidents related to low noise electric vehicles were rare and mostly occurred during low-speed driving. As driving experience increases, drivers perceive the low noise characteristics of electric vehicles as a more comfortable driving experience and do not consider it to pose a higher safety threat to other road users.

On the other hand, the analysis of factors influencing the severity of traffic accidents has also received significant attention. Chen et al. used a ridge regression model to study the effect of economic development indicators on road traffic accident fatality rates in China and five European and American countries, and found that the results were completely different due to differences in economic development (Chen Xiyang et al., 2023). AlKheder et al. compared three data mining models used for accident severity analysis and found that Bayesian networks had more accurate predictive performance (AlKheder et al., 2020). Wang Lei et al. used random forest, Bayesian, BP neural network, and support vector machine to analyze the road environmental factors affecting the prediction of highway tunnel traffic accidents. The results showed that random forest had better reliability (Wang et al., 2019). Similarly, Lee et al. found that the random forest model performed the best in the analysis of traffic accident models (Lee et al., 2020). Xu proposed a one-way traffic organization scheme demonstration and evaluation method using VISSIM, which has certain practical significance (Xu, 2022). Bokaba, T et al. analyzed machine learning algorithms like AdaBoost, logistic regression, naive Bayes, and random forest in analyzing the severity of traffic accidents (Bokaba et al., 2022). They also employed the SMOTE algorithm to address data imbalance issues and obtained similar results, with random forest having higher prediction accuracy and better performance. Zhou et al. combined methods such as SMOTE-ENN and cost-sensitive learning to address data imbalance issues and used the SHAP method for model interpretation (Zhou et al., 2018). The research found that cost-sensitive learning yielded the best results in handling data imbalance problems. Islam et al. proposed a new data augmentation technique called variational autoencoder (VAE) to address class imbalance issues in traffic accident data (Islam et al., 2021). They compared it with other methods such as SMOTE and adaptive synthetic sampling (ADASYN) and found that VAE showed improved specificity and sensitivity to varying degrees while better overcoming overfitting issues. Su et al. quantitatively analyzed the severity of traffic accidents under different types and proposed a new evaluation index, which is of some reference and significance (Su and Niu, 2022).

Based on the extensive research conducted by different scholars on the factors influencing the severity of accidents involving new energy vehicles, this study aims to utilize a larger dataset of UK traffic accidents involving new energy vehicles and their associated factors. With the use of ensemble learning algorithms and data balancing techniques, the study will explore the influencing factors of accident severity. Additionally, the study will use explanations methods based on machine learning to reveal the underlying mechanisms between accident severity and its influencing factors.

2 Methodology

2.1 Ensemble learning

Ensemble learning refers to the algorithm that combines multiple learners to accomplish a learning task. It typically involves generating multiple individual learners and then combining them using certain strategies. Based on different approaches in forming individual learners, ensemble learning methods are mainly divided into Boosting and Bagging. Boosting is a type of method that can boost weak learners into strong learners, focusing on reducing bias, which represents the deviation between the expected predictions of the learning algorithm and the true results. Some commonly used Boosting algorithms include AdaBoost (Adaptive Boosting) (Freund and Schapire, 1996), GBDT (Gradient Boosting Decision Tree) (Friedman, 2001), XGBoost (Extreme Gradient Boosting) (Chen et al., 2020), LightGBM (Light Gradient Boosting Machine) (Bentéjac et al., 2021), and CatBoost (Gradient Boosting + Categorical Features) (Dorogush et al., 2018). In this study, we select XGBoost, LightGBM, and CatBoost, which are based on the GBDT algorithm framework, as the modeling algorithms. Overall, the use of numerical simulation for road and traffic accident research is a hot topic today (Prokhorenkova et al., 2018).

2.1.1 XGBoost

XGBoost is a machine learning algorithm that can perform stably and effectively in different scenarios (Chen et al., 2020). Regularized boosting is one of its core techniques, and the regularization objective function used is represented as follows:

$$\zeta(\phi) = \sum_i l(\hat{y}_i, y_i) + \sum_k \Omega(f_k) \tag{1}$$

where ϕ represents the model parameters to be calibrated through training data, $\hat{y}_i$ represents the predicted label value of the i-th

sample, y_i represents the true label value of the i-th sample. $l(\hat{y}_i, y_i)$ represents a differentiable convex loss function that measures the prediction value of the model by evaluating the discrepancy between predicted value $\hat{y}_i$ and true value y_i, f_k represents the scoring function for the output of the k-th tree, which evaluates the prediction performance of each tree. Ω represents the regularization term of the model, which controls model complexity through penalty.

$$\Omega(f) = \gamma T + \frac{1}{2}\lambda\|\omega\|^2 \tag{2}$$

where γ represents the complexity coefficient of the leaves, T is the total number of leaves, λ is the penalty factor, and ω is the score vector of the leaves.

Next, we need to calculate the optimal solution of the objective function. The following equation represents the error function for the i-th sample at the t-th iteration:

$$\zeta^{(t)} = \sum_{i=1}^{n} l\left(y_i, \hat{y}_i^{(t-1)} + f_t(X_i)\right) + \Omega(f_t) \tag{3}$$

By performing a second-order Taylor expansion and simplification of the objective function, we obtain:

$$\tilde{\zeta}^{(t)} = \sum_{i=1}^{n}\left[g_i f_t(X_i) + \frac{1}{2}h_i f_t^2(X_i)\right] + \Omega(f_t) \tag{4}$$

where, $g_i = \partial_{\hat{y}(t-1)} l(y_i, \hat{y}_i^{(t-1)})$, $h_i = \partial^2_{\hat{y}(t-1)} l(y_i, \hat{y}_i^{(t-1)})$.

Next, given a fixed tree structure, in order to minimize the objective function, we set the derivative of Equation 4 to zero. This yields the optimal predicted score for each leaf:

$$\omega_j^* = -\frac{\sum_{i\in I_j} g_i}{\sum_{i\in I_j} h_i + \lambda} \tag{5}$$

where $I_j = \{i | q(X_i) = j\}$ indicates the sample set used by the j-th leaf.

Substituting Equation 5 into the objective function, we can solve for the optimal solution:

$$\tilde{\zeta}^{(t)}(q) = -\frac{1}{2}\sum_{j=1}^{T}\frac{\left(\sum_{i\in I_j} g_i\right)^2}{\sum_{i\in I_j} h_i + \lambda} + \gamma T \tag{6}$$

After determining the loss function and the optimal solution, the next step is to determine the tree structure, specifically how to select the optimal splitting node. The basic idea of the splitting criterion in XGBoost is consistent with decision trees: using a greedy algorithm to enumerate all nodes, calculate the information gain before and after each node split, and select the node with the maximum information gain. Let I_L, I_R represent the sample sets for the left and right leaf nodes after the split, respectively. $I = I_L \bigcup I_R$. The information gain definition in XGBoost is shown in Eq. 7.

$$\xi_{split} = \frac{1}{2}\left[\frac{\left(\sum_{i\in I_L} g_i\right)^2}{\sum_{i\in I_L} h_i + \lambda} + \frac{\left(\sum_{i\in I_R} g_i\right)^2}{\sum_{i\in I_R} h_i + \lambda} - \frac{\left(\sum_{i\in I} g_i\right)^2}{\sum_{i\in I} h_i + \lambda}\right] - \gamma \tag{7}$$

2.1.2 LightGBM

LightGBM borrows some of the histogram algorithms used in GBDT (Bentéjac et al., 2021). This algorithm finds the best split point based on feature histograms. The computational complexity is mainly influenced by the cost of constructing histograms, which is O (sample size × feature size). Therefore, the key to reducing computational complexity is to reduce the number of samples and features. As a result, LightGBM proposes two new techniques to reduce the number of features and samples, thus improving the computational efficiency of the algorithm. These techniques are Gradient-based One-Side Sampling (GOSS) and Exclusive Feature Bundling (EFB).

The GOSS algorithm focuses on reducing the number of samples by using the calculated information gain as the judging criterion. It discards samples with small gradients that have little impact on the information gain and retains samples with larger gradients that have a greater impact on the information gain. Let O be the training dataset at a fixed node in the decision tree, and let $n_O = \sum I[x_i \in O]$ represent the variance gain of feature j for the split at point d, which is defined as follows:

$$V_{j|O}(d) = \frac{1}{n_O}\left(\frac{\left(\sum_{\{x_i\in O:\, x_{ij} < d\}} g_i\right)^2}{n^j_{l|O}(d)} + \frac{\left(\sum_{\{x_i\in O:\, x_{ij} < d\}} g_i\right)^2}{n^j_{r|O}(d)}\right) \tag{8}$$

where, $n^j_{l|O}(d) = \sum I[x_i \in O:\, x_{ij} \le d]$, $n^j_{r|O}(d) = \sum I[x_i \in O:\, x_{ij} \le d]$, x_i is defined as the variance gain of feature j for the split at point d in the training dataset, where g_i represents the negative gradient of the i-th sample.

GOSS first sorts the absolute values of the gradients of the training samples. It then selects the top "a" sample with the largest gradients as subset A. Next, it randomly samples "b" samples from the remaining samples with smaller gradients A^c to construct subset B. Finally, the estimated variance gain is computed on the union of subsets A and B, using the following calculation:

$$\tilde{V}_j(d) = \frac{1}{n}\left(\frac{\left(\sum_{x_i\in A_l} g_i + \frac{1-a}{b}\sum_{x_i\in B_l} g_i\right)^2}{n^j_l(d)} + \frac{\left(\sum_{x_i\in A_r} g_i + \frac{1-a}{b}\sum_{x_i\in B_r} g_i\right)^2}{n^j_r(d)}\right) \tag{9}$$

where, $A_l = \sum\{x_i \in A:\, x_{ij} \le d\}$, $A_r = \sum\{x_i \in A:\, x_{ij} \le d\}$, $B_l = \sum\{x_i \in B:\, x_{ij} \le d\}$, $B_r = \sum\{x_i \in B:\, x_{ij} \le d\}$, The coefficient $(1-a)/b$ is used to enhance the algorithm's attention to samples with small gradients.

High-dimensional data is often sparse, and in a sparse feature space, many features are mutually exclusive. One possible approach to reduce the number of features is to bind mutually exclusive features together, and the EFB algorithm is based on this idea. The problem of binding mutually exclusive features can be divided into two parts: binding rules and binding methods. EFB introduces the greedy bundling rule, which transforms the problem of feature binding into a graph coloring problem to solve. The graph coloring problem belongs to the NP-hard problem class. Once the feature binding rules are determined, the binding method needs to be defined. EFB proposes the Merge Exclusive Features method to address this issue.

Based on the above methods, the LightGBM algorithm significantly reduces the computational complexity of the training task while ensuring model performance. This leads to faster computation speed and reduced memory usage. The advantages of LightGBM are even more significant in large-scale data tasks.

2.1.3 CatBoost

CatBoost is a gradient boosting decision tree (GBDT) framework algorithm that uses oblivious decision trees as base learners (Dorogush et al., 2018). It aims to address gradient bias and prediction shift issues and directly handles categorical features. In order to tackle gradient bias, CatBoost optimizes the GBDT algorithm by using unbiased estimates of the gradient step to compute leaf values at the first step.

Machine learning tasks involve a wide variety of feature types, such as categorical features, continuous features, and so on. Categorical features refer to a set of discrete category data with no inherent ordering, such as categories for accident vehicles, colors, animals, etc. Most machine learning algorithms cannot directly process data with categorical features as training data. They first require encoding the categorical data into numerical form. Common encoding methods include ordinal encoding and one-hot encoding. One-hot encoding creates a binary feature for each category within a feature. It adds a new binary feature to the data, representing whether or not it belongs to that category. When the cardinality of the categorical feature is low, such as for gender, one-hot encoding expands the feature space and avoids the issue of meaningless order in category values. However, when the cardinality of the categorical feature is high, using one-hot encoding can result in too many new features, greatly increasing data dimensionality and computational complexity. Considering the similarity between different categories within a categorical feature, it is possible to reclassify the feature by clustering, reducing the number of categories. After that, one-hot encoding can be applied. Target statistics (TS) is one such method. In the simple TS method, the mean value of each category within the categorical feature is used as the basis for reclassification. This method is known as greedy TS. In this method, the classification of the k-th training sample for categorical feature i. i can be replaced by a numerical feature equal to a certain target statistic x_k^i. The calculation method is as follows:

$$\hat{x}_k^i = \frac{\sum_{j=1}^{n} \left\{x_j^i = x_k^i\right\} \cdot y_i + ap}{\sum_{j=1}^{n} \left\{x_j^i = x_k^i\right\} + a} \tag{10}$$

whereas a is a constant greater than 0, p is the average target value of the dataset, and y_i is the target value for category i.

The drawback of this method is that the constant $\hat{x}_k^i$ is calculated based on the target value y_k of x_k, which leads to the problem of target leakage. When there are differences in data distribution between the training and testing sets, it can result in conditional shift. CatBoost introduces a more effective method called Ordered TS. Ordered TS is based on sorting rules, so the TS value of each sample is only related to the observed history. Inspired by online learning algorithms that use time series training samples, in order to apply this method to the standard offline setting, a random sequence σ is introduced as the pair of training samples. When calculating the TS value for training samples, let $D_k = \left\{x_j: \sigma(j) < \sigma(k)\right\}$, and when calculating the TS value for testing samples, let $D_k = D$. Therefore, Ordered TS satisfies various requirements for TS calculation, and the calculation method is as follows:

$$\hat{x}_k^i = \frac{\sum_{x_j \in D_k} \left\{x_j^i = x_k^i\right\} \cdot y_i + ap}{\sum_{x_j \in D_k} \left\{x_j^i = x_k^i\right\} + a} \tag{11}$$

The meaning of the parameters in the formula is the same as above.

After addressing the conditional shift caused by target leakage, another issue that needs to be dealt with is prediction shift. CatBoost proposes an approach called ordered boosting, similar to the ordered TS method, to overcome this problem. The key feature of symmetric decision trees is that they use the same splitting criteria throughout the entire tree. This ensures that the tree's leaves are more balanced, less prone to overfitting, and significantly speeds up computation during testing. It not only efficiently handles categorical features but also forms new features by combining different features for analysis, maximizing the utilization of data information and improving model performance.

2.2 Class imbalance handling

When using machine learning algorithms for classification tasks, it is generally assumed that the distribution of data classes is balanced. However, when training models using real-world traffic accident data, it is common to encounter a phenomenon where the model achieves high prediction accuracy but poor overall performance. For instance, in traffic accident data, the proportion of fatal accidents is usually lower compared to non-fatal accidents. During the training process, the algorithm may tend to predict all accidents as non-fatal to improve overall prediction accuracy. However, this can result in the model performing poorly in predicting the minority class, which in this case is the fatal accidents. This issue is known as class imbalance (Johnson and Khoshgoftaar, 2019). On the other hand, there are scenarios where the importance of the minority class samples far outweighs that of the majority class samples. For example, accurately predicting a fatal accident holds significantly higher practical value and social impact compared to the other class. Effectively addressing imbalanced data is one of the key challenges in machine learning. Currently, there are two main methods for handling data imbalance that are relatively mature: data resampling and cost-sensitive learning (Ofek et al., 2017). Data resampling methods primarily include oversampling, undersampling, ensemble sampling, and a combination of oversampling and undersampling. This article will mainly introduce oversampling, undersampling, combination sampling, and cost-sensitive learning.

2.2.1 Oversampling

The basic idea of oversampling is to increase the number of minority class samples based on the existing minority class samples. This can be achieved through random sampling or artificial synthesis, aiming to balance the data distribution between minority and majority class samples. The most typical oversampling method is synthetic minority oversampling technique (SMOTE) (Chawla et al., 2002).

The SMOTE algorithm is an improvement over the random oversampling algorithm. The former approach, which uses a strategy of randomly duplicating samples to increase the minority class samples, can lead to overfitting and poor generalization of the model. SMOTE addresses this issue by automatically synthesizing new samples based on the minority class samples. The algorithm follows these steps: using the Euclidean distance as the criterion, calculate the distance between each minority class sample $\boldsymbol{x_i}$ and the set of minority class samples $\boldsymbol{M}$ to obtain its k nearest neighbors sample $\tilde{\boldsymbol{x}}_{\boldsymbol{ij},\boldsymbol{j}\in(\boldsymbol{0},\boldsymbol{k}]}$; randomly select samples $\tilde{\boldsymbol{x}}_{\boldsymbol{ij}}$ from the k nearest neighbors of the minority class samples, based on the desired number of generated samples; generate a new sample $\boldsymbol{x_s}$ based on $\boldsymbol{x_i}$ and $\tilde{\boldsymbol{x}}_{\boldsymbol{ij}}$. The generation method is as follows:

$$\boldsymbol{x_s} = \boldsymbol{x_i} + \boldsymbol{rand}(\boldsymbol{0},\boldsymbol{1}) \times \left(\tilde{\boldsymbol{x}}_{\boldsymbol{ij}} - \boldsymbol{x_i}\right) \tag{12}$$

2.2.2 Undersampling

Unlike oversampling, undersampling focuses on reducing the number of majority class samples through random discarding or specific rules to achieve data balance. Depending on the rules used for discarding, undersampling methods can be divided into random majority under-sampling with replacement, Edited Nearest Neighbours (ENN) (Wilson, 1972), Extraction of majority-minority Tomek links (Tomek links) (Tomek, 1976), and other techniques.

ENN is a data cleaning technology that aims to achieve undersampling by removing data with overlapping relationships based on certain rules. For any sample in the dataset, if more than half of its k nearest neighbors have a different class, this sample will be selectively removed.

2.2.3 Combination sampling

Although the above two methods partially address the problem of data imbalance, they also have limitations. For example, the SMOTE algorithm can cause the boundaries between classes to become blurry, and the ENN algorithm has limited ability to clean up majority class samples and cannot control the quantity discarded. One such method is SMOTE-ENN, which combines the SMOTE and ENN sampling techniques. It first uses the SMOTE algorithm to oversample the minority class samples and then cleans the data using the ENN algorithm. The advantage of this approach is that it addresses the issue of blurry boundaries caused by the SMOTE algorithm through the data cleaning process of the ENN algorithm. Additionally, since SMOTE increases the number of data samples, the ENN algorithm can clean up more samples.

2.2.4 Cost-sensitive learning

Cost-sensitive learning (CSL) is a machine learning approach that considers the costs or losses associated with different classification errors during model training and prediction (Johnson and Khoshgoftaar, 2019). In cost-sensitive learning, each class's classification error is assigned a different cost value. These costs can be pre-determined or adjusted based on specific problem domains and requirements. This article focuses on implementing cost-sensitive learning by increasing the weights of misclassified classes. Compared to resampling methods, cost-sensitive learning is computationally efficient and maintains good model performance. It offers more significant advantages in large data scenarios.

In this paper, cost-sensitive learning is implemented using the third-party library scikit-learn in Python (Fabian et al., 2011). It achieves cost-sensitive learning by altering the weights of each class, and the weight calculation method for each class is as follows:

$$\boldsymbol{W_i} = \boldsymbol{T} / (\boldsymbol{n} \times \boldsymbol{N_i}) \tag{13}$$

where, $\boldsymbol{T}$ is the total number of samples, $\boldsymbol{n}$ is the number of classes, and $\boldsymbol{N_i}$ is the number of samples of class $\boldsymbol{i}$.

2.3 SHAP principle

SHAP (Shapley Additive Explanation) is a game theory method based on the classical Shapley value and its related extensions (Shapley, 1953). It establishes a connection between optimal credit allocation and local explanations, and can be used to explain the outputs of various machine learning models. Typically, simple models with fewer parameters have good global interpretability, meaning they can recognize the interaction relationships between independent variables and the target variable on the complete dataset. On the other hand, complex models (such as ensemble models) have less transparent modeling processes and are difficult to interpret globally. Therefore, local methods are often used to bypass the complexity of the model itself and analyze the predictive behavior of individual samples or groups of samples in order to obtain the mechanisms of interaction between independent variables and the target variable, which is also known as the local interpretability of the model. SHAP is based on the second type of explanation strategy, which uses a relatively simple but interpretable model as an explanation model for complex models. This is also a model-agnostic explanation method. However, due to the large number of feature subsets, obtaining the model outputs for each feature subset requires a huge computational cost and is time-consuming. Therefore, Lundberg subsequently proposed TreeSHAP to improve the computation speed of tree-based ensemble models (Lundberg et al., 2020). TreeSHAP optimizes the computation method of Shapley values by calculating them based on the nodes of the tree model, rather than generating subsets through sampling all features. Additionally, TreeSHAP enhances analysis of the dependencies between variables, allowing for the identification of feature interaction relationships within the model. The XGBoost, LightGBM, and CatBoost models used in this study are all tree-based ensemble models, so TreeSHAP is used for visualizing explanations of the established accident severity model.

3 Accident severity modeling based on ensemble learning

3.1 Data preprocessing

Considering the background of the development of new energy vehicles, this study selected road safety data from 2009 to 2019 in the United Kingdom. After a simple screening and exclusion of some variables, the statistical results are shown in Table 1.

TABLE 1 Statistics on accidents involving new energy vehicles.

Variable distribution statistics	Variable	Statistics on accidents involving new energy vehicles
Data category	Accidents	21374(1.8%)
	Vehicles	44298(1.93%)
	Casualties	29170(1.77%)
Severity of the accident	Fatality	121(0.57%)
	Serious injury	2476(11.58%)
	Minor injury	18777(87.85%)
Degree of Injury (Pedestrian)	Fatality	31(0.87%)
	Serious injury	634(17.70%)
	Minor injury	2916(81.43%)
Degree of injury (cycles)	Fatality	4(0.15%)
	Serious injury	376(13.70%)
	Minor injury	2364(86.15%)

TABLE 2 Confusion matrix for binary classification problem.

True result	Predicted result	
	Positive	Negative
Positive	TP	FN
Negative	FP	TN

Due to the large amount of accident data involving new energy vehicles in the dataset used in this study, as well as the large number of accident groups, the computation efficiency is low when using resampling methods to address data imbalance issues. If the model tuning process is added, the computational power is severely insufficient. Moreover, ensemble algorithms typically construct models with performance close to the optimal model under default parameters, and the performance improvement brought by tuning is limited. On the other hand, different data imbalance handling methods can bring greater performance improvement to the model. Therefore, in the stage of selecting data balancing methods, no tuning is performed. Instead, tuning is carried out after obtaining the best data balancing method. In this study, Bayesian search, which is faster and performs better, is selected as the main tuning method. The model selection is based primarily on G-mean, with AUC and accuracy as secondary evaluation criteria, as shown in Eqs 14–18.

$$Accuracy = \frac{TP + TN}{TP + TN + FP + FN} \tag{14}$$

$$G - mean = \sqrt{Recall \times Specificity} \tag{15}$$

$$Specificity = \frac{TN}{TN + FP} \tag{16}$$

$$Recall = \frac{TP}{TP + FN} \tag{17}$$

The meanings of TN, TP, FP, and FN are shown in Table 2.

$$AUC = \frac{\sum_{i \in positive\ class} rank_i - \frac{M \times (M+1)}{2}}{M \times N} \tag{18}$$

where i represents the i-th sample in the positive examples, $rank_i$ represents the rank of the probability score for the i-th sample, M and N represent the number of positive and negative samples respectively, and $\sum_{i \in positive\ class} rank_i$ represents the sum of rank positions for all positive example samples.

3.2 Analysis of accident modeling involving new energy vehicles

3.2.1 Comprehensive accident modeling and analysis for new energy vehicles

3.2.1.1 Road and environmental factors

Results of performance evaluation for the comprehensive accident modeling of new energy vehicles, considering road and environmental factors, are shown in Table 3. Before parameter tuning, the maximum G-mean value was 59.01%, the maximum AUC value was 60.23%, and the highest accuracy for classifying severe injury accidents was 48.15%. Compared to the 2.14% without addressing data imbalance, it represents an increase of 46.01%. These maximum values were obtained using the LightGBM model with cost-sensitive learning for data balancing. Furthermore, through comparative analysis of models using the same modeling algorithm but different data balancing methods, it was found that the model with cost-sensitive learning performed better in classifying minority class samples (severe injury accidents), and this gap is difficult to compensate for through parameter tuning. However, the differences between different modeling algorithms were relatively small and could be easily leveled off through hyperparameter optimization. Therefore, considering efficiency and performance comprehensively, this paper only conducted parameter tuning for models using cost-sensitive learning, and then selected the best-performing model. The tuning results show that the performance of all models has slightly improved. Among

TABLE 3 Performance measurement table of comprehensive accident road and environmental factor classification model for new energy vehicles.

Model	Evaluation metrics	Data balancing processing					
		Before tuning					After tuning
		None	SMOTE	ENN	SMOTEENN	CSL	CSL
XGBoost	Overall accuracy (%)	88.60	88.38	85.51	83.80	66.01	69.94
	Severe casualties accuracy(%)	3.85	3.85	12.54	18.09	46.44	49.15
	Minor injuries accuracy (%)	99.02	98.77	94.48	91.88	68.41	72.49
	AUC (%)	51.43	51.31	53.51	54.98	57.43	60.82
	G-mean (%)	19.52	19.49	34.42	40.77	56.36	59.69
LightGBM	Overall accuracy (%)	88.93	88.74	87.17	84.59	69.67	63.37
	Severe casualties accuracy(%)	2.14	2.99	9.97	16.10	**48.15**	**58.83***
	Minor injuries accuracy (%)	99.60	99.28	96.66	93.01	72.32	63.93
	AUC (%)	50.87	51.14	53.31	54.56	**60.23**	**61.38***
	G-mean (%)	14.59	17.23	31.05	38.69	**59.01**	**61.33***
CatBoost	Overall accuracy (%)	88.99	88.41	87.26	84.45	68.60	67.72
	Severe casualties accuracy(%)	2.56	3.85	10.26	18.52	46.15	51.27
	Minor injuries accuracy (%)	99.61	98.81	96.73	92.56	71.35	70.03
	AUC (%)	51.09	51.33	53.49	55.54	58.75	60.65
	G-mean (%)	15.98	19.49	31.50	41.40	57.39	59.92

Notes: Bolded data represents the optimal values of the indicators before tuning, while bolded data with * represents the optimal values of the indicators after tuning.

them, the model constructed by LightGBM and CSL performed the best. After tuning, the G-mean increased by 2.32%, the AUC value increased by 1.15%, and the accuracy of severe injury accidents classification improved by 10.68%. Therefore, this model is the optimal model in this round.

3.2.1.2 Vehicle factors

In the performance evaluation results of the comprehensive accident modeling for the entire fleet of new energy vehicles, considering vehicle factors (as shown in Table 4), the maximum G-mean value was 61.04%, the maximum AUC value was 61.09%, and the highest accuracy for classifying severe injury accidents was 58.61%. These maximum values were obtained using the LightGBM model with cost-sensitive learning for data balancing. The tuning results indicate that the model constructed by CatBoost and CSL is the optimal model. After tuning, the G-mean increased to 61.65%, the AUC value increased to 61.65%, and the accuracy of severe injury accidents classification improved to 61.80%.

3.2.1.3 Casualty factors

In the performance evaluation results of the comprehensive accident modeling for casualty factors of the entire fleet of new energy vehicles (as shown in Table 5), the maximum G-mean value was 62.48%, the maximum AUC value was 62.91%, and the highest accuracy for classifying severe injury accidents was 55.57%. These maximum values were obtained using the LightGBM model with cost-sensitive learning for data balancing. However, the optimal model after tuning has changed to a model based on the CatBoost algorithm, with a G-mean increasing to 64.63%, an AUC value increasing to 64.68%, and an improved accuracy of severe injury accidents classification to 62.20%.

3.2.2 Analysis of accidents between new energy vehicles and pedestrians

3.2.2.1 Road and environmental factors

In the performance evaluation results of the road and environmental factors modeling for accidents between new energy vehicles and pedestrians (as shown in Table 6), the maximum G-mean value was 52.63%, the maximum AUC value was 54.39%, and the highest accuracy for classifying severe injury accidents was 40.64%. These maximum values were obtained using the LightGBM model with cost-sensitive learning for data balancing. The tuning results showed that the model built by LightGBM and CSL performed the best, serving as the optimal model in this round. After tuning, the G-mean increased by 7.24%, the AUC value increased by 5.87%, and the accuracy for classifying severe injury accidents improved by 12.84%.

3.2.2.2 Vehicle factors

In the performance evaluation results of the vehicle factors modeling for accidents between new energy vehicles and pedestrians (as shown in Table 7), the maximum G-mean value was 55.73%, the maximum AUC value was 57.33%, and the highest accuracy for classifying severe injury accidents was 43.86%. These maximum values were obtained using the XGBoost model with cost-sensitive learning for data balancing. After tuning, the model that

TABLE 4 Performance measurement table of comprehensive accident vehicle factor classification model for new energy vehicles.

Model	Evaluation metrics	Data balancing processing					
		Before tuning					After tuning
		None	SMOTE	ENN	SMOTEENN	CSL	CSL
XGBoost	Overall accuracy (%)	87.91	87.41	85.06	83.15	65.71	62.30
	Severe casualties accuracy(%)	2.44	1.63	12.21	16.97	50.91	60.05
	Minor injuries accuracy (%)	99.58	99.13	95.01	92.19	67.73	62.60
	AUC (%)	51.01	50.38	53.61	54.58	59.32	61.33
	G-mean (%)	15.59	12.70	34.06	39.55	58.72	61.31
LightGBM	Overall accuracy (%)	87.95	87.64	86.27	83.26	62.97	62.68
	Severe casualties accuracy(%)	0.44	0.94	8.14	16.78	**58.61**	60.24
	Minor injuries accuracy (%)	99.90	99.48	96.94	92.34	63.57	63.01
	AUC (%)	50.17	50.21	52.54	54.56	**61.09**	61.63
	G-mean (%)	6.62	9.67	28.09	39.36	**61.04**	61.61
CatBoost	Overall accuracy (%)	87.91	87.41	85.06	83.15	65.71	61.54
	Severe casualties accuracy(%)	2.44	1.63	12.21	16.97	50.91	**61.80***
	Minor injuries accuracy (%)	99.58	99.13	95.01	92.19	67.73	61.50
	AUC (%)	51.01	50.38	53.61	54.58	59.32	**61.65***
	G-mean (%)	15.59	12.70	34.06	39.55	58.72	**61.65***

Bolded data represents the optimal values of the indicators before tuning, while bolded data with * represents the optimal values of the indicators after tuning.

TABLE 5 Performance measurement table of comprehensive accident casualty factor classification model for new energy vehicles.

Model	Evaluation metrics	Data balancing processing					
		Before tuning					After tuning
		None	SMOTE	ENN	SMOTEENN	CSL	CSL
XGBoost	Overall accuracy (%)	89.42	76.20	78.63	83.89	68.59	65.54
	Severe casualties accuracy(%)	2.02	35.43	25.76	18.00	54.56	61.30
	Minor injuries accuracy (%)	99.30	80.81	84.61	91.34	70.17	66.01
	AUC (%)	50.66	58.12	55.18	54.67	62.36	63.66
	G-mean (%)	14.18	53.51	46.68	40.54	61.87	63.62
LightGBM	Overall accuracy (%)	89.62	75.80	80.24	83.70	68.76	68.58
	Severe casualties accuracy(%)	0.90	38.47	23.06	19.01	**55.57**	57.37
	Minor injuries accuracy (%)	99.66	80.02	86.71	91.02	70.25	69.84
	AUC (%)	50.28	59.24	54.88	55.02	**62.91**	63.61
	G-mean (%)	9.47	55.48	44.72	41.60	**62.48**	63.30
CatBoost	Overall accuracy (%)	89.38	76.65	84.32	83.70	68.95	66.66
	Severe casualties accuracy(%)	1.35	36.00	20.02	18.67	54.89	**62.20***
	Minor injuries accuracy (%)	99.34	81.25	91.59	91.06	70.54	67.16
	AUC (%)	50.34	58.62	55.81	54.87	62.72	**64.68***
	G-mean (%)	11.58	54.08	42.82	41.23	62.23	**64.63***

Bolded data represents the optimal values of the indicators before tuning, while bolded data with * represents the optimal values of the indicators after tuning.

TABLE 6 Performance measurement table of comprehensive accident road and environmental factor classification model for new energy vehicles-pedestrian accidents.

Model	Evaluation metrics	Data balancing processing					
		Before tuning					After tuning
		None	SMOTE	ENN	SMOTEENN	CSL	CSL
XGBoost	Overall accuracy (%)	78.10	76.80	66.80	68.00	61.80	67.80
	Severe casualties accuracy(%)	5.88	8.02	34.22	26.74	36.90	41.18
	Minor injuries accuracy (%)	94.71	92.62	74.29	77.49	67.53	73.92
	AUC (%)	50.30	50.32	54.26	52.11	52.21	57.55
	G-mean (%)	23.60	27.26	50.42	45.52	49.92	55.17
LightGBM	Overall accuracy (%)	79.30	77.70	67.80	70.20	63.00	64.50
	Severe casualties accuracy(%)	6.42	6.95	31.55	27.81	**40.64**	**53.48***
	Minor injuries accuracy (%)	96.06	93.97	76.14	79.95	68.14	67.04
	AUC (%)	51.24	50.46	53.84	53.88	**54.39**	**60.26***
	G-mean (%)	24.83	25.56	49.01	47.15	**52.63**	**59.87***
CatBoost	Overall accuracy (%)	81.30	80.30	72.20	71.00	65.50	62.00
	Severe casualties accuracy(%)	5.35	9.63	25.67	24.60	36.36	47.46
	Minor injuries accuracy (%)	98.77	96.56	82.90	81.67	72.20	65.13
	AUC (%)	52.06	53.09	54.29	53.14	54.28	56.29
	G-mean (%)	22.98	30.49	46.13	44.82	51.24	55.60

Bolded data represents the optimal values of the indicators before tuning, while bolded data with * represents the optimal values of the indicators after tuning.

TABLE 7 Performance measurement table of comprehensive accident vehicle factor classification model for new energy vehicles-pedestrian accidents.

Model	Evaluation metrics	Data balancing processing					
		Before tuning					After tuning
		None	SMOTE	ENN	SMOTEENN	CSL	CSL
XGBoost	Overall accuracy (%)	77.87	76.96	65.21	64.85	66.03	60.02
	Severe casualties accuracy(%)	13.16	11.40	**43.86**	42.11	33.77	50.00
	Minor injuries accuracy (%)	94.83	94.14	70.80	70.80	74.48	62.64
	AUC (%)	53.99	52.77	**57.33**	56.45	54.13	56.32
	G-mean (%)	35.32	32.76	**55.73**	54.60	50.15	55.97
LightGBM	Overall accuracy (%)	77.78	77.41	65.39	64.30	63.84	62.11
	Severe casualties accuracy(%)	7.02	8.77	38.16	40.35	39.47	48.62
	Minor injuries accuracy (%)	96.32	95.40	72.53	70.57	70.23	65.45
	AUC (%)	51.67	52.09	55.34	55.46	54.85	**57.04***
	G-mean (%)	26.00	28.93	52.61	53.36	52.65	56.42
CatBoost	Overall accuracy (%)	78.42	77.96	70.40	64.57	62.57	58.74
	Severe casualties accuracy(%)	5.70	9.65	27.19	42.54	39.47	**53.21***
	Minor injuries accuracy (%)	97.47	95.86	81.72	70.34	68.62	60.11
	AUC (%)	51.59	52.76	54.46	56.44	54.05	56.66
	G-mean (%)	77.87	76.96	65.21	64.85	66.03	60.02

Bolded data represents the optimal values of the indicators before tuning, while bolded data with * represents the optimal values of the indicators after tuning.

TABLE 8 Performance measurement table of comprehensive accident casualty factor classification model for new energy vehicles-pedestrian accidents.

Model	Evaluation metrics	Data balancing processing					
		Before tuning					After tuning
		None	SMOTE	ENN	SMOTEENN	CSL	CSL
XGBoost	Overall accuracy (%)	79.35	76.84	69.77	70.05	64.37	64.00
	Severe casualties accuracy(%)	6.40	12.32	37.93	30.05	38.42	**47.78***
	Minor injuries accuracy (%)	96.33	91.86	77.18	79.36	70.41	67.78
	AUC (%)	51.37	52.09	57.55	54.70	54.42	**57.78***
	G-mean (%)	24.84	33.63	54.11	48.83	52.01	**56.91***
LightGBM	Overall accuracy (%)	80.47	77.02	71.91	70.70	64.56	64.00
	Severe casualties accuracy(%)	4.93	14.78	36.95	32.02	**42.86**	44.83
	Minor injuries accuracy (%)	98.05	91.51	80.05	79.70	69.61	68.46
	AUC (%)	51.49	53.15	**58.50**	55.86	56.23	56.65
	G-mean (%)	21.98	36.78	54.38	50.52	**54.62**	55.40
CatBoost	Overall accuracy (%)	80.74	79.44	75.81	72.84	64.56	64.09
	Severe casualties accuracy(%)	0.00	9.85	28.08	26.60	40.39	45.32
	Minor injuries accuracy (%)	99.54	95.64	86.93	83.60	70.18	68.46
	AUC (%)	49.77	52.75	57.50	55.10	55.29	56.89
	G-mean (%)	22.98	30.49	46.13	44.82	51.24	55.60

Bolded data represents the optimal values of the indicators before tuning, while bolded data with * represents the optimal values of the indicators after tuning.

combined cost-sensitive learning and the CatBoost algorithm demonstrated the best overall performance. Its G-mean increased to 56.56%, the AUC value of 56.66% was close to the maximum value (57.04%), and the accuracy for classifying severe injury accidents increased by 53.21%, showing a remarkable improvement of 14%. Therefore, this model was selected as the optimal model for this round.

3.2.2.3 Casualty factors

In the performance evaluation results of the injury factors modeling for accidents between new energy vehicles and pedestrians (as shown in Table 8), the maximum G-mean value was 54.62%, the maximum AUC value was 58.50%, and the highest accuracy for classifying severe injury accidents was 42.86%. These maximum values were obtained using the LightGBM model with cost-sensitive learning and undersampling for data balancing. After tuning, the maximum values for G-mean, AUC, and accuracy for classifying severe injury accidents were 56.91%, 57.78%, and 47.78%, respectively. These values were achieved by combining cost-sensitive learning with the XGBoost model. Therefore, this model was selected as the optimal model for this stage.

3.2.3 Analysis of modeling accidents between new energy vehicles and bicycles

3.2.3.1 Road and environmental factors

As shown in Table 9, the performance evaluation results of the road and environmental factors model for accidents between new energy vehicles and bicycles, the maximum G-mean value is 49.61%, the maximum AUC value is 57.26%, and the highest accuracy rate for classifying severe and fatal accidents is 30.56%. These maximum values are obtained from the LightGBM model and the CatBoost model, both of which use a hybrid sampling method and cost-sensitive learning for data balancing. After parameter tuning, the optimal model that combines cost-sensitive learning and the XGBoost algorithm achieves a G-mean of 59.72%, an increased AUC value of 59.87%, and an improved accuracy rate of 55.56% for classifying severe and fatal accidents, with an increase of approximately 94%.

3.2.3.2 Vehicle factors

As shown in Table 10, in the performance evaluation results of the vehicle factors model, the maximum G-mean value is 54.68%, the maximum AUC value is 57.12%, and the highest accuracy rate for classifying severe and fatal accidents is 40.60%. All these maximum values are obtained from the CatBoost model, which uses cost-sensitive learning for data balancing. After parameter tuning, the optimal model that combines cost-sensitive learning and the XGBoost algorithm achieves a G-mean of 55.27%, an increased AUC value of 56.00%, and an improved accuracy rate of 47.01% for classifying severe and fatal accidents, with an increase of approximately 16%.

3.2.3.3 Casualty factors

As shown in Table 11, in the performance evaluation results of the vehicle factors model, the maximum G-mean value is 49.64%, the maximum AUC value is 52.36%, and the highest accuracy rate for classifying severe and fatal accidents is 40.74%. These maximum values are obtained from the LightGBM and CatBoost models, both

TABLE 9 Performance measurement table of comprehensive accident road and environmental factor classification model for new energy vehicles-bicycle accidents.

Model	Evaluation metrics	Data balancing processing					
		Before tuning					After tuning
		None	SMOTE	ENN	SMOTEENN	CSL	CSL
XGBoost	Overall accuracy (%)	85.91	83.93	73.67	76.51	66.63	63.04
	Severe casualties accuracy(%)	9.26	6.48	21.30	25.00	28.70	**55.56***
	Minor injuries accuracy (%)	97.72	95.86	81.74	84.45	72.47	64.19
	AUC (%)	53.49	51.17	51.52	54.73	50.59	**59.87***
	G-mean (%)	30.08	24.93	41.72	45.95	45.61	**59.72***
LightGBM	Overall accuracy (%)	86.03	85.04	73.79	78.12	68.60	65.27
	Severe casualties accuracy(%)	2.78	4.63	22.22	28.70	**30.56**	51.85
	Minor injuries accuracy (%)	98.86	97.43	81.74	85.73	74.47	67.33
	AUC (%)	50.82	51.03	51.98	57.22	52.51	59.59
	G-mean (%)	16.57	21.24	42.62	**49.61**	47.70	59.09
CatBoost	Overall accuracy (%)	86.03	85.04	81.71	78.86	71.32	70.21
	Severe casualties accuracy(%)	0.00	3.70	18.52	27.78	29.63	30.56
	Minor injuries accuracy (%)	99.29	97.57	91.44	86.73	77.75	76.32
	AUC (%)	49.64	50.64	54.98	**57.26**	53.69	53.44
	G-mean (%)	0.00	19.01	41.15	49.08	48.00	48.29

Bolded data represents the optimal values of the indicators before tuning, while bolded data with * represents the optimal values of the indicators after tuning.

TABLE 10 Performance measurement table of comprehensive accident vehicle factor classification model for new energy vehicles-bicycle accidents.

Model	Evaluation metrics	Data balancing processing					
		Before tuning					After tuning
		None	SMOTE	ENN	SMOTEENN	CSL	CSL
XGBoost	Overall accuracy (%)	84.92	84.50	75.38	72.83	69.85	62.43
	Severe casualties accuracy(%)	6.84	7.69	20.94	25.64	31.20	**47.01***
	Minor injuries accuracy (%)	97.87	97.24	84.41	80.65	76.26	64.99
	AUC (%)	52.36	52.46	52.67	53.15	53.73	**56.00***
	G-mean (%)	25.87	27.35	42.04	45.48	48.77	**55.27***
LightGBM	Overall accuracy (%)	84.98	84.98	80.43	76.35	67.78	64.92
	Severe casualties accuracy(%)	0.85	3.85	17.95	21.37	39.74	43.59
	Minor injuries accuracy (%)	98.94	98.44	90.79	85.47	72.43	68.46
	AUC (%)	49.90	51.14	54.37	53.42	56.09	56.03
	G-mean (%)	9.20	19.46	40.37	42.74	53.65	54.63
CatBoost	Overall accuracy (%)	85.71	85.53	82.80	75.44	68.94	62.67
	Severe casualties accuracy(%)	0.85	3.42	7.26	19.66	**40.60**	46.58
	Minor injuries accuracy (%)	99.79	99.15	95.32	84.69	73.64	65.34
	AUC (%)	50.32	51.28	51.29	52.17	**57.12**	55.96
	G-mean (%)	9.24	18.41	26.32	40.80	**54.68**	55.17

Bolded data represents the optimal values of the indicators before tuning, while bolded data with * represents the optimal values of the indicators after tuning.

TABLE 11 Performance measurement table of comprehensive accident casualty factor classification model for new energy vehicles-bicycle accidents.

Model	Evaluation metrics	Data balancing processing					
		Before tuning					After tuning
		None	SMOTE	ENN	SMOTEENN	CSL	CSL
XGBoost	Overall accuracy (%)	86.65	58.62	63.47	73.42	55.58	58.13
	Severe casualties accuracy(%)	0.93	37.96	28.70	23.15	43.52	41.67
	Minor injuries accuracy (%)	99.58	61.73	68.72	81.01	57.40	60.61
	AUC (%)	50.25	49.85	48.71	52.08	50.46	51.14
	G-mean (%)	9.60	48.41	44.41	43.30	49.98	50.26
LightGBM	Overall accuracy (%)	86.77	58.13	65.90	77.91	57.89	59.47
	Severe casualties accuracy(%)	0.00	38.89	25.93	17.59	**40.74**	**41.67***
	Minor injuries accuracy (%)	99.86	61.03	71.93	87.01	60.47	62.15
	AUC (%)	49.93	49.96	48.93	52.30	50.61	**51.91***
	G-mean (%)	0.00	48.72	43.18	39.12	**49.64**	**50.89***
CatBoost	Overall accuracy (%)	86.65	58.62	63.71	73.91	60.68	60.07
	Severe casualties accuracy(%)	0.00	37.04	26.85	23.15	37.04	38.89
	Minor injuries accuracy (%)	99.72	61.87	69.27	81.56	64.25	63.27
	AUC (%)	49.86	49.45	48.06	**52.36**	50.64	51.08
	G-mean (%)	0.00	47.87	43.13	43.45	48.78	49.60

Bolded data represents the optimal values of the indicators before tuning, while bolded data with * represents the optimal values of the indicators after tuning.

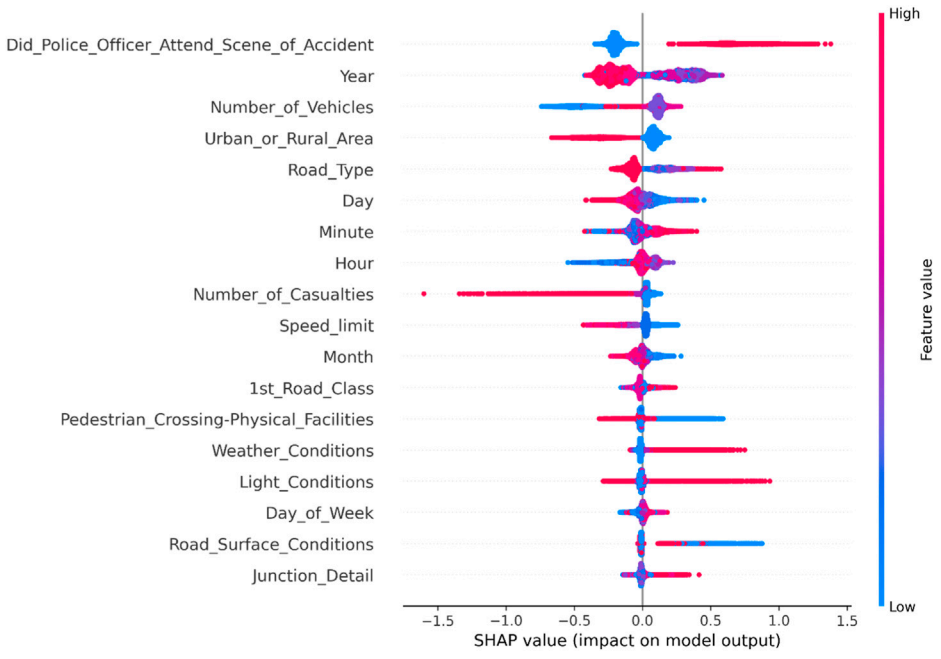

FIGURE 1
Summary diagram of road and environmental factors in overall accidents involving new energy vehicles.

of which use cost-sensitive learning and hybrid sampling for data balancing. After parameter tuning, the data shows that the model constructed by LightGBM and cost-sensitive learning is the best model. It achieves an increase of 1.35% in G-mean, an increase of 1.30% in AUC value, and an improvement of 0.93% in accuracy rate for classifying severe and fatal accidents.

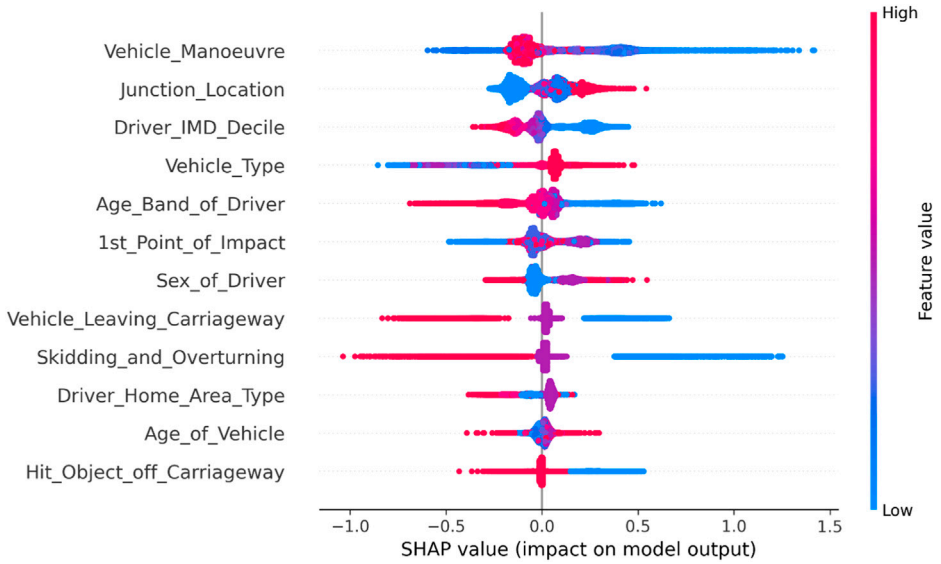

FIGURE 2
Summary diagram of vehicle factors in overall accidents involving new energy vehicles.

4 Explanation of the severity model for new energy vehicle accidents

4.1 Overall accident analysis

4.1.1 Road and environmental factors

As shown in Figure 1, in the overall analysis of accidents involving new energy vehicles, the presence of police at the scene generally indicates a higher severity level, often resulting in serious injuries or fatalities. Compared to accidents involving two vehicles colliding, accidents involving bicycles and multiple vehicles tend to be more severe. In terms of spatial dimension, the incidence of traffic accidents is higher in urban areas, but the severity level is often minor injuries. On the other hand, accidents occurring in suburban areas, ramps, and near pedestrian facilities tend to have more severe casualties. The severity level of accidents on road segments with speed limits higher than 30 mph is also higher. From a temporal perspective, there has been an increase in the number of accidents involving new energy vehicles in recent years, and they generally show higher severity levels. Additionally, accidents occurring at the end of the month, end of the year, and during early morning hours are generally more severe.

4.1.2 Vehicle factors

From Figure 2, it can be observed that accidents involving new energy vehicles are more severe during high-speed maneuvers (lane changing, overtaking), and the severity level is often higher when accidents occur in non-intersection areas. Furthermore, drivers of new energy vehicles from families with better socioeconomic conditions are more prone to serious and fatal accidents during their travel. The presence of more vulnerable modes of transportation (bicycles) among the vehicles involved in the accident also leads to higher severity levels. Moreover, older drivers are more likely to increase the severity level of traffic accidents. On the other hand, collisions occurring at the front of the vehicle, or when the vehicle hits roadside objects (curbs, barriers), objects outside the lane (walls, ditches, etc.), or rollovers, are more likely to result in casualties.

4.1.3 Casualty factors

As shown in Figure 3, among the factors affecting casualties in overall accidents involving new energy vehicles, the type of injured individuals has the most significant impact on the severity of the accidents. Individuals driving or riding in less protective modes of transportation are more prone to severe injuries and fatalities. Additionally, traffic accidents tend to cause more severe harm to older individuals. The severity of injuries also varies among individuals from different regions, with residents of suburban areas being more prone to severe injuries and fatalities. When the injured individual is a pedestrian, the severity of injuries is generally higher, leading to a higher likelihood of severe injuries or fatalities.

4.2 Analysis of pedestrian accidents

4.2.1 Road and environmental factors

From Figure 4, it can be seen that in new energy vehicle-pedestrian accidents, whether the police are present or not remains the primary indicator of the severity of the accidents. From a spatial perspective, it is observed that accidents in suburban areas and on high-speed limit sections are more likely to result in severe injuries or fatalities, consistent with the overall characteristics of accidents involving new energy vehicles. However, there are also differences, such as when a new energy vehicle-pedestrian accident occurs at an intersection, it is more likely to cause serious injuries or fatalities. From a temporal perspective, recently occurring accidents of this nature have shown higher

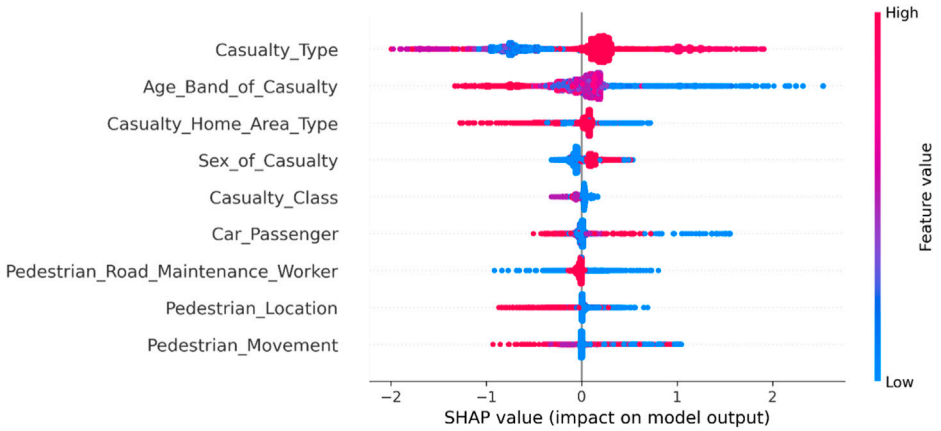

FIGURE 3
Summary diagram of casualty factors in overall accidents involving new energy vehicles.

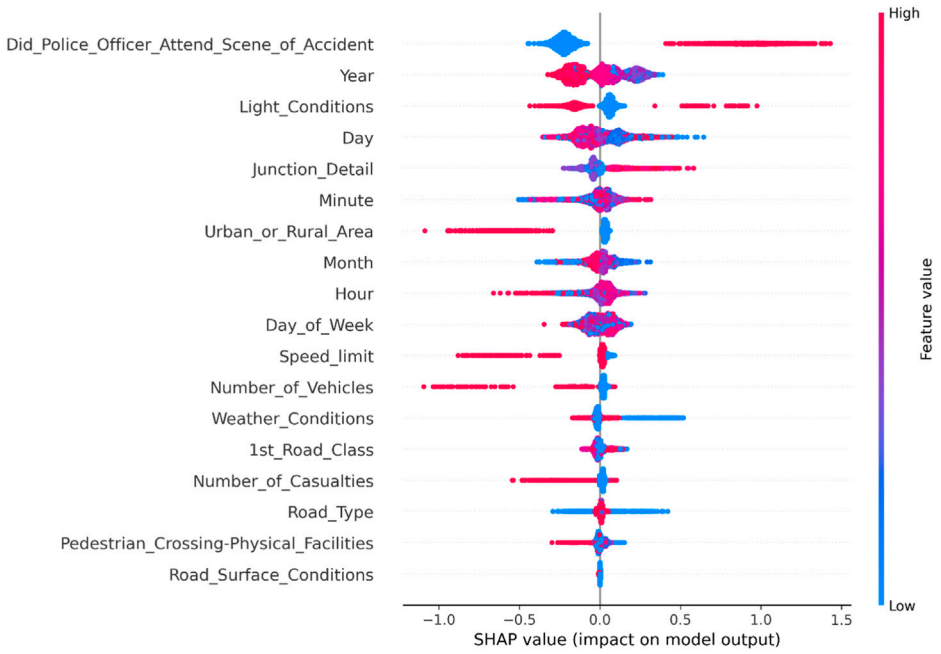

FIGURE 4
Summary diagram of road and environmental factors in new energy vehicle-pedestrian accidents.

severity and greater quantity, but with overall stability. Similarly, serious traffic accidents are more likely to occur at the end of the month, year-end, midnight, and early morning. Additionally, accidents that occur at night in unlit areas tend to have a higher severity.

4.2.2 Vehicle factors

From Figure 5, it can be seen that in terms of vehicle factors in new energy vehicle-pedestrian accidents, vehicles in high-speed motion, vehicles controlled by drivers with better economic conditions or older age, and vehicles with older age are more likely to be involved in severe traffic accidents. Additionally, accidents are more likely to occur when vehicles are inside intersections or when vehicles collide with lane edges, objects outside the road, or experience rollovers. These characteristics are consistent with the overall characteristics of accidents involving new energy vehicles.

4.2.3 Casualty factors

Through the analysis of Figure 6, it is found that in new energy vehicle-pedestrian accidents, the age of the injured individuals has a significant impact on the severity of the accidents. Younger victims tend to have lower injury severity, while older individuals generally suffer more severe injuries. Additionally, more serious traffic

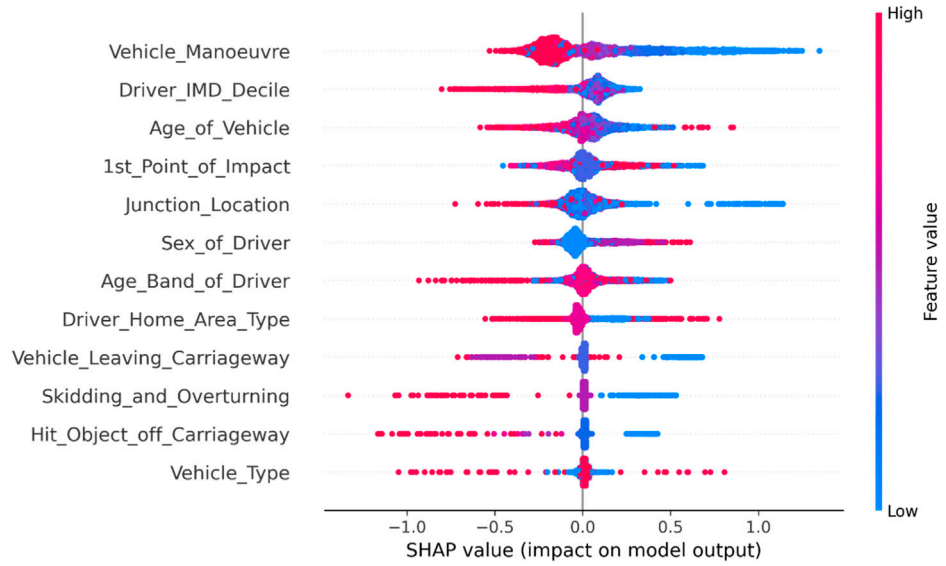

FIGURE 5
Summary diagram of vehicle factors in new energy vehicle-pedestrian accidents.

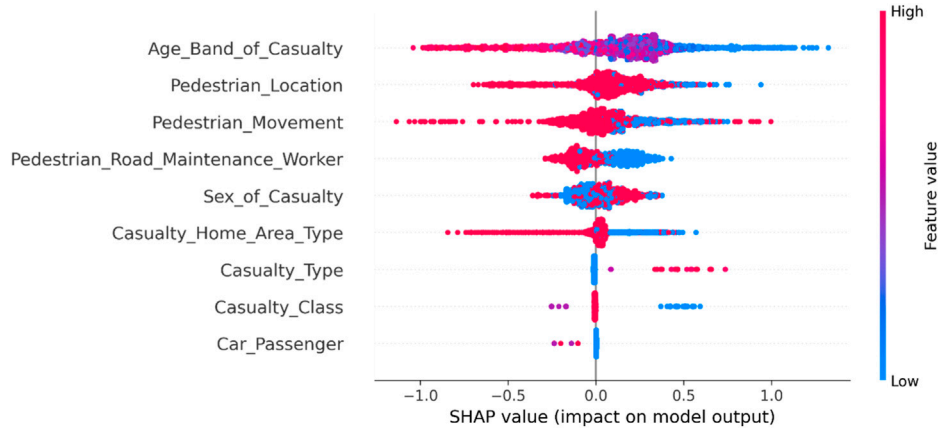

FIGURE 6
Summary diagram of factors related to casualties in new energy vehicle-pedestrian accidents.

accidents are prone to occur in the vicinity of pedestrian sidewalks undergoing construction work, and male gender or victims residing in suburban areas generally have more severe injuries.

4.3 Analysis of bicycle accidents

4.3.1 Road and environmental factors

From Figure 7, it can be observed that in new energy vehicle-bicycle accidents, the year has a greater impact on the severity of the accidents compared to the presence of police at the scene. In addition to similar findings, weekdays *versus* weekends also have a significant influence on such accidents, with higher severity in new energy vehicle-bicycle accidents occurring on weekends.

4.3.2 Vehicle factors

As shown in Figure 8, in new energy vehicle-bicycle accidents, factors such as whether it occurred at an intersection, driver's economic condition, vehicle age, driver's age, and vehicle's motion state have a significant impact on the severity of the accidents. Vehicles traveling outside intersections, younger vehicles in terms of age, or vehicles controlled by older drivers are more prone to severe traffic accidents. Similarly, accidents involving vehicles in high-speed motion, collisions with lane edges, or rollovers tend to have higher severity.

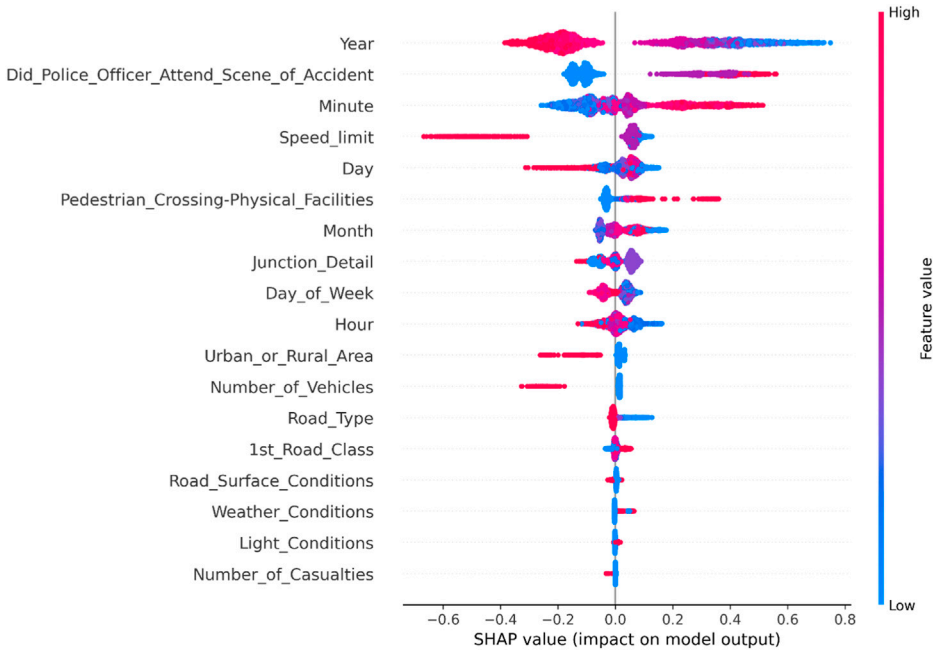

FIGURE 7
Summary diagram of road and environmental factors related to new energy vehicle-bicycle accidents.

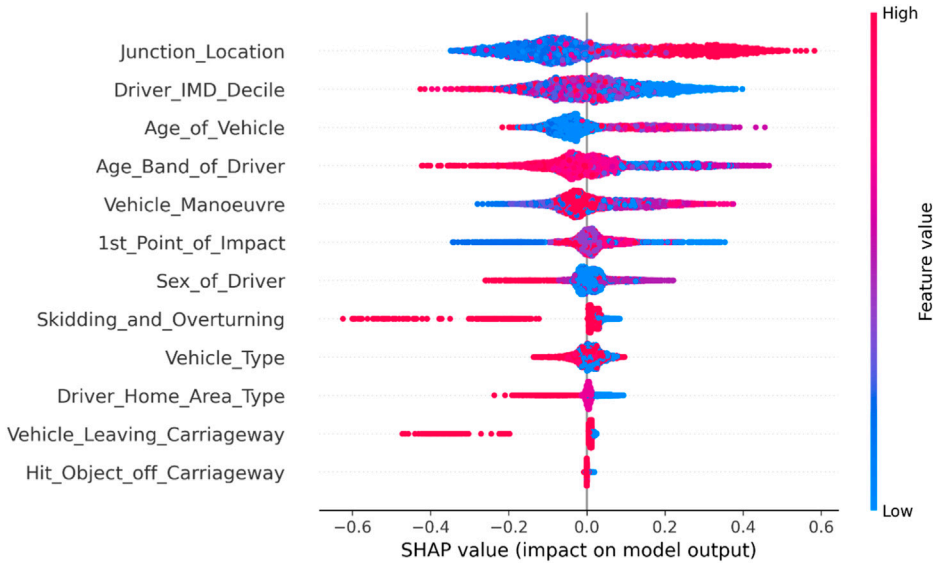

FIGURE 8
Summary diagram of vehicle factors related to new energy vehicle-bicycle accidents.

4.3.3 Casualty factors

From Figure 9, it can be observed that in new energy vehicle-pedestrian accidents, older individuals and male individuals tend to have higher severity of injuries, and victims residing in suburban areas generally have more severe injuries. On the other hand, the severity of new energy vehicle-pedestrian accidents can also be increased when pedestrian walkways are under construction.

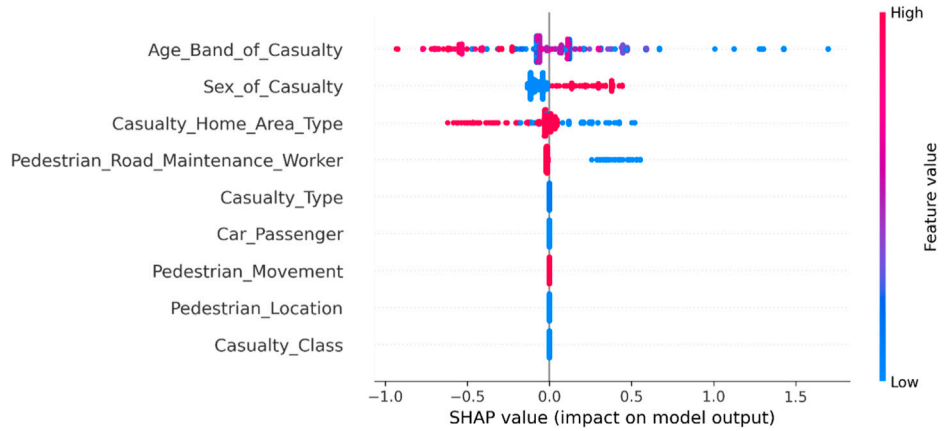

FIGURE 9
Summary diagram of factors related to casualties in new energy vehicle-bicycle accidents.

5 Conclusion

1) During the process of model building, it was found that cost-sensitive learning is more effective and efficient in handling imbalanced data issues compared to resampling methods. When comparing tree-based ensemble algorithms, LightGBM demonstrated overall stability and higher computational efficiency. XGBoost showed a balance between computational efficiency and model performance. CatBoost, on the other hand, was more time-consuming and exhibited less stability in performance across different datasets.
2) New energy vehicles are more common in urban areas, but they tend to have lower accident severity. On the other hand, accidents that occur in towns or suburban areas may be less frequent but often more severe. Additionally, accidents involving older vehicles, vehicles in high-speed maneuvers (overtaking, changing lanes, etc.), vehicles deviating from lanes, colliding with road edges (curbs, median barriers, etc.), or vehicles overturning tend to have higher severity. Furthermore, vehicles driven by male drivers or drivers with better economic conditions are more prone to serious traffic accidents. This is because male drivers or drivers with better economic conditions tend to focus more on driving experience and may exhibit aggressive driving behaviors. Elderly individuals (drivers or passengers) or individuals using vehicles with poor protection (bicycles, motorcycles) and pedestrians are also prone to serious traffic accidents. This is due to the weaker adaptability and recovery ability of elderly individuals, making them more susceptible to severe injuries or fatalities. Additionally, bicycles and pedestrians are in a vulnerable position in traffic accidents, lacking sufficient protective measures, which can result in serious injuries or fatalities.
3) In pedestrian and bicycle accidents involving new energy vehicles, in addition to the aforementioned characteristics, it has been observed that serious traffic accidents are more likely to occur when pedestrian walkways are under construction. Furthermore, in pedestrian accidents, it has been found that poorly illuminated sections at night are prone to serious traffic accidents. Additionally, when pedestrians engage in improper crossing behaviors (e.g., jaywalking), serious injuries and fatalities are more likely to occur. On the other hand, an anomalous finding has been observed in new energy vehicle-bicycle accidents. It has been found that vehicles with a shorter service time and better condition are more prone to serious traffic accidents, which differs significantly from the influencing mechanisms in other types of accidents.

Data availability statement

The original contributions presented in the study are included in the article/supplementary materials, further inquiries can be directed to the corresponding author.

Author contributions

ZZ: Writing–original draft, Writing–review and editing. ZN: Investigation, Software, Writing–review and editing. YL: Methodology, Writing–original draft. XM: Project administration, Validation, Conceptualization, Writing–review and editing. SS: Writing–original draft.

Funding

The authors declare that no financial support was received for the research, authorship, and/or publication of this article.

Conflict of interest

Author XM was employed by Jiaoke Transport Consultants Ltd.

The remaining authors declare that the research was conducted in the absence of any commercial or financial relationships that could be construed as a potential conflict of interest.

Publisher's note

References

AlKheder, S., AlRukaibi, F., and Aiash, A. (2020). Risk analysis of traffic accidents' severities: an application of three data mining models. *ISA Trans.*, 106. doi:10.1016/j.isatra.2020.06.018

Bentéjac, C., Csörgő, A., and Martínez-Muñoz, G. (2021). A comparative analysis of gradient boosting algorithms. *Artif. Intell. Rev.* 54, 1937–1967. doi:10.1007/s10462-020-09896-5

Bokaba, T., Doorsamy, W., and Paul, B. S. (2022). Comparative study of machine learning classifiers for modelling road traffic accidents. *Appl. Sci.* 12 (2), 828. doi:10.3390/app12020828

Chawla, N. V., Bowyer, K. W., Hall, L. O., and Kegelmeyer, W. P. (2002). SMOTE: synthetic minority over-sampling technique. *J. Artif. Intell. Res.* 16, 321–357. doi:10.1613/jair.953

Chen, J., Zhao, F., Sun, Y., and Yin, Y. (2020). Improved XGBoost model based on genetic algorithm. *Int. J. Comput. Appl. Technol.* 62 (3), 240–245. doi:10.1504/ijcat.2020.106571

Chen, X., Qu, W., and Liu, C. (2023b). Research on correlations between national economic development and road traffic safety based on the ridge regression. *J. Munic. Technol.* 41 (7), 1–6. doi:10.19922/j.1009-7767.2023.07.001

Chen, Y., Zhang, L., and Zhou, J. (2023a). Optimization of traffic safety facilities in highway tunnels based on driver’s visual perception. *J. Intelligent Constr.* doi:10.26599/JIC.2023.9180028

Cocron, P., and Krems, J. F. (2013). Driver perceptions of the safety implications of quiet electric vehicles. *Accid. Analysis Prev.* 58, 122–131. doi:10.1016/j.aap.2013.04.028

Dorogush, A. V., Ershov, V., and Gulin, A. (2018). CatBoost: gradient boosting with categorical features support. Available at: https://arxiv.org/abs/1810.11363.

Fabian, P., Gaël, V., Alexandre, G., Vincent, M., Bertrand, T., Olivier, G., et al. (2011). Scikit-learn: machine learning in Python. *J. Mach. Learn. Res.* 12, 2825–2830. doi:10.5555/1953048.2078195

Fleury, S., Jamet, É., Roussarie, V., Bosc, L., and Chamard, J. C. (2016). Effect of additional warning sounds on pedestrians' detection of electric vehicles: an ecological approach. *Accid. Analysis Prev.* 97, 176–185. doi:10.1016/j.aap.2016.09.002

Freund, Y., and Schapire, R. E. (1996) Experiments with a new boosting algorithm. Proceedings of the 13th International Conference on Machine Learning, Bari, Italy, July 1996.

Friedman, J. H. (2001). Greedy function approximation: a gradient boosting machine. *Ann. Statistics* 29 (5), 1189–1232. doi:10.1214/aos/1013203451

Garay-Vega, L., Hastings, A., Pollard, J. K., Zuschlag, M., and Stearns, M. (2010). *Quieter cars and the safety of blind pedestrians: phase I*. Washington, D.C: National Highway Transportation Safety Agency, 1–151.

Goodes, P., Bai, Y. B., and Meyer, E. (2009). Investigation into the detection of a quiet vehicle by the blind community and the application of an external noise emitting system. *SAE Tech. Pap.*, 4970. doi:10.4271/PT-143/4

Islam, Z., Abdel-Aty, M., Cai, Q., and Yuan, J. (2021). Crash data augmentation using variational autoencoder. *Accid. Analysis Prev.*, 151. doi:10.1016/j.aap.2020.105950

Johnson, J. M., and Khoshgoftaar, T. M. (2019). Survey on deep learning with class imbalance. *J. Big Data* 6 (1), 27–54. doi:10.1186/s40537-019-0192-5

Lee, J., Yoon, T., Kwon, S., and Lee, J. (2020). Model evaluation for forecasting traffic accident severity in rainy seasons using machine learning algorithms: seoul city study. *Appl. Sci. Switz.* 10 (1), 129. doi:10.3390/app10010129

Lundberg, S. M., Erion, G., Chen, H., DeGrave, A., Prutkin, J. M., Nair, B., et al. (2020). Explainable AI for trees: from local explanations to global understanding. *Nat. Mach. Intell.* 2 (1), 2522–5839. doi:10.48550/arXiv.1905.04610

Ofek, N., Rokach, L., Stern, R., and Shabtai, A. (2017). Fast-CBUS: a fast clustering-based undersampling method for addressing the class imbalance problem. *Neurocomputing* 243, 88–102. doi:10.1016/j.neucom.2017.03.011

Parizet, E., Ellermeier, W., and Robart, R. (2014). Auditory warnings for electric vehicles: detectability in normal-vision and visually-impaired listeners. *Appl. Acoust.* 86, 50–58. doi:10.1016/j.apacoust.2014.05.006

Prokhorenkova, L., Gusev, G., Vorobev, A., Dorogush, A. V., and Gulin, A. (2018). Catboost: unbiased boosting with categorical features. *Adv. Neural Inf. Process. Syst.*, 6638–6648. doi:10.5555/3327757.3327770

Shapley, L. S. (1953). A value for n-person games. *Contributions Theory Games* 28 (2), 307–317. doi:10.7249/P0295

Su, W., and Niu, X. (2022). Safety evaluation model of mixed traffic flow at plane intersections. *J. Munic. Technol.* 90 (5), 50–54. doi:10.19922/j.1009-7767.2022.05.050

Tomek, I. (1976). Two modifications of CNN. *IEEE Trans. Syst. Man Cybern.* 6 (11), 769–772. doi:10.1109/TSMC.1976.4309452

Wall Emerson, R., Naghshineh, K., Hapeman, J., and Wiener, W. (2011). A pilot study of pedestrians with visual impairments detecting traffic gaps and surges containing hybrid vehicles. *Transp. Res. Part F Traffic Psychol. Behav.* 14 (2), 117–127. doi:10.1016/j.trf.2010.11.007

Wang, L., Qiu, F., Xia, Y., and Han, X. (2019). Traffic accident prediction of highway tunnel based on road environmental factors. *Tunn. Constr.* 39 (08), 1301–1307. doi:10.3973/j.issn.2096-4498.2019.08.011

Wilson, D. L. (1972). Asymptotic properties of nearest neighbor rules using edited data. *IEEE Trans. Syst. Man Cybern.* 2 (3), 408–421. doi:10.1109/tsmc.1972.4309137

Wogalter, M. S., Lim, R. W., and Nyeste, P. G. (2014). On the hazard of quiet vehicles to pedestrians and drivers. *Appl. Ergon.* 45 (5), 1306–1312. doi:10.1016/j.apergo.2013.08.002

Xu, M. (2022). Research on one-way traffic in small block with dense road network. *J. Munic. Technol.* 40 (11), 117–123. doi:10.19922/j.1009-7767.2022.11.117

Zhou, B., Li, Z., and Zhang, S. (2018). Comparison of factors affecting crash severities in hit-and-run and non-hit-and-run crashes. *J. Adv. Transp.* 2018, 1–11. doi:10.1155/2018/8537131

frontiers | Frontiers in Energy Research

TYPE Original Research
PUBLISHED 29 November 2023
DOI 10.3389/fenrg.2023.1295404

OPEN ACCESS

EDITED BY
Meng Jia,
Shandong University of Science and Technology, China

REVIEWED BY
Minda Ren,
Inner Mongolia University of Technology, China
Quanman Zhao,
Shandong Jianzhu University, China

*CORRESPONDENCE
Guo Guihong,
858535193@qq.com
Ding Longting,
dltphd2018@163.com

RECEIVED 16 September 2023
ACCEPTED 24 October 2023
PUBLISHED 29 November 2023

CITATION
Xiaoyan D, Guihong G, Bori C, Zheng C and Longting D (2023), Analysis of the correlation between the pavement structure combinations and pavement performance using experimental sections.
Front. Energy Res. 11:1295404.
doi: 10.3389/fenrg.2023.1295404

Analysis of the correlation between the pavement structure combinations and pavement performance using experimental sections

Ding Xiaoyan[1], Guo Guihong[2]*, Cong Bori[3], Chen Zheng[2] and Ding Longting[3]*

[1]Shandong Hi-Speed Group Co., Ltd., Jinan, China, [2]Shandong Hi-Speed Engineering Test Co., Ltd., Jinan, China, [3]Innovation Research Institute, Shandong Hi-Speed Group Co., Ltd., Jinan, China

The new generation of pavement technology with the goal of longevity is an important supporting technology that can promote the achievement of sustainable development of high-speed roadways. To further investigate the evolution trend of long-life pavement performance, this paper paved experimental sections to explore the correlations between pavement structure combinations and pavement performances. This paper presented four experimental sections with different pavement structures, asphalt concrete layer thicknesses, and pavement materials. Then, this paper analyzed the effects of the seasonal factors, pavement structure, and lanes on the deflection value and rut depth from three dimensions by the Pearson correlation coefficient (PCC). Finally, this paper used the analysis of variance (ANOVA) to analyze the relationships between the layer thickness of various materials in the pavement structure and the pavement performances, including the deflection value, international roughness index (IRI), texture depth (TD), British Pendulum Number (BPN), sideway force coefficient (SFC), rut depth, and disease area. The results showed that the seasonal factors significantly affected the deflection values of pavement structures with PCCs of 0.61, 0.72, 0.53, and 0.78. The high temperatures increased the average deflection values by 22.85%, 72.88%, 77.61%, and 88.13%, respectively. Under the influence of high temperature in summer and traffic loads, the increased ranges of average rut depth were −0.2%, 4.89%, 9.56%, and 7.31%, respectively. The results of ANOVA showed that the pavement structure type and thickness of each structural layer significantly affected the deflection value, and there also was a strong correlation between the pavement structure type, thickness, BPN, and SFC with p-values less than 0.05. Increasing the thickness of the asphalt surface was beneficial for reducing the area of defects, while laying the semi-rigid base layer was beneficial for maintaining the deflection value and rut depth at a lower level.

KEYWORDS

asphalt pavement, long-life, pavement structure, experimental section, performance, analysis of variance

1 Introduction

Achieving durable asphalt pavements could minimize the structural damage caused by minor pavement cracks, which would reduce the high repair and maintenance costs. The structure and technology of long-life asphalt pavement had been proven to be an effective way to improve the pavement quality and service life (Bushmeyer, 2002; Ferne, 2006; Wang and Zhou, 2019). However, theoretical analysis, mechanical calculation, finite element analysis, and other methods were commonly used in the study of pavement structure performances (Yang et al., 2010; Martin et al., 2012; Zheng, 2014). There was a certain deviation between the calculated results and the actual values. Therefore, it is necessary to construct the experimental sections with the long-life pavement structures to explore the correlation between the pavement structure combinations and pavement performances, and to further investigate the evolution trend of long-life pavement performances.

The long-life pavement structures had received widespread attention. After continuous research and development, researchers conducted many meaningful research studies and achievements, especially regarding the relationships between pavement structure combinations and pavement performances. Xu and Sun (1996) analyzed the effects of pavement structure combinations on the performances of asphalt pavements and established a quantitative relationship between the pavement structure combinations and road performances, and a prediction model for road performance. Cui et al. (2008) established a finite element model using the measured tire loads and analyzed the mechanical characteristics of asphalt pavement structures. The research results showed that increasing the thickness of the surface layer and the modulus of the middle layer was very beneficial for handling the inter-stress. Liu (2012) established four types of pavement structure combination models using ABAQUS software and analyzed the stress and strain distribution characteristics inside the long-life asphalt pavement structure with a semi-rigid base under the conditions of different axle types and vehicle speeds. Wang et al. (2013) analyzed the structural plasticity damage of composite pavement (continuous reinforcement concrete pavement and asphalt concrete) and studied the laws of structural stresses and damages under different loading conditions. The analysis results showed that there were differences in the distribution of structural damage along the depth range. Zhu et al. (2023) prepared a new composite geomaterial layer for the pavement structure with a semi-rigid base to reduce the impact of reflective cracks and prolonged the service time of the pavement structure. The results showed that the composite geomaterial layer prolonged the time of crack expansion from the subgrade to the surface layer and improved the structural life of the pavement by 78.3% compared to the control group. To evaluate the effects of asphalt concrete mixtures on pavement performance, seven different flexible pavement structures were investigated using AASHTOWare Pavement ME Design. The results manifested that the mixture types and their positions in the structure had profound effects on pavement performances and inter-stress (Shakhan et al., 2023).

During the serviceable period, the performance evolution of long-life pavement structures under environmental factors and traffic loads had received much attention. Conducting the experimental sections was the most effective method to obtain the evolution law of road performances. At present, based on the physical simulation test, full-scale loop roads, and the accelerated loading test, many scholars have conducted research on the degradation of pavement structural performance. Erlingsson (2010) conducted accelerated load tests to study the response behavior and performance of commonly

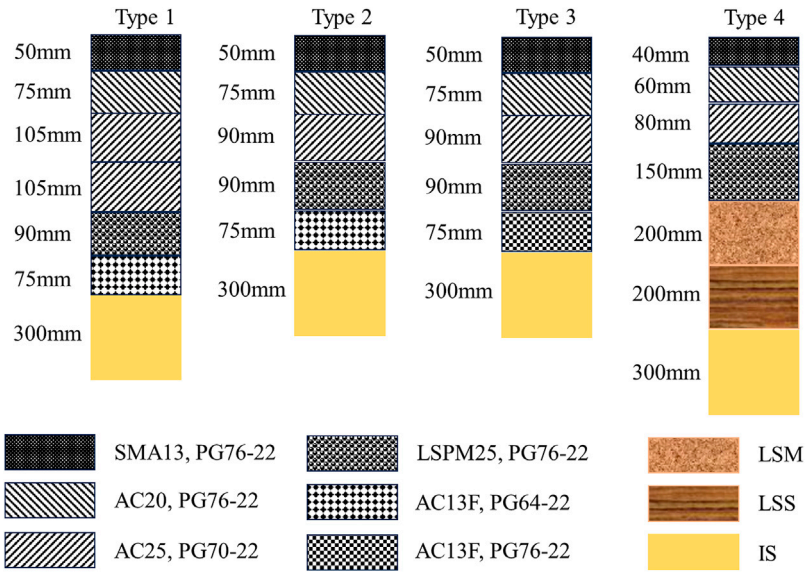

FIGURE 1
Layer thickness and materials of the pavement structure.

TABLE 1 Abbreviations for pavement structural materials.

Material	Named	Material	Named
Stone matrix asphalt (the maximum nominal particle size is 13 mm)	SMA13	Lime–fly ash-stabilized macadam	LSM
Asphalt mixture (the maximum nominal particle size is 20 mm)	AC20	Lime–fly ash-stabilized soil	LSS
Asphalt mixture (the maximum nominal particle size is 25 mm)	AC25	Improvement soil	IS
Asphalt mixture (densely mixed fine-grained type, the maximum nominal particle size is 13 mm)	AC13F	Large stone porous asphalt mixes (the maximum nominal particle size is 25 mm)	LSPM25

TABLE 2 Thickness of various materials in the pavement structure (mm).

Pavement structure	Conventional asphalt mixture thickness	LSPM thickness	AC13FA thickness	AC13FB thickness	LSS and IS thickness	Total thickness
Type 1	335	90	75	0	0	500
Type 2	215	90	75	0	0	380
Type 3	215	90	0	75	0	380
Type 4	180	150	0	0	400	730

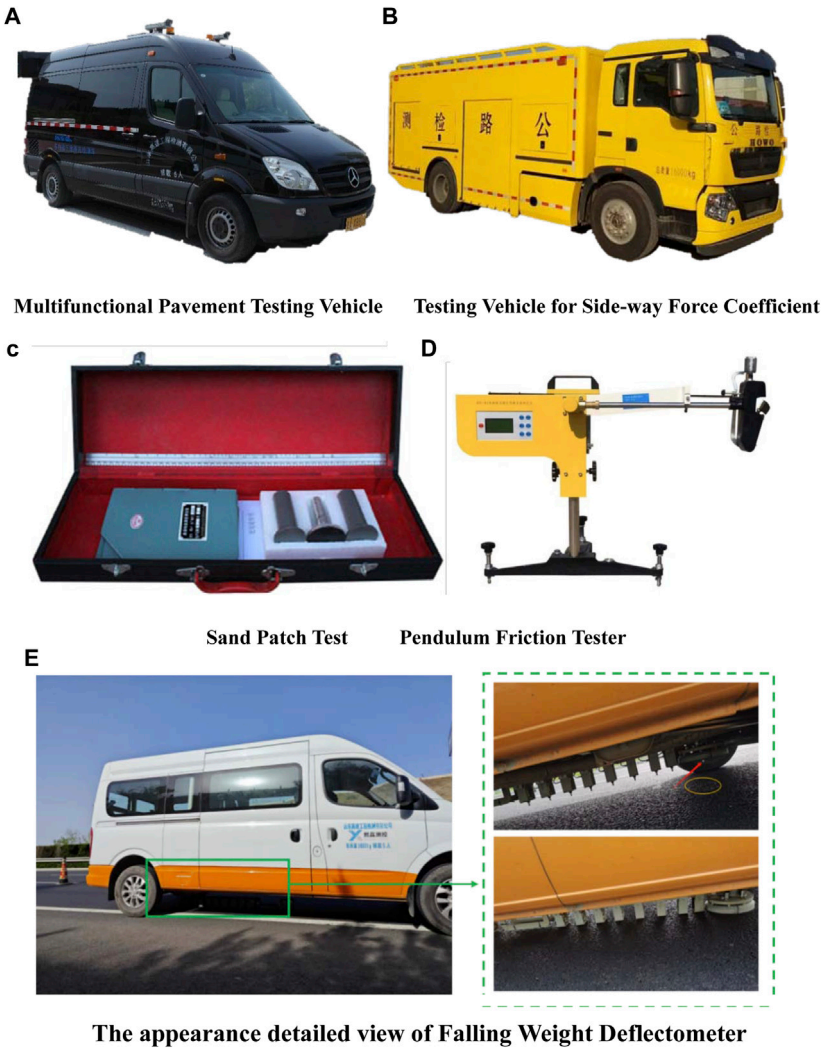

FIGURE 2
Appearance of the testing equipment. **(A)** Multifunctional pavement testing vehicle. **(B)** Testing vehicle for determining the sideway force coefficient. **(C)** Sand patch test. **(D)** Pendulum friction tester. **(E)** Detailed view of the falling weight deflectometer.

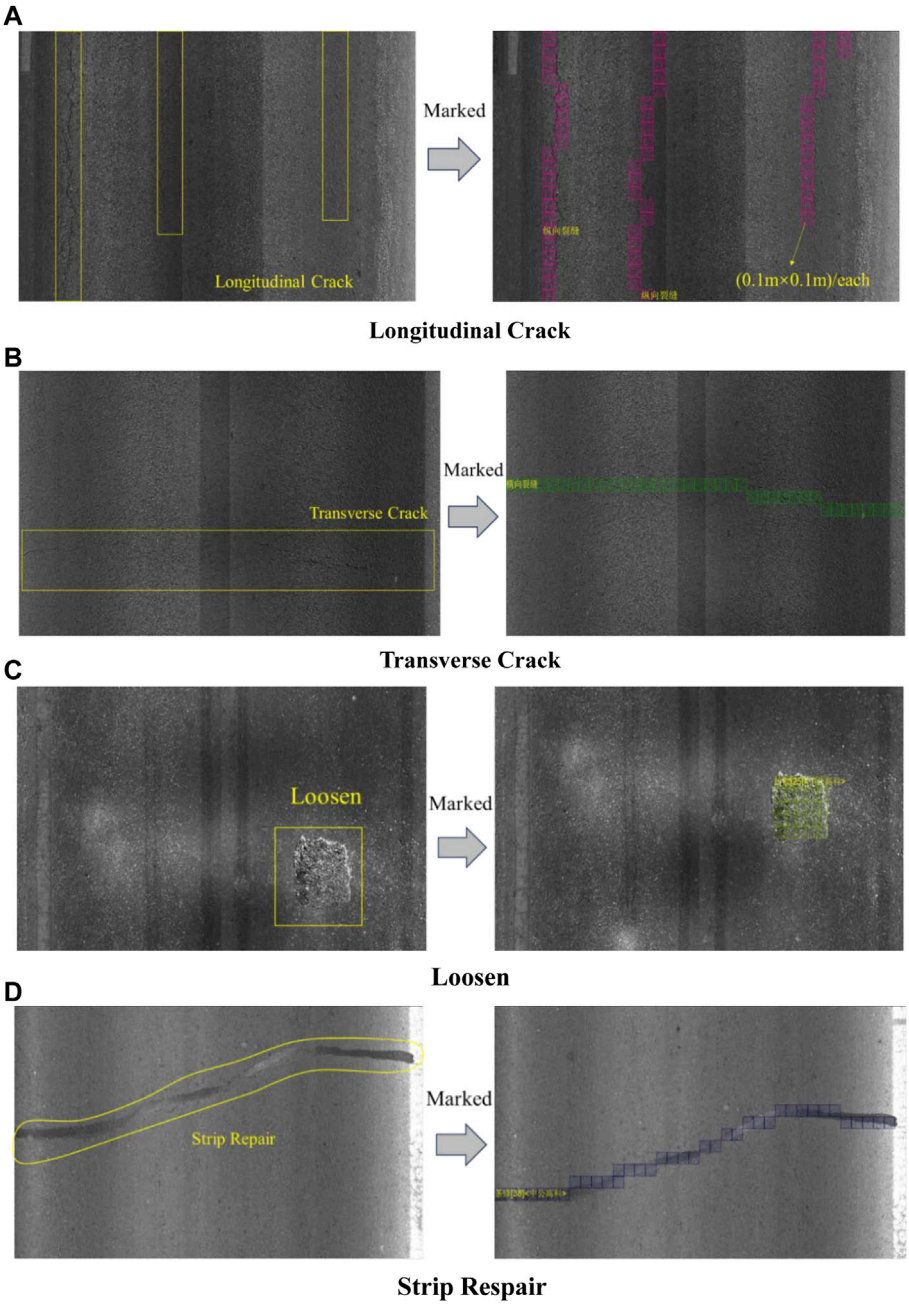

FIGURE 3
Marking process of the disease area. **(A)** Longitudinal crack. **(B)** Transverse crack. **(C)** Loosen. **(D)** Strip repair.

used pavement structures in Sweden. The results showed that the actual measurement results of rutting depth could be fitted and predicted by the Power function. In addition, the rise of groundwater level increased the permanent deformation of the pavement structure. Zhou studied the structural and mechanical responses of asphalt pavement and the nonlinear characteristics of pavement materials using full-scale tests, material tests, and actual measurement verification. The method for analyzing asphalt pavement structures based on material nonlinearity was established (Zhou et al., 2018; Zhou and Wang, 2018). Yang et al. (2021) assessed the difference in the performances of pavement structures under conventional loading and accelerated loading by the accelerated pavement tests (APTs). The test results showed that the pavement would produce deeper rutting under the same axle loading cycle in the context of APT, forming an accelerated loading effect. Ritter et al. (2012) analyzed and compared the structural performance of flexible road pavements throughout the service life through APT. The measurement results showed a significant decrease in the structural strength of two full-scale flexible road pavements.

The comparison of the data showed that there were significant differences in the total decrease of structural strength and the rate of deterioration. Chun et al. (2017) evaluated the structural benefits of a prime coat by APT. Two full-scale field test sections were built using different interlayer conditions between asphalt concrete and the base layer. The experimental results indicated that the prime coat application was beneficial for slowing down the decay of pavement structural performance, including fatigue cracking, top-down cracking, and subgrade rutting. Zhu S. et al. (2023) studied the skid resistance and its evolution trend prediction models of different asphalt mixtures using a small accelerated loading device (MLS11). The results showed that the dense-graded asphalt mixtures with a smaller oil–stone ratio had better skid resistance.

From the aforementioned research, the literature showed that many researchers have conducted extensive research on the effects of pavement structure on performances and have achieved many meaningful research achievements (Lee et al., 2007; Wang et al., 2022; Zhu et al., 2023). However, they only observed a single pavement structure, used relatively single pavement structural materials, and mainly used the accelerated pavement test or simulation software to explore the relationship between the long-life pavement structure and performances. Therefore, based on the experimental section and the observation data, this paper will analyze the correlations between pavement performance differences and pavement structures, and study the effects of pavement structures, seasonal factors, and the thickness of the structure layer on road performances. The research results can provide theoretical support for the design and performance prediction of long-life pavement structures.

2 Pavement structure and materials

With the continuously growing traffic volume and vehicle axle load, the structural damage of highway pavements is becoming increasingly prominent. The asphalt pavement with a semi-rigid base is the typical pavement structure in China. The practice has proved that simply increasing the thickness and strength of the semi-rigid base cannot meet the requirements of road performance and service life. To explore the relationship between pavement structures and service performances, this paper selected three pavement structures, including the full-depth asphalt pavement structure, composite base asphalt pavement structure, and the semi-rigid base asphalt pavement structure, as the experimental sections. In the full-depth asphalt pavement, the asphalt mixture was used for all courses above the subgrade or improved subgrade and laid directly on the prepared subgrade. Figure 1 shows the layer thickness and materials of the four pavement structure types. Table 1 shows the abbreviation for the materials in the pavement structure. Under the same conditions, this paper conducted experimental sections and compared the performances of different pavement structure types. Furthermore, the performance grade (PG) represents the performance of asphalt. AC13F with PG76-22 show better high-temperature performance than AC13F with PG64-22. Table 2 shows the thickness of the materials in the pavement structure.

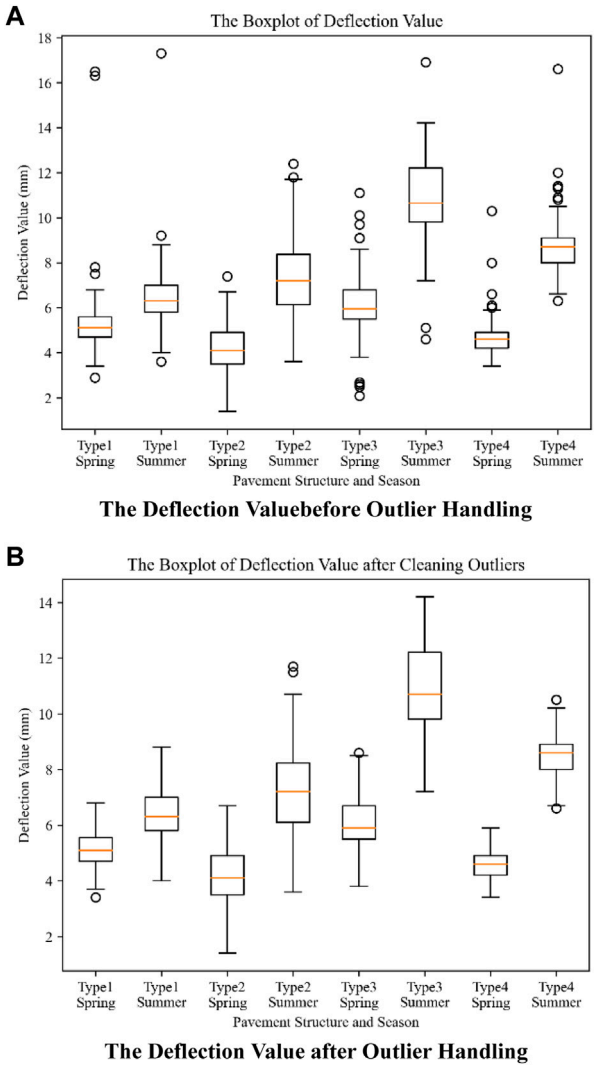

FIGURE 4
Box plots of deflection values before and after outlier handling. **(A)** Deflection value before outlier handling. **(B)** Deflection value after outlier handling.

3 Methods

3.1 Experimental scheme

In this study, the performance evaluation indicators of the long-life pavement contain the deflection value, rut depth, roughness, anti-slip ability, and disease area. The first and second performance observations of the experimental section were conducted in spring and summer, respectively. To explore the relationship between the pavement structure types and pavement performances, we collected three research works based on the data from the experimental road sections and some historical detection data, and three research works were conducted.

i. This paper explores the effects of pavement structure types on the deflection value, rut depth, skid resistance, and disease area. Among them, the skid resistance contains the texture depth

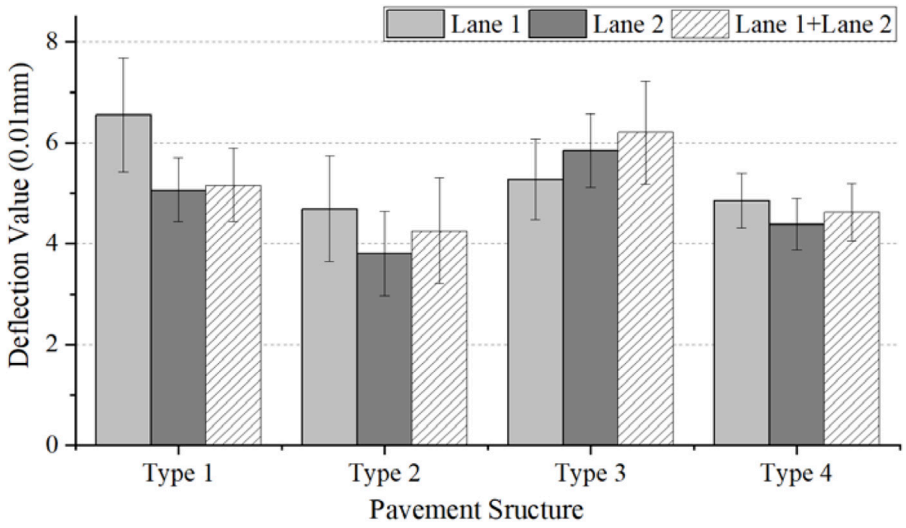

FIGURE 5
Deflection value of the pavement structure.

(TD), British Pendulum Number (BPN), sideway force coefficient (SFC), and international roughness index (IRI).

ii. Then, this paper explores the correlation between the pavement structure and pavement performances from three dimensions: seasonal factors, pavement structure, and lanes. The Shandong province is in the temperate monsoon climate region, and the average temperature in the spring is 12°C–18°C and in the summer is 28°C–32°C. Therefore, this paper explores the influence of seasonal factors on the deflection value and rut depth.

iii. Finally, this paper analyzes the correlations between the pavement structural layer thickness and pavement performances using analysis of variance.

3.2 The evaluation method of road performance

This paper uses the multifunctional pavement testing vehicle, testing vehicle for sideway force coefficient, falling weight deflectometer, sand patch test, and pendulum friction tester to evaluate the performances of the experimental sections. Figure 2 shows the appearance and details of the testing equipment. According to T0974, T0935, and T0975 of the Field Test Methods of Highway Subgrade and Pavement (JTG 3450-2019) (Research institute of highway ministry of transport, 2019), the multifunctional pavement testing vehicle measured the roughness, rut depth, and disease area of the road surface. Based on T0961, T0964, and T0965 of the Field Test Methods of Highway Subgrade and Pavement (TG 3450-2019), the skid resistance performances, including TD, BPN, and SFC, were appraised with the sand patch test, pendulum friction tester, and testing vehicle for determining the sideway force coefficient. Following T0953, this paper utilized the falling weight deflectometer to measure the deflection value of the pavement structure. For the roughness, rut depth, BPN, and disease area of the road surface, five parallel tests were conducted under the same test condition. For others, three parallel tests were conducted.

3.3 Research methods for pavement surface damage

To quantitatively appraise the grade of pavement surface diseases, this paper calculated the areas of transverse cracks, longitudinal cracks, loosens, and strip repair on the pavement surface. The calculation steps for the disease area were as follows: i. the multifunctional pavement testing vehicle collected the image information on the pavement surface. ii. Using the square grid (0.1 m × 0.1 m), the diseased areas in the image were marked. iii. The software program automatically calculated the number of squares to obtain the disease areas. Figure 3 shows the effect of automatic disease labeling.

3.4 Interquartile range method

The interquartile range (IQR) is a method in descriptive statistics to determine the difference between the third quartile (Q_3) and the first quartile (Q_1). The IQR is usually used to construct a box plot and provide a brief graphical overview of the probability distribution. IQR of the box plot is often used to filter the outliers in the data, providing a standard for identifying the outliers. The outliers are often defined as values less than Q_1-1.5IQR or greater than Q_3+1.5IQR. The interquartile range (IQR) represents the difference between Q_3 and Q_1.

3.5 Analysis of variance (ANOVA)

Analysis of variance (ANOVA) is used to measure the significance of differences in the mean values of two or more samples. The calculation steps for ANOVA are as follows:

i. Establishing hypothesis testing, H_0: multiple sample populations with equal mean values, meaning that the

10.3389/fenrg.2023.1295404

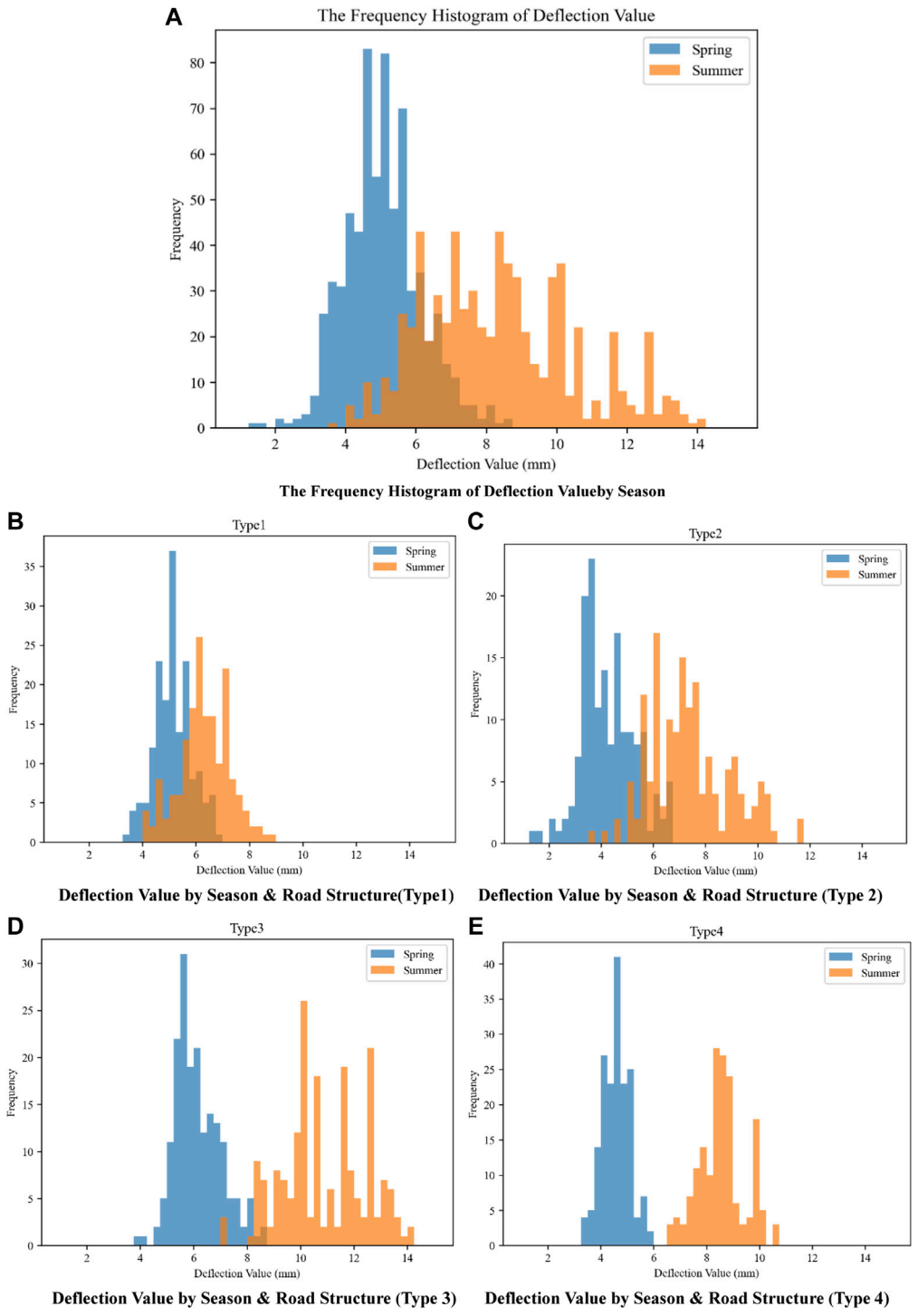

FIGURE 6
Frequency histogram of deflection value by season and road structure. **(A)** Frequency histogram of deflection value by season. **(B)** Deflection value by season and road structure (type 1). **(C)** Deflection value by season and road structure (type 2). **(D)** Deflection value by season and road structure (type 3). **(E)** Deflection value by season and road structure (type 4).

independent variable significantly affects the dependent variable. H_1: multiple sample populations with unequal or incomplete mean values, indicating the weak correlation between the independent variable and the dependent variable. The inspection level was 0.05 (α).

ii. Calculating the F-value of the test statistic; Eqs 1–7 show the calculation process of F.
iii. Determining the p-value, providing the significance level, and making the decisions. At the level of significance ($\alpha = 0.05$) and confidence interval (95%), the probability value (P) was

10.3389/fenrg.2023.1295404

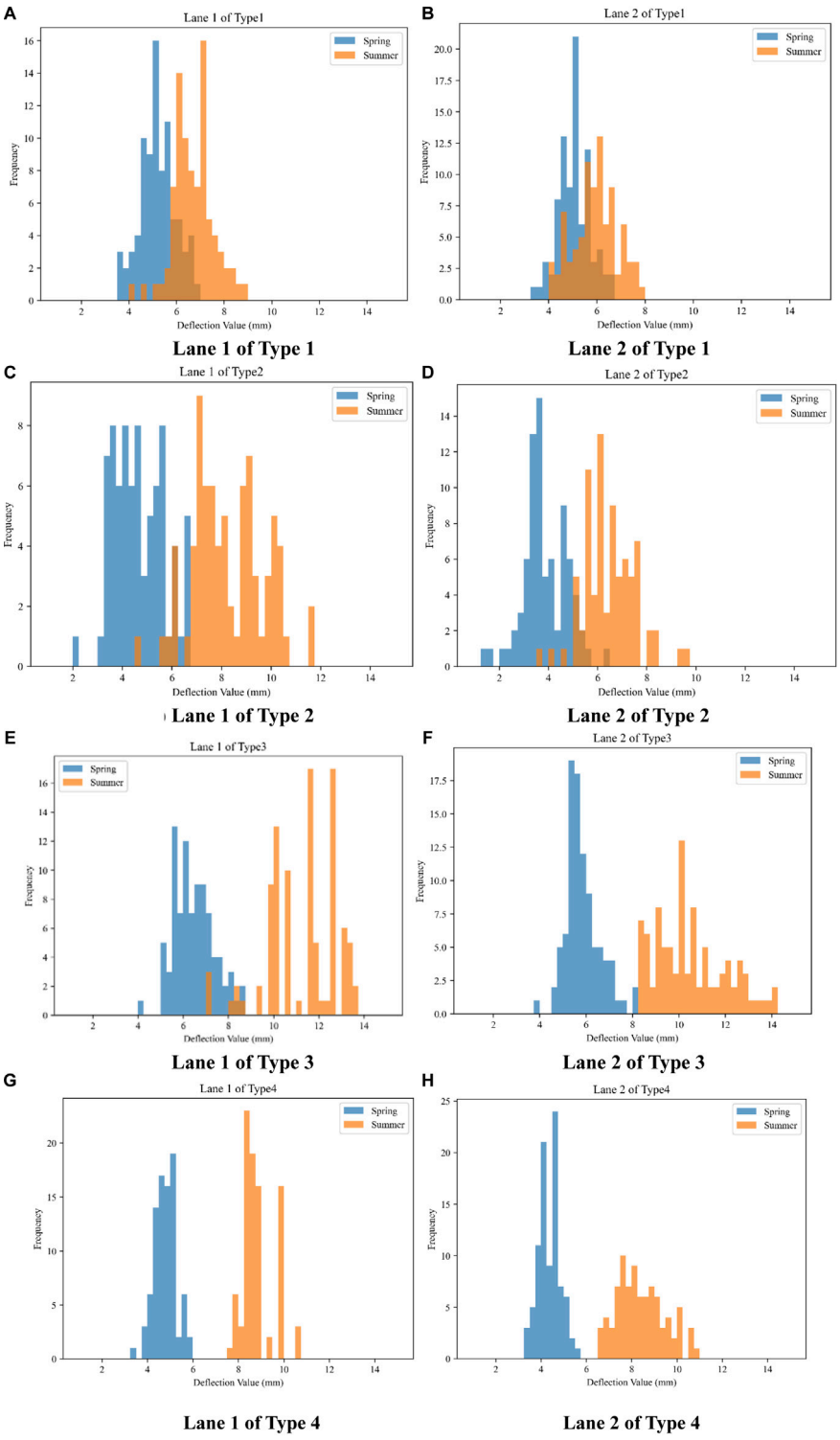

FIGURE 7
Frequency histogram of the deflection value by season, road structure, and lane. **(A)** Lane 1 of type 1. **(B)** Lane 2 of type 1. **(C)** Lane 1 of type 2. **(D)** Lane 2 of type 2. **(E)** Lane 1 of type 3. **(F)** Lane 2 of type 3. **(G)** Lane 1 of type 4. **(H)** Lane 2 of type 4.

TABLE 3 Descriptive statistics of deflection value by season and road structure.

Season and road structure	Number	Mean (0.01 mm)	Std	Minimum (0.01 mm)	Maximum (0.01 mm)	Median (0.01 mm)
Type 1-Spring	171	5.12	0.69	3.4	6.8	5.1
Type 1-Summer	173	6.29	0.95	4.0	8.8	6.3
Type 2-Spring	157	4.24	1.03	1.4	6.7	4.1
Type 2-Summer	156	7.33	1.55	3.6	11.7	7.2
Type 3-Spring	183	6.12	0.87	3.8	8.6	5.9
Type 3-Summer	189	10.87	1.57	7.2	14.2	10.7
Type 4-Spring	175	4.55	0.51	3.4	5.9	4.6
Type 4-Summer	170	8.56	0.85	6.6	10.5	8.6

obtained. If $p > 0.05$, H_0 was accepted, and If $P < 0.05$, H_1 was accepted (Liu et al., 2009; Research institute of highway ministry of transport, 2019; Ye et al., 2021; Liu and Jia, 2023; Rosopa and King, 2023).

$$SS_B = \sum_{j=1}^{k} n_j \left(\bar{X}_j - \bar{X}_i\right)^2, \tag{1}$$

$$SS_w = \sum_{j=1}^{k} \sum_{i=1}^{n} n_j \left(\bar{X}_{ij} - \bar{X}_j\right)^2, \tag{2}$$

$$MS_w = \frac{SS_w}{df_w}, \tag{3}$$

$$MS_B = \frac{SS_B}{df_B}, \tag{4}$$

$$df_B = k-1, \tag{5}$$

$$df_w = n_1 - 1 + n_2 - 1 + \ldots + n_k - 1 = N - k, \tag{6}$$

$$F = \frac{MS_B}{MS_w} = \frac{SS_B/df_B}{SS_w/df_w}. \tag{7}$$

In this study, the independent variables include the thicknesses of the conventional asphalt mixture (AM), LSPM, AC13FA, AC13FB, LSS, IS, and total thickness. The deflection value, IRI, TD, BPN, SFC, rut depth, and disease area are the dependent variables.

3.6 Pearson correlation coefficient

The Pearson correlation coefficient, a commonly used statistical method, can assess the strength and direction of the linear relationship between two variables. Its value range is between −1 and 1, where −1 represents a perfect negative correlation, 1 represents a perfect positive correlation, and 0 represents no correlation. The Pearson correlation coefficient can be calculated based on the covariance and standard deviation of two variables, as shown in Eq. 8. The Pearson correlation coefficient is the product of the covariance of two variables divided by their respective standard deviations, resulting in a low sensitivity of the Pearson correlation coefficient to variable scales. Therefore, it can be used for correlation analysis between variables at different scales.

$$r = \frac{1}{n-1} \sum_{i=1}^{n} \left(\frac{X_i - \bar{X}}{\sigma_X}\right)\left(\frac{Y_i - \bar{Y}}{\sigma_Y}\right) \tag{8}$$

4 Results and discussion

4.1 Relationship between the pavement structure and deflection values

To investigate the impact of seasonal factors on the bearing capacity of pavement structures, the deflection values for the four pavement structure types were collected in both spring and summer, and data analysis was conducted. To ensure comprehensive analysis, three dimensions were selected: overall analysis, analysis based on both the season and road structure, and analysis based on the season, road structure, and lane. Figure 4A shows the box plot of the deflection values for the four types. Data preprocessing, the removal of missing values and outliers, was performed on the collected deflection values. The outliers were handled using the interquartile range method. Considering the differences in the bearing capacity of different pavement structures, outlier handling was performed based on the seasonal and road structural dimensions. Figure 4B shows the box plot after the outlier handling process.

The pavement structure affected the deflection value of the pavement structure. Figure 5 shows the average deflection value of each pavement structure. The type 4 and type 2 pavement structures have lower deflection values, indicating that the semi-rigid base and asphalt mixtures with the lower performance grade (PG) can improve the strength and bearing capacity of pavement structures. In addition, the pavement structure (type 1) has the largest thickness of the asphalt mixture, and the asphalt mixture with viscoelastic properties cannot provide relatively high strength and bearing capacity for pavement structures. The asphalt mixtures with the higher PG cannot provide sufficient bearing capacity for the type 3 pavement structure.

Frequency histograms of the deflection values were plotted for the three data dimensions, as shown in Figures 6, 7. The deflection values were divided into intervals of 0.5, and the descriptive statistics, such as sample size, mean, standard deviation, minimum value, maximum value, and median, were calculated using statistical methods. The results are shown in Table 3. Based on Figure 6 and Table 3, it can be observed that the deflection values of the four pavement structures varied with the seasons and had higher values in summer than in spring. In terms of the deflection value distribution, the values in summer are

TABLE 4 Descriptive statistics of deflection value by season and road structure.

Season, road structure, and lane	Number	Mean (0.01 mm)	Std	Minimum (0.01 mm)	Maximum (0.01 mm)	Median (0.01 mm)
Type 1-Lane 1-Spring	84	5.20	0.73	3.7	6.8	5.20
Type 1-Lane 1-Summer	86	6.68	0.84	4.0	8.8	6.60
Type 1-Lane 2-Spring	87	5.05	0.64	3.4	6.7	5.00
Type 1-Lane 2-Summer	87	5.92	0.90	4.1	7.9	5.90
Type 2-Lane 1-Spring	78	4.64	1.01	2.2	6.7	4.55
Type 2-Lane 1-Summer	77	8.24	1.44	4.6	11.7	8.10
Type 2-Lane 2-Spring	79	3.85	0.89	1.4	6.4	3.70
Type 2-Lane 2-Summer	79	6.44	1.08	3.6	9.5	6.40
Type 3-Lane 1-Spring	89	6.44	0.88	4.1	8.6	6.40
Type 3-Lane 1-Summer	96	11.24	1.52	7.2	13.5	11.70
Type 3-Lane 2-Spring	94	5.82	0.74	3.8	8.0	5.70
Type 3-Lane 2-Summer	93	10.48	1.53	8.3	14.2	10.20
Type 4-Lane 1-Spring	86	4.76	0.48	3.4	5.9	4.80
Type 4-Lane 1-Summer	89	8.83	0.69	7.5	10.7	8.70
Type 4-Lane 2-Spring	89	4.34	0.46	3.4	5.5	4.30
Type 1-Lane 1-Spring	86	8.39	1.04	6.6	10.8	8.25

TABLE 5 Correlation of deflection value by different dimensions.

Dimension		Pearson correlation coefficient	*p*-value
Season	Spring and summer	0.66	0.00
Season and road structure	Type 1-Spring and summer	0.22	0.00
	Type 2-Spring and summer	0.83	0.00
	Type 3-Spring and summer	0.76	0.00
	Type 4-Spring and summer	0.35	0.00
Season, road structure, and lane	Type 1-Lane 1-Spring and summer	0.35	0.00
	Type 1-Lane 2-Spring and summer	0.05	0.62
	Type 2-Lane 1-Spring and summer	0.83	0.00
	Type 2-Lane 2-Spring and summer	0.78	0.00
	Type 3-Lane 1-Spring and summer	0.85	0.00
	Type 3-Lane 2-Spring and summer	0.64	0.00
	Type 4-Lane 1-Spring and summer	0.41	0.00
	Type 4-Lane 2-Spring and summer	0.24	0.03

more dispersed compared to the values in spring, which is due to the higher temperature in summer. The viscosity of the asphalt concrete surface layer with the viscoelastic properties increases under high temperatures, resulting in an increase in the deflection value. Among them, the seasonal factor has the least impact on the deflection values of the type 1 structure, and the type 1 structure shows smaller distribution dispersion in both spring and summer. The thickness of the asphalt concrete layer in the type 1 structure is the largest. Owing to the same thermal conductivity coefficient (Jiao et al., 2020; Jia et al., 2023; Liu et al., 2023), the heat on the road surface continues to transmit downward, and the overall heat of the road structure is

10.3389/fenrg.2023.1295404

TABLE 6 Difference in average values of the deflection value under different seasons, pavement structures, and lanes.

Season, road structure, and lane	Difference in average value
Spring and summer	3.30
Type 1-Spring and summer	1.17
Type 2-Spring and summer	4.02
Type 3-Spring and summer	4.79
Type 4-Spring and summer	2.10
Type 1-Lane 1-Spring and summer	1.47
Type 1-Lane 2-Spring and summer	0.88
Type 2-Lane 1-Spring and summer	4.00
Type 2-Lane 2-Spring and summer	4.04
Type 3-Lane 1-Spring and summer	4.90
Type 3-Lane 2-Spring and summer	4.69
Type 4-Lane 1-Spring and summer	2.63
Type 4-Lane 2-Spring and summer	1.59

relatively low. Therefore, the effect of high temperature on the deflection value is relatively small. The asphalt concrete layer of other pavement structures is relatively thin, and the thermal conductivity coefficient of the asphalt concrete layer is different from that of other structural layers. The heat on the road surface is maintained at a high level due to the inability to effectively transfer it downward. Therefore, the high temperature significantly affects the deflection values of the type 2, 3, and 4 pavement structures. Furthermore, the type 4 structure shows smaller distribution dispersion in both spring and summer. This may be because the cement-stabilized crushed stone mixture has a larger layer thickness and high stiffness, and is less influenced by the temperature in the type 4 pavement structure. Although the properties of asphalt concrete are greatly influenced by temperature, their thinner thickness cannot change the overall stiffness characteristics of the pavement structure; therefore, the data on the deflection value in the type 4 pavement structure are relatively stable.

To further quantify the correlation of deflection values with seasonal changes, a correlation analysis was conducted. Tables 4, 5 show the Pearson correlation coefficients and significance levels (p-values). It indicates that the seasonal factors can affect the deflection value of the pavement structure, ignoring the influence of the different pavement structures. Table 5 shows that the type 2 and type 3 pavement structures have a strong correlation between deflection values in spring and summer, while the correlation between deflection values of the type 1 and type 4 pavement structures in spring and summer is weak. This may be because the type 3 structures contain a thicker asphalt concrete layer, while the type 4 structure contains a semi-rigid base with high stiffness.

Figure 7 shows the frequency histogram of the deflection value by season, road structure, and lane. Table 5 shows the correlation of deflection values under the conditions of different pavement structures, seasons, and lanes. The type 2 and type 3 pavement structures have a strong correlation between deflection values in spring and summer, and changing lanes will not change this conclusion.

Furthermore, this paper calculated the differences in the average values of the deflection value under different seasons, pavement structures, and lanes to further explore the differences in the bearing capacity of the four pavement structures. Under the influence of high temperatures in summer and traffic loads, the comparison of the average deflection values of different pavement structures is shown in Table 6. It indicated that for the type 3 structure, the difference between the deflection values in summer and spring was the largest, followed by the type 2 structure, and the smallest value was for the type 1 structure. This means that the bearing capacity of pavement

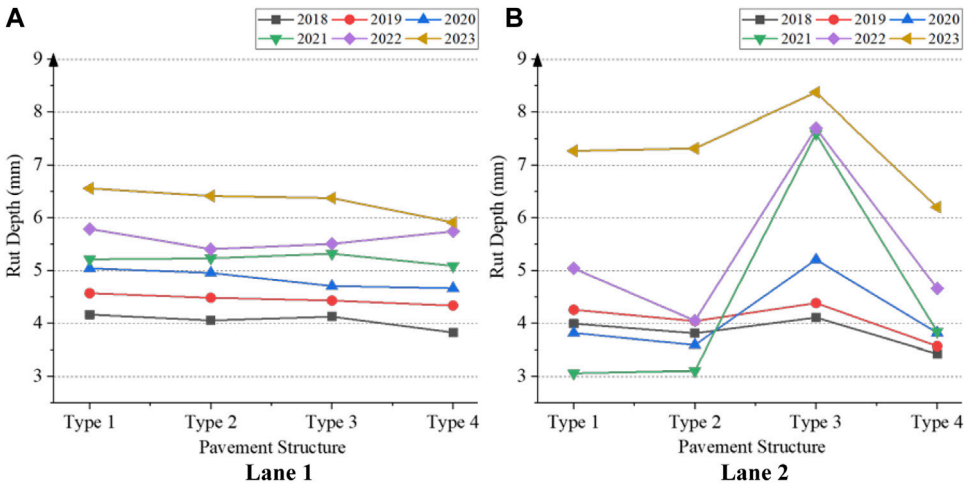

FIGURE 8
Development trend of rutting depth in the pavement structure. **(A)** Lane 1. **(B)** Lane 2.

structures with a thicker asphalt concrete layer is easily affected by the high temperature in summer.

4.2 Relationship between the pavement structure and rut depth

Figure 8 shows the development trend of the rut depth in the pavement structure. For lane 1, the pavement structure could not affect the rut depth. For lane 2, the pavement structure could affect the rut depth. The main vehicle types for lane 2 and lane 1 are heavy vehicles and light vehicles, respectively. On the whole, the type 4 structure has the smallest rut depth, and the type 2 structure has the largest rut depth.

To investigate the seasonal impact on the rut depth, the data on the rut depth for the four pavement structures were collected during the spring and summer seasons. The data analysis was conducted using the same three dimensions as the analysis of the deflection values. In terms of data preprocessing, the same method that was used for preprocessing the deflection values was employed. The box plots before and after preprocessing are shown in Figure 8.

Figure 9 shows the frequency histograms of rut depth for the three data dimensions. The rut depth was divided into intervals of 0.5, and the descriptive statistics, such as the sample size, mean, standard deviation, minimum value, maximum value, and median, were calculated using statistical methods. The results are presented in Table 7.

Figure 10 and Tables 7, 8 show that the rut depth of the pavement structure undergoes slight changes after the effects of high temperatures in summer and traffic loads. The rut depth in summer is slightly higher than that in spring, which can be attributed to the longer cycle of rut formation. To further quantify the correlation between the rut depth and seasonal variations, the correlation analysis was conducted using the same three data dimensions, as mentioned previously. The Pearson correlation coefficients and corresponding significance levels (p-values) were used to characterize the correlation. The results are presented in Table 9.

Table 9 shows that the overall correlation for the type 2 pavement structure is relatively strong. However, for the individual lanes of the type 2 pavement structure, the correlation coefficients are 0.33 and 0.31, respectively, indicating that they have weaker correlations. This may be attributed to the smaller sample size for individual lanes and the smaller variations in rut depth between spring and summer seasons. Therefore, the lane-based correlation analysis has a higher chance of randomness, and the analysis based on the dimensions of season and pavement structure is more reliable. The significant difference in correlation coefficients between the two lanes of the type 4 pavement structure also supports this point.

Considering the correlation analysis based on the dimensions of season and pavement structure, under the influence of high temperatures in summer and traffic loads, the rut depth of the four pavement structures has undergone significant changes, and seasonal factors have an impact on the rut depth. This paper calculates the differences in the average values of rut depth under different seasons, pavement structures, and lanes, as shown in Table 10.

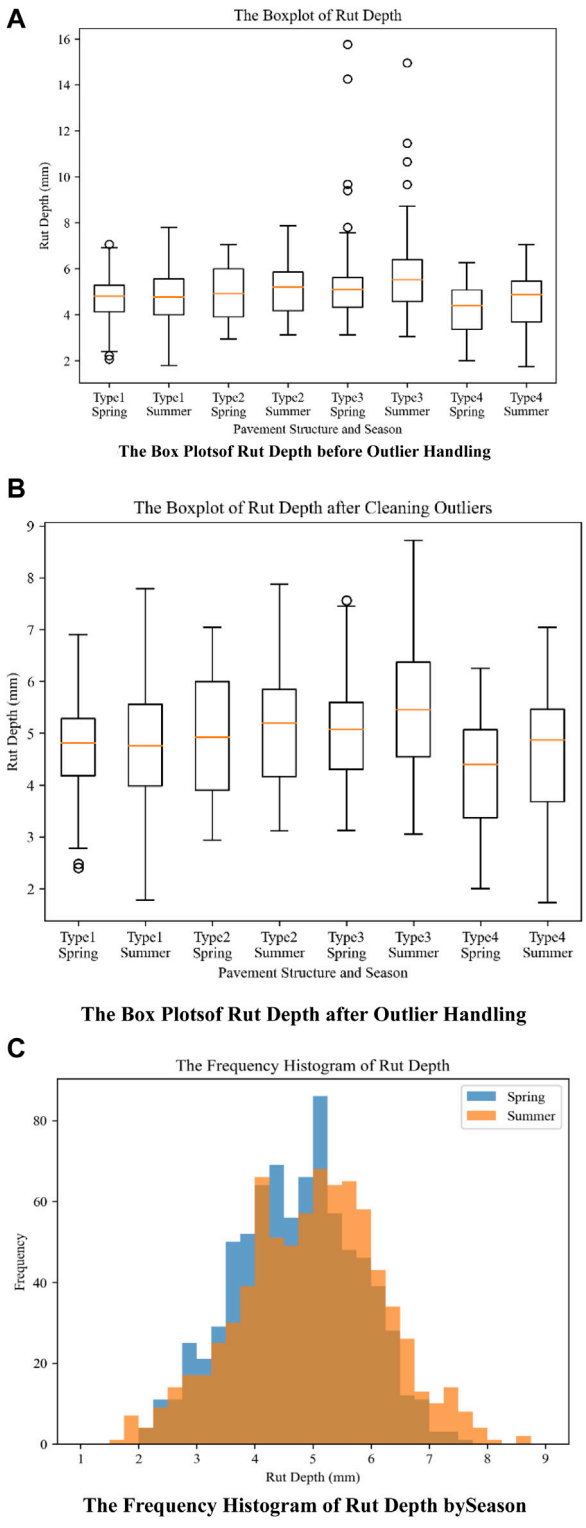

FIGURE 9
Frequency histogram of the rut depth. **(A)** Box plots of the rut depth before outlier handling. **(B)** Box plots of the rut depth after outlier handling. **(C)** Frequency histogram of the rut depth by season.

To further explore the differences in the anti-rut ability of the four pavement structures, this paper calculates the newly added rut depth between spring and summer. Under the influence of high

TABLE 7 Descriptive statistics of rut depth by season and road structure.

Season and road structure	Number	Mean (0.01 mm)	Std	Minimum (0.01 mm)	Maximum (0.01 mm)	Median (0.01 mm)
Type 1-Spring	197	4.71	0.90	2.40	6.90	4.81
Type 1-Summer	200	4.70	1.12	1.78	7.79	4.76
Type 2-Spring	200	4.91	1.15	2.94	7.04	4.92
Type 2-Summer	200	5.15	1.10	3.12	7.87	5.20
Type 3-Spring	195	5.02	0.93	3.13	7.56	5.07
Type 3-Summer	196	5.50	1.21	3.06	8.72	5.45
Type 4-Spring	200	4.24	1.09	2.00	6.25	4.40
Type 4-Summer	200	4.55	1.24	1.73	7.04	4.87

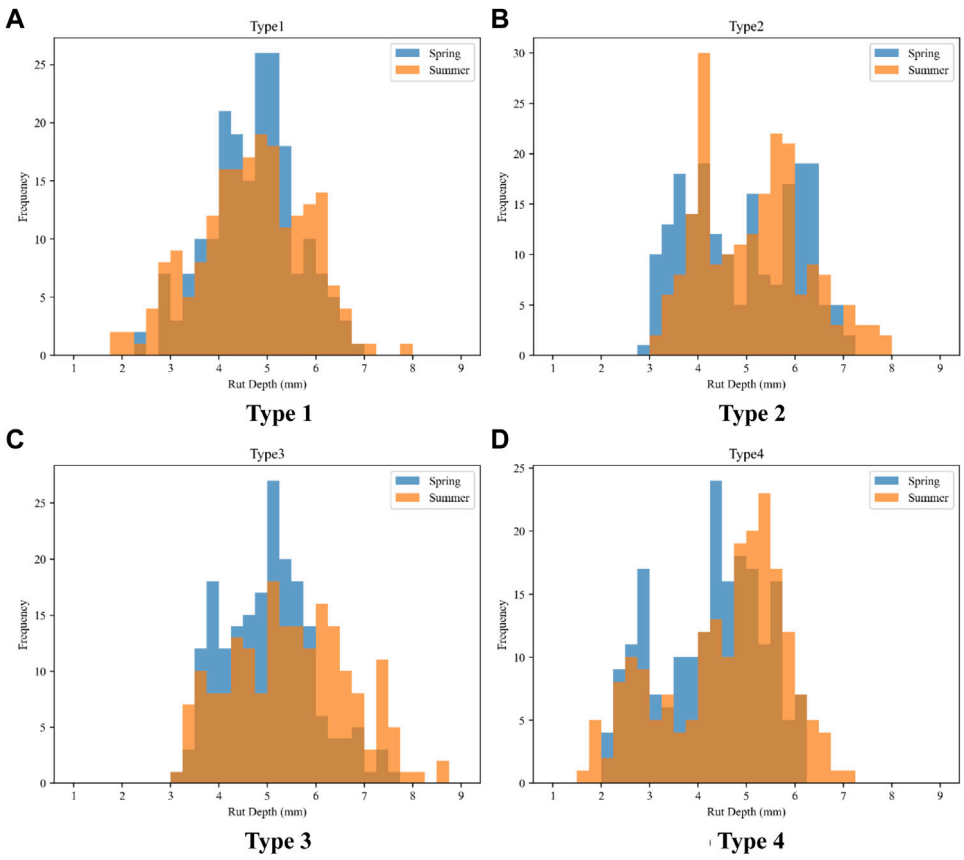

FIGURE 10
Frequency histogram of the rut depth by season and road structure. **(A)** Type 1. **(B)** Type 2. **(C)** Type 3. **(D)** Type 4.

temperatures in summer and traffic loads, the newly added rut depth of the type 3 pavement structure is the largest, followed by that of the type 2 pavement structure, and the smallest one is that of the type 1 pavement structure. This indicates that the type 3 pavement structure has the best anti-rut ability, while the type 1 pavement structure has the worst anti-rut ability.

4.3 Relationship between the pavement structure and skid resistance

Figure 11 shows the TD, BPN, and SFC of the different pavement structures. For TD and BPN, there is little difference between lanes 1 and 2. The SFC of lane 1 is larger than that of lane 2.

TABLE 8 Descriptive statistics of the rut depth by season and road structure.

Season, road structure, and lane	Number	Mean (0.01 mm)	Std	Minimum (0.01 mm)	Maximum (0.01 mm)	Median (0.01 mm)
Type 1-Lane 1-Spring	99	5.12	0.71	2.78	6.90	5.03
Type 1-Lane 1-Summer	100	5.02	1.02	2.76	7.79	5.03
Type 1-Lane 2-Spring	98	4.30	0.88	2.40	6.67	4.23
Type 1-Lane 2-Summer	100	4.38	1.13	1.78	7.12	4.41
Type 2-Lane 1-Spring	100	5.77	0.80	3.58	7.04	6.00
Type 2-Lane 1-Summer	100	6.00	0.74	4.66	7.87	5.82
Type 2-Lane 2-Spring	100	4.04	0.69	2.94	5.95	3.92
Type 2-Lane 2-Summer	100	4.30	0.63	3.12	6.15	4.16
Type 3-Lane 1-Spring	100	5.15	0.66	3.60	7.38	5.19
Type 3-Lane 1-Summer	100	5.93	0.97	3.06	8.05	6.00
Type 3-Lane 2-Spring	95	4.88	1.14	3.13	7.56	4.59
Type 3-Lane 2-Summer	96	5.05	1.28	3.33	8.72	4.72
Type 4-Lane 1-Spring	100	4.92	0.75	2.88	6.25	5.02
Type 4-Lane 1-Summer	100	5.32	0.82	1.97	7.04	5.43
Type 4-Lane 2-Spring	100	3.57	0.94	2.00	5.77	3.45
Type 1-Lane 1-Spring	100	3.79	1.11	1.73	5.77	3.86

TABLE 9 Correlation of the rut depth by different dimensions.

Dimension		Pearson correlation coefficient	*p*-value
Season	Spring and summer	0.69	0.0
Season and road structure	Type 1-Spring and summer	0.61	0.0
	Type 2-Spring and summer	0.72	0.0
	Type 3-Spring and summer	0.53	0.0
	Type 4-Spring and summer	0.78	0.0
Season, road structure, and lane	Type 1-Lane 1-Spring and summer	0.47	0.00
	Type 1-Lane 2-Spring and summer	0.64	0.00
	Type 2-Lane 1-Spring and summer	0.33	0.00
	Type 2-Lane 2-Spring and summer	0.31	0.00
	Type 3-Lane 1-Spring and summer	0.34	0.00
	Type 3-Lane 2-Spring and summer	0.62	0.00
	Type 4-Lane 1-Spring and summer	0.26	0.01
	Type 4-Lane 2-Spring and summer	0.85	0.00

TABLE 10 Difference in average values of the rut depth under different seasons, pavement structures, and lanes.

Season, road structure, and lane	Difference in the average value
Spring and summer	0.25
Type 1-Spring and summer	0.00
Type 2-Spring and summer	0.34
Type 3-Spring and summer	0.45
Type 4-Spring and summer	0.27
Type 1-Lane 1-Spring and summer	−0.11
Type 1-Lane 2-Spring and summer	0.11
Type 2-Lane 1-Spring and summer	0.33
Type 2-Lane 2-Spring and summer	0.35
Type 3-Lane 1-Spring and summer	0.10
Type 3-Lane 2-Spring and summer	0.78
Type 4-Lane 1-Spring and summer	0.15
Type 4-Lane 2-Spring and summer	0.32

Testing vehicle for determining the sideway force coefficient can help detect the difference in the friction coefficients between lanes 1 and 2, but the sand patch test and pendulum friction test cannot achieve this. There are little differences in TD, BPN, and SFC among the different pavement structures. In terms of TD, the differences

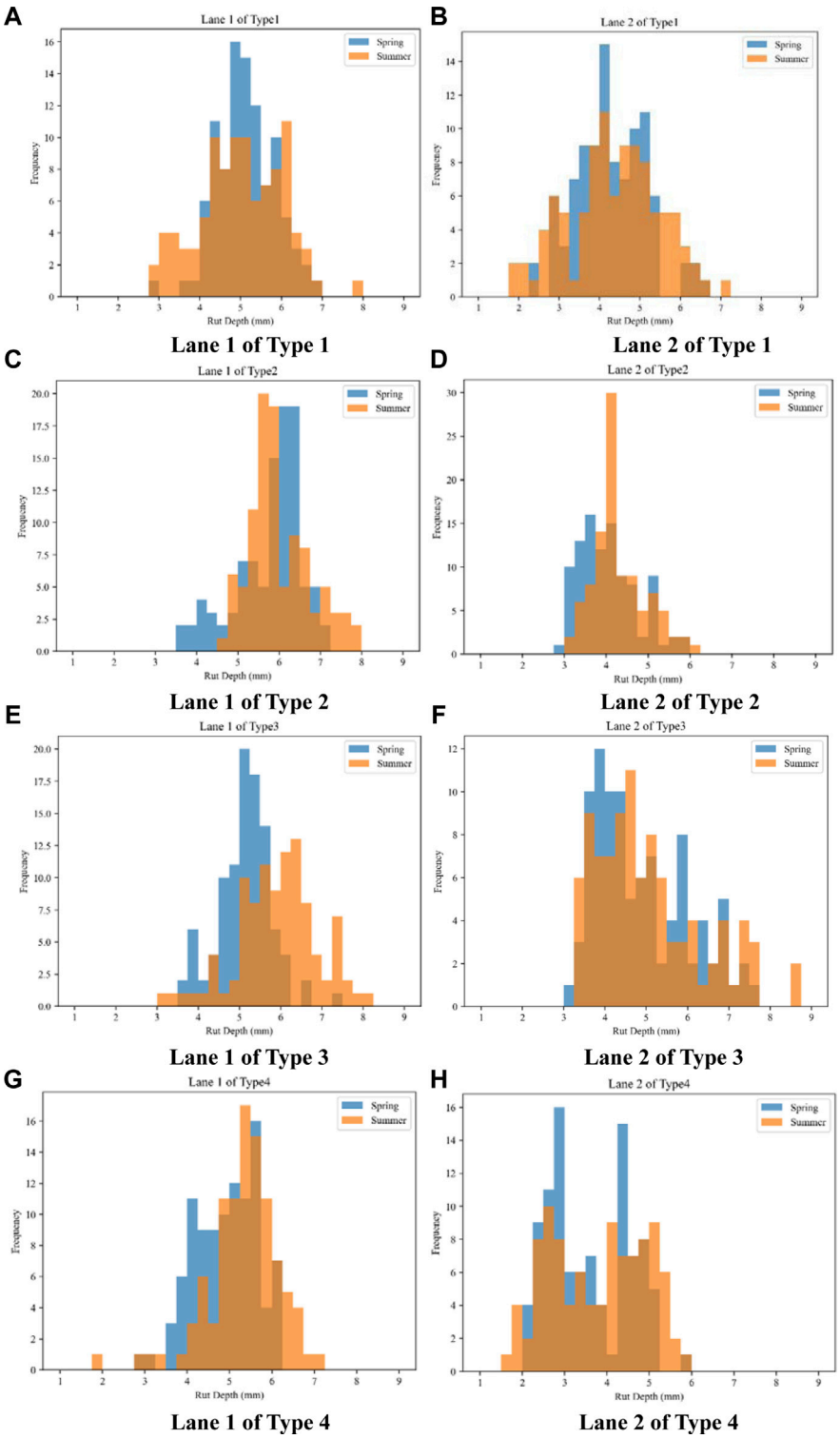

FIGURE 11
SFC, BPN, and TD of different pavement structures. **(A)** SFC of different pavement structures in spring. **(B)** BPN of different pavement structures in summer. **(C)** TD of different pavement structures in summer.

between the maximum and minimum values of the four pavement structures are 5.1%, 12.5%, and 6.9% for lane 1, lane 2, and lane 1 + 2, respectively. In terms of BPN, they are 15.5%, 10.9%, and 14.3%. In terms of SFC, they are 0.8%, 7.4%, and 2.4%.

TD and BPN in spring are greater than those in summer, which may be because of the softening of the asphalt of the pavement surface, resulting in a slight decrease, with a decrease of less than 10% in skid resistance ability. This means that the data comparison from the two

10.3389/fenrg.2023.1295404

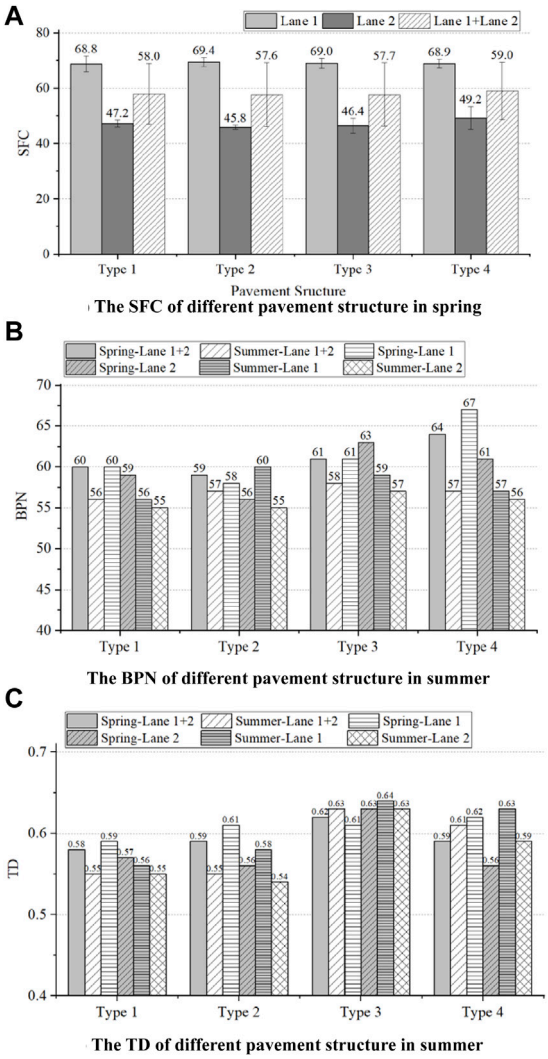

FIGURE 12
Disease type and area of different pavement structures. **(A)** Disease area of the pavement structure in spring and summer. **(B)** Disease type and the area of pavement structure in spring.

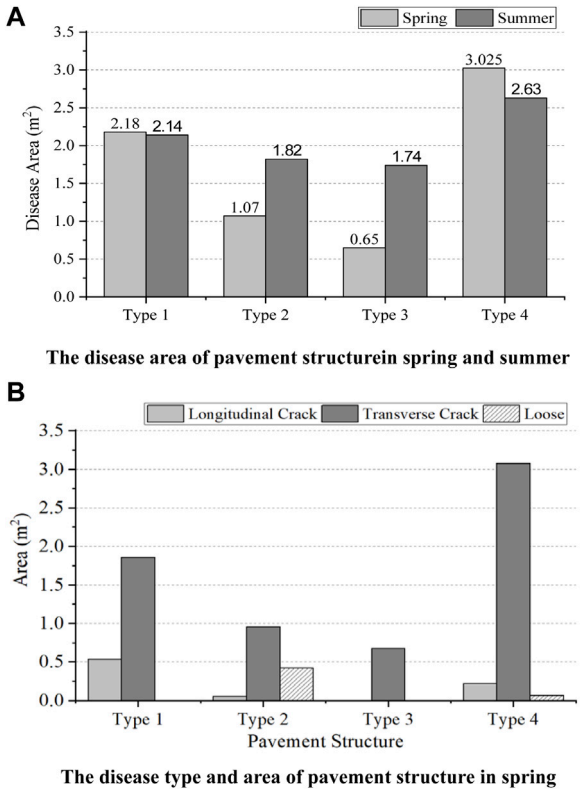

FIGURE 13
IRI in different seasons and its development trend. **(A)** Development trend of IRI in pavement structures. **(B)** IRI of pavement structures in spring and summer.

seasons did not reveal the law of the impact of different pavement structures on the skid resistance performance.

4.4 Relationship between the pavement structure and disease area

The data from lane 1 are mainly used to evaluate the relationship between the pavement structure and disease area, IRI. Figure 12A shows the disease areas of pavement structures. The asphalt pavement with a semi-rigid base and the asphalt pavement with a flexible base have the largest and the smallest disease areas, respectively. The disease area of type 3 is smaller than that of type 2, indicating that asphalt with a larger PG can help reduce the occurrence of pavement surface disease. In addition, the semi-rigid base can increase the strength of the pavement structure, reduce the deflection value, and increase the disease areas of the pavement surface. Figure 12B shows the disease type and area of the pavement structure, indicating that the main disease of the four pavement structures is transverse cracks. The area of the transverse crack in type 4 is 1.7 times, 3.2 times, and 4.5 times than that of type 1, type 2, and type 3, respectively. This may be because the semi-rigid base is prone to fracture under the action of thermal expansion and reflect to the asphalt mixture layer.

Figure 12A shows the diseased areas of pavement structures in spring and summer. The diseased areas of the type 2 and 3 pavement structures have increased, while the diseased areas of the type 1 and 4 pavement structures have slightly decreased. With the different heat transfer coefficients of pavement materials, the internal temperature diffusion efficiency of the pavement structure is low, resulting in a higher temperature on the surface of the pavement. Under the action of traffic loads, some crack diseases have self-healed.

4.5 Relationship between the pavement structure and IRI

Figure 13A shows the development trend of IRI in the pavement structure. As the service life increases, the IRI

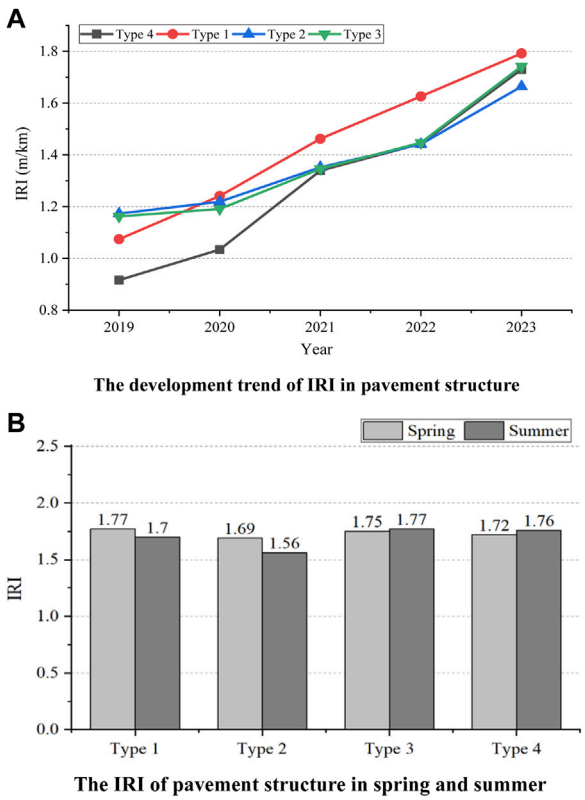

FIGURE 14
Frequency histogram of the rut depth by season, road structure, and lane. **(A)** Lane 1 of type 1. **(B)** Lane 2 of type 1. **(C)** Lane 1 of type 2. **(D)** Lane 2 of type 2. **(E)** Lane 1 of type 3. **(F)** Lane 2 of type 3. **(G)** Lane 1 of type 4. **(H)** Lane 2 of type 4.

gradually increases. Overall, type 1 has the highest IRI, while other pavement structures have relatively small differences in IRI. Figure 14 shows that lane 1 in type 1 has the deepest rut depth, and Figure 11 shows that there are significant differences in the disease area between types 1, 2, and 3. It indicates that there is a strong correlation between IRI and rut depth, while a weak correlation with the disease area. In terms of the influence of seasonal factors on IRI, Figure 13B shows IRI of different pavement structures in spring and summer. The degree of influence of seasonal factors on IRI is within 5%, indicating that the seasonal factor has no effect on IRI.

4.6 Result of statistical analysis

Based on ANOVA, the effects of the pavement structure type (type), the thicknesses of the conventional asphalt mixture (AM), LSPM, AC13FA, AC13FB, LSS, IS, and pavement structure (total) on the deflection value, IRI, TD, BPN, SFC, rut depth, and disease area were analyzed. Table 11 shows F and p-values of ANOVA. The results show that the pavement structure type and thicknesses of each structure layer significantly affect the deflection value. There is a strong correlation between the type, thickness (AM, LSPM, AC13FA, LSS, and total), BPN, and SFC (lane 2). There are weak relationships between the type and thicknesses of each structure layer and the rut depth, TD, SFC (lane 1), disease area, and IRI.

5 Conclusion

This paper had paved the experimental sections to research the relationships between the pavement structures and pavement performances containing the rut depth, TD, BPN, SFC, IRI, deflection value, and disease area. This paper also intensively studied the effects of seasonal factors, pavement structures, and lanes on the deflection value and rut depth by the Pearson correlation coefficient. Finally, the correlations between the layer thickness of various materials and pavement performance were evaluated by ANOVA. The following are some research conclusions obtained:

i. The pavement structures affected the deflection value, rut depth, and disease area of the road surface but did not relate to BPN, TD, and SFC. The results of ANOVA showed that the pavement structure type and thicknesses of the structural layer affected the deflection value significantly. There was a strong correlation between the structure type, thickness, BPN, and SFC. There were weak relationships between the structure type, thicknesses of each structural layer and rut depth, TD, disease area, and IRI.
ii. The seasonal factors significantly affected the deflection values and rut depth of pavement structures. The high temperatures increased the average deflection values by 22.85%, 72.88%, 77.61%, and 88.13% for the four types, respectively. Under the influence of high temperatures in summer and traffic loads, the increased ranges of the average rut depth were −0.2%, 4.89%, 9.56%, and 7.31%, respectively.
iii. The semi-rigid base layer helped enhance the strength and bearing capacity of the pavement structure. The pavement structure with a semi-rigid base had a smaller deflection value and rut depth, and the largest disease area.
iv. Increasing the thickness of the asphalt mixture was beneficial for reducing the disease area but not for increasing the structural strength of the pavement structure. The pavement structure with the asphalt mixture of low PG at the bottom layer had a smaller deflection value, rut depth, and disease area.

The previous analysis indicated that the pavement structure type and material thickness influenced the pavement performances. In complex service environments, pavement structures underwent performance degradation due to environmental factors and vehicle loads. In future research, with the continuous observation of experimental sections and accumulation of experimental data, the correlation between the environment, traffic load, pavement structure, and pavement

TABLE 11 Results of analysis of variance.

Project		Type	AM	LSPM	AC13FA	AC13FB	LSS	Total
BPN (lane 1)	F	4.484	6.570	13.062	5.603	0.776	13.062	6.570
	p	**0.009**	**0.004**	**0.001**	**0.023**	0.384	**0.001**	**0.004**
BPN (lane 2)	F	3.643	0.543	4.107	6.530	0.854	5.854	6.543
	p	**0.022**	0.586	**0.050**	**0.015**	0.364	**0.032**	**0.026**
Deflection value (lane 1)	F	76.93	20.85	33.37	53.97	214.23	33.37	20.85
	p	**0.000**	**0.000**	**0.000**	**0.000**	**0.000**	**0.000**	**0.000**
Deflection value (lane 2)	F	142.56	22.54	38.17	84.93	297.58	38.17	22.54
	p	**0.000**	**0.000**	**0.000**	**0.000**	**0.000**	**0.000**	**0.000**
Rut depth (lane 1)	F	2.078	2.84	3.626	4.89	0.422	3.626	2.84
	p	0.120	0.072	0.065	**0.033**	0.520	0.065	0.072
Rut depth (lane 2)	F	0.559	0.785	1.413	0.573	0.099	1.413	0.785
	p	0.645	0.464	0.242	0.454	0.755	0.242	0.464
SFC (lane 1)	F	0.172	0.148	0.033	0.052	0.006	0.033	0.148
	p	0.915	0.863	0.856	0.821	0.937	0.856	0.863
SFC (lane 2)	F	2.904	4.254	7.512	2.231	1.033	7.512	4.254
	p	**0.048**	**0.022**	**0.009**	0.144	0.316	**0.009**	**0.022**
TD (lane 1)	F	0.129	0.192	0.103	0.138	0.011	0.103	0.192
	p	0.942	0.826	0.750	0.713	0.915	0.750	0.826
TD (lane 2)	F	1.367	0.591	0.681	1.042	4.015	0.681	0.591
	p	0.268	0.559	0.415	0.314	0.053	0.415	0.559
Disease area	F	0.996	1.388	1.902	0.008	1.627	1.902	1.388
	p	0.406	0.263	0.176	0.929	0.210	0.716	0.263
IRI	F	0.625	0.932	1.006	0.780	0.000	1.006	0.932
	p	0.604	0.403	0.322	0.383	0.987	0.322	0.403

The meaning of bold values is that factors have an impact on the results.

performance will be deeply explored, providing a basis for the design of long-life pavement structures.

Data availability statement

The raw data supporting the conclusion of this article will be made available by the authors, without undue reservation.

Author contributions

DX: formal analysis, funding acquisition, resources, and writing–review and editing. GG: methodology, project administration, writing–original draft, and writing–review and editing. CB: investigation and writing–original draft. CZ: data curation and writing–review and editing. DL: investigation, supervision, and writing–original draft.

Funding

The author(s) declare financial support was received for the research, authorship, and/or publication of this article. This study was sponsored by the Key Science and Technology Projects in the Transportation Industry (No. 2022-MS1-016) and the Transportation Technology Plan in Shandong Province (2022B63). The authors are grateful for the financial supports.

Conflict of interest

Authors DX was employed by Shandong Hi-Speed Group Co., Ltd. Authors GG and CZ were employed by Shandong Hi-Speed Engineering Test Co., Ltd. CB and DL were employed by Innovation Research Institute, Shandong Hi-speed Group Co., Ltd.

Publisher's note

References

Bushmeyer, B. (2002). The quest for long-life asphalt pavement. *Better Roads* 72 (2), 30–37.

Chun, S., Kim, K., Park, B., and Greene, J. (2017). Evaluation of structural benefits of prime coat application for flexible pavements using Accelerated Pavement Testing (APT). *Ksce J. Civ. Eng.* 21 (1), 141–149. doi:10.1007/s12205-016-0746-4

Cui, P., Shao, M., Hu, X., and Sun, L. (2008). Finite element analysis for perpetual pavements structural combinations. *J. Tongji Univ. Nat. Sci.* 36 (10), 1388–1394. doi:10.3321/j.issn:0253-374X.2008.10.015

Erlingsson, S. (2010). Impact of water on the response and performance of a pavement structure in an accelerated test. *Road Mater. Pavement Des.* 11 (4), 863–880. doi:10.1080/14680629.2010.9690310

Ferne, B. (2006). Long-life pavements-a European study by ELLPAG. *Int. J. Pavement Eng.* 7 (2), 91–100. doi:10.1080/10298430600619059

Jia, M., Sha, A., Jiang, W., Li, X., and Jiao, W. (2023). Developing a solid–solid phase change heat storage asphalt pavement material and its application as functional filler for cooling asphalt pavement. *Energy Build.* 285 (15), 112935. doi:10.1016/j.enbuild.2023.112935

Jiao, W., Sha, A., Liu, Z., Jiang, W., Hu, L., Li, X., et al. (2020). Utilization of steel slags to produce thermal conductive asphalt concretes for snow melting pavements. *J. Clean. Prod.* 261 (10), 121197. doi:10.1016/j.jclepro.2020.121197

Lee, H. J., Lee, J. H., and Park, H. M. (2007). Performance evaluation of high modulus asphalt mixtures for long life asphalt pavements. *Constr. Build. Mater.* 21 (5), 1079–1087. doi:10.1016/j.conbuildmat.2006.01.003

Liu, K., Zhang, X., Wang, F., Da, Y., and Xu, P. (2023). Thermal transfer analysis method for judging the best time of removing the steel bridge deck asphalt pavement by induction heating. *Therm. Sci. Eng. Prog.* 37 (1), 101611. doi:10.1016/j.tsep.2022.101611

Liu, N. (2012). Field test and analysis on mechanical response of semi-rigid base of long-life asphalt pavement, master dissertation. *Harbin Inst. Technol.*

Liu, S., Cao, W., Fang, J., and Shang, S. (2009). Variance analysis and performance evaluation of different crumb rubber modified (CRM) asphalt. *Constr. Build. Mater.* 23 (7), 2701–2708. doi:10.1016/j.conbuildmat.2008.12.009

Liu, W., and Jia, Y. (2023). Comparison of type I error and statistical power between state trace analysis and analysis of variance. *J. Math. Psychol.* 2023 (114), 102767. doi:10.1016/j.jmp.2023.102767

Martin, J., Harvey, J. T., Long, F., Lee, E., Monismith, C. L., Herritt, K., et al. (2012). Long-life rehabilitation design and construction. *Transp. Res. Circular* 503, 50–65.

Research institute of highway ministry of transport (2019). *Field test methods of highway subgrade and pavement (JTG 3450)*. Beijing, China: China Communications Press Co., Ltd.

Ritter, J., Rabe, R., and Wolf, A. (2012). Analysis of the long-term structural performance of flexible pavements using full-scale accelerated pavement tests. *Procedia - Soc. Behav. Sci.* 48 (1), 1244–1253. doi:10.1016/j.sbspro.2012.06.1100

Rosopa, P., and King, B. (2023). *Analysis of variance: univariate and multivariate approaches*. Fourth Edition. Clemson University, Clemson, SC, United States: International Encyclopedia of Education, 529–535.

Shakhan, M. R., Topal, A., and Sengoz, B. (2023). Investigation of asphalt concrete mixture types in different layers in asphalt pavement: a mechanistic approach. *J. Eng. Res.* 11 (1), 100027. doi:10.1016/j.jer.2023.100027

Wang, B., Huang, W., Yang, J., and Zhang, L. (2013). Analyses of structural damage and parameter sensitivity for CRCP+AC composite pavement. *J. Traffic Transp. Eng.* 13 (5), 17–26.

Wang, L., Wei, J., Wu, W., Zhang, X., Xu, X., Yan, X., et al. (2022). Technical development and long-term performance observations of long-life asphalt pavement: a case study of Shandong Province. *J. Road Eng.* 2 (2), 369–389. doi:10.1016/j.jreng.2022.11.001

Wang, X., and Zhou, X. (2019). Equivalent mechanical method for asphalt pavement structure based on material nonlinearity. *China J. Highw. Transp.* 32 (8), 25–34. doi:10.19721/j.cnki.1001-7372.2019.08.002

Xu, Z., and Sun, L. (1996). Effects of asphalt pavement structural combinations on pavement conditions. *J. Tongji Univ.* 24 (5), 515–519.

Yang, H. L., Wang, S. J., Miao, Y. H., and Sun, F. y. (2021). Effects of accelerated loading on the stress response and rutting of pavements. *J. Zhejiang Univ. Sci.* 22, 514–527. doi:10.1631/jzus.a2000259

Yang, Y., Wang, L., Wei, J., and Ma, J. (2010). Typical pavement structure dynamic response data collection and analysis under heavy vehicle loading. *J. Highw. Transp. Res. Dev. Engl. Ed.* 27 (5), 11–16. doi:10.3969/j.issn.1002-0268.2010.05.003

Ye, J., Lin, X., Mo, S., Jia, L., Chen, Y., Cheng, Z., et al. (2021). Orthogonal study and analysis of variance on a thermal management system for high-power LED package. *Microelectron. J.* 108, 104969. doi:10.1016/j.mejo.2020.104969

Zheng, J. (2014). New structure design of durable asphalt pavement based on life increment. *China J. Highw. Transp.* 27 (1), 1–7. doi:10.3969/j.issn.1001-7372.2014.01.001

Zhou, X., and Wang, X. (2018). A large-scale test method for mechanical response of pavement structure. *Adv. Mater. Sci. Eng.* 2018 (12), 1–12. doi:10.1155/2018/2642409

Zhou, X., Wang, X., Yuan, Y., and Li, C. (2018). Using large-scale test to investigate the surface strain of cement/asphalt concrete. *Constr. Build. Mater.* 170 (MAY10), 603–612. doi:10.1016/j.conbuildmat.2018.02.217

Zhu, S., Ji, X., Yuan, H., Li, H., and Xu, X. (2023b). Long-term skid resistance and prediction model of asphalt pavement by accelerated pavement testing. *Constr. Build. Mater.* 375, 131004. doi:10.1016/j.conbuildmat.2023.131004

Zhu, Z., Xiao, P., Kang, A., Wu, Z., Kou, C., Ren, Z., et al. (2023a). Research on the road performance of self-adhesive basalt fiber geotextiles based on the background of long-life pavements. *Constr. Build. Mater.* 392, 131776. doi:10.1016/j.conbuildmat.2023.131776

frontiers | Frontiers in Energy Research

TYPE Original Research
PUBLISHED 30 November 2023
DOI 10.3389/fenrg.2023.1328676

OPEN ACCESS

EDITED BY
Di Wang,
University of Ottawa, Canada

REVIEWED BY
Quantao Liu,
Wuhan University of Technology, China
Fan Zhang,
Aalto University, Finland

*CORRESPONDENCE
Zhengguang Wu,
zgwu@yzu.edu.cn

RECEIVED 27 October 2023
ACCEPTED 20 November 2023
PUBLISHED 30 November 2023

CITATION
Li B, Zhou Y, Wu Z, Kang A, Wu B and Luo C (2023), Influence of basalt fiber on performance of thin overlayer asphalt mixtures based on multiple experimental methods.
Front. Energy Res. 11:1328676.
doi: 10.3389/fenrg.2023.1328676

Influence of basalt fiber on performance of thin overlayer asphalt mixtures based on multiple experimental methods

Bo Li[1,2], Yangyang Zhou[1], Zhengguang Wu[1,2]*, Aihong Kang[1,2], Bangwei Wu[1,2] and Chufan Luo[1]

[1]College of Civil Science and Engineering, Yangzhou University, Yangzhou, China, [2]Research Center for Basalt Fiber Composite Construction Materials, Yangzhou, China

Because of the fast deterioration speed of the surface function of conventional asphalt pavement, thin overlayer with many advantages has been applied to the pavement surface. However, due to problems such as insufficient stripping resistance and cracking resistance, the performance of the thin overlayer needs to be further improved. To achieve this target, basalt fiber was introduced into two types of thin overlayer asphalt mixtures (Open graded friction course, OGFC-5, and Stone matrix asphalt mixture, SMA-5). The wheel tracking test and uniaxial penetration test for high temperature deformation resistance, low temperature bending beam test and indirect tensile asphalt (IDEAL) cracking test for cracking resistance, cantabro test for stripping resistance, and friction coefficient test for skid resistance were conducted to evaluate various performance of thin overlayer asphalt mixtures, along with the dynamic modulus test for dynamic mechanical response. The results showed that adding basalt fiber could enhance the high temperature deformation resistance, low temperature cracking resistance, intermediate temperature cracking resistance and stripping resistance of the thin overlayer, while having no significant impact on skid resistance. Furthermore, adding basalt fiber could increase the modulus in the high temperature region and decrease the modulus in the low temperature region of the thin overlayer asphalt mixtures, indicating thin overlayer with basalt fiber presenting superior both high temperature and low temperature performance. In addition, the evaluation indexes of S_{LT} and S_{HT} proposed from dynamic modulus test exhibited good consistency with the results of the performance tests.

KEYWORDS

thin overlayer asphalt mixture, basalt fiber, performance test, dynamic modulus, correlation analysis

1 Introduction

Due to long-term direct exposure to the external environment, suffering from the multiple influences of temperature fluctuation, rain erosion and vehicle load, the surface function of some asphalt pavements decays rapidly (Ding et al., 2022; Li et al., 2023; Yaqub et al., 2023). The thin overlayer has superior service performance, outstanding skid resistance and drainage performance, which not only enhances pavement service life, but also greatly

TABLE 1 Indexes of SBS modified asphalt.

Indexes		Results	Requirements
Softening point/°C		86	≥55
Penetration (25°C)/0.1 mm		71	60–80
Ductility (5 cm/min, 5°C)/cm		48	≥30
Recovery of elasticity (25°C)/%		76	≥65
RTFOT residue	Weight change/%	−0.08	±1.0
	Penetration ratio/%	86	≥60
	Residual ductility (15°C)/cm	37	≥20

TABLE 2 Indexes of basalt fiber.

Indexes	Results
Break strength/MPa	2,218
Break elongation/%	2.67
Elastic modulus/GPa	88
Acidity coefficient	5.3

TABLE 3 Indexes of lignin fiber.

Indexes	Results
Ash content/%	19.3
pH value	7.6
Asphalt absorption	6.2 m^a

[a]m is the mass of lignin fiber.

improves the safety and comfort of the vehicle travel (Chen et al., 2019; Cui et al., 2021). In order to solve the problem of surface function deterioration, thin overlayer has been widely used in both new road construction and road maintenance projects (Correia and Zornberg, 2018; Almaali and Al-Busaltan, 2021; Jin T. et al., 2023).

However, the thin overlayer also has low durability due to its thin thickness and small aggregate particle size, which is manifested as insufficient cracking resistance, stripping resistance and high temperature deformation resistance (Ingrassia et al., 2012; Liu et al., 2019; Han et al., 2021). These problems limit further application of thin overlayer in pavement engineering. Huang et al. (2020) mixed cellulose fiber and basalt fiber into SMA and conducted experiments to determine the optimal mixing ratio. The findings indicated that the high temperature deformation resistance of the mixture increased with the increase of basalt fiber incorporation. The study conducted by Zhao et al. (2020) revealed that basalt fiber exhibited superior enhancement in the low temperature performance of asphalt mixture compared to lignin fiber and polyester fiber. As a new type of fiber commonly used in asphalt pavement surface layers, basalt fiber exhibits favorable reinforcement effect on asphalt mixtures, including significant enhancement in cracking resistance, rutting resistance and other performance (Zhang Y. et al., 2022; Zhang M. et al., 2022). Therefore, it can be considered that basalt fiber has great potential in improving the performance of thin overlayer, though few studies concerning this topic. Since a surface layer is directly subjected to the dynamic interaction of temperature and load, the dynamic mechanical response of the thin overlayer is also very important, in addition to the conventional experiments (Javilla et al., 2017; Jin et al., 2021; Liu et al., 2023). The dynamic modulus test was conducted using temperature and load frequency as environmental variables (Gudmarsson et al., 2015; Qin et al., 2019; Zhang C. et al., 2022), which gets closer to the realistic state than the conventional pavement performance test conditions. The master curve could be drawn, so that the dynamic modulus under extreme conditions could be predicted (Ling et al., 2017; Podolsky et al., 2018).

In this research, the influence of basalt fiber on the performance of OGFC-5 and SMA-5 was studied by multiple performance tests and dynamic modulus test. In addition, the results of dynamic modulus test and related performance tests (the wheel tracking test, uniaxial penetration test and low temperature bending beam test) were compared and analyzed.

2 Materials and mixture design

2.1 Materials

In this research, SBS modified asphalt was selected. The performance tests of the asphalt were conducted with the Chinese standard of JTG E20-2011 (JTG, 2011), and the indexes are displayed in Table 1. The coarse and fine aggregates selected were all basalt aggregates.

The basalt fiber (BF) was used in OGFC and SMA, and lignin fiber (LF) was only used in SMA. The technical indexes of the fibers are displayed in Tables 2, 3, and the macroscopic appearances of the fibers are illustrated in Figure 1.

2.2 Mixture design

The OGFC-5 and SMA-5 gradations were selected for the asphalt mixture design, and the gradation curves of the two types of mixtures are displayed in Figure 2. There were four kinds of asphalt mixtures tested in this study, ordinary OGFC-5 without fiber, OGFC-5-BF with basalt fiber (0.3% by mixture mass), SMA-5 with only lignin fiber (0.3%), and SMA-5-BF with lignin fiber (0.1%) and basalt fiber (0.3%). The optimum asphalt content (OAC) and volumetric properties of the four asphalt mixtures, including voids in mineral aggregate (VMA), volume of air voids (VV), and voids filled with asphalt (VFA), are shown in Table 4.

3 Test methods

3.1 High temperature deformation resistance tests

3.1.1 Wheel tracking test

Wheel tracking test is usually conducted to test high temperature deformation resistance of mixtures. The test was conducted according to JTG E20-2011 (JTG, 2011), with three duplicates

10.3389/fenrg.2023.1328676

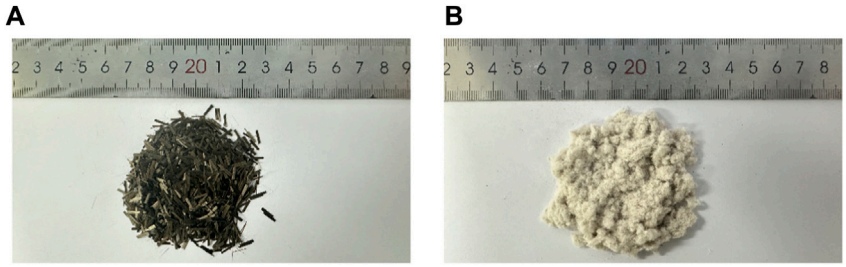

FIGURE 1
Macroscopic appearances of fibers: **(A)** Basalt fiber; **(B)** Lignin fiber.

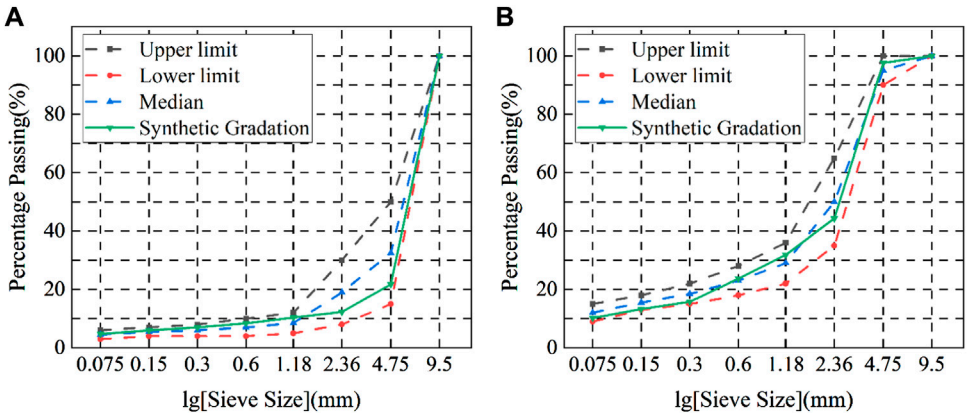

FIGURE 2
Gradation curves of asphalt mixtures: **(A)** OGFC-5; **(B)** SMA-5.

TABLE 4 Optimum asphalt content and volumetric properties of asphalt mixtures.

Types	OAC/%	VMA/%	VV/%	VFA/%
OGFC-5	5.0	27.5	19.6	28.7
OGFC-5-BF	5.1	27.3	19.3	29.3
SMA-5	6.5	17.3	4.0	76.9
SMA-5-BF	6.3	17.0	3.6	78.8

per group. The evaluation index is dynamic stability (*DS*), which is determined by Eq. 1.

$$DS = \frac{(t_2 - t_1) \times N}{d_2 - d_1} \times C_1 \times C_2 \quad (1)$$

in this equation, d_1 is the deformation depth corresponding to t_1 time (45 min), mm; d_2 is the deformation depth corresponding to t_2 time (60 min), mm; C_1 and C_2 are the test coefficients, in this study, $C_1 = C_2 = 1.0$; and N is the speed of the wheel, 42 cycles/min.

3.1.2 Uniaxial penetration test

Uniaxial penetration test is usually conducted to test high temperature deformation resistance of mixtures. The test was conducted according to JTG D50-2017 (JTG, 2017), with five duplicates per group. The evaluation index of shear strength (R_τ), can be determined by Eqs 2, 3.

$$\sigma_p = \frac{P}{A} \quad (2)$$

$$R_\tau = f_\tau \times \sigma_p \quad (3)$$

in this equation, σ_p is the penetration stress, MPa; P is the peak load of the specimen, N; A is the cross-sectional area of the pressing tool, mm^2; and f_τ is stress coefficient, which is 0.35.

3.2 Cracking resistance tests

3.2.1 Low temperature bending beam test

Low temperature bending beam test is usually conducted to test low temperature cracking resistance of mixtures. The test was conducted according to JTG E20-2011 (JTG, 2011), with four duplicates per group. The evaluation index is the failure strain (ε_B), which is determined by Eq. 4.

$$\varepsilon_B = \frac{6hd}{L^2} \quad (4)$$

in this equation, h is the height and L is the span of the specimen, mm; and d is the mid-span deflection of the specimen when damaged, mm.

3.2.2 IDEAL cracking test

IDEAL cracking test is usually conducted to test intermediate temperature cracking resistance of mixtures. The test was conducted according to ASTM D8225-19 (ASTM D8225-19, 2019), with three duplicates per group. The evaluation indexes are crack initiation work (W_S) and cracking tolerance index (CT_{index}), which are determined by Eqs 5, 6.

$$W_S = \int_0^{l_{100}} P dl \tag{5}$$

in this equation, P is the load, N; l is the displacement, mm; l_{100} is the displacement at peak load in the load-displacement curve.

$$CT_{index} = \frac{G_f}{|m_{75}|} \times \frac{l_{75}}{D} \tag{6}$$

in this equation, G_f is the fracture energy, J/m^2; l_{75} is the displacement at 75% peak load in the rear section of the load-displacement curve, mm; $|m_{75}|$ is absolute value of the rate of change at the 75% peak load in the rear section of the load-displacement curve, which is calculated by interpolation.

3.3 Stripping resistance test

Cantabro test is usually conducted to test stripping resistance of mixtures. The test was conducted according to JTG E20-2011 (JTG, 2011), with four duplicates per group. The specimens were firstly immersed in a water bath at 20°C for 20 h, and then put into the Los Angeles abrasion machine after being dried. The test was running for 10 min at the speed of 30 r/min. The evaluation index is the cantabro mass loss (ΔS), which is determined by Eq. 7.

$$\Delta S = \frac{m_0 - m_1}{m_0} \times 100 \tag{7}$$

in this equation, m_0 and m_1 are the total mass of the specimen before and after the cantabro test, g.

3.4 Skid resistance test

The friction coefficient (British pendulum number, *BPN*) test is usually conducted to test skid resistance of mixtures. The test was conducted according to JTG 3450-2019 (JTG, 2019), with three duplicates specimens per group. Each specimen was measured five times. The evaluation index is British pendulum number at 20°C (BPN_{20}), which is determined by Eq. 8.

$$BPN_{20} = BPN_T + \Delta BPN \tag{8}$$

in this equation, BPN_T is the British pendulum number corresponding to test temperature; ΔBPN is the temperature correction number.

The indexes of the performance tests are summarized in Table 5.

3.5 Dynamic modulus test

Dynamic modulus test was conducted according to JTG E20-2011 (JTG, 2011), and the compression dynamic modulus of mixtures was obtained. In this test, specimens with the diameter of 100 mm and height of 150 mm were prepared, with four duplicates in each group. The dynamic modulus test procedures are roughly displayed in Figure 3.

TABLE 5 Evaluation indexes of conventional performance tests.

Tests	Indexes	Units
Wheel tracking test	*DS*	cycles/mm
Uniaxial penetration test	R_t	MPa
Low temperature bending beam test	ε_B	με
IDEAL cracking test	W_S	J
	CT_{index}	/
Cantabro test	ΔS	%
Friction coefficient test	BPN_{20}	/

Asphalt mixture has the time-temperature equivalence property. Thus, dynamic modulus measured at other temperatures can be converted to the reference temperature (normally 20°C) by shift factor $\alpha(T)$ (Tan et al., 2020). Finally, the dynamic modulus master curve founded on the Sigmoidal function can be formed with the reference of NCHRP 9-29, so as to evaluate mechanical performance of mixtures. Sigmoidal function is shown in Eqs 9–13.

$$\lg|E^*| = \delta + \frac{|E^*|_{max} - \delta}{1 + e^{\beta + \gamma \lg \omega_r}} \tag{9}$$

in this equation, $|E^*|$ is the dynamic modulus of specimen, MPa; $|E^*|_{max}$ is the maximum dynamic modulus, MPa; ω_r is the reduced frequency, Hz; and δ,β, and γ are fitting parameters. $|E^*|_{max}$ is determined by Hirsch model, as shown in Eq. 10.

$$|E^*|_{max} = P_c\left[4200000\left(1 - \frac{VMA}{100}\right) + 435000\left(\frac{VFA \cdot VMA}{10000}\right)\right] + \frac{1 - P_c}{\left[\frac{\left(1 - \frac{VMA}{100}\right)}{4200000} + \frac{VMA}{435000 VFA}\right]} \tag{10}$$

where P_c is an intermediate variable in the model calculation process, which is determined by Eq. 11.

$$P_c = \frac{\left(20 + \frac{435000 VFA}{VMA}\right)^{0.58}}{650 + \left(\frac{435000 VFA}{VMA}\right)^{0.58}} \tag{11}$$

where VMA and VFA are the volumetric properties of the specimen, %.

ω_r is the reduced frequency, which is to convert loading frequency at different temperatures into the frequency at the reference temperature by shift factor. The conversion between loading frequency and reduced frequency is determined by Arrhenius equation, as displayed in Eqs 12, 13.

$$\lg \omega_r = \lg \omega + \lg \alpha(T) \tag{12}$$

$$\lg \alpha(T) = \frac{\Delta E_a}{19.14714}\left(\frac{1}{T + 273.15} - \frac{1}{T_r + 273.15}\right) \tag{13}$$

where ω is the loading frequency, Hz; T is the test temperature, °C; T_r is the reference temperature, °C; and ΔE_a is the activation energy, which is a fitting parameter.

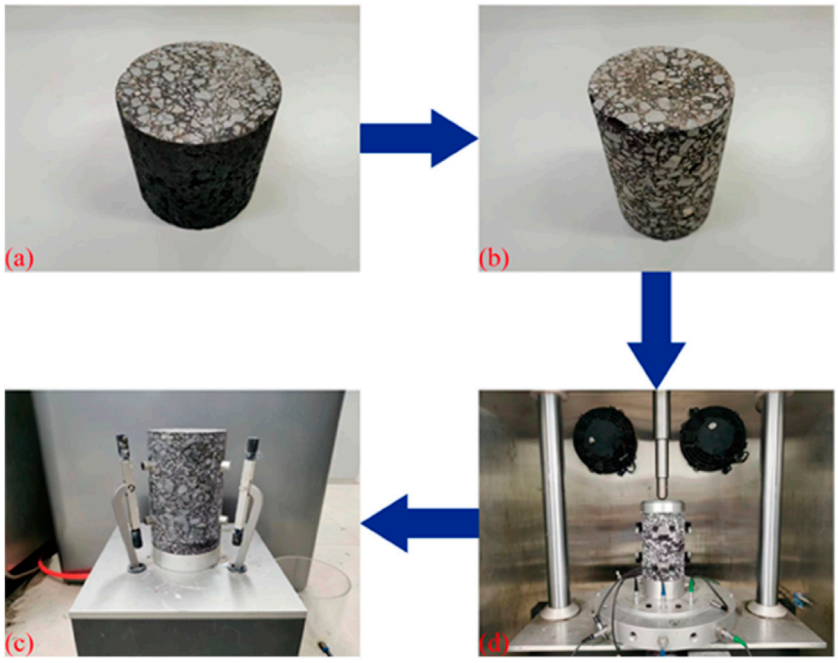

FIGURE 3
The dynamic modulus test procedures: **(A)** Specimen preparation; **(B)** Core sample drilling; **(C)** Sensor installation; **(D)** Testing.

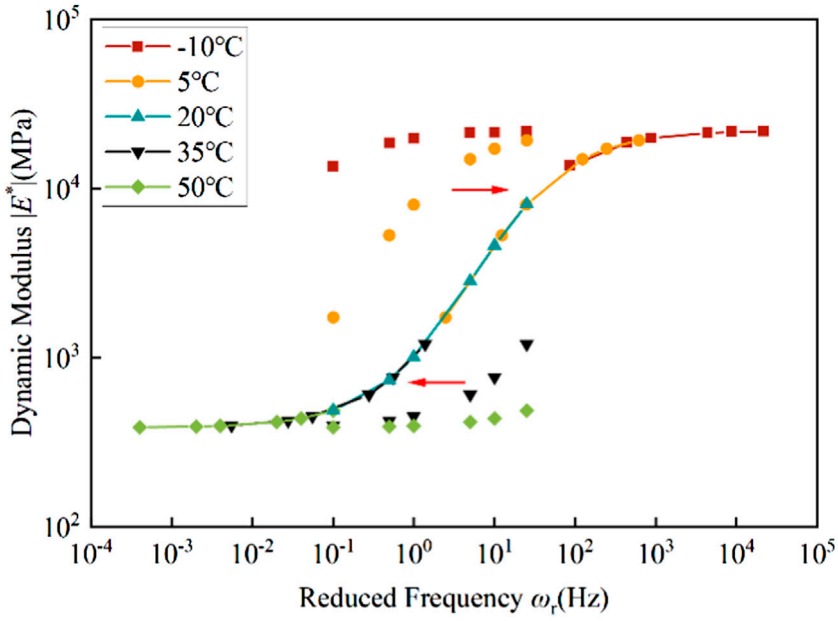

FIGURE 4
Shift process of each part of the loading frequency section.

The converting process of the master curve is illustrated in Figure 4. It can be seen from Figure 4 that the high frequency section was obtained by shifting the low temperature parts of the loading frequency section, while the low frequency section was obtained by shifting the high temperature parts of the loading frequency section. Hence, the high frequency section of the mater curve reflects the low temperature performance of mixtures while the low frequency section reflects the opposite.

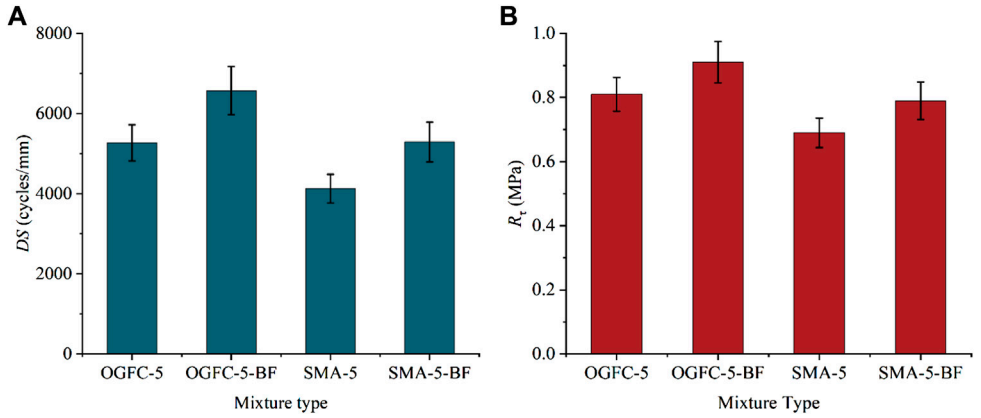

FIGURE 5
The results of high temperature deformation resistance tests: **(A)** *DS*; **(B)** R_{τ}.

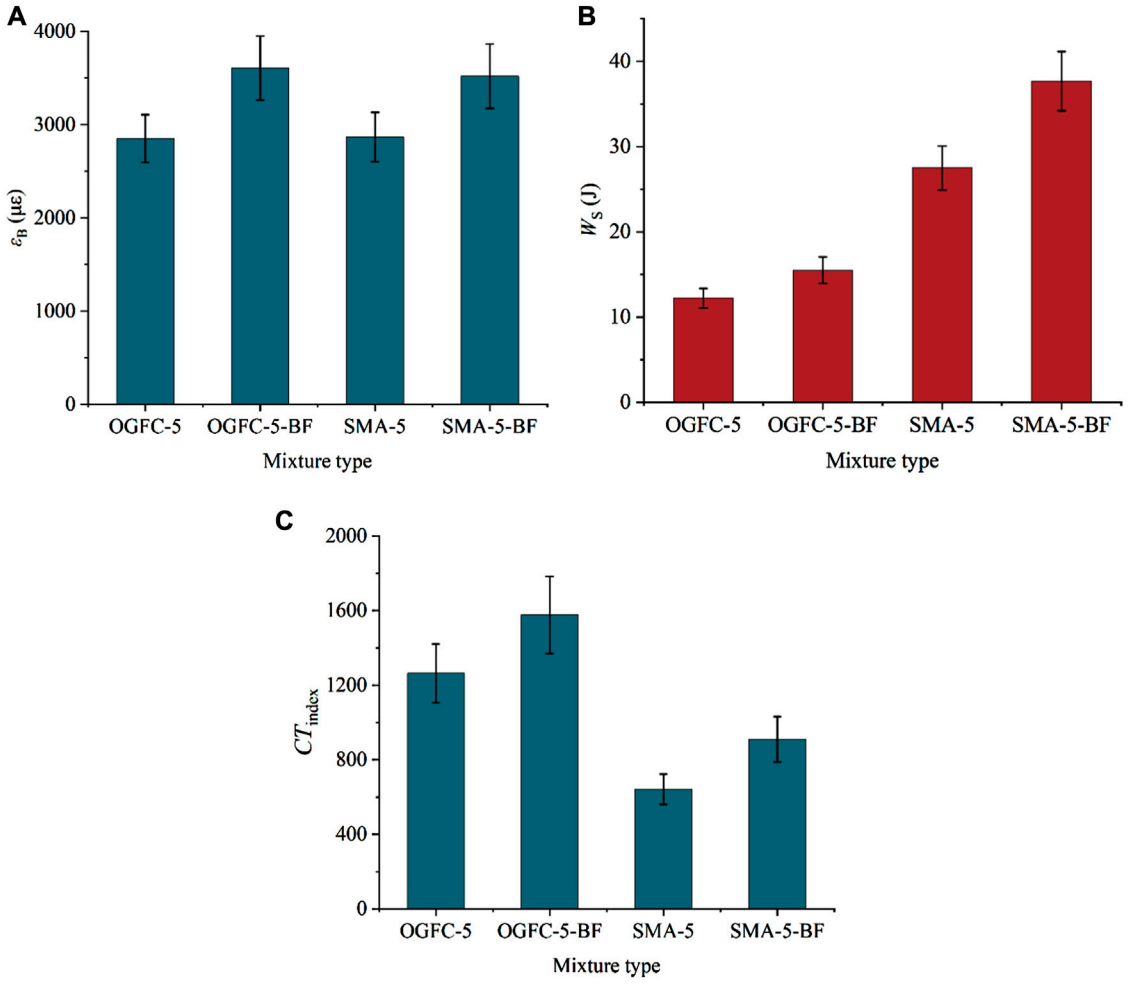

FIGURE 6
The results of cracking resistance tests: **(A)** ε_B; **(B)** W_S; **(C)** CT_{index}.

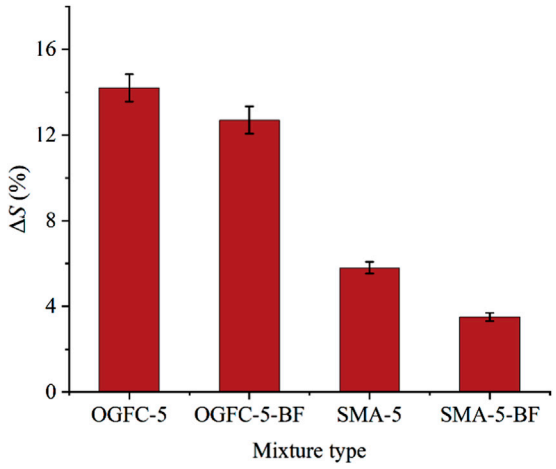

FIGURE 7
The results of stripping resistance test.

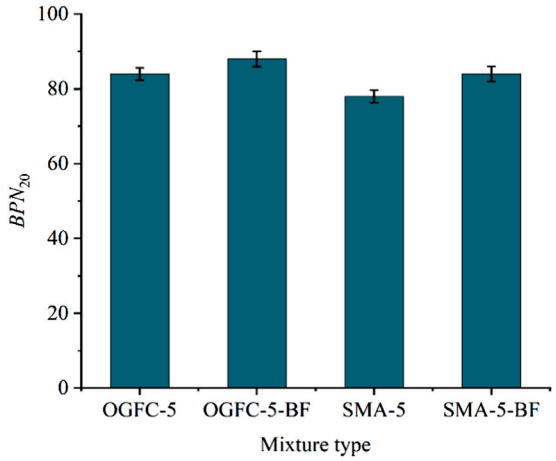

FIGURE 8
The results of skid resistance test.

4 Results and discussion

4.1 High temperature deformation resistance

DS and R_τ characterize high temperature deformation resistance of mixtures. As seen in Figures 5A, B, after adding basalt fiber, *DS* and R_τ of OGFC-5 increased by 24.7% and 12.3% respectively, while those of SMA-5 increased by 28.1% and 14.5% respectively. The results refer that adding basalt fiber could enhance the high temperature deformation resistance of the two thin overlayer asphalt mixtures, though a slightly greater enhancement could be observed on SMA-5 than OGFC-5. This phenomenon might be attributed to the fact that the addition of fiber could enhance the modulus of asphalt binder (Lou et al., 2022; Xie and Wang, 2023), thereby reducing the internal flow deformation of thin overlayer asphalt mixtures at high temperatures.

4.2 Cracking resistance

ε_B characterizes low temperature cracking resistance of mixtures. As seen in Figure 6A, after adding basalt fiber, ε_B of OGFC-5 and SMA-5 increased by 26.4% and 22.7% respectively. The results refer that adding basalt fiber could enhance the low temperature cracking resistance of the two thin overlayer asphalt mixtures, though a slightly greater enhancement could be observed on OGFC-5 than SMA-5. In addition, it can be found that ε_B values of OGFC-5 and SMA-5 (or OGFC-5-BF and SMA-5-BF) were at the same level, indicating the two types of mixtures demonstrated the approximate low temperature cracking resistance. Zhao et al. (2020) found that the addition of basalt fiber, lignin fiber and polyester fiber could enhance the low temperature cracking resistance of asphalt mixture to different degrees. Among these fibers, basalt fiber demonstrated the optimal improvement effect.

W_S and CT_{index} characterize intermediate temperature cracking resistance of mixtures. W_S reflects the resistance of crack formation, and CT_{index} reflects the resistance of crack expansion. As seen in Figures 6B, C, after adding basalt fiber, W_S and CT_{index} of OGFC-5 increased by 26.7% and 24.8% respectively, while those of SMA-5 increased by 37.1% and 41.7% respectively. The results indicate that adding basalt fiber could increase the intermediate temperature cracking resistance of the two thin

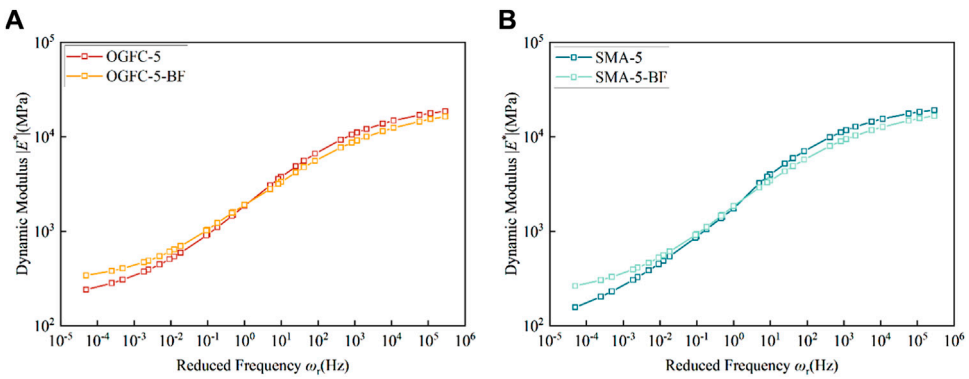

FIGURE 9
The results of dynamic modulus test: **(A)** Master curves of OGFC-5 and OGFC-5-BF; **(B)** Master curves of SMA-5 and SMA-5-BF.

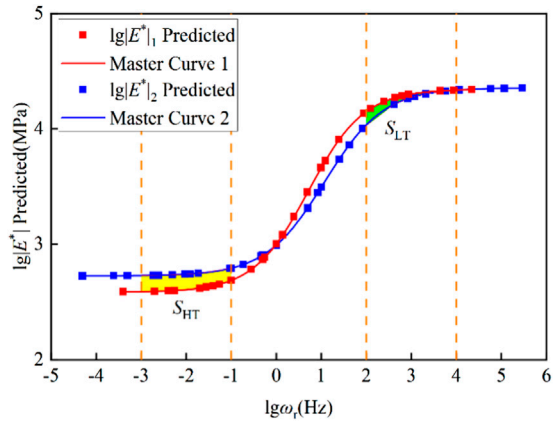

FIGURE 10
Schematic diagram of S_{LT} and S_{HT} calculation.

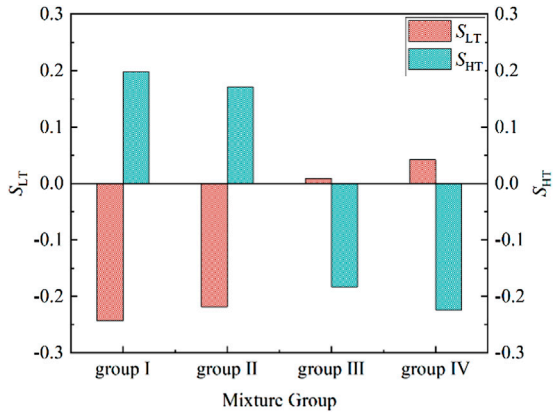

FIGURE 11
Calculation results of S_{LT} and S_{HT}.

overlayer asphalt mixtures, and a greater enhancement could be observed on SMA-5 than OGFC-5. This phenomenon might be attributed to the fact that the addition of fiber could enhance the toughness of asphalt binder (Wang et al., 2023; Xie and Wang, 2023), thereby delaying the cracking of thin overlayer asphalt mixtures at low and intermediate temperature. Furthermore, due to the lower volume of air voids (VV) and higher voids filled with asphalt (VFA) in SMA-5, the reinforcing effect of fiber in its asphalt binder was more pronounced, resulting in superior enhancement effect of intermediate temperature cracking resistance.

4.3 Stripping resistance

ΔS characterizes stripping resistance of mixtures. As seen in Figure 7, after adding basalt fiber, ΔS of OGFC-5 and SMA-5 decreased by 10.6% and 39.7% respectively. The results present that adding basalt fiber could strengthen the stripping resistance of the two thin overlayer asphalt mixtures, and a greater enhancement could be

TABLE 6 Grouping of asphalt mixtures.

Groups	Group I	Group II	Group III	Group IV
Mixture 1	OGFC-5	SMA-5	OGFC-5	OGFC-5-BF
Mixture 2	OGFC-5-BF	SMA-5-BF	SMA-5	SMA-5-BF

TABLE 7 Values of the index vectors.

Index vectors	X_1	X_2	X_3	X_4	X_5
Corresponding indexes	*DS*	R_τ	ε_B	S_{LT}	S_{HT}
x_{i1}	1,302	0.10	754	−0.243	0.198
x_{i2}	1,161	0.10	650	−0.218	0.171
x_{i3}	−1,142	−0.12	17	0.009	−0.183
x_{i4}	−1,283	−0.12	−87	0.042	−0.224

TABLE 8 Results of the correlation coefficients.

Groups	(X_1, X_5)	(X_2, X_5)	(X_3, X_4)
Results	0.9994	0.9960	−0.9995

observed on SMA-5 than OGFC-5. Zhang et al. (2020) observed that basalt fiber, polyester fiber and polyacrylonitrile fiber could effectively improve the stripping resistance of OGFC mixture, and the enhancement effect was superior when the basalt fiber content was between 0.15% and 0.30%. This phenomenon might be due to that the addition of fiber could increase the adhesion effect between asphalt binder and aggregates (Pei et al., 2021; Guo et al., 2023), thereby strengthening the overall integrity of thin overlayer asphalt mixtures.

4.4 Skid resistance

BPN_{20} (20°C) characterizes skid resistance of mixtures. As seen in Figure 8, after adding basalt fiber, BPN_{20} of OGFC-5 and SMA-5 only increased by 4.8% and 7.7% respectively. It means that adding basalt fiber presented no obvious effect on the skid resistance of the two mixtures, the reason might be that the addition of fibers caused hardly changes on the surface microtexture of thin overlayer asphalt mixtures, which is the key factor affecting the skid resistance (Xue et al., 2022). The addition of basalt fiber could only slightly change the surface macrotexture of mixtures, and the contribution to the improvement of skid resistance was very small, resulting in very limited enhancement effect.

4.5 Dynamic mechanical response

By the method described in the Section 3.5, the measured dynamic modulus data of OGFC-5, OGFC-5-BF, SMA-5, and SMA-5-BF were respectively fitted to master curves, which are displayed in Figure 9.

Asphalt mixtures present both elastic and viscous characteristics. The mixture is mainly elastic at low temperature and viscous at high temperature, which is primarily due to the complexity of the asphalt (Büchner et al., 2019; Jin D. et al., 2023). The mixture is prone to cracking

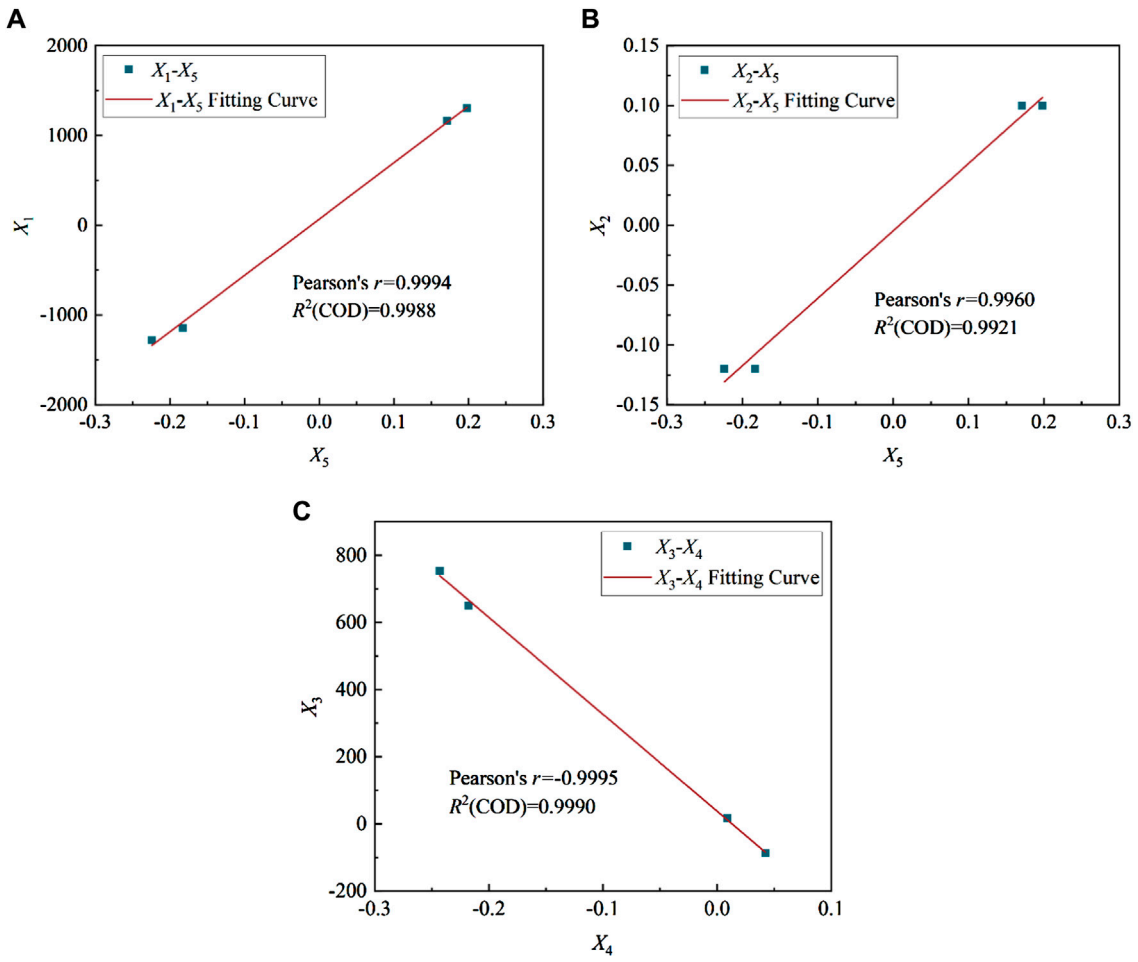

FIGURE 12
Two-dimensional distribution diagrams of the index vector groups: **(A)** (X_1, X_5); **(B)** (X_2, X_5); **(C)** (X_3, X_4).

at low temperature and excellent deformation ability is essential. Therefore, smaller modulus of the mixture should be desirable at low temperature. The mixture is prone to rutting at high temperature and good resistance to deformation is necessary. Subsequently, bigger modulus of the mixture should be desirable at high temperature. As shown in Figure 9, for both types of mixtures, adding basalt fiber could decrease the dynamic modulus of high frequency (low temperature) region, and increase the dynamic modulus of low frequency (high temperature) region.

In order to quantitatively analyze the dynamic modulus changes of mixtures caused by basalt fiber, the indexes S_{LT} and S_{HT} were introduced. S_{LT} and S_{HT} are determined by Eqs 14, 15, and the calculation diagram is displayed in Figure 10.

$$S_{LT} = \int_{2}^{4} \left(\lg|E^*|_2 - \lg|E^*|_1\right) \mathrm{d}\left(\lg\omega_r\right) \tag{14}$$

$$S_{HT} = \int_{-3}^{-1} \left(\lg|E^*|_2 - \lg|E^*|_1\right) \mathrm{d}\left(\lg\omega_r\right) \tag{15}$$

S_{LT} and S_{HT} are relative indexes. When $S_{LT} < 0$, it means low temperature performance of mixture 2 is greater than that of mixture 1. When $S_{HT} > 0$, it means high temperature performance of mixture 2 is greater than that of mixture 1. The four mixtures were divided into the following groups for analysis, as shown in Table 6.

The S_{LT} and S_{HT} indexes of the four groups of mixtures were calculated respectively and the results are illustrated in Figure 11.

It was found from Figure 11 that the S_{LT} values of mixtures in group I and group II were all negative. It meant that adding basalt fiber could decease the modulus in low temperature region, resulting in superior low temperature cracking resistance for both of the mixtures. Besides, the S_{LT} values of mixtures in group III and group IV were closer to zero, indicating the low temperature performance of OGFC-5 and SMA-5 was roughly the same. On the opposite, the S_{HT} values of mixtures in group I and group II were all positive. It referred that adding basalt fiber caused an increase in the modulus in high temperature region, which was also desirable to improve the high temperature deformation resistance. In addition, the S_{HT} values of mixtures in group III and group IV were also negative, indicating that the high temperature deformation resistance of OGFC-5 was better than that of SMA-5, which was accordance with the high temperature performance test results. Overall, after adding basalt fiber, the dynamic modulus of the two types of mixtures decreased in the high frequency (low temperature) section and increased in the low frequency (high temperature) section, reflecting that adding basalt fiber could enhance both of the low temperature and high temperature performance of mixtures.

4.6 Comparative analysis

Based on the correlation analysis, the consistency of the indexes S_{LT} and S_{HT} with the performance test indexes was investigated. The degree of correlation is determined by the Pearson correlation coefficient, as expressed by Eq. 16.

$$r = \frac{Cov(X_i, X_j)}{\sigma_i \sigma_j} = \frac{\sum(X_i - \overline{X_i})(X_j - \overline{X_j})}{\sqrt{\sum(X_i - \overline{X_i})^2 \sum(X_j - \overline{X_j})^2}} \quad (16)$$

where X_i and X_j are index vectors.

Before analyzing the correlation, the index vectors needed to be constructed. The groups used in dynamic modulus test were also used herein. The index vector X_1 corresponded to the index *DS* of the wheel tracking test, the index vector X_2 corresponded to the index R_τ of the uniaxial penetration test, the index vector X_3 corresponded to the index ε_B of the low temperature bending beam test, the index vector X_4 corresponded to the index S_{LT} introduced in the dynamic modulus test, and the index vector X_5 corresponded to the index S_{HT} introduced in the dynamic modulus test. The values of the index vectors are displayed in Table 7.

Correlation analysis was performed through combining (X_1, X_5), (X_2, X_5), and (X_3, X_4), and the correlation coefficient results are displayed in Table 8.

As can been seen from Table 8 that the three index vector groups of (X_1, X_5), (X_2, X_5), and (X_3, X_4) were all highly correlated, and the correlation coefficients were all above 0.9960. The results showed that the index *DS* and R_τ showed a great correlation degree with index S_{HT}, and the index ε_B presented a great correlation degree with index S_{LT}. By analyzing the two-dimensional distribution of the three groups, the evaluation consistency was further studied. The two-dimensional distribution diagrams are shown in Figure 12. It can be observed from Figure 12 that, the (X_1, X_5) and (X_3, X_4) groups had a strong linear correlation, all data points basically fell on the fitting curve with the R^2 above 0.9980. The linear correlation of (X_2, X_5) group was slightly weaker, and the data points had a certain fluctuation from the fitting curve with the R^2 around 0.9920. Overall, the two evaluation indexes introduced in the dynamic modulus test were exactly consistent with the performance test indexes, which could be used to predict and characterize high temperature and low temperature performance of thin overlayer mixtures.

5 Conclusion

In this research, the influence of basalt fiber on the performance of the thin overlayer was studied by multiple performance tests and the dynamic modulus test. In addition, the consistency between the introduced indexes (S_{LT} and S_{HT}) and the evaluation indexes in performance tests was analyzed. The conclusions are as follows:

(1) Adding basalt fiber can increase *DS* and R_τ presenting high temperature deformation resistance by around 26% and 13% respectively, increase ε_B presenting low temperature cracking resistance by around 24%, and increase W_S and CT_{index} presenting intermediate temperature cracking resistance by more than 26% and 24% respectively of thin overlayer mixtures.
(2) Adding basalt fiber can enhance stripping resistance, but causes no obvious influence on skid resistance of thin overlayer mixtures.
(3) Adding basalt fiber can decrease dynamic modulus in the high frequency section and increase it in the low frequency section, indicating both low temperature and high temperature performance of thin overlayer mixtures can be improved.
(4) The results of the dynamic modulus test and performance tests demonstrate good consistency. The indexes S_{LT} and S_{HT} can be used to evaluate low temperature and high temperature performance of thin overlayer mixtures.

In future research, more test methods can be used to study the influence of basalt fiber on the performance of the thin overlayer. In addition, the influence of fiber type on the performance of the thin overlayer also need to be further studied.

Data availability statement

The raw data supporting the conclusion of this article will be made available by the authors, without undue reservation.

Author contributions

BL: Conceptualization, Formal Analysis, Methodology, Project administration, Visualization, Writing–original draft. YZ: Data curation, Formal Analysis, Investigation, Methodology, Visualization, Writing–original draft. ZW: Conceptualization, Formal Analysis, Project administration, Supervision, Writing–review and editing. AK: Conceptualization, Funding acquisition, Methodology, Project administration, Supervision, Writing–review and editing. BW: Formal Analysis, Funding acquisition, Methodology, Project administration, Writing–review and editing. CL: Investigation, Methodology, Visualization, Writing–original draft.

Funding

The author(s) declare financial support was received for the research, authorship, and/or publication of this article. This research was funded by the National Natural Science Foundation of China, Grant Numbers 52008365 and 52178439. In addition, this research was funded by the Postgraduate education and teaching reform and practice project of Yangzhou University, grant number JGLX 2021_010, and the Yangzhou Government-Yangzhou University Cooperative Platform Project for Science and Technology Innovation, Grant Number YZ2020262.

Acknowledgments

The authors want to thank the assistance of the Yangzhou University Test Center for providing some of the test instruments and materials.

Conflict of interest

The authors declare that the research was conducted in the absence of any commercial or financial relationships that could be construed as a potential conflict of interest.

Publisher's note

References

Almaali, Y. A., and Al-Busaltan, S. (2021). Permanent deformation characteristics of modified thin overlay bitumen mixtures comprising waste polymers. *Mater. Today Proc.* 42 (5), 2717–2724. doi:10.1016/j.matpr.2020.12.711

ASTM D8225-19 (2019). *Standard test method for determination of cracking tolerance index of asphalt mixture using the indirect tensile cracking test at intermediate temperature*. West Conshohocken, USA: ASTM.

Büchner, J., Wistuba, P. M., Remmler, T., and Wang, D. (2019). On low temperature binder testing using DSR 4 mm geometry. *Mater. Struct.* 52, 113. doi:10.1617/s11527-019-1412-3

Chen, S., Gong, F., Ge, D., You, Z., and Sousa, J. B. (2019). Use of reacted and activated rubber in ultra-thin hot mixture asphalt overlay for wet-freeze climates. *J. Clean. Prod.* 232, 369–378. doi:10.1016/j.jclepro.2019.05.364

Correia, N. S., and Zornberg, J. G. (2018). Strain distribution along geogrid-reinforced asphalt overlays under traffic loading. *Geotext. Geomembr.* 46 (1), 111–120. doi:10.1016/j.geotexmem.2017.10.002

Cui, P., Wu, S., Xiao, Y., Liu, Q., and Wang, F. (2021). Hazardous characteristics and variation in internal structure by hydrodynamic damage of BOF slag-based thin asphalt overlay. *J. Hazard. Mater.* 412, 125344. doi:10.1016/j.jhazmat.2021.125344

Ding, X., Rath, P., Giraldo-Londoño, O., Buttlar, W. G., and Ma, T. (2022). Fracture modeling of rubber-modified binder based on Discrete Element Method. *J. Clean. Prod.* 380, 135017. doi:10.1016/j.jclepro.2022.135017

Gudmarsson, A., Ryden, N., Benedetto, H. D., and Sauzéat, C. (2015). Complex modulus and complex Poisson's ratio from cyclic and dynamic modal testing of asphalt concrete. *Constr. Build. Mater.* 88, 20–31. doi:10.1016/j.conbuildmat.2015.04.007

Guo, Y., Tataranni, P., and Sangiorgi, C. (2023). The use of fibres in asphalt mixtures: a state of the art review. *Constr. Build. Mater.* 390, 131754. doi:10.1016/j.conbuildmat.2023.131754

Han, Y., Zhao, Y., Jiang, J., Ni, F., and Zhao, X. (2021). Effects of design parameters and moisture conditions on interface bond strength between thin friction course (TFC) and underlying asphalt pavements. *Constr. Build. Mater.* 269, 121347. doi:10.1016/j.conbuildmat.2020.121347

Huang, Y., Liu, Z., Liu, L., Zhang, Y., and Xu, Q. (2020). Hybrid modification of Stone mastic asphalt with cellulose and basalt fiber. *Adv. Mater. Sci. Eng.* 2020, 1–11. doi:10.1155/2020/5671256

Ingrassia, L. P., Virgili, A., and Canestrari, F. (2012). Effect of geocomposite reinforcement on the performance of thin asphalt pavements: accelerated pavement testing and laboratory analysis. *Case Stud. Constr. Mater.* 12, e00342. doi:10.1016/j.cscm.2020.e00342

Javilla, B., Fang, H., Mo, L., Shu, B., and Wu, S. (2017). Test evaluation of rutting performance indicators of asphalt mixtures. *Constr. Build. Mater.* 155, 1215–1223. doi:10.1016/j.conbuildmat.2017.07.164

Jin, D., Wang, J., You, L., Ge, D., Liu, C., Liu, H., et al. (2021). Waste cathode-ray-tube glass powder modified asphalt materials: preparation and characterization. *J. Clean. Prod.* 314, 127949. doi:10.1016/j.jclepro.2021.127949

Jin, D., Yin, L., Xin, K., and You, Z. (2023b). Comparison of asphalt emulsion-based chip seal and hot rubber asphalt-based chip seal. *Case Stud. Constr. Mater.* 18, e02175. doi:10.1016/j.cscm.2023.e02175

Jin, T., Liu, L., Yang, R., Sun, L., and Yuan, J. (2023a). Investigation of interlayer bonding performance between asphalt concrete overlay and Portland cement concrete using inclined shear fatigue test. *Constr. Build. Mater.* 400, 132681. doi:10.1016/j.conbuildmat.2023.132681

Jtg, (2011). *Standard test methods of bitumen and bituminous mixtures for highway engineering*. Beijing, China: China Communications Press.

Jtg, (2017). *Specifications for design of highway asphalt pavement*. Beijing, China: China Communications Press.

Jtg, (2019). *Field test methods of highway subgrade pavement*. Beijing, China: China Communications Press.

Li, Y., Zou, Z., Zhang, J., and He, Y. (2023). Study on the evolution of airport asphalt pavement integrated distress based on association rule mining. *Constr. Build. Mater.* 3691, 130565. doi:10.1016/j.conbuildmat.2023.130565

Ling, M., Luo, X., Gu, F., and Lytton, R. L. (2017). Time-temperature-aging-depth shift functions for dynamic modulus master curves of asphalt mixtures. *Constr. Build. Mater.* 157, 943–951. doi:10.1016/j.conbuildmat.2017.09.156

Liu, F., Pan, B., Bian, J., and Zhou, C. (2023). Experimental investigation on the performance of the asphalt mixture with ceramic fiber. *J. Clean. Prod.* 384, 135585. doi:10.1016/j.jclepro.2022.135585

Liu, Z., Luo, S., Quan, X., Wei, X., Yang, X., and Li, Q. (2019). Laboratory evaluation of performance of porous ultra-thin overlay. *Constr. Build. Mater.* 204, 28–40. doi:10.1016/j.conbuildmat.2019.01.147

Lou, K., Xiao, P., Tang, Q., Wu, Y., Wu, Z., and Pan, X. (2022). Research on the micro-nano characteristic of basalt fiber and its impact on the performance of relevant asphalt mastic. *Constr. Build. Mater.* 318, 126048. doi:10.1016/j.conbuildmat.2021.126048

Pei, Z., Lou, K., Kong, H., Wu, B., Wu, X., Xiao, P., et al. (2021). Effects of fiber diameter on crack resistance of asphalt mixtures reinforced by basalt fibers based on digital image correlation Technology. *Materials* 14 (23), 7426. doi:10.3390/ma14237426

Podolsky, J. H., Williams, R. C., and Cochran, E. (2018). Effect of corn and soybean oil derived additives on polymer-modified HMA and WMA master curve construction and dynamic modulus performance. *Int. J. Pavement Res. Technol.* 11 (6), 541–552. doi:10.1016/j.ijprt.2018.01.002

Qin, X., Ma, L., and Wang, H. (2019). Comparison analysis of dynamic modulus of asphalt mixture: indirect tension and uniaxial compression test. *Transp. A* 15, 165–178. doi:10.1080/23249935.2018.1517133

Tan, G., Wang, W., Cheng, Y., Wang, Y., and Zhu, Z. (2020). Master curve establishment and complex modulus evaluation of SBS-modified asphalt mixture reinforced with basalt fiber based on generalized sigmoidal model. *Polymers* 12 (7), 1586. doi:10.3390/polym12071586

Wang, W., Yang, L., Cui, H., Wu, F., Cheng, Y., and Liang, C. (2023). Freeze–thaw damage mechanism analysis of SBS asphalt mixture containing basalt fiber and lignocellulosic fiber based on microscopic void characteristics. *Polymers* 15 (19), 3887. doi:10.3390/polym15193887

Xie, T., and Wang, L. (2023). Optimize the design by evaluating the performance of asphalt mastic reinforced with different basalt fiber lengths and contents. *Constr. Build. Mater.* 363, 129698. doi:10.1016/j.conbuildmat.2022.129698

Xue, X., Zheng, X., Guan, B., Liu, J., Ding, D., Xiong, R., et al. (2022). Long-term skid resistance of high-friction surface treatment of pavement using high-alumina refractory waste. *Constr. Build. Mater.* 351, 128961. doi:10.1016/j.conbuildmat.2022.128961

Yaqub, R., Bandyopadhyay, A., and Ali, H. (2023). Exploring the potential of onboard energy scavenging subsystems for generating valuable data. *Front. Energy Res.* 11, 1259676. doi:10.3389/fenrg.2023.1259676

Zhang, C., Shi, F., Cao, P., and Liu, K. (2022a). The fracture toughness analysis on the basalt fiber reinforced asphalt concrete with prenotched three-point bending beam test. *Case Stud. Constr. Mater.* 16, e01079. doi:10.1016/j.cscm.2022.e01079

Zhang, J., Huang, W., Zhang, Y., Lv, Q., and Yan, C. (2020). Evaluating four typical fibers used for OGFC mixture modification regarding drainage, raveling, rutting and fatigue resistance. *Constr. Build. Mater.* 253, 119131. doi:10.1016/j.conbuildmat.2020.119131

Zhang, M., Zhao, H., Fan, L., and Yi, J. (2022c). Dynamic modulus prediction model and analysis of factors influencing asphalt mixtures using gray relational analysis methods. *J. Mater. Res. Technol.* 19, 1312–1321. doi:10.1016/j.jmrt.2022.05.120

Zhang, Y., Gu, Q., Kang, A., Ding, X., and Ma, T. (2022b). Characterization of mesoscale fracture damage of asphalt mixtures with basalt fiber by environmental scanning electron microscopy. *Constr. Build. Mater.* 344, 128188. doi:10.1016/j.conbuildmat.2022.128188

Zhao, H., Guan, B., Xiong, R., and Zhang, A. (2020). Investigation of the performance of basalt fiber reinforced asphalt mixture. *Appl. Sci.* 10 (5), 1561. doi:10.3390/app10051561

frontiers | Frontiers in Energy Research

TYPE Original Research
PUBLISHED 29 December 2023
DOI 10.3389/fenrg.2023.1337846

OPEN ACCESS

EDITED BY
Di Wang,
University of Ottawa, Canada

REVIEWED BY
Peng Lin,
Delft University of Technology, Netherlands
Fan Zhang,
Aalto University, Finland

*CORRESPONDENCE
Aimin Sha,
ams@chd.edu.cn
Jie Wang,
j.wang@rioh.cn

RECEIVED 13 November 2023
ACCEPTED 30 November 2023
PUBLISHED 29 December 2023

CITATION
Chang R, Sha A and Wang J (2023), Effect of warm mix agent on the chemo-mechanical performance of binder with different oil sources.
Front. Energy Res. 11:1337846.
doi: 10.3389/fenrg.2023.1337846

Effect of warm mix agent on the chemo-mechanical performance of binder with different oil sources

Rong Chang[1,2], Aimin Sha[1]* and Jie Wang[2]*

[1]Key Laboratory for Special Area Highway Engineering of Ministry of Education, Chang'an University, Xi'an, China, [2]Research Institute of Highway Ministry of Transport, Beijing, China

In this study, three typical oil source asphalt binders, Karamay asphalt A, CNOOC 36-1 asphalt B, Qinhuangdao CNPC asphalt C, were selected to prepare asphalt binders together with the warm mix agent Evotherm M1. The effects of warm mix agents on asphalt from different oil sources were experimentally studied via dynamic shear rheological (DSR), thermogravimetric analysis (TG), and Raman spectroscopy tests. The asphalt binders with different oil sources exhibit different properties. The rheological test results indicate that the addition of warm mix agent can slow down the decrease of asphalt viscosity during the aging process and the aging of asphalt. The results of the thermogravimetric test showed that the residual mass of asphalt with the addition of a warm mix agent significantly decreased after aging. Warm mixing agents can slow down the conversion of lightweight components to heavy components during the aging process of asphalt. By calculating the reflectivity of asphalt in Raman spectroscopy, it can be concluded that the reflectivity of asphalt decreases after adding a warm mix agent. The warm mixing agent reduces the degree of thermal evolution of asphalt. Warm mixing agents can make the chemical components in asphalt relatively stable and less prone to further pyrolysis or cracking reactions.

KEYWORDS

warm mixed asphalt, chemical additives, oil source, rheological properties, peak temperature, saddle index, asphalt reflectance

1 Introduction

Building a low-carbon society has become a strategic focus worldwide. The construction temperature of hot mix asphalt mixture is generally 160°C~180°C (Qiu et al., 2012; Zhang et al., 2023). The mixing temperature of rubber asphalt and special modified asphalt can even reach over 190°C. This not only requires a large amount of heating fuel, but also generates a large amount of harmful and toxic substances such as greenhouse gases and asphalt smoke. The working temperature of Warm Mix Asphalt (WMA) is usually between 90°C and 130°C. It can be divided into chemical process, foam process and organic additive process (Guo et al., 2017; Hou et al., 2017).

Chemical additives such as warm mix asphalt can reduce the working temperature by up to 35°C~55°C. Additives can reduce the surface tension of the aggregate asphalt interface, improve low-temperature coating and construction workability (Xu and Huang, 2010; Sun et al., 2011; Bowers et al., 2014). At present, there are various types of asphalt on the market, and the performance of asphalt after adding warm mix agents shows diversity. This results in varying quality and implementation effects of warm mix asphalt, making it difficult to estimate the impact on the final pavement performance (Dong et al., 2017).

By studying the warm mixing characteristics of asphalt from different oil sources, it is beneficial to choose the compatibility between asphalt and warm mixing agents. Further explore the impact mechanism of additives on the chemical components of asphalt, and ultimately improve the application effect of warm mix asphalt in road engineering.

This article selects three representative oil sources of road petroleum asphalt and uses dynamic shear rheological test (DSR), thermogravimetric analysis test (TG), and Raman spectroscopy test to study the characteristics of warm mixed asphalt from different oil sources. The article explores the influence of warm mixing agents on the performance and chemical composition of asphalt. It can guide the selection and analysis of warm mixed asphalt.

2 Materials and testing methods

2.1 Materials

According to the type of asphalt oil source, we selected three representative 70 # road asphalt as samples, which are labeled as: Karamay asphalt (A), CNOOC 36-1 asphalt (B), and Qinhuangdao CNPC asphalt (C).

Karamay asphalt is made from high quality naphthenic base heavy oil in Block 9. The process of blending vacuum residue with deoiled asphalt is used to produce road petroleum asphalt (Badre et al., 2006; Menapace et al., 2016). Karamay asphalt belongs to naphthenic base crude oil, which has the characteristics of low solidifying point, low wax content, low sulfur content and high resin content. It is currently the only road petroleum asphalt with a density less than 1 g/cm^3, which has the characteristics of high dynamic viscosity and high ductility after aging. Mainly used in areas with large temperature differences between day and night, long exposure to sunlight, and strong ultraviolet radiation.

CNOOC 36-1 asphalt is made from rare crude oil from the Suizhong 36-1 oilfield. Suizhong crude oil is a low sulfur cycloalkyl, high acid heavy oil with high density, low wax content, and high gum content. It has the characteristics of high low-temperature ductility, good low-temperature crack resistance, and good water stability.

Qinhuangdao China Petroleum Asphalt is mainly composed of Venezuelan Persian Cane crude oil. This crude oil has high acid value, heavy metal content, and residual carbon, while it has low saturated hydrocarbon content, high gum and asphaltene content, and low wax content.

In this study, three different original asphalt recorded as AO, BO, CO. Three types of asphalt added with warm mix agents are respectively recorded as AP, BP, CP.

The performance index test results of three types of asphalt are shown in Table 1. The test method refer to the "Test Specification for Asphalt and Asphalt Mixtures in Highway Engineering" (JTG E20).

The warm mixing agent Evotherm M1 is a surface active dosage form developed by Meadwestvaco in the United States. The warm mixing agent is a dark brown liquid at room temperature.

2.2 Preparation for warm mix asphalt binder

The preparation method of warm mixed asphalt binder: Heat the asphalt to 135°C. Calculate the amount of warm mix additives added (based on 0.6% of asphalt mass). Slowly pour the weighed warm mixing agent into the asphalt in a mixed state, with a speed of 200-300 r/min and a mixing time of 20–30 min.

2.3 Test and evaluation method

In this study, the rheological properties, thermal stability, and molecular structure information of three representative oil sources

TABLE 1 Asphalt performance indicators.

Project		Unit	A	B	C	Method
Penetration 100 g, 5 s, 15°C, 25°C, 30°C		0.1 mm	22	21	24	T0604
		0.1 mm	72	68	71	
		0.1 mm	112	113	116	
Penetration index, PI		-	−1.14	−1.27	−0.81	T0604
Softening point, $T_{R\&B}$		°C	46.0	46.5	47.5	T0606
Dynamic viscosity, 60°C		Pa·s	223.5	232.5	256.9	T0620
Ductility 5 cm/min, 10°C		Cm	>100	>100	49	T0605
Wax content		%	1.9	1.8	1.3	T0615
Flash point, COC		°C	278	287	312	T0611
Solubility		%	99.5	99.7	99.71	T0607
Density, 15°C		g/cm^3	0.977	1.011	1.049	T0603
RTFOT	Quality change	%	0.060	−0.070	−0.070	T0609
	Residual penetration ratio	%	67.4	64.8	64.8	T0604
	Residual ductility, 10°C	cm	12	9	9	T0605

of asphalt before and after warm mixing were studied. Dynamic shear rheological test, thermogravimetric analysis test, and Raman spectroscopy test were used.

2.3.1 Rheological performance tests

This study used the dynamic mechanical analysis method ASTM D7175 to test and analyze the rheological properties of asphalt. Test the high-temperature rheological properties of warm mixed asphalt as a function of temperature. Using a frequency of 10 rad/s. Scan with a temperature range of 58°C~82°C, and test at 6°C intervals (Qian et al., 2001). The constant temperature curing time at each temperature point is 10 min. Through rheological analysis, the viscoelastic indicators of asphalt before and after warm mixing, such as high temperature domain modulus of elasticity (G′) and phase angle, are obtained through testing(δ), Viscous modulus (G″), rutting factor (G*/sin δ) Etc.

2.3.2 Thermogravimetric analysis test

Thermogravimetric analysis is an analytical technique that measures the mass changes of samples at different temperatures under program-controlled temperature conditions. Warm mixed asphalt undergoes corresponding chemical changes, decomposition, and composition changes at a certain temperature, accompanied by changes in quality (Abo-Qudais and Al-Shweily, 2007; Hsu et al., 2011; Wang et al., 2022). This study uses thermogravimetric analysis to evaluate the thermal stability of warm mixed asphalt binder. In thermogravimetric analysis, test conditions are set based on the physical and chemical properties of warm mix asphalt, and appropriate sample quality and heating rate are selected. Excessive heating speed can lead to significant errors or reaction delays in obtaining real-time quality and other information of the sample. If the heating rate is too slow, it may not reflect the true state of thermal decomposition of warm mixed asphalt. In this study, METTLER TOLEDO's TGA/DSC 2 1600HT was used to test the thermal gravimetric analysis of asphalt before and after the addition of a warm mix agent and the aging effect. The test temperature was selected from 0°C to 800°C, and the heating rate was 10°C/min.

2.3.3 Raman spectra

Raman spectroscopy, as a scattering spectrum, can obtain information on molecular vibration and rotation (Wang et al., 2015). In this study, Horiba LabRAM HR Evolution was used to measure the changes in molecular structure of asphalt before and after warm mixing. Identify the size, intensity, and shape of Raman shifts in warm mix asphalt.

Asphalt samples can exhibit typical D and G peaks (Curtis et al., 1993). There may be interference from background signals in the original spectrogram, and it is necessary to perform background removal and peak splitting processing on the spectrogram to obtain effective spectral information.

The parameters of the Raman spectrum are shown in the Figure 1: H is the peak height, W is the half peak width, S is the lowest point between the D and G peaks, and H '/S is defined as the saddle index (Tan and Guo, 2014).

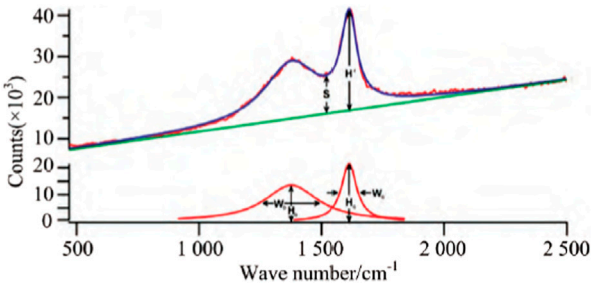

FIGURE 1
Raman spectral parameters.

3 Results and discussions

3.1 Rheological properties of warm mix asphalt

Temperature scanning experiments were conducted on three typical asphalt samples before and after adding warm mix agents under three conditions: original asphalt, RTFOT, and PAV after RTFOT. An available DSR was used for rheological testing to obtain the changes in rutting factor and phase angle under different aging conditions.

The elastic modulus of warm mixed asphaltvaries with different oil sources, mainly determined by the interaction forces between its components and asphalt molecules. The rutting factor and phase angle of different asphalt before and after warm mixing under different aging conditions are shown in Figure 2.

From the scanning results, it can be seen that as the temperature increases, the rutting factor of asphalt decreases and the phase angle increases. This means that the viscosity of asphalt decreases and the resistance to rutting decreases. The rutting factors are as follows: AO+RFTOT+PAV>AO+RFTOT>AO. After experiencing short-term and long-term aging, the modulus of asphalt continues to increase. The rutting factor of warm mixed asphalt is: AP + RFTOT + PAV>AP + RFTOT>AP. The rutting factor of warm mixed asphalt gradually increases with the deepening of aging degree. Comparing the rutting factors of asphalt and warm mix asphalt under the same aging state, it can be seen that the rutting factor of warm mix asphalt is slightly greater than the rutting factor of the original asphalt. The addition of warm mix agents makes asphalt have stronger resistance to deformation. After RTFOT, the rutting factor of warm mix asphalt is the same as that of the original asphalt. After experiencing both short and long-term aging, the rutting factor of asphalt in its original state is greater than that of warm mix asphalt. From this, it can be seen that the addition of warm mix agents can slow down the aging and hardening degree of the base asphalt.

Phase angle δ As the aging state changes, there is a continuous increasing trend within the scanning temperature range. The phase angle of the original asphalt sample is in descending order: AO>AO+RTFOT>AO+RTFOT+PAV.

As the aging degree deepens, the phase angle gradually decreases and the viscosity of asphalt gradually decreases. The phase angle of

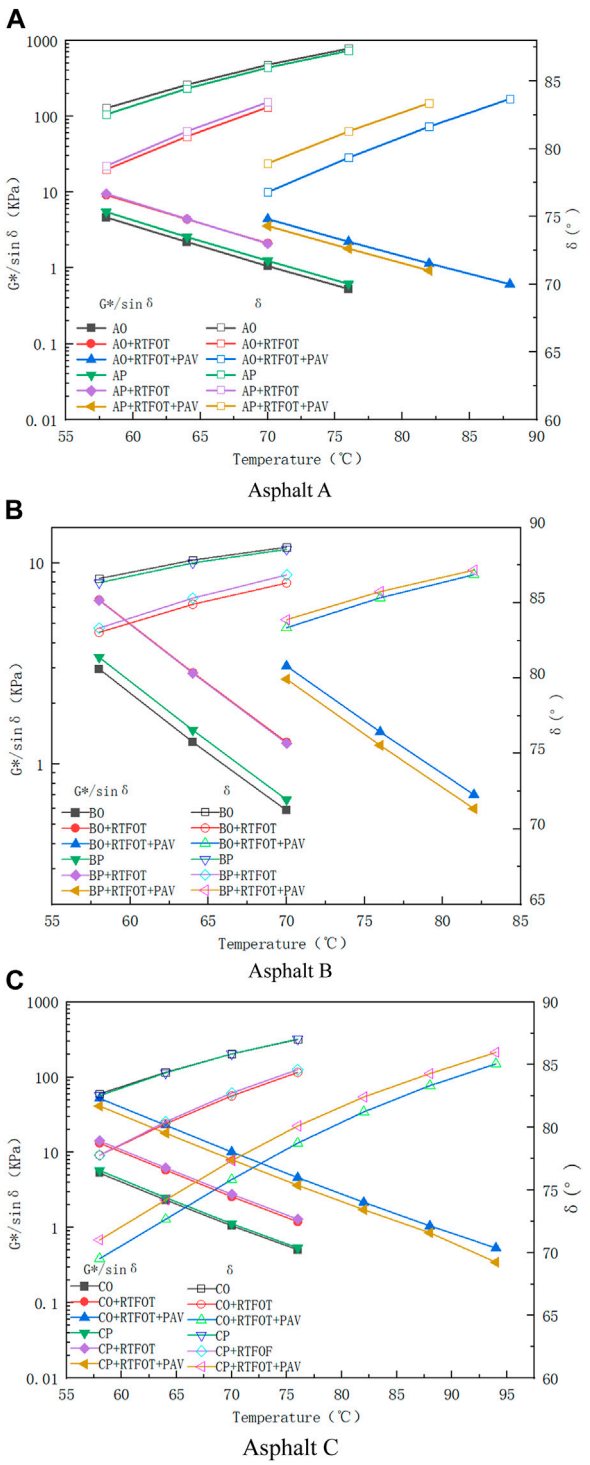

FIGURE 2
Rheological properties of warm mixed asphalt with different oil sources. **(A)** Asphalt A, **(B)** Asphalt B, **(C)** Asphalt C.

warm mixed asphalt is in the order of AP>AP+RTFOT>AP+RTFOT+PAV, which is consistent with the phase angle variation of the original asphalt sample.

Comparing the phase angles of asphalt and warm mix asphalt under the same aging effect, it can be seen that the phase angle of warm mix asphalt is slightly smaller than the phase angle of the original asphalt. The addition of warm mix agent slightly reduces the viscosity of asphalt, further explaining the principle that warm mix agent can mix at low temperature. After RTFOT, the phase angle of warm mixed asphalt is slightly greater than that of the original asphalt. After short and long-term aging, the phase angle of warm mix asphalt is much greater than that of the original asphalt. The phase angle characterizes the viscosity of asphalt, and the smaller the phase angle, the smaller the viscosity of asphalt. The addition of warm mix agents can delay the decrease in viscosity of asphalt under aging and alleviate its aging.

In the lower temperature scanning stage, the deeper the aging degree of asphalt, the better the content of high molecular weight components in asphalt. Asphalt binders exhibit better elastic properties, resulting in lower phase angles compared to other aging stages. As the temperature increases, the asphalt material gradually softens and tends towards viscous flow dynamics. The asphalt samples with deeper aging degree show a faster increase in viscosity composition and a significant increase in phase angle with the increase of temperature.

B asphalt and C asphalt exhibit similar rheological properties as A asphalt. The delaying effect of warm mix agent on B asphalt is not as good as A asphalt. The performance is better when mixed with asphalt A.

3.2 Thermal stability of warm mixed asphalt

This study controls the temperature rise and fall rate of the sample, and then measures the mass change of the sample at different temperatures. Determine the thermal decomposition of asphalt at different temperatures. Test the mass loss rate of the sample before and after warm mixing at different temperatures. Analyze the influence of warm mixing agents on the thermal stability of asphalt.

The quality of asphalt remains basically unchanged between 0°C and 214.46°C, and its performance remains stable. The quality of asphalt will not be lost during the heating and mixing process of asphalt and aggregates at 214°C. Asphalt begins to experience mass loss from 296°C. The thermal decomposition process is basically completed at around 500°C. Asphalt materials are basically completely carbonized.

The thermal decomposition process of asphalt after PAV basically ends at around 543°C, and the thermogravimetric curve remains stable. After adding a warm mixing agent to asphalt, there is basically no effect on the inflection point temperature and residual quality of the original asphalt sample. After long-term aging, the residual mass of the original sample increases, while the residual mass of the warm mixing agent decreases.

As the temperature increases, each component in asphalt begins to decompose. The original small molecules and decomposed small molecules in asphalt gradually break free from intermolecular forces and escape from the asphalt material (Hou et al., 2015; Hou et al., 2016). Therefore, the thermal stability of asphalt before and after warm mixing is evaluated by analyzing the inflection point temperature and residual mass ratio of the thermogravimetric curve of asphalt materials.

The inflection point temperature and residual mass data of three types of asphalt are shown in the Table 2.

TABLE 2 Thermal weight loss data of different asphalt under different aging conditions.

Asphalt	Peak temperature (°C)	Residual mass (%)	Asphalt	Peak temperature (°C)	Residual mass (%)
AO	468.17	8.88	AO-PAV	467.83	10.71
AP	472.33	8.67	AP-PAV	468.0	6.47
BO	468.33	9.6	BO-PAV	468.00	11.29
BP	470.67	10.32	BP-PAV	464.33	10.62
CO	464.00	13.6	CO-PAV	464.33	14.62
CP	459.83	13.13	CP-PAV	459.83	11.34

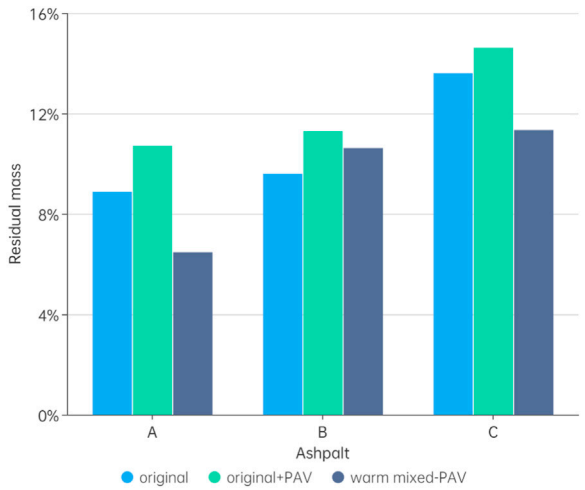

FIGURE 3
Different residual qualities of asphalt.

Analyze the residual quality changes of three types of asphalt samples, long-term aging PAV, and warm mix asphalt after long-term aging PAV, as shown in Figure 3.

The residual mass of asphalt from different oil sources gradually increases with long-term aging. Aging can cause the association and aggregation of asphalt molecules. The addition of warm mix agents will have a certain impact on the composition and microstructure of asphalt components. After the aging of warm mix asphalt binder, the residual quality significantly decreases, indicating that the warm mix agent will slow down the conversion of light components to heavy components in the aging process of asphalt. Warm mix agents can reduce the molecular association of asphalt during aging and slow down the aging of asphalt.

By comparing the residual quality of different types of asphalt, A asphalt has the smallest residual quality after thermogravimetric analysis, followed by B asphalt. C asphalt has more carbonized components that have not been decomposed. The residual mass of asphalt with more asphaltene content after thermogravimetric analysis is greater. Asphalt has a high content of asphaltene and is prone to carbonization. The higher the content of non decomposable components at high temperatures, the higher the residual mass ratio of thermogravimetry. Generally, components that cannot be decomposed above 460°C have larger molecular weights, more condensed aromatic rings, and are prone to carbonization. Therefore, there will be significant differences in the residual quality of asphalt from different oil sources.

3.3 Molecular structure changes of warm mixed asphalt

This study used Raman spectroscopy to test the changes in molecular structure and chemical bond information of warm mixed asphalt from different oil sources. Raman spectroscopy is a non-destructive spectroscopy technique that uses laser irradiation of asphalt samples to measure the changes in photon energy scattered by asphalt, thereby obtaining molecular structure and composition information before and after warm mixing of asphalt (Shan et al., 2010).

This study used HORIBA Scientific LabRAM HR Evolution for Raman spectroscopy testing. Raman spectroscopy is a surface test with a detection depth of about 10 nm and a spot size of 1um.The Raman spectra of three different types of warm mixed asphalt were shown in Figure 4.

Based on the Raman spectra of each asphalt, determine the positions of the D and G peaks and perform peak fitting. Obtain quantitative characterization parameters for the D and G peaks, mainly including: (Zhang et al., 2023) Peak position: W_D and W_G represent the positions of D and G peaks, respectively; (Qiu et al., 2012) Half height width: $FWHM_D$ and $FWHM_G$; (Guo et al., 2017) Peak height: H; (Hou et al., 2017) Half peak width: W; (Sun et al., 2011) S is the lowest point between the D and G peaks; (Bowers et al., 2014) Saddle index: H '/S.

Wilkins et al. [*] proposed a method for peak separation of asphalt Raman spectra through extensive experimental data analysis, and provided a formula for calculating asphalt reflectance using Raman spectral parameters. The formula for calculating the reflectance of asphalt Raman spectroscopy parameters is:

$$R_0\%(cal) = -3.291 + 7.432\log(VG - VD) - 0.306\log(saddle\ index) - 2.935 logFWHMG - 3.118 logFWHMD$$

In the formula, v_D and v_G are the peak positions of D and G peaks, with peak spacing of (v_G-v_D). The half width at half height of D and G peaks is FWHM-D and FWHM-G and the saddle index. Calculate the Raman spectral parameters of different types of asphalt in the Table 3.

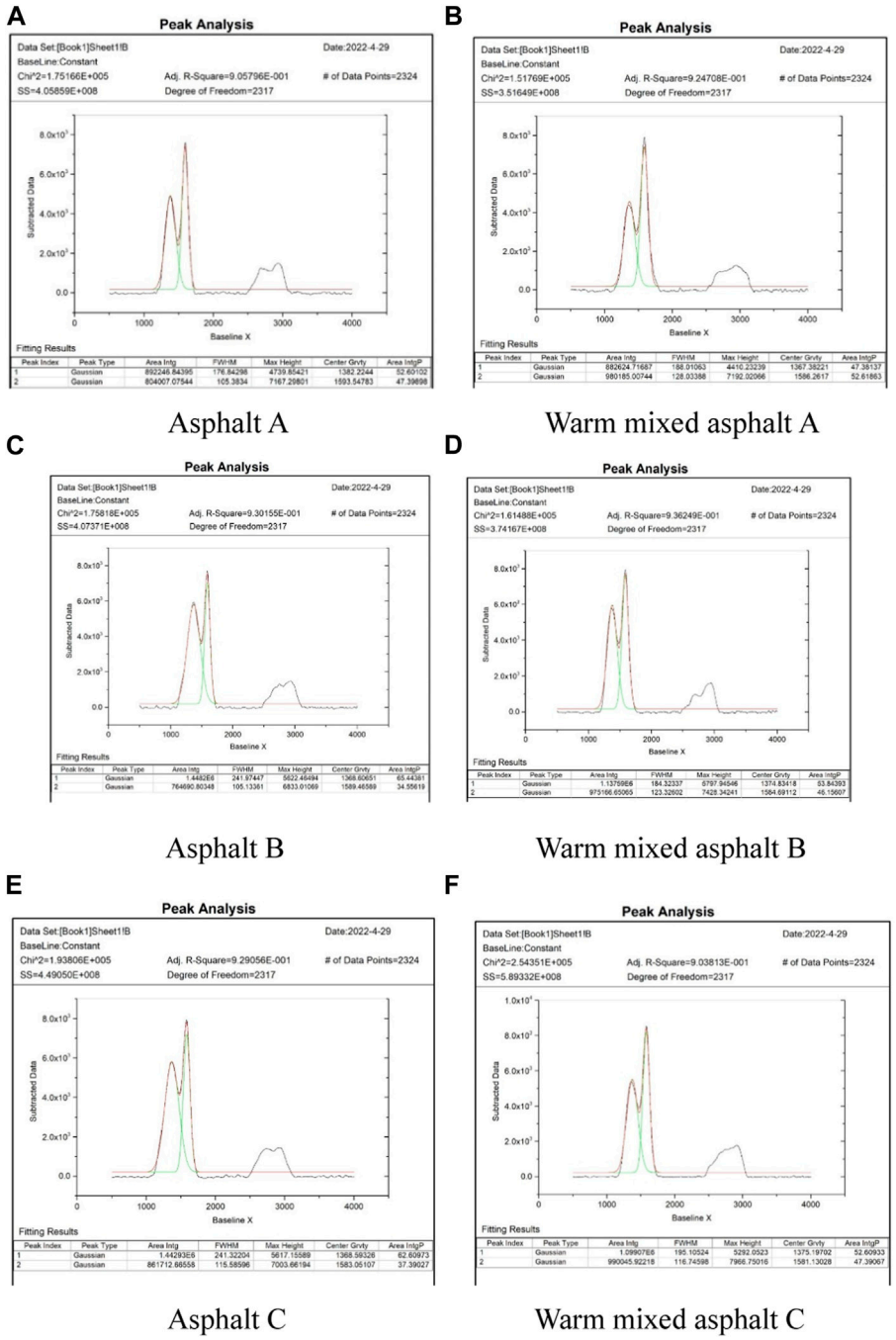

FIGURE 4
Raman spectra of three different types of warm mixed asphalt. **(A)** Asphalt A, **(B)** Warm mixed asphalt A, **(C)** Asphalt B, **(D)** Warm mixed asphalt B, **(E)** Asphalt C, and **(F)** Warm mixed asphalt C.

Raman spectroscopy parameters can better characterize the maturity of asphalt. By using the Lorentz peak fitting method to process the original test results, effective characteristic parameters of Raman peaks can be obtained. The saddle index and reflectance changes of asphalt before and after warm mixing can be analyzed as shown in the Figure 5.

As the degree of thermal evolution gradually increases, the alkane structure in asphalt gradually decreases. Due to the association effect, the spacing between aromatic ring structures decreases, resulting in an increase in reflectivity. The warm mix agent reduces the degree of thermal evolution of asphalt. The reflectivity of different types of asphalt decreases after adding warm mix agents. The decrease in thermal evolution indicates that the components in asphalt are relatively stable and less prone to further thermal decomposition.

TABLE 3 Raman spectroscopic parameters of asphalt.

Asphat	FWHM (D)/cm^{-1}	Area(D)/cm^{-1}	FWHM (G)/cm^{-1}	Area (G)/cm^{-1}	V_G-V_D/cm^{-1}	Saddle index/S	Reflectivity/%
AO	188.011	882625	128.034	980187.7	218.88	2.33	0.71
AP	176.84	892246.8	105.38	804007.1	211.32	2.90	0.90
BO	241.97	1448200	105.13	764690.8	220.85	1.91	0.68
BP	184.32	1137590	123.32	975166.7	209.86	2.10	0.67
CO	241.322	1442930	115.58	861712.7	214.46	1.67	0.48
CP	195.1	1099070	116.74	990045.9	205.94	2.19	0.59

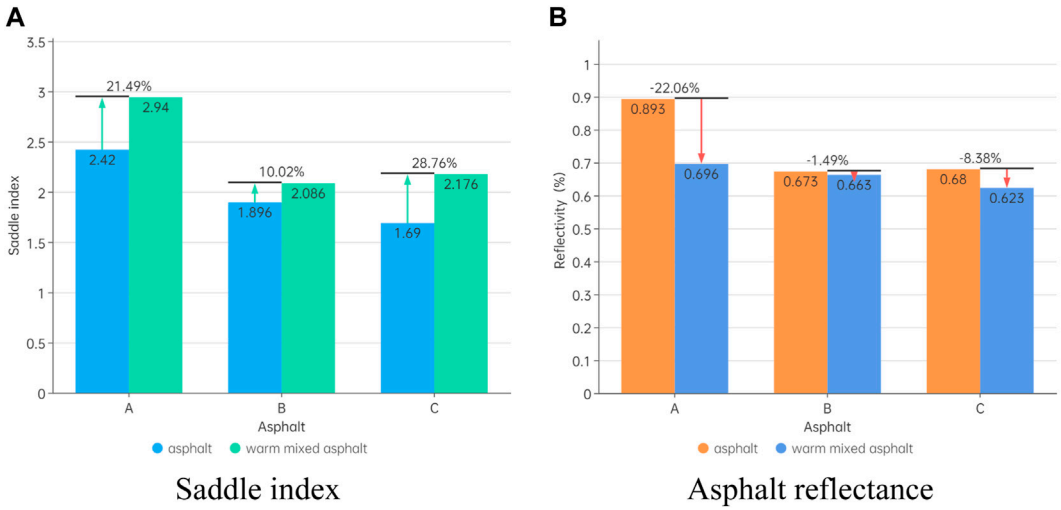

FIGURE 5
Asphalt Raman parameters. **(A)** Saddle index. **(B)** Asphalt reflectance.

4 Conclusion

Through dynamic shear rheological test, thermal weight loss test, and Raman spectroscopy test, the rheological properties, thermal decomposition stability, and the influence of temperature mixing agents on the microstructure of three typical oil source asphalt were studied. The results indicate that asphalt binders with different oil sources exhibit different warm mix properties.

(1) The addition of warm mix agents can delay the decrease in viscosity of asphalt under aging and alleviate the aging of asphalt.
(2) Asphalt with high asphaltene content has a large residual mass after thermal decomposition. Warm mix agents can slow down the molecular association of asphalt during the aging process. The residual mass of warm mixed asphalt after thermal decomposition has decreased.
(3) The reflectivity of different types of asphalt decreases after adding warm mix agents, indicating that warm mix agents reduce the degree of thermal evolution of asphalt. Warm mixing agents can make the components in asphalt relatively stable and less prone to further pyrolysis or cracking reactions.

Data availability statement

The original contributions presented in the study are included in the article/supplementary material, further inquiries can be directed to the corresponding authors.

Author contributions

RC: Writing–original draft. AS: Writing–review and editing. JW: Writing–review and editing.

Funding

The author(s) declare financial support was received for the research, authorship, and/or publication of this article. Supported by the Program Fund of Non-Metallic Excellence and Innovation Center for Building Materials, 2022TDA2-4.

Conflict of interest

The authors declare that the research was conducted in the absence of any commercial or financial relationships that could be construed as a potential conflict of interest.

Publisher's note

References

Abo-Qudais, S., and Al-Shweily, H. (2007). Effect of aggregate properties on asphalt mixtures stripping and creep behavior. *Constr. Build. Mater.* 21 (9), 1886–1898. doi:10.1016/j.conbuildmat.2005.07.014

Badre, S., Goncalves, C. C., Norinaga, K., Gustavson, G., and Mullins, O. C. (2006). Molecular size and weight of asphaltene and asphaltene solubility fractions from coals, crude oils and bitumen. *Fuel* 85 (1), 1–11. doi:10.1016/j.fuel.2005.05.021

Bowers, B. F., Huang, B., Shu, X., and Miller, B. C. (2014). Investigation of reclaimed asphalt pavement blending efficiency through GPC and FTIR. *Constr. Build. Mater.* 50, 517–523. doi:10.1016/j.conbuildmat.2013.10.003

Curtis, C. W., Ensley, K., and Epps, J. (1993). *Fundamental properties of asphalt-aggregate interactions including adhesion and absorption[R]. No. SHRP-A-341*. Washington, DC: National Research Council.

Dong, Z., Liu, Z., Wang, P., and Gong, X. (2017). Nanostructure characterization of asphalt-aggregate interface through molecular dynamics simulation and atomic force microscopy. *Fuel* 189, 155–163. doi:10.1016/j.fuel.2016.10.077

Guo, M., Tan, Y., Wang, L., and Hou, Y. (2017). Diffusion of asphaltene, resin, aromatic and saturate components of asphalt on mineral aggregates surface: molecular dynamics simulation. *Road Mater. Pavement Des.* 18 (3), 149–158. doi:10.1080/14680629.2017.1329870

Hou, Y., Sun, W., Das, P., Song, X., Wang, L., Ge, Z., et al. (2016). Coupled Navier–Stokes phase-field model to evaluate the microscopic phase separation in asphalt binder under thermal loading. *J. Mater. Civ. Eng.* 28 (10), 04016100. doi:10.1061/(asce)mt.1943-5533.0001581

Hou, Y., Wang, L., Pauli, T., and Sun, W. (2015). Investigation of the asphalt self-healing mechanism using a phase-field model. *J. Mater. Civ. Eng.* 27 (3), 04014118. doi:10.1061/(asce)mt.1943-5533.0001047

Hou, Y., Wang, L., Wang, D., Guo, M., Liu, P., and Yu, J. (2017). Characterization of bitumen micro-mechanical behaviors using AFM, phase dynamics theory and MD simulation. *Materials* 10 (2), 208. doi:10.3390/ma10020208

Hsu, C. S., Hendrickson, C. L., Rodgers, R. P., McKenna, A. M., and Marshall, A. G. (2011). Petroleomics: advanced molecular probe for petroleum heavy ends. *J. mass Spectrom.* 46 (4), 337–343. doi:10.1002/jms.1893

Menapace, I., Masad, E., Papavassiliou, G., and Kassem, E. (2016). Evaluation of ageing in asphalt cores using low-field nuclear magnetic resonance. *Int. J. Pavement Eng.* 17 (10), 847–860. doi:10.1080/10298436.2015.1019503

Qian, K., Robbins, W. K., Hughey, C. A., Cooper, H. J., Rodgers, R. P., and Marshall, A. G. (2001). Resolution and identification of elemental compositions for more than 3000 crude acids in heavy petroleum by negative-ion microelectrospray high-field Fourier transform ion cyclotron resonance mass spectrometry. *Energy and Fuels* 15 (6), 1505–1511. doi:10.1021/ef010111z

Qiu, J., Van de Ven, M., Wu, S., Yu, J., and Molenaar, A. (2012). Evaluating self healing capability of bituminous mastics. *Exp. Mech.* 52 (8), 1163–1171. doi:10.1007/s11340-011-9573-1

Shan, L., Tan, Y., Underwood, S., and Kim, Y. R. (2010). Application of thixotropy to analyze fatigue and healing characteristics of asphalt binder. *Transp. Res. Rec.* 2179 (1), 85–92. doi:10.3141/2179-10

Sun, D. Q., Zhang, L. W., and Zhang, X. L. (2011). Quantification of SBS content in SBS polymer modified asphalt by FTIR. *Trans. Tech. Publ.* 287, 953–960. doi:10.4028/www.scientific.net/amr.287-290.953

Tan, Y., and Guo, M. (2014). Micro-and nano-characteration of interaction between asphalt and filler. *J. Test. Eval.* 42 (5), 20130253–20131097. doi:10.1520/jte20130253

Wang, D., Baliello, A., Poulikakos, L., Vasconcelos, K., Kakar, M. R., Giancontieri, G., et al. (2022). Rheological properties of asphalt binder modified with waste polyethylene: an interlaboratory research from the RILEM TC WMR. *Resour. Conservation Recycl.* 186, 106564. doi:10.1016/j.resconrec.2022.106564

Wang, P., Dong, Z., Tan, Y., and Liu, Z. y. (2015). Investigating the interactions of the saturate, aromatic, resin, and asphaltene four fractions in asphalt binders by molecular simulations. *Energy and Fuels* 29 (1), 112–121. doi:10.1021/ef502172n

Xu, T., and Huang, X. (2010). Study on combustion mechanism of asphalt binder by using TG–FTIR technique. *Fuel* 89 (9), 2185–2190. doi:10.1016/j.fuel.2010.01.012

Zhang, F., Sha, A., Cao, Y., Wang, W., Song, R., and Jiao, W. (2023). Characterization of self-healing properties of asphalt pavement materials containing carbon nanotubes: from the binder and mix level based on grey relational analysis. *Constr. Build. Mater.* 404, 133323. doi:10.1016/j.conbuildmat.2023.133323

frontiers | Frontiers in Energy Research

TYPE Original Research
PUBLISHED 08 January 2024
DOI 10.3389/fenrg.2023.1348557

OPEN ACCESS

EDITED BY
Meng Jia,
Shandong University of Science and Technology, China

REVIEWED BY
Ziming Liu,
Tongji University, China
Jiaming Wu,
University of Jinan, China

*CORRESPONDENCE
Chuanhai Li,
15665716260@163.com

RECEIVED 03 December 2023
ACCEPTED 18 December 2023
PUBLISHED 08 January 2024

CITATION
Chu F, Li C, Wu C and Wang Y (2024), Research on the hydration process of solid waste–based cementitious materials and application in roadbase.
Front. Energy Res. 11:1348557.
doi: 10.3389/fenrg.2023.1348557

Research on the hydration process of solid waste–based cementitious materials and application in roadbase

Feng Chu[1], Chuanhai Li[2]*, Chuanshan Wu[1] and Yansheng Wang[3]

[1]Shandong Hi-speed Construction Management Group Co., Ltd., Jinan, China, [2]Shandong Hi-Speed Engineering Testing Co., Ltd., Jinan, China, [3]Geotechnical and Structural Engineering Research Center, Shandong University, Jinan, China

In order to improve the high-value utilization of industrial solid waste materials, this study prepared a solid waste–based cementitious material (SWCM) using slag, fly ash, desulfurization gypsum, and gangue. The mechanical strength and hydration process of the SWCM and an ordinary Portland cement (OPC) were studied. The results showed that the compressive strength of the SWCM was lower than that of OPC at 3 d, but the compressive strength exceeded that of OPC after 7 d. The isothermal calorimetry results showed that the induction period of the SWCM was five times that of OPC, and the total 4 d exothermic amount of OPC was 1.7 times that of the SWCM. XRD and SEM showed that the hydration products of the SWCM were mainly ettringite (AFt) and hydrated calcium silicate gel (C-S-H). The unconfined compressive strength and dry shrinkage of stabilized macadam were also studied by using the SWCM to replace OPC. The results indicated that the unconfined compressive strength of the SWCM-stabilized macadam is comparable to that of the OPC-stabilized macadam. The dry shrinkage strain was only 79.7% of the OPC-stabilized macadam.

KEYWORDS

SWCM, strength, microscopic characteristics, SWCM-stabilized macadam, unconfined compressive strength, flexural strength, dry shrinkage

1 Introduction

Portland cement is widely used in infrastructure construction due to abundance of its raw materials and low price, especially in the semi-rigid base layer of pavements (Dobiszewska et al., 2023; Griffiths et al., 2023; Guo et al., 2023). It has been estimated that more than 4,000 tons of cement is used for each kilometer of high-grade asphalt pavement base (Wiranata et al., 2022). The production of large quantities of Portland cement brings economic benefits while posing serious challenges to natural resources and the environment. Over the past few years, a great deal of attention has been given to the development of specialty cementitious materials that can reduce CO_2 emissions and lower energy and limestone consumption (Mo et al., 2017; Zhang et al., 2021; Sun et al., 2022a). At the same time, with the accelerating process of modernization, the emission of granulated blast furnace slag, desulfurization gypsum, fly ash, and other industrial solid wastes continues to increase (Zhao et al., 2016; Zhao et al., 2022; Xu et al., 2023). It is imperative to carry out the utilization of industrial solid waste to prepare environmentally friendly cementitious materials.

TABLE 1 Chemical content of raw materials (w/%).

	CaO	SiO_2	Al_2O_3	MgO	Fe_2O_3	SO_3	Loss
S95 Slag	44.71	29.29	14.85	7.33	0.39	1.28	2.15
Gangue	3.44	49.93	36.17	0.80	5.79	1.12	2.75
Desulfurization gypsum	35.35	1.56	0.80	0.35	0.12	44.74	17.08
Cement clinker	63.21	21.06	6.74	3.24	3.45	0.58	1.72

Granulated blast furnace slag is an industrial by-product obtained by quenching and cooling the molten residue of combustion in the ironmaking process, which has been widely used because of its high pozzolanic activity and latent hydraulicity (Matthes et al., 2018). As a typical aluminum silicate mineral, the main composition of slag is similar to that of Portland cement clinker, which is mainly a compound of CaO-Al_2O_3-SiO_2-MgO. With the increase in CaO and Al_2O_3, the contents of SiO_2 and TiO_2 decrease in slag, and the hydration process is gradually enhanced (Wang et al., 2022). Desulfurization gypsum is a by-product of flue gas desulfurization in power plants; the main component is $CaSO_4{\cdot}2H_2O$ (Koralegedara et al., 2019). Fly ash is the main solid waste from coal-fired power plants. Fly ash, as an additive to concrete, improves the plasticity and fluidity of concrete and increases its strength and durability (Grabias-Blicharz and Franus, 2023). In recent years, some studies have been conducted on the mechanism of shrinkage and enhancement behavior of desulfurization gypsum–slag–cement cementitious material for stabilized macadam (Li et al., 2017; Ju et al., 2019; Ou-Ming et al., 2019; Deng et al., 2020; Qing-qing, 2021; Qian et al., 2022). The results show that gypsum can promote the hydration reaction of slag. Besides, gypsum can promote the generation of ettringite (AFt) to achieve the micro-expansion of the volume to reduce shrinkage and deformation. Qing-qing (2021) found that compounding of fly ash and slag improved the mechanical properties and shrinkage characteristics of cement-stabilized macadam significantly. Ou-Ming et al. (2019) found that early strength and dry shrinkage could be improved by adding slag and gypsum to cement–lime–fly ash-stabilized macadam. The results show that the pozzolanic reaction is between slag and lime, and the dihydrate gypsum leads to the formation of a large number of AFt. At present, the technology of preparing solid waste–based cementitious materials (SWCMs) based on multi-source solid waste is becoming increasingly widespread, and the application of solid waste–based cementitious materials in road engineering is becoming more and more extensive.

In this study, S95 slag, desulfurization gypsum, and gangue were first used as the main components to prepare solid waste–based cementitious materials (SWCMs), and mechanical strength, hydration process, and hydration products were investigated. Then, the SWCM was used to prepare stabilized macadam materials, and the unconfined compressive strength, flexural strength, and dry shrinkage were studied. The research results provide a basis for the high-value utilization of solid waste materials. The use of SWCM has excellent mechanical strength and smaller dry shrinkage strain, providing reference for the design and performance evaluation of stabilized macadam.

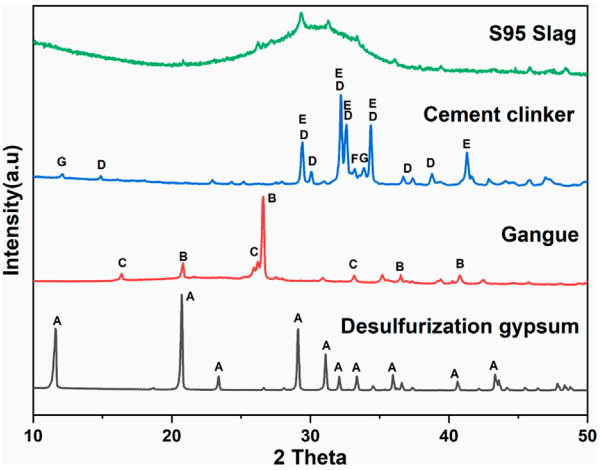

FIGURE 1
The XRD pattern of raw materials (A: $CaSO_4{\cdot}2H_2O$, B: SiO_2, C: Mullite, D: Alite, E: Belite, F: C_3A, and G: C_4AF).

2 Experimental program

2.1 Raw materials

S95 slag, desulfurization gypsum, gangue, and cement clinker were adopted in the experiment. The chemical compositions and mineral components are shown in Table 1 and Figure 1, respectively.

2.2 SWCM preparation and test procedure

2.2.1 Physical properties

According to the composition of the SWCM given in Table 2, the various types of raw materials in accordance with the proportion of mixing were ground in the ball mill for 1 h to obtain SWCM. The specimens were prepared in the size of 40 mm × 40 mm × 160 mm for mechanical properties according to the Chinese standard GB/T17671-1999 "Method of testing cements–Determination of strength". The samples were demolded after 48 h, and then maintained in water at 20°C ± 1°C. The compressive strength and flexural strengths were tested at 3 d, 7 d, and 28 d.

2.2.2 Calorimetry

The hydration heat evolution rate and total hydration heat emission of cementitious materials were measured by using an isothermal calorimeter (TAM Air) at 25 C within 100 h. All the experiments were performed at a W/C = 0.5 by mass. Furthermore,

TABLE 2 Composition of SWCM.

	Cement clinker	S95 slag	Gangue	Desulfurization gypsum
Proportion (%)	5	63	20	12

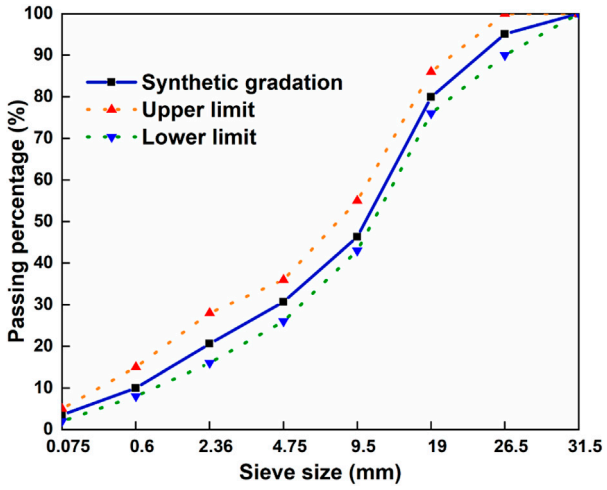

FIGURE 2
Gradation of mixtures.

2 g cement and 1 g water were placed into standard glass bottles and then put in the device. Then, the mixture was stirred quickly and put into the chamber to measure hydration heat.

2.2.3 Microstructure analysis

Sand-free hardened paste samples at 7 d and 28 d were taken for testing. The samples were immersed in anhydrous ethanol for 48 h to terminate the hydration reaction and then dried at 40°C for 48 h. XRD data were collected by using the Bruker AXS D8 Advance diffractometer device and collected in 2θ from 10° to 60°. SEM images were investigated using a Zeiss field emission scanning electron microscope.

2.3 Mixture preparation and experimental program

2.3.1 Mixture and sample preparation

Skeleton-dense gradation was used for preparing cement-stabilized macadam, and the gradation curve is shown in Figure 2. The cementitious materials were selected as 3%, 4%, 5%, and 6% by weight of the total aggregates. The mixed samples were compacted at different water content by using compaction methods in the Chinese standard JTG E51-2009. The optimum water content was determined on the basis of the curve of water content *versus* dry density. The detailed results of cement-stabilized macadam are given in Table 3.

2.3.2 7 d Unconfined compressive strength

The mechanical properties of cement-stabilized macadam were evaluated by using the unconfined compressive strength test. The dimensions of specimens were 150 mm in diameter and 150 mm in height. The specimens were tested at 20°C at a loading rate of 1 mm/min after the specimens were cured for 28 d under the standard condition. The unconfined compressive strength values were calculated according to the respective failure loads. Nine replicate specimens were be tested to ensure the reliability and accuracy of every average result.

2.3.3 Flexural strength

All the specimens were prepared by compacting at the respective maximum dry density and optimum moisture content. A series of beam specimens with the size of 100 mm × 100 mm × 400 mm were used to determine the flexural strength. The specimens were tested at 20°C at a loading rate of 0.05 mm/min after the specimens were cured for 28 d under the standard condition. Six replicate specimens were tested to ensure the reliability and accuracy of every average result. The test apparatus of flexural strength is presented in Figure 3.

2.3.4 Dry shrinkage

The specimens for the dry shrinkage test were made into transoms of 100 mm × 100 mm × 400 mm. After the samples were cured at standard conditions for 7 d, they were moved to the environment room at 20°C and 60% RH for the dry shrinkage test. The samples were placed and secured in the retraction equipment as shown in Figure 4, and the data were recorded continuously for 30 d. These data were used to get the water loss rate and dry shrinkage strain based on Eq. 1 and Eq. 2, respectively.

$$\text{Water loss rate: } w_i = (m_i - m_{i+1})/m_p, \quad (1)$$

$$\text{Dry shrinkage strain: } \varepsilon_i = (\overline{X_i} - \overline{X_{i+1}})/L0, \quad (2)$$

where w_i is the water loss rate of the i-th test; m_i is the i-th tested mass of the specimen; m_p is the mass of the dried specimens; ε_i is the dry shrinkage strain of the i-th test; X_i is the length of the i-th measurement; and $L0$ is the length of the specimen.

3 Results and discussion

3.1 Mechanical strength

The mechanical strength of cementitious materials is shown in Figure 5. As shown, the compressive strength of the SWCM increases with the curing days, the early strength is lower than that of ordinary Portland cement (OPC), but the later strength exceeds that of OPC. The compressive strength of the SWCM is much lower than that of OPC, with a compressive strength of 14.3 MPa at 3 d. The compressive strength of the SWCM is higher than that of OPC after 7 d. The compressive strength of the SWCM reaches 52.3 MPa, which is 12.2% higher than that of

TABLE 3 Compaction test results of stabilized macadam.

Cementitious material content (%)	SWCM		OPC	
	Optimum water content (%)	Maximum dry density (g/cm^3)	Optimum water content (%)	Maximum dry density (g/cm^3)
3	3.8	2.307	3.6	2.310
4	4.7	2.315	4.4	2.318
5	5.5	2.324	5.5	2.327
6	6.2	2.333	5.9	2.335

According to the above maximum dry density and optimum water content, the mixtures were filled into the molds and compacted by using a static compression machine to achieve 98% maximum dry density. The compacted samples were demolded after 24 h.

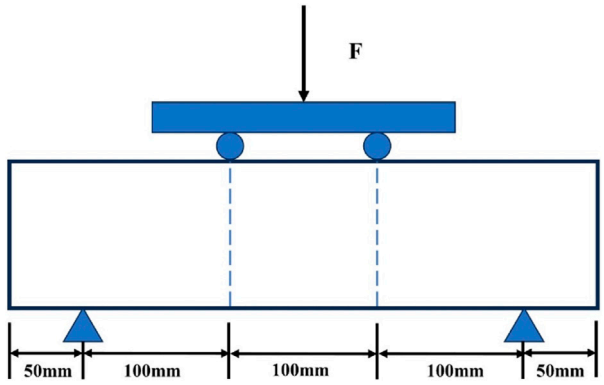

FIGURE 3
Schematic representation of the flexural strength test.

FIGURE 4
Drying shrinkage measuring instrument.

OPC at 28 d. The increased regulation of flexural strength is similar to that of compressive strength, and the flexural strength gradually increases with curing age. The early flexural strength of the SWCM is comparable to that of OPC, and after curing for 7 d, the flexural strength becomes much higher than that of OPC, reaching 6.8 MPa. The flexural strength at 28 d is 9.2 MPa, which is 22.7% higher than that of OPC. Comparing the two cementitious materials, the flexural and compressive strength ratios of the SWCM is higher than that of OPC at all ages, which is attributed to its higher flexural strength.

3.2 Isothermal calorimetric method

The hydration process of the SWCM and OPC can be monitored by using the isothermal calorimetric method, in which the hydration process is reflected by hydration heat flow and total heat. The hydration heat flow and total heat of the SWCM and OPC within 100 h are shown in Figure 6. It can be seen that the hydration rate of the SWCM is slower and less exothermic than that of OPC. The hydration heat flow of the SWCM and OPC is very high during the first minutes, which is mainly attributed to ionic dissolution and the reaction of calcium aluminate with gypsum. After the initial hydration period, the heat flow becomes slower, and the hydration reaction enters the induction period. The induction period of the SWCM is very long, approximately 30 h, which is about five times longer than that of OPC, which is approximately 6 h. The second exothermic peak of the hydration reaction follows the accelerated period, and the second exothermic peak of OPC occurs at 23 h, with a heat flow value of 1.88 mw/g. However, the second exothermic peak of the SWCM is prolonged and is approximately 17 h, and the heat flow value is 1.09 mw/g at 40 h. Then, the heat flow value of the SWCM is higher than that of OPC. The total heat of OPC before 10 h is low, while it increases greatly later. The exothermic heat of the SWCM hydration exceeds 250 J/g within 100 h. Before approximately 35 h, the total heat of the SWCM is low, up to 100 h, and its total heat reaches 150 J/g, which is approximately 60% that of OPC. Lower exothermic hydration can reduce temperature stress and maintain specimen volume stability.

3.3 Microstructure of pastes

Figure 7 represents the XRD patterns of SWCM and OPC pastes at the curing age of 7 d and 28 d, respectively. For OPC, the main crystalline product of hydration is calcium hydroxide (CH), and with the prolongation of the hydration, the diffraction peaks of silicate minerals weaken, while the diffraction peaks of CH continue to increase. It can be seen that the main crystal hydration products of SWCM pastes at 7 d are AFt and unreacted gypsum. The AFt

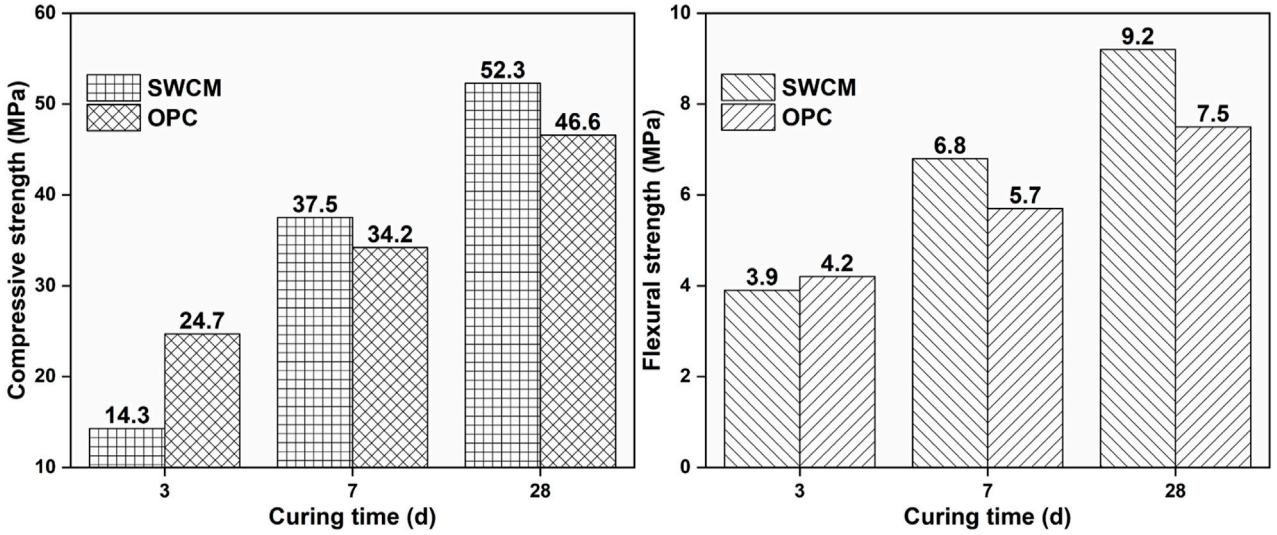

FIGURE 5
Mechanical strength of SWCM and OPC.

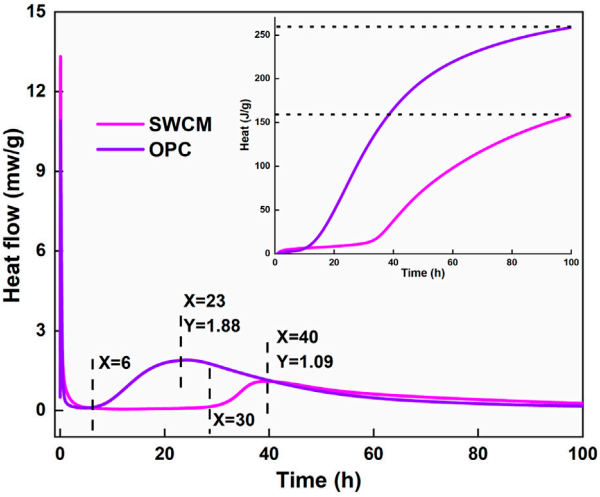

FIGURE 6
Isothermal calorimetric measurements of SWCM and OPC.

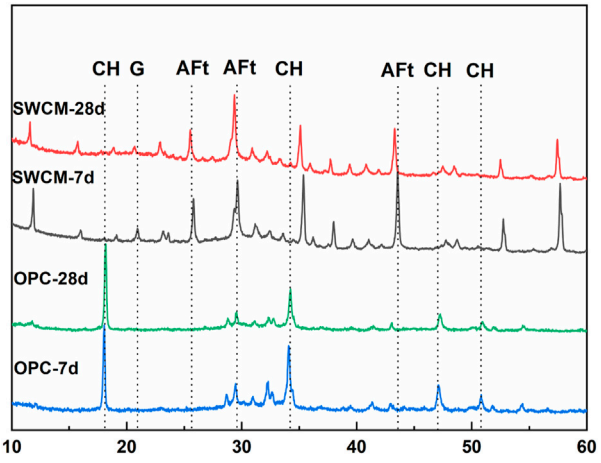

FIGURE 7
XRD patterns of samples in different curing ages.

diffraction peak of the SWCM specimen enhances and the gypsum diffraction peak weakens at the curing age of 28 d, which indicates that a large amount of gypsum is consumed to produce AFt. According to Figure 6, the hydration reactivity of the SWCM is very slow at an early age, which affects the formation of hydration products.

Figure 8 shows the morphology of hydration products of OPC and the SWCM at 7 d and 28 d, respectively. A large amount of hexagonal-like CH and a small amount of needle-like AFt are presented on the surface of the OPC specimens at 7 d, while a large amount of unreacted cement clinker is embedded in the pastes. This is in agreement with the XRD results given in Figure 7. For the SWCM, the needle-like AFt is found to grow up and fill the pores in the pastes under SEM. Besides, a lot of C-S-H gel is also found at 28 d, and the needle-like AFt is wrapped by C-S-H gel, forming a relatively denser structure. A large number of needle-like AFt forms a spatial reticulation structure, reaching the role of fiber reinforcement and improving the flexural strength, which also reveals the reason for the high ratio of flexural and compressive strength of the SWCM.

The SWCM is a cementitious material that utilizes gypsum and CH to activate the potential hydraulic reactivity of slag to produce AFt, which improves flexural strength and achieves micro-expansion (Liu et al., 2019; Liu et al., 2020). The simplified hydration process of the SWCM is demonstrated in Eq. 3 (Angulski da Luz and Hooton, 2019). A proportion of cement clinker occurs initially encountering water, providing CH, which promotes the dissolution of Ca^{2+} and Al^{3+} in the slag. The reactive

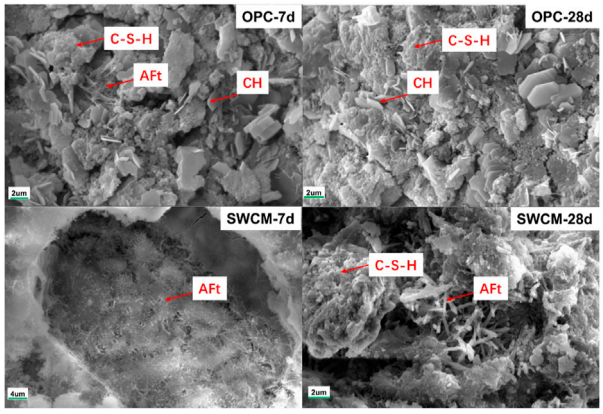

FIGURE 8
Samples in different curing ages under SEM.

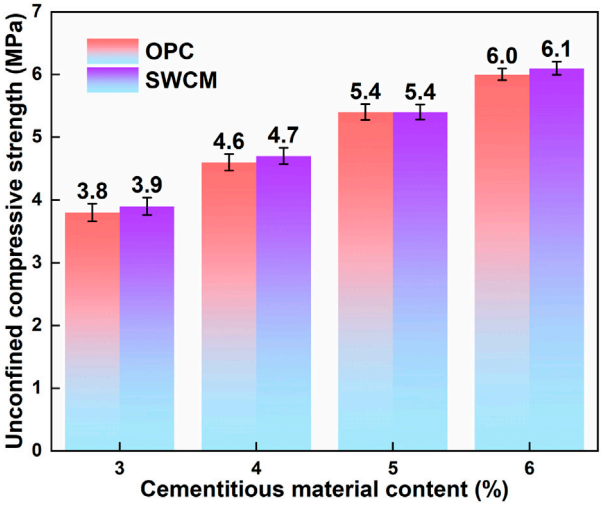

FIGURE 9
Relationship between unconfined compressive strength and cementitious material type and content.

Ca^{2+} and Al^{3+} react with the calcium sulfate from gypsum forming AFt and C-S-H gel.

$$C_5S_3A + CH + C\$ + H \rightarrow C - S - H + AFt. \quad (3)$$

3.4 7 d Unconfined compressive strength

Figure 9 shows the unconfined compressive strength of samples with different cementitious materials. It can be seen from Figure 9 that the 7 d unconfined compressive strength is increased with increasing content of cementitious materials. The strength representative value of the specimen reaches 4.7 MPa when the dosage of the SWCM is 4%, which is comparable to OPC-stabilized macadam. All of the specimens satisfy the strength requirements for roadbases of highways in the Technical Guidelines for Construction

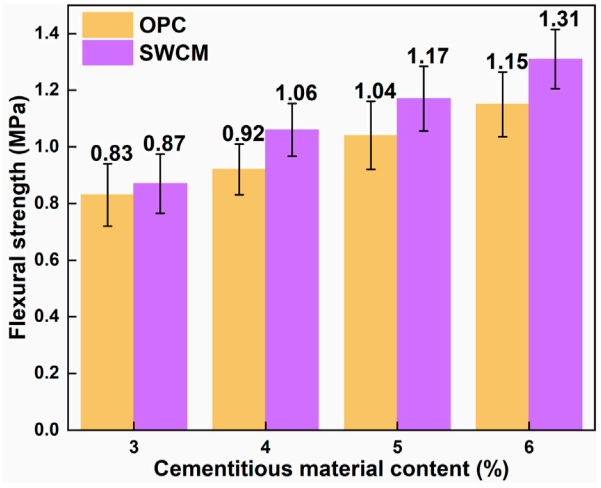

FIGURE 10
Relationship between flexural tensile strength and cementitious material type and content.

of Highway Roadbases (JTG/T F20-2015). The strength value of the stabilizing macadam mainly depends on the following three aspects (Liang et al., 2020): first, the skeleton embedding effect between coarse aggregates; second, the filling effect of fine aggregates; and third, the bonding effect from the cementitious material and the aggregates. Under the same condition of grading, the increase in binder dosage improves the bonding effect between the cementitious material and aggregates, which makes the 7 d unconfined compressive strength value of the specimen increase further. Comparing the two cementitious materials, the representative values of the unconfined compressive strength of SWCM-stabilized aggregates at the same dosage are comparable to that of OPC.

3.5 Flexural strength

Figure 10 \shows that the cementitious material is one of the important factors affecting the flexural strength of stabilizing macadam materials. The flexural strength of the stabilizing macadam increases linearly with increasing content of cementitious materials. The flexural strength of the OPC-stabilized macadam increases from 0.83 MPa to 1.15 MPa when the OPC content increases from 3% to 6%, a 38.5% increase. The flexural strength of the SWCM-stabilized macadam increases from 0.87 MPa to 1.31 MPa when the SWCM content increases from 3% to 6%, a 33.5% increase. Comparing the results of the flexural tensile strength of the two cementitious material-stabilized macadam, the ability of SWCM-stabilized macadam materials to resist bending and tensile deformation is better than that of OPC-stabilized cement, and the bending and tensile strength of the SWCM-stabilized macadam are increased by approximately 15% at the dosage of 4%, which is related to the hydration products of the two cementitious materials. This is corroborated by the SEM and XRD results.

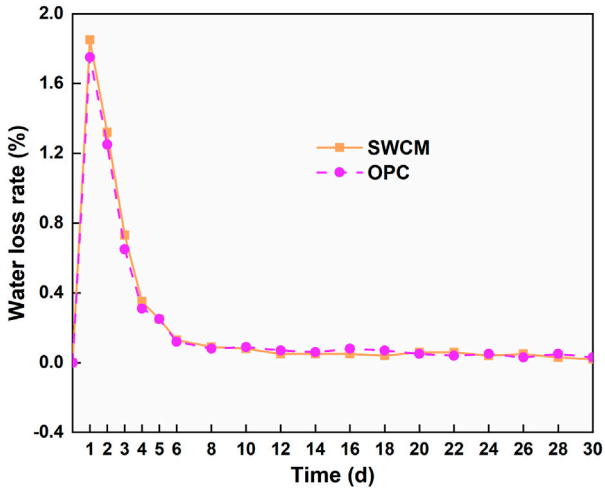

FIGURE 11
Water loss rate of the dry shrinkage test.

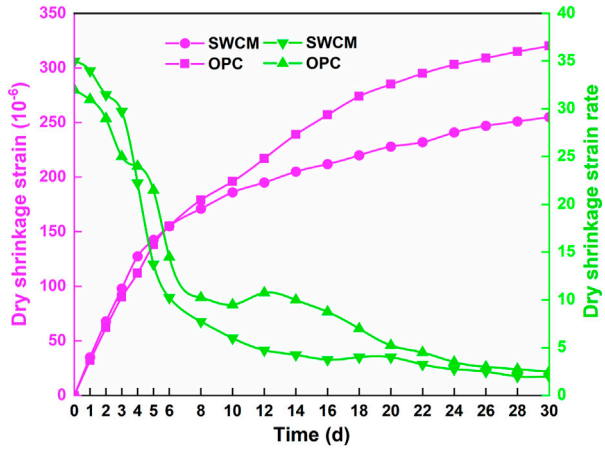

FIGURE 12
Variation of dry shrinkage strain and dry shrinkage strain rate with time.

3.6 Dry shrinkage

The dry shrinkage is an important index to measure the crack resistance and deformation characteristics of stabilized macadam, so it is necessary to analyze the dry shrinkage property of cement-stabilized macadam (Sun et al., 2022b). In this study, we compared the dry shrinkage property of SWCM-stabilized macadam and OPC-stabilized macadam by using 4% of the cementitious material as an example.

Figure 11 shows the results of water loss with age for the two cementitious material-stabilized macadam. Most of the water loss occurs in the first 6 days of the dry shrinkage test and decreases with the extension of the test age. The rate of water loss decreases gradually at the early age and stabilizes at the later age. This is due to the fact that the cement-stabilized macadam specimens contain free water, which evaporates first, followed by capillary water, resulting in a higher rate of water loss at the early test. The water loss rate of SWCM-stabilized macadam is higher than that of OPC-stabilized macadam at the early test, which is caused by its high optimum water content.

Figure 12 shows the variation of dry shrinkage strain and dry shrinkage strain rate with time for the two cementitious material-stabilized macadam. The dry shrinkage strain rate is the first-order derivative of the dry shrinkage strain, and the larger the value, the faster the change of dry shrinkage strain. From the results shown in Figure 12, it can be seen that the dry shrinkage strain increases gradually with an increase in curing age, and the dry shrinkage strain rate decreases gradually. This indicates that the dry shrinkage strain tends to level off, which is more obvious after the 10th day. The SWCM-stabilized macadam is a much smaller dry shrinkage strain than OPC-stabilized macadam. The difference between the two cementitious material-stabilized macadam increases with time. At the end of the test, the dry shrinkage strain of the SWCM-stabilized macadam is 255×10^{-6}, which is only 79.7% of the dry shrinkage strain of the OPC-stabilized macadam, which is 320×10^{-6}. The dry shrinkage strain is related to the hydration products of cementitious materials, and the composition of the hydration products of the SWCM materials is different from that of OPC.

4 Conclusion

In this work, SWCM is prepared by using slag, fly ash, desulfurization gypsum, and gangue. In the process of further discussing the unconfined compressive strength, flexural tensile strength, and dry shrinkage of stabilizing macadam, the following conclusions can be drawn:

(1) The compressive strength of the SWCM increases with the curing days, the early strength is lower than that of OPC, but later the strength exceeds that of OPC.
(2) The hydration rate of the SWCM is slower and less exothermic than that of OPC. The exothermic heat of hydration of the SWCM is approximately 60% that of OPC within 100 h.
(3) Microstructure results show that the hydration products of the SWCM are mainly AFt and C-S-H gel, and a large number of AFt intertwines to form a skeleton, which improves the bending and tensile strength.
(4) The 7 d unconfined compressive strength of the SWCM-stabilized macadam material is comparable to that of the OPC-stabilized macadam, and the 7 d unconfined compressive strength of the 4% SWCM meets the specification of roadbases' strength requirements.
(5) The ability of the SWCM-stabilized macadam to resist bending and tensile deformation is better than that of OPC-stabilized macadam, and the bending and tensile strength are increased by approximately 15% at the dosage of 4%.
(6) SWCM-stabilized macadam is a much smaller dry shrinkage strain than OPC-stabilized macadam. The dry shrinkage strain of SWCM-stabilized macadam is only 79.7% of OPC-stabilized macadam.

Data availability statement

The original contributions presented in the study are included in the article/Supplementary Material; further inquiries can be directed to the corresponding author.

Author contributions

FC: Data curation, investigation, methodology, and manuscript writing–original draft. CL: Conceptualization and manuscript writing–review and editing. CW: Data curation, investigation, methodology, and manuscript writing–original draft. YW: Conceptualization, formal analysis, project administration, and manuscript writing–review and editing.

Funding

The authors declare that financial support was received for the research, authorship, and/or publication of this article. This study was financially supported by the Shandong Province Key R&D Program (Major Technological Innovation) (No. 2020CXGC011405). The authors gratefully acknowledge their financial support.

Conflict of interest

Authors FC and CW were employed by Shandong Hi-speed Construction Management Group Co., Ltd. Author CL was employed by Shandong Hi-Speed Engineering Testing Co., Ltd.

The remaining authors declare that the research was conducted in the absence of any commercial or financial relationships that could be construed as a potential conflict of interest.

Publisher's note

References

Angulski da Luz, C., and Hooton, R. D. (2019). Influence of supersulfated cement composition on hydration process. *J. Mater. Civ. Eng.* 31 (6), 04019090. doi:10.1061/(asce)mt.1943-5533.0002720

Deng, C., Jiang, Y., Yuan, K., Tian, T., and Yi, Y. (2020). Mechanical properties of vertical vibration compacted lime–fly ash-stabilized macadam material. *Constr. Build. Mater.* 251, 119089. doi:10.1016/j.conbuildmat.2020.119089

Dobiszewska, M., Bagcal, O., Beycioğlu, A., Goulias, D., Köksal, F., Płomiński, B., et al. (2023). Utilization of rock dust as cement replacement in cement composites: an alternative approach to sustainable mortar and concrete productions. *J. Build. Eng.* 69, 106180. doi:10.1016/j.jobe.2023.106180

Grabias-Blicharz, E., and Franus, W. (2023). A critical review on mechanochemical processing of fly ash and fly ash-derived materials. *Sci. Total Environ.* 860, 160529. doi:10.1016/j.scitotenv.2022.160529

Griffiths, S., Sovacool, B. K., Del Rio, D. D. F., Foley, A. M., Bazilian, M. D., Kim, J., et al. (2023). Decarbonizing the cement and concrete industry: a systematic review of socio-technical systems, technological innovations, and policy options. *Renew. Sustain. Energy Rev.* 180, 113291. doi:10.1016/j.rser.2023.113291

Guo, Y., Luo, L., Liu, T., Hao, L., Li, Y., Liu, P., et al. (2023). A review of low-carbon technologies and projects for the global cement industry. *J. Environ. Sci.* 136, 682–697. doi:10.1016/j.jes.2023.01.021

Ju, C., Liu, Y., Yu, Z., and Yang, Y. (2019). Cement-lime-fly ash bound macadam pavement base material with enhanced early-age strength and suppressed drying shrinkage via incorporation of slag and gypsum. *Adv. Civ. Eng.* 2019, 1–10. doi:10.1155/2019/8198021

Koralegedara, N. H., Pinto, P. X., Dionysiou, D. D., and Al-Abed, S. R. (2019). Recent advances in flue gas desulfurization gypsum processes and applications–A review. *J. Environ. Manag.* 251, 109572. doi:10.1016/j.jenvman.2019.109572

Li, W., Lang, L., Lin, Z., Wang, Z., and Zhang, F. (2017). Characteristics of dry shrinkage and temperature shrinkage of cement-stabilized steel slag. *Constr. Build. Mater.* 134, 540–548. doi:10.1016/j.conbuildmat.2016.12.214

Liang, C., Wang, Y., Tan, G., Zhang, L., Zhang, Y., and Yu, Z. (2020). Analysis of internal structure of cement-stabilized macadam based on industrial CT scanning. *Adv. Mater. Sci. Eng.* 2020, 1–10. doi:10.1155/2020/5265243

Liu, S., Fang, P., Ren, J., and Li, S. (2020). Application of lime neutralised phosphogypsum in supersulfated cement. *J. Clean. Prod.* 272, 122660. doi:10.1016/j.jclepro.2020.122660

Liu, S., Wang, L., and Yu, B. (2019). Effect of modified phosphogypsum on the hydration properties of the phosphogypsum-based supersulfated cement. *Constr. Build. Mater.* 214, 9–16. doi:10.1016/j.conbuildmat.2019.04.052

Matthes, W., Vollpracht, A., Villagrán, Y., Kamali-Bernard, S., Hooton, D., and Gruyaert, E. (2018). Ground granulated blast-furnace slag. Properties of fresh and hardened concrete containing supplementary cementitious materials: state-of-the-art report of the RILEM technical committee 238-SCM. *Work. Group* 4, 1–53. doi:10.1007/978-3-319-70606-1_1

Mo, L., Zhang, F., Panesar, D. K., and Deng, M. (2017). Development of low-carbon cementitious materials via carbonating Portland cement–fly ash–magnesia blends under various curing scenarios: a comparative study. *J. Clean. Prod.* 163, 252–261. doi:10.1016/j.jclepro.2016.01.066

Ou-Ming, X. U., Shi-Heng, W., Min, B., Xuan, L., and Lian-Cheng, Z. (2019). Influence of fly ash and granulated blast furnace slag on strength and shrinkage characteristics of cement stabilized crushed stone. *J. Guangxi Univ. Nat Sci Ed)* 44 (2), 509–515. doi:10.13624/j.cnki.issn.1001-7445.2019.0509

Qian, G., Zhong, Y., Li, X., Peng, H., Su, J., and Huang, Z. (2022). Experimental study on the road performance of high content of phosphogypsum in the lime–fly ash mixture. *Front. Mater.* 9, 935113. doi:10.3389/fmats.2022.935113

Qing-qing, L. U. (2021). Strength enhancement and shrinkage reduction mechanism of desulfurized gypsum cement stabilized aggregates. *J. Jilin Univ. Technol. Ed.* 51 (1), 252–258. doi:10.13229/j.cnki.jdxbgxb20200242

Sun, C., Zhang, J., Yan, C., Yin, L., Wang, X., and Liu, S. (2022a). Hydration characteristics of low carbon cementitious materials with multiple solid wastes. *Constr. Build. Mater.* 322, 126366. doi:10.1016/j.conbuildmat.2022.126366

Sun, Y., Li, L., Liao, J., and Huang, C. (2022b). Dry shrinkage performance of cement-stabilized reclaimed lime-fly ash macadam. *Constr. Build. Mater.* 331, 127332. doi:10.1016/j.conbuildmat.2022.127332

Wang, Y., Xu, L., He, X., Su, Y., Miao, W., Strnadel, B., et al. (2022). Hydration and rheology of activated ultra-fine ground granulated blast furnace slag with carbide slag and anhydrous phosphogypsum. *Cem. Concr. Compos.* 133, 104727. doi:10.1016/j.cemconcomp.2022.104727

Wiranata, D. Y., Yang, S. H., Akgul, C. M., Hsien, H. Y., and Nugraha, M. Z. P. (2022). Use of coal ash cement stabilized material as pavement base material: laboratory characterization and field evaluation. *Constr. Build. Mater.* 344, 128055. doi:10.1016/j.conbuildmat.2022.128055

Xu, L., Wang, J., Li, K., Li, M., Lin, S., Hao, T., et al. (2023). Investigations on the rehydration of recycled blended SCMs cement. *Cem. Concr. Res.* 163, 107036. doi:10.1016/j.cemconres.2022.107036

Zhang, J., Tan, H., Bao, M., Liu, X., Luo, Z., and Wang, P. (2021). Low carbon cementitious materials: sodium sulfate activated ultra-fine slag/fly ash blends at ambient temperature. *J. Clean. Prod.* 280, 124363. doi:10.1016/j.jclepro.2020.124363

Zhao, H. X., Zhou, F. S., Lm, A. E., Liu, J. L., and Zhou, Y. (2022). A review on the industrial solid waste application in pelletizing additives: composition, mechanism and process characteristics. *J. Hazard. Mater.* 423, 127056. doi:10.1016/j.jhazmat.2021.127056

Zhao, J., Wang, D., Yan, P., Zhang, D., and Wang, H. (2016). Self-cementitious property of steel slag powder blended with gypsum. *Constr. Build. Mater.* 113, 835–842. doi:10.1016/j.conbuildmat.2016.03.102

frontiers | Frontiers in Energy Research

TYPE Original Research
PUBLISHED 11 January 2024
DOI 10.3389/fenrg.2023.1352383

OPEN ACCESS

EDITED BY
Meng Jia,
Shandong University of Science and Technology, China

REVIEWED BY
Xingliang Liu,
Chongqing Jiaotong University, China
Lin Tian,
Yantai University, China

*CORRESPONDENCE
Yaping Dong,
yapingdong@xupt.edu.cn
Jinliang Xu,
xujinliang@chd.edu.cn

RECEIVED 08 December 2023
ACCEPTED 20 December 2023
PUBLISHED 11 January 2024

CITATION
Dong Y, Li T and Xu J (2024), Modeling of vehicle carbon emissions on horizontal curve road sections.
Front. Energy Res. 11:1352383.
doi: 10.3389/fenrg.2023.1352383

Modeling of vehicle carbon emissions on horizontal curve road sections

Yaping Dong[1]*, Tong Li[1] and Jinliang Xu[2]*

[1]School of Modern Post, Xi'an University of Posts and Telecommunications, Xi'an, China, [2]School of Highway, Chang'an University, Xi'an, China

The high carbon emissions of vehicles traveling on horizontal curve road sections cannot be ignored. Facing the difficulty of accurately quantifying the carbon emission of driving on horizontal curves and the unknown causes of high carbon emission, this study proposes to construct a carbon emission prediction model applicable to road sections with different planar geometries. The direct and indirect effects of horizontal curve alignment on vehicle carbon emissions are represented in the model in terms of travel stabilization and speed changes, respectively. A lateral force coefficient parameter was introduced into the model to integrate the carbon emission quantification problem for different planar geometry sections. Meanwhile, field tests were conducted to assess the reliability of the model and the research findings. The model reveals that the geometric parameters of horizontal curves that affect carbon emissions are the radius of the circular curve, the superelevation, and the length of the gentle curve. The root causes of high carbon emissions on horizontal curve road sections are curve driving resistance and speed fluctuations. Under the free-flow driving condition of the highway, the maximum curve radius affecting the carbon emissions of passenger cars and trucks is 400 m and 550 m, respectively. The research results can realize the carbon emission quantification of vehicles on the road sections with different plane geometries. Also, it is helpful to control the high carbon emission of vehicles traveling on horizontal curve road sections.

KEYWORDS

horizontal curve section, radius, superelevation, lateral force coefficient, carbon emission, circular curve, transition curve

1 Introduction

The higher carbon emissions typically emitted by vehicles on curved roads have attracted the attention of scholars. Actual road projects have a variety of planar geometries, different values of plane geometry indicators, and varying vehicle speeds (Wang et al., 2019). The mechanisms of these factors on carbon emissions are yet to be explored. If we can accurately assess the quantitative impact of horizontal curve alignment on vehicle carbon emissions, explain the causal mechanism of high carbon emissions from curved roadway travel, and reveal the controllable influencing factors, it will help to mitigate the high carbon emissions caused by road horizontal curve alignment, which will bring long-lasting and significant economic and environmental benefits.

Existing research on vehicle carbon emission prediction has formed a more authoritative database and a mature theoretical framework, including the physical model represented by CMEM (Ataei et al., 2021), and the statistical model represented

by MOVES (Lin et al., 2019). Pan et al. (2020) implemented a gradient-enhanced regression tree-based algorithm to predict the carbon emissions of new energy buses on longitudinal slopes section over the fuel cycle. Moradi and Miranda-moreno. (2020) used a support vector regression algorithm to establish a vehicle fuel consumption model parameterized by speed, acceleration, and longitudinal slope gradient. Existing vehicle carbon emission models focus on the high carbon emissions emitted by vehicles traveling uphill, and lack the consideration of the geometric alignment of horizontal curves, thus limiting the accurate prediction of carbon emissions from vehicles traveling on curved roads.

The geometric linearity of horizontal curves is strongly associated with increased vehicle carbon emissions (Ding and Jin, 2018). Vehicle kinematics theory indicates that vehicles are subjected to centrifugal forces when traveling on curved roadways. Given a constant speed, the smaller the radius of the curve, the greater the centrifugal force on the vehicle. Centrifugal forces can affect the vehicle's lateral stability and driving comfort, and can even cause the driver to slow down before entering a curve (Fitzpatrick et al., 2000). Ko. (2015) used MOVES to model the incremental carbon emissions caused by speed fluctuations of a passenger car on a flat curved roadway. David et al. (2018) obtained a statistical model of vehicle carbon emissions on horizontal curve road sections by regressing measured data with curvature change rate, average speed, and its deviation as parameters. Dong et al. (2019) measured the carbon emission rate of diesel trucks with different curve radius on the highway, concluded that when the radius of the circular curve is greater than 500 m, the vehicle speed is stably close to 100 km/h, and the incremental carbon emission caused by the micro-change of the vehicle speed is very small, and the vehicle carbon emission is almost equal to that of the flat straight road section. Zhang et al. (2019) obtained the carbon emission of a heavy-duty diesel vehicle on a circular curve section without superelevation by conducting real measurements and MOVES simulations on a flat straight road, and pointed out that the carbon emission decreases with the increase of curve radius. The critical curve radius that affects carbon emission is 550 m.

The stability of driving on curved roads affects the driving energy of the vehicle (Zhang et al., 2016), generating corresponding carbon emissions. From the perspective of driving dynamics, the additional cornering resistance of a vehicle, also known as curve driving resistance, is mainly determined by the road surface friction coefficient, wheel angle, and tire load (Peng et al., 2020). The actual horizontal curve road section is usually accompanied by a superelevation, which will reduce the lateral force coefficient of the curved road (Yin et al., 2020). The effect of the installation of superelevation on the curve driving resistance and carbon emissions is currently unknown.

After years of in-depth research, scholars have constructed a clear theoretical framework of vehicle carbon emissions and carried out empirical studies on the high carbon emission patterns of traveling vehicles on curved roads. The results of the study show that the horizontal curve alignment is closely related to vehicle carbon emissions. The direct effect of the horizontal curve line shape on carbon emissions lies in the stability of the vehicle, and the indirect effect lies in the change of operating speed. There is a clear path of research and good progress has been made, however there are still some issues to be resolved. Firstly, there are various plane geometry indicators, which make it more difficult to quantify the carbon emission of vehicles on different plane line conditions. Second, the mechanism of high carbon emissions from traveling on curved roads is not yet clear. These are the challenges that this study is dedicated to solving. As a result, this study is committed to constructing a prediction model of vehicle carbon emissions on horizontal curve sections of roads, and revealing the causal mechanism of high carbon emissions of traveling vehicles on curved roads.

The structure of this manuscript is organized as follows. In section 2, a theoretical model of carbon emission of vehicles traveling on curved roads is constructed, a simplified field test scheme for horizontal curve road sections is derived and proposed, and then field tests are conducted to collect carbon emission data. In section 3, based on the field measurement data, the minimum radius values affecting the carbon emissions of passenger cars and trucks are clarified, and the prediction effectiveness of the vehicle carbon emission model is evaluated. In section 4, a consistent comparison with existing research results is made, and the findings and limitations of the study are briefly summarized. The conclusion section summarizes the research results and their significance.

2 Methods

A combination of theoretical analysis and field trials was used to ensure the reliability of the findings. Specifically, a theoretical model of vehicle carbon emissions on horizontal curve road sections was established through theoretical derivation, revealing the influence mechanism of plane geometry indicators on vehicle carbon emissions. Through the rational design of the field test program, the field test is carried out to measure the carbon emissions of the vehicles on the actual curved roads. Then analyze the change rule of carbon emission of vehicles driving on the curved road. The accuracy of the model prediction is also evaluated with the test data.

2.1 Theoretical modeling of carbon emissions from traveling vehicles on curved roads

The direct effect of road geometry on vehicle carbon emissions lies in the stability of traveling vehicles, and the indirect effect is reflected in the operating speed fluctuation. This study reveals the effect of plane geometry metrics on carbon emissions by analyzing the stability of a vehicle at a constant speed. On the other hand, the carbon emission model of variable-speed traveling on curved roads was developed to reveal the carbon emission rules caused by speed changes under the influence of road alignment.

2.1.1 Direct effect of horizontal curve alignment on vehicle carbon emissions

To ensure the lateral stability and smoothness of traveling, the circular curve will be designed to be superelevated in the lateral

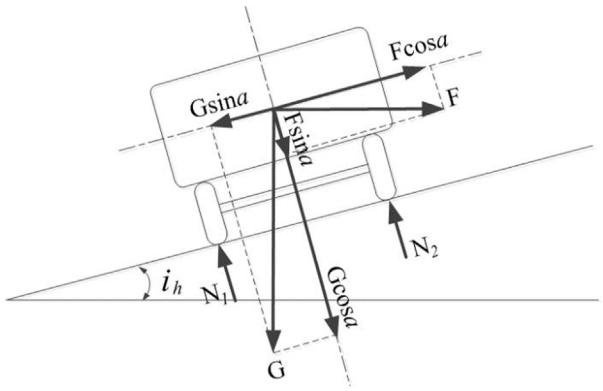

FIGURE 1
Force analysis of a vehicle on a circular curve with an superelevation setting.

direction. On the circular curve segments on the horizontal curve, the superelevation cross slope reaches the full superelevation form. The force analysis of a vehicle is shown in Figure 1. The force balance of the vehicle is as shown in Eq. 1.

$$F\cos\alpha - G\sin\alpha = m\mu \tag{1}$$

The lateral inclination of the roadway is generally small, and $\sin\alpha \approx \tan\alpha = i_h$, $\cos\alpha = 1$. where i_h is the value of superelevation. The lateral force coefficient can be calculated from Eq. 2 on circular curved roadway sections with superelevation (AASHTO, 2011).

$$\mu = \frac{V^2}{gR} - i_h \tag{2}$$

Setting the superelevation on the circular curve can offset all or part of the centrifugal force, and the remaining centrifugal force is balanced by the side deflection force acting on the front and rear tires, and the total side deflection force acting on the tires can be calculated by Eq. 3.

$$F_L = mg\mu = \frac{mV^2}{R} - mgi_h \tag{3}$$

A tire produces a lateral deflection angle under the action of a lateral deflection force. For the force on a single tire, the cornering stiffness C_a is usually used to characterize the lateral deflection force corresponding to a 1 rad lateral deflection angle, which reflects the deformation characteristics of the tire (You and Jeong, 2002), as shown in Eq. 4.

$$F_L = C_a\partial \tag{4}$$

where C_a represents tire cornering stiffness (kN/rad). ∂ refers to the tire side deflection angle (rad).

When the vehicle is accurately steered, the centrifugal acceleration is less than 0.4 g, the tire turning stiffness can be regarded as a constant, and the side deflection force and side deflection angle have a linear positive correlation with the turning stiffness as a scaling factor. In this case, the side deflection force is in the range of 0–2000 N and the side deflection angle is less than 3°. (Mitschke and Wallentowitz, 2014).

$$F_{yf} = \frac{(mV^2/R - mgi_h)L_r}{L} \tag{5}$$

$$F_{yr} = \frac{(mV^2/R - mgi_h)L_f}{L} \tag{6}$$

The problem of stability of a vehicle traveling on a curved road is determined by the lateral dynamic characteristics. In the vehicle monorail model shown in Figure 2, the dynamic response of the vehicle is Eq. 7.

$$\begin{cases} mV(\dot\beta+\dot\varphi)\sin\beta - m\dot V\cos\beta + F_{xr} + F_{xf}\cos\delta - F_{yf}\sin\delta - F_r - F_a = 0 \\ mV(\dot\beta+\dot\varphi)\cos\beta + m\dot V\sin\beta - F_{yr} - F_{xf}\sin\delta - F_{yf}\cos\delta - mgi_h = 0 \\ I_Z\ddot\varphi - (F_{xf}\sin\delta - F_{yf}\cos\delta)L_f + F_{yr}L_r = 0 \end{cases} \tag{7}$$

where F_{ii} (ii = xf, yf) is the fraction of the front wheel drive force in the X and Y-axes directions (N). F_{jj} (jj = xr,yr) indicates the rear wheel drive force components in the X and Y-axes directions (N). δ is the front wheel steering angle (°). β indicates the lateral deflection angle at the center of mass (°). φ is the traverse angle (°). L_f indicates the front wheelb'ase (m). L_r is the rear wheelbase (m).

When the vehicle is accurately steered, $\dot\beta = 0, \dot\varphi = 0$. Assuming that the front wheel angle of rotation and the lateral deflection angle at the center of mass are small, their cosines are approximately 1 and their multiplication is approximately 0. Derivation of Eq. 7 leads to the combined force exerted by the vehicle in the longitudinal direction shown in Eq. 8.

$$F_{xf} + F_{xr} = F_r + F_a - (mv\dot\varphi - mgi_h)\left(\sin\beta - \frac{L_f}{L}\sin\delta\right) \tag{8}$$

$$\sin\beta = \frac{L_r}{L}\sin\delta - \frac{L_r}{L}\sin\partial_f - \frac{L_f}{L}\sin\partial_r \tag{9}$$

where ∂f, ∂r indicate the lateral deflection angle of the front and rear axles (°). L indicates the wheelbase(m).

When the vehicle is accurately steered, the load is uniformly distributed on the four tires, the turning stiffness and side deflection angle of the tires are equal (Wong, 2008), and the specific characteristic conditions are shown in Eq. 10 and Eq. 11, Eq. 12 and Eq. 13.

$$L_f = L_r \tag{10}$$

$$C_{af} = C_{ar} = C_a \tag{11}$$

$$\partial f = \partial r = \partial \tag{12}$$

$$C_{av} = nC_a \tag{13}$$

Combining Eq. 9–14 can be obtained.

$$\sin\beta = \frac{L_r}{L}\sin\delta - \sin\partial \tag{14}$$

Substituting Eq. 14 into Eq. 8 leads to Eq. 15.

$$F_{xf} + F_{xr} = F_r + F_a + \left(\frac{mV^2}{R} - mgi_h\right)\sin\partial \tag{15}$$

The curve driving resistance, F_k, can be obtained as shown in Eq. 16.

$$F_k = \left(\frac{mV^2}{R} - mgi_h\right)\sin\partial \tag{16}$$

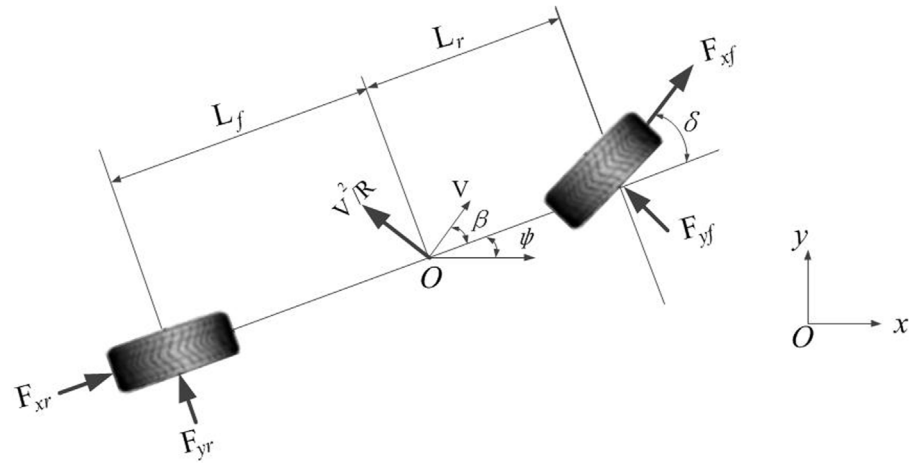

FIGURE 2
Vehicle monorail model.

Based on the linear characteristics of the turning stiffness, the curve driving resistance and the curve driving resistance work done by the vehicle in the circular curve section where the superelevation is set up can be expressed by Equation. 17 and Equation. 18.

$$F_k = \frac{\left(mV^2/R - mgi_h\right)^2}{nCa} \tag{17}$$

$$W_k = \frac{\left(mV^2/R - mgi_h\right)^2}{nCa} S_k \tag{18}$$

where W_k represents the work done by the curve driving resistance(N m). S_k denotes trip mileage (m). n indicates the number of tires.

Due to its high load attributes, trucks are usually equipped with a non-independent suspension system to increase the load-carrying capacity and to avoid large side deflection angles of the tires during cornering operation. Non-independent suspension systems cause the left and right wheels to interact with each other, which generates suspension resistance and depletes part of the vehicle's mechanical energy (Wong, 2008). The independent suspension system used in passenger cars does not have this part of the energy consumption. The energy consumption induced by a truck turning on a curved road is determined by the curve driving resistance and the suspension resistance, as shown in Eq. 19.

$$W_k = \left[\frac{\left(mV^2/R - mgi_h\right)^2}{nCa} + F_{tc}\right] S_k \tag{19}$$

where F_{tc} indicates the suspension resistance due to the mass on the spring(N).

When the vehicle is traveling at a uniform speed in a circular curve section with superelevation, the carbon emission model is shown in Eq. 20. It shows that in the section of circular curves with superelevation, the plane geometry indicators that have an impact on vehicle carbon emissions include curve radius and superelevation. The mechanical characteristic parameter that has an impact on vehicle carbon emissions is the lateral force coefficient.

$$CO_2 = (W_r + W_a + W_k) n_{co2} + C_0 + C_T \tag{20}$$

where W_r and W_a represents the work done by rolling resistance and air resistance, respectively (N m). C_0 and C_T represent carbon emissions (kg) from idle fuel consumption and carbon emissions from diesel exhaust cleaning, respectively, and the calculation methods are detailed in the authors' previous research literature (Dong et al., 2020). n_{co2} is the conversion factor between the driving energy and the carbon emission. Based on the positive correlation between the energy and carbon emissions of vehicle fuels, the authors' previous research literature (Dong et al., 2023) used the IPCC. (2006) to obtain carbon emission rates of 0.296 $kgCO_2/MJ$ and 0.213 $kgCO_2/MJ$ for gasoline and diesel engines, respectively.

In particular, from Eq. 17, the curve driving resistance for a circular curve section without superelevation is shown in Eq. 21. This directly reveals the direct effect of curve radius on carbon emissions, where the curve driving resistance is proportional to the square of the centrifugal acceleration, proportional to the fourth power of the vehicle speed, and proportional to the square of the lateral deflection angle, as shown in Eq. 22 and Eq. 23. The longitudinal speed of the tire is equivalent to the traveling speed, and the lateral acceleration of the tire is approximately equal to the centrifugal acceleration of the vehicle.

$$F_k = F_L \alpha = \frac{mV^2\alpha}{R} = \frac{m^2V^4}{4C_aR^2} \tag{21}$$

$$F_k \propto \left(\frac{V^2}{Rg}\right)^2 \tag{22}$$

$$F_k \propto \alpha^2 \tag{23}$$

When the passenger car maintains a uniform speed on a circular curve road section, the work done by the curve driving resistance is shown in Eq. 24. The incremental carbon emission caused by the curve driving resistance is called the vehicle turning carbon emissions. It is inversely proportional to the square of the curve radius and proportional to the fourth power of the speed.

$$W_k = \frac{m^2V^4}{4C_aR^2} S_k \tag{24}$$

2.1.2 Indirect effects of horizontal curve alignment on vehicle carbon emissions

The indirect effect of horizontal curve alignment on vehicle carbon emissions is reflected in changes in operating speed. Vehicles traveling on flat curve roads with small radius usually exhibit significant speed fluctuations (Bonneson and Pratt, 2009; Wen and Eric, 2010). As the radius of the circular curve gets larger, the operating speed of the vehicle on the flat curve section gradually tends to stabilize, and the difference between the entry speed and the speed at the midpoint of the curve gradually decreases (Paolo, 2018). The greater the change in vehicle speed, the greater the inertial resistance, which will cause a change in carbon emissions.

When the vehicle drives through the curve with variable speed, the resistance along the direction of the traveling trajectory includes rolling resistance, air resistance, inertia resistance, and curve driving resistance. By integrating Eq. 18 and Eq. 24 in the travel time, the curve driving resistance can be obtained for the vehicle traveling at variable speed. The work done by the curve driving resistance of a passenger car traveling at variable speed on a circular curve section and a transition curve section are Eq. 25 and Eq. 26, respectively. For trucks, these are Eq. 27 and Eq. 28, respectively.

$$W_{k\text{-Circular-car}} = \int_0^t \frac{\left[mV(t)^2/R - mgi_h\right]^2}{4C_a} dS_k(t) \tag{25}$$

$$W_{k\text{-Transition-car}} = \int_0^t \frac{\left[mV(t)^2/R(t) - mgi_h(t)\right]^2}{4C_a} dS_k(t) \tag{26}$$

$$W_{k\text{-Circular-truck}} = \int_0^t \frac{\left[mV(t)^2/R - mgi_h\right]^2}{nC_a} dS_k(t) + F_{tc}S_k \tag{27}$$

$$W_{k\text{-Transition-truck}} = \int_0^t \left\{ \frac{\left[mV(t)^2/R(t) - mgi_h(t)\right]^2}{nC_a} + F_{tc}(t) \right\} dS_k(t) \tag{28}$$

Based on the power load of the vehicle traveling at variable speed on the horizontal curve roadway, the vehicle carbon emission model can be obtained as shown in Eq. 29.

$$CO_2 = (W_r + W_a + W_k + W_e + W_t' + Q_h)n_{co2} + C_0 + C_T \tag{29}$$

where W_k is equal to the integral of the curve driving resistance over the traveling time. W_e represents the work done by inertial resistance (N m). W_t' denotes the work done by the engine counter drag force at idle coasting (N m). Q_h indicates the mechanical energy consumed by the braking force (N m) (Dong et al., 2023).

Compared with the vehicle carbon emission model for a flat curved road section at uniform speed, the variable speed model takes into account the fact of the curve driving resistance. The curve driving resistance during travel varies with speed. The variable speed model takes into account the work done by the inertial drag during acceleration and deceleration, the work done by the engine counter-drag during idling, and the braking loss energy during braking.

In terms of driving resistance distribution, speed change affects vehicle carbon emissions in three ways, specifically, i.e., speed change not only generates inertial resistance, affects rolling resistance and air resistance, but also affects the curve driving resistance.

2.2 Measurement of carbon emissions from curve-driving

Given that the direct effect of road geometry on vehicle carbon emissions lies in the stability of driving, and the indirect effect is reflected in the change of operating speed, this study proposes to carry out uniform speed driving and variable speed driving tests respectively. Specifically, the test vehicle is required to drive at a constant speed to measure the carbon emissions caused by the driving stability of curved roads. Then, the field road following test is carried out to reveal the changes in the carbon emissions caused by changes in the driving speed of curved roads.

2.2.1 Field trial design

The road plane linear conditions and speed determine the carbon emissions. From the perspective of vehicle dynamics, the lateral force can be regarded as an intermediate parameter for the influence of these factors on carbon emission. Vehicle carbon emission modeling under different plane linear conditions can be regarded as a relationship model between lateral force coefficients and carbon emissions. Such a treatment can simplify the analysis of the combined effects of different plane geometry indicators on carbon emissions, while ensuring the reliability of the research findings.

For passenger cars, the work done by the curve driving resistance on the circular curve and transition curve sections is shown in Eq. 30 and Eq. 31, respectively, which is characterized by the lateral force coefficient as the dependent variable. For trucks, it is Eq. 32 and Eq. (33).

$$W_{k\text{-Circular-car}} = \frac{m^2g^2\mu^2}{4C_a}S_k \tag{30}$$

$$W_{k\text{-Transition-car}} = \int_0^t \frac{m^2g^2\mu(t)^2}{4C_a} dS_k(t) \tag{31}$$

$$W_{k\text{-Circular-truck}} = \frac{m^2g^2\mu^2}{nC_a}S_k + F_{tc}S_k \tag{32}$$

$$W_{k\text{-Transition-truck}} = \int_0^t \left[\frac{m^2g^2\mu(t)^2}{nC_a} + F_{tc}(t) \right] dS_k(t) \tag{33}$$

This in turn allows for field tests to be conducted using the lateral force coefficient as the dependent variable to validate the accuracy of the model. The intermediate parameter of the transverse force coefficient was adopted as a control variable during the test, avoiding the effects of multiple factors on carbon emissions. Experimenting with this way would simplify to a greater extent the assessment of field test data for carbon emission modeling and avoid the complexity and redundancy of the experiment.

For the specific relationship between the lateral force coefficient and carbon emission, there is no authoritative research result for clear reference. How to explore the change of transverse force of actual traveling on a circular curve roadway, and the carbon emission rules under the condition of transverse force? To address this question, conducting a field test is an essential key link. In this experiment, a circular curve of different radii was measured at a flat automobile test track to measure the lateral force coefficients and carbon emissions under different radii of

the circular curve. After evaluating the reliability of the carbon emission model for the circular curve section without superelevation, a few data are taken to further validate the carbon emission model for the circular curve section under different superelevation conditions. This test program can not only gradually verify the carbon emission model under different plane line conditions, but also ensure the reliability of the test results and research findings.

Vehicles in a small radius curve, tend to drive at low speeds, resulting in high lateral force coefficients, and there is a general acceleration and deceleration behavior. As the radius increases, the speed gradually increases, which is more favorable for driving stability. The coefficient of lateral force decreases gradually and the speed stabilizes after going from 0.4 to 0.15. The radius, if increased to infinity, the lateral force coefficients become smaller to zero value. Scholars have been obtained through field tests, when the radius is greater than 550 m, the speed is stable and tends to 100 km/h (Cruz et al., 2017). The existing literature on the speed variation rule presents two ideas that can be used to guide the design of the carbon emission test in this manuscript. Specifically, the magnitude of the lateral force coefficient affects the acceleration and deceleration speeds of a vehicle on a circular curve section, which determines the maximum curve radius that affects carbon emissions. The carbon emission increment caused by the acceleration and deceleration can be obtained by calculating the carbon emission difference between the conditions of normal driving on the circular curve roadway, and uniform speed driving on the flat straight roadway. The value of uniform speed is the speed at the midpoint position of the curve. The carbon emission under the condition of uniform speed can be predicted based on the model constructed by the author's previous research (Xu et al., 2020). Secondly, the vehicle turning carbon emissions can be obtained by finding the difference of carbon emissions from the vehicle uniform speed operation test on the circular curve and the flat and straight road sections.

Based on the above analysis, the field trial program was designed as follows.

At a flat automobile test site, a circular curve without over-height is placed on site as a test section. The field test was divided into two parts, namely, normal driving and uniform speed driving tests. The normal driving test uses radius as a control parameter to capture carbon emissions, aiming to determine the minimum radius value of the circular curve that does not affect carbon emissions. The speed value is the operating speed at the midpoint of the curve as measured in a normal driving test. The normal driving test requires one group of drivers to drive normally on circular curve sections. The uniform driving test requires another group of drivers to drive uniformly at the target speed in circular curve sections and flat straight sections. Under the condition of the same vehicle speed, the difference in carbon emission between the uniform speed driving test on the circular curve section and the uniform speed driving test on the flat section is the vehicle turning carbon emissions caused by the curve driving resistance. The difference in carbon emissions between normal and constant speed driving tests on the circular curve section under the condition of the same radius is the carbon emission caused by speed fluctuations.

The results of carbon emission tests on circular curved sections carried out at the automobile test site can reveal the carbon emission rules of vehicles with different lateral force coefficients. By integrating Eq. 2 and, Eq. 18 Eq. 19, it can be inferred that when the value of the lateral force system is constant, the carbon emission prediction results are consistent regardless of the change in the plane linear condition. This result clarifies the reliability of the prediction model from the theoretical point of view for the circular curve section with superelevation settings, and the transition curve section. In addition, this manuscript also evaluates the accuracy of the model predictions from an empirical perspective. The test sections were selected to be a gently sloping circular curve section of the Xi-Han Expressway with a superelevation setting. A gently curved section of the roadway was designed and sampled at the automotive proving grounds. The transition curve sections were designed and routed at the automotive proving grounds.

The transition curve test sections were set up on the automobile test site. The test results were used to assess the accuracy of vehicle carbon emission predictions for transitional curve sections without excessive superelevation. The theoretical model shows that for both circular and transition curves, the lateral force coefficient can be regarded as a mechanically characterized parameter that affects vehicle carbon emissions. The lateral force coefficients have the same effect on vehicle carbon emissions for both circular curve sections and transition curve road sections. At the same time, the transition curve can be regarded as a circular curve section with gradual changes in curvature and superelevation. If the carbon emission prediction accuracy of the circular curve section with superelevation reaches a high level, it can be equated with the same prediction accuracy of the carbon emission on the transition curve section.

Test data from vehicles traveling normally on a circular curve section at the automobile test site were used to assess the reliability of the carbon emission model for vehicles traveling on the circular curve sections under variable speed conditions.

2.2.2 Field test methodology

To clarify the minimum radius of the curve that does not affect the carbon emissions of passenger cars and trucks respectively, this test focuses on the test section of the curve with a radius between 100 m and 600 m. The results of the field test are compared with the carbon emissions of vehicles on flat straight road sections to determine the minimum radius of the circular curve that affects carbon emissions. The circular curve and flat straight test sections were measured at the automobile test site. There are 13 circular curve test sections with radii of 100 m, 150 m, 200 m, 250 m, 300 m, 350 m, 400 m, 450 m, 500 m, 550 m, 600 m, 800 m, and 1500 m respectively. In the normal driving test of the circular curve section, the speeds at the beginning and end points of the circular curve and the midpoint of the curve need to be recorded, and the carbon emission is accounted for based on the instantaneous fuel consumption. In a uniform speed test on circular curve sections, the carbon emissions of a specified speed at a uniform speed need to be measured.

In the selected circular curve test section of Xibao Expressway, one group of drivers was asked to drive at a certain speed and the other group of drivers was asked to drive normally.

For the carbon emission tests under two different driving conditions, namely, constant speed and variable speed, it is strictly controlled that the two groups of drivers should not be

TABLE 1 Design details for transition curve sections.

No.	R_{-back}(m)	R_{-front}(m)	L_c(m)
1	100	∞	110
2	200	∞	85
3	300	∞	150
4	400	∞	190
5	200	300	190
6	300	400	110
7	200	300	190
8	300	400	110

exchanged with each other. The tests all collected at least 40 sets of valid fuel consumption data to ensure the reliability of the carbon emission modeling assessment conducted subsequently. To facilitate the comparison of the carbon emissions of different driving distances, the carbon emission rate of 100 km was used to characterize the carbon emissions of the vehicle.

(1) Test vehicles

Two types of passenger cars and three types of trucks are selected as typical vehicles, which are referenced from the results of the authors' survey (Dong et al., 2023) on the proportion of vehicle types in China's highway traffic volume in recent years. The two passenger cars are a small sedan, represented by the Chevrolet McLaren, and an urban crossover, represented by the Chevrolet Copacetic, hereafter denoted by Car I Car II, respectively. The three trucks are Dongfeng medium truck, Jiefang heavy-duty truck, and Jiefang tractor, which are denoted as Truck I, Truck II, and Truck III, respectively, in the following. The test vehicles were categorized into two vehicle types: passenger cars and trucks, taking into account the differences in operating speeds and lateral force coefficients between passenger cars and trucks on horizontal curve sections.

(2) Test road sections

To measure the direct effect of road plane alignment on vehicle carbon emissions and exclude the effect of route longitudinal section alignment on carbon emissions, the Chang'an University automobile test site was chosen as the test site. By measuring and setting up 13 circular curve test sections in the automobile test site, the radii of the circular curves are 100 m, 150 m, 200 m, 250 m, 300 m, 350 m, 400 m, 450 m, 500 m, 550 m, 600 m, 800 m, and 1500 m, respectively, and the automobile test site is a flat cement concrete pavement, the longitudinal slopes slope ranges from −1~1%, and there is no set road cross slope. Due to the site size limitation, the size of the radius of the circular curves was changed by changing the size of the radius of the circular curves one by one to measure the carbon emission of the vehicles under different radii of the circular curves. The route and inner and outer edges of the test section were placed and positioned using a total station.

TABLE 2 Design details for circular curve sections with superelevation setting.

No.	R(m)	i_h(%)	i(%)
1	550	4	0.5
2	290	6	−1
3	280	6	−0.7
4	450	6	−0.85
5	175	7	−1.65

The geometrical lines of the test sections, which are circular and transition curve, are obtained by sampling at the automobile test site. The design indicators for the transition curve sections are shown in Table 1.

Considering that the actual curved roads are set with superelevation, six circular curved sections with superelevation were selected as test road sections on the Xi-Han Freeway. The design indicators for the selected test sections are shown in Table 2.

(3) Test instruments

The instruments selected for this test are as follows: Portable Automobile USB E-CAN Measuring Instrument, JDSZ-EP-1-1D Vehicle-mounted Diesel Fuel Consumption Measuring Instrument, Laptop Computer, Total Station Instrument, Sigma Split Anemometer AS8336, Digital Camera and Crash Bucket.

(4) Motorists

In the normal driving test, the driver is required to drive normally and is not allowed to drive aggressively to obtain the value of the maximum radius of the curve that affects the speed of the vehicle. The constant speed test requires the driver to drive at different speeds to obtain the additional carbon emissions of the vehicle as determined by different lateral force coefficients.

3 Results

The field test data can be used to analyze the carbon emission rules of vehicles on horizontal curve road sections, and also to assess the reliability of the carbon emission model for vehicles on horizontal curve road sections.

3.1 Minimum radius affecting vehicle carbon emissions

The speed change curve of the test vehicle under normal driving conditions on the circular curve section is shown in Figure 3. Characteristic points 1, 2, and 3 in the figure indicate the starting point, midpoint, and end position of the circular curve test road, respectively.

In Figure 3, when the radius of the curve is larger than a certain value, the operating speed shows a "U-shaped" trend. The vehicle will take certain deceleration behavior before entering the curve, and

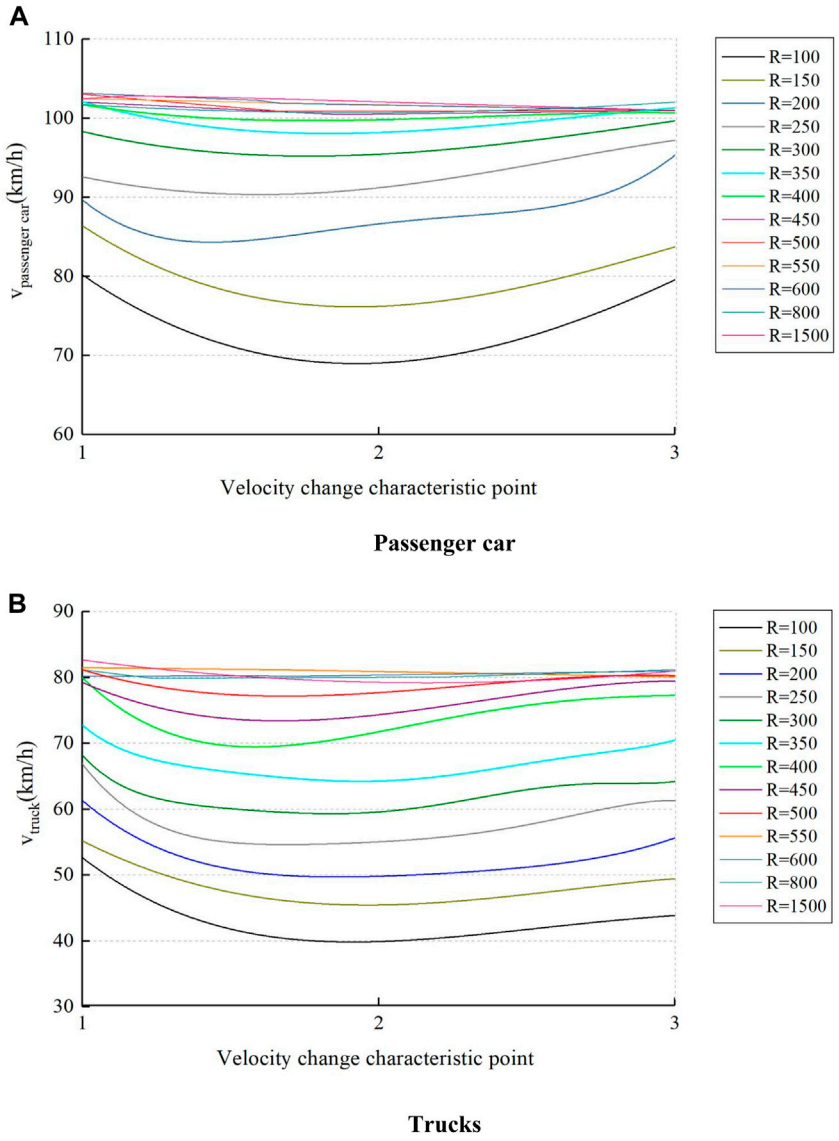

FIGURE 3
Vehicle velocity profile on the circular curve section. **(A)** speed profile of passenger cars. **(B)** speed profile of trucks.

after passing the midpoint of the curve, the vehicle continuously accelerates out of the curve. For the same radius of the curve section, the vehicle enters the curve after the maximum deceleration. The smaller the radius, the more obvious the change in running speed. In addition, the smaller the radius, the lower the running speed at the midpoint of the curve; the larger the radius, the higher the running speed at the midpoint of the curve. As the radius increases, the lateral force coefficient decreases. For the passenger car, when the curve radius is 100 m, the speed is low, and the transverse force coefficient u is close to 0.4; with the increment of the radius, the speed increases gradually, and the transverse force coefficient decreases gradually; until the radius is 400 m, the speed reaches 100 km/h, and the transverse force coefficient is 0.15. This running speed law is similar to that of the measured results of Russo et al. (2016) and Sil et al. (2019); while the transverse force variation law is in general agreement with the measured results of Bonneson. (2000), who conducted the transverse force coefficient test on dry pavements of U.S. highways. For the truck, when the radius of the circular curve is greater than or equal to 550 m, the vehicle speed tends to be stabilized and reaches 80 km/h. This is consistent with the measured results of Cruz et al. (2017). This shows that the basic data of vehicle operating speed measured in this test has a certain degree of reliability, which can reflect the change rule of speed and lateral force of actual traveling under different radii. Vehicle carbon emission data obtained under the conditions of this law are also reliable, and the test results are shown in Figure 4. Among them, V-middle is used to indicate the vehicle speed at the midpoint of the curve.

Figures 3, 4 show that the speed fluctuations of vehicles are significant when driving in small radius sections, presenting higher carbon emissions. As the radius increases, the magnitude of the change in running speed gradually slows down, and the carbon emission gradually decreases. When the radius gradually increases to 400 m and 550 m, the running speed of the test passenger car and

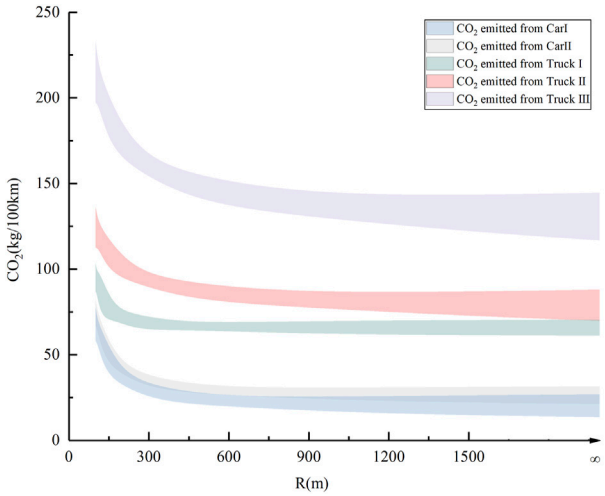

FIGURE 4
Normal driving test results of the test vehicle on the circular curve sections.

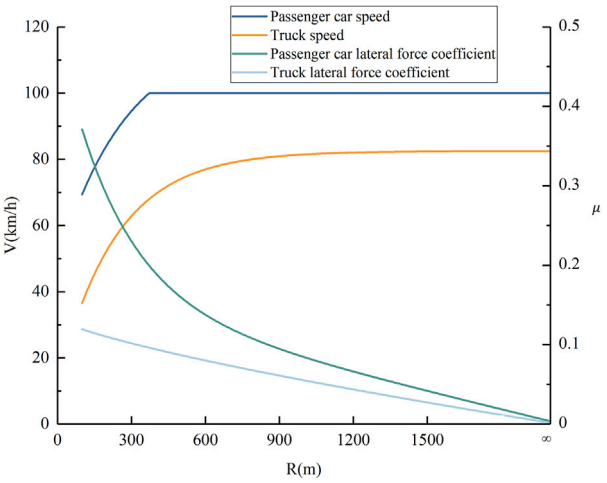

FIGURE 5
Lateral force coefficient of the test vehicles.

truck increases and tends to stabilize to 100 km/h and 80 km/h respectively. The lateral force coefficient gradually decreases and reaches 0.2 and 0.09 respectively. The carbon emission gradually decreases and tends to stabilize, and is close to that on the flat straight road section. Compared with the carbon emission of vehicles on flat straight roads, the maximum relative errors of the carbon emission of passenger cars and trucks are 7.26% and 8.08% respectively, which are both less than 10%. That is to say, under this driving condition, the increment of vehicle carbon emission is caused by the work done by the curve driving resistance, and the maximum growth rate is 8.08%, which is less than 10%. It can be concluded that when the radius of the circular curve is larger than the maximum radius that affects the carbon emission, the vehicle speed remains stable, and the curve driving resistance is small, resulting in a smaller difference in carbon emissions of the vehicle compared to a flat straight road.

The results show that under actual free-flow driving conditions, the maximum curve radius affecting the carbon emissions of passenger cars and trucks are 400 m and 550 m, respectively.

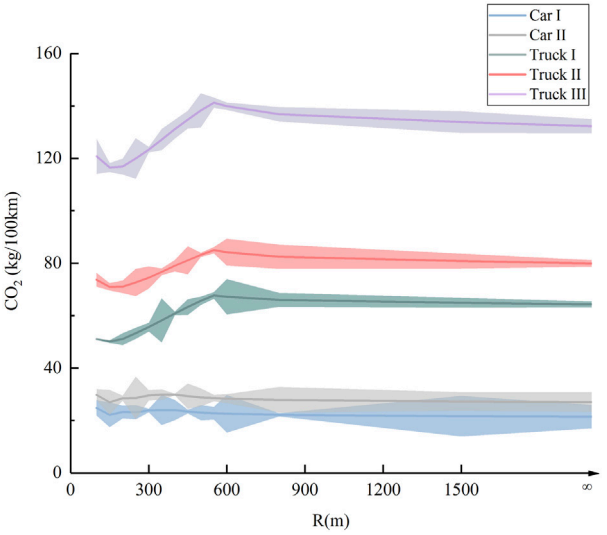

FIGURE 6
Uniform speed test results of vehicles on circular curve sections.

3.2 Validation of vehicle carbon emission models at uniform velocity

(1) Circular curve section

The variation of lateral force coefficients for passenger cars and trucks is shown in Figure 5. The prediction results of the carbon emission model are shown in Figure 6.

The maximum relative error between the predicted and measured carbon emission values is 8.39%, which is less than 10%, indicating that the carbon emission model has a high prediction level under this driving condition.

The results of the evaluation show that the modeling of the relationship between the lateral force coefficient and carbon emissions achieves a high level of prediction. The lateral force coefficient is determined by curvature and superelevation. It can be inferred theoretically that the prediction model is also accurate for carbon emission quantification on circular curve sections with superelevation setting, and transition curve sections.

(2) Circular curve section with superelevation setting

To verify the predictive effectiveness of the constructed model from an empirical point of view, the carbon emission data of the test vehicles on the circular curved road sections with superelevation were compared, as shown in Figure 7. The test road sections were selected from the actual highways. The test vehicle travels to overcome the curve driving resistances, the resistance caused by ultra-high cross-slopes, and the gradient resistance from the

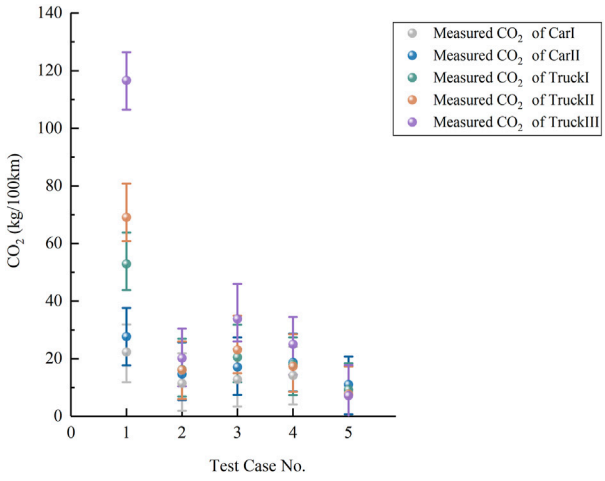

FIGURE 7
Test results of vehicles on circular curve sections with superelevation setting.

longitudinal slopes of the actual road. Regarding the quantification of the effect of longitudinal slope gradient on carbon emissions, it was estimated using the longitudinal profile vehicle carbon emission model from the authors' previous literature.

The prediction results show that the maximum relative errors of the carbon emission prediction results for passenger cars and trucks are 7.42% and 9.60%, respectively, which are less than 10%, indicating that the prediction level of the vehicle carbon emission model is higher in the circular curve section with superelevation setting.

(3) Transition curve section

The results of the passenger car and truck carbon emission tests on the transition curve test section are shown in Figure 8. R_{-front}、R_{-back} and L_c denote the radius of the circular curve before and after the transition curve section and the length of the transition curve section. For passenger cars and trucks, the maximum relative errors of the predicted and measured carbon emissions on the transition curve section are 7.40% and 8.09%, respectively, which are both less than 10%.

In addition to the assessment of the prediction accuracy of the model, the reliability of the model should also be examined. By analyzing the predicted and measured values of carbon emissions from vehicles on the horizontal curve sections, the consistency between the prediction results and the measured results is tested. The Adj-R^2 of the model is 0.915, indicating that the carbon emission model explains the measured data to a high degree. The asymptotic Sig of the chi-square test is 0.010, which is less than 0.05, indicating that the model explains the measured data to a high degree and is statistically significant.

The theoretical model shows that when a vehicle travels through a circular curve section at a constant speed, the lateral force coefficient does not change, and the curve driving resistance of the curve and its determined carbon emissions from the vehicle curve are constants. In the transition curve section where the curvature varies continuously, the vehicle curve carbon emission will change with it. Taking the horizontal curve measured at the automobile testing site as an example, the carbon emission profile of the vehicle traveling at a constant speed of 80 km/h is predicted and plotted as shown in Figure 9. It can visually characterize the carbon emission rules under different plane linear conditions. Among them, $CO_{2\text{-Curve}}$ is used to reflect the influence of horizontal curve alignment on carbon emission.

In Figure 9, the vehicle carbon emission rate of the gently curved section shows a horizontal segmental change. The vehicle carbon emission rate is a constant value in the circular curve section, and changes in the curve trend in the transition curve section. The longer the length of the transition curve is, the more gentle the change of vehicle carbon emission rate is.

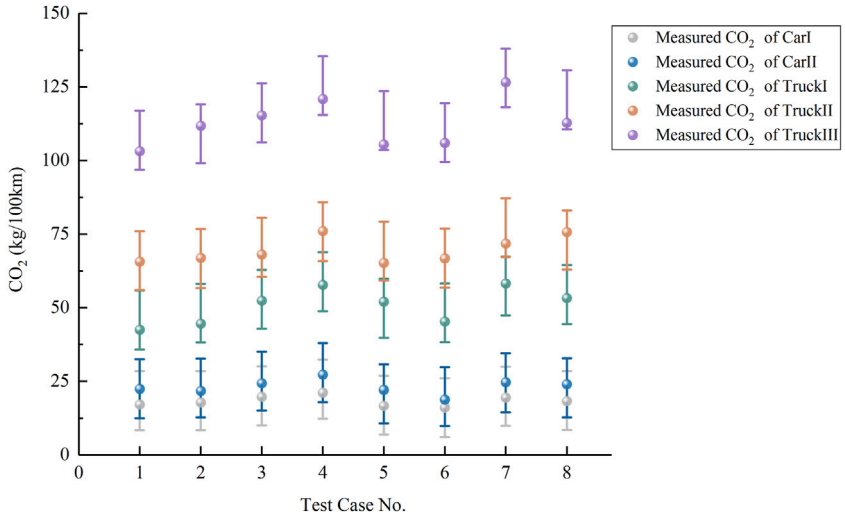

FIGURE 8
Test results of vehicles on transition curve section.

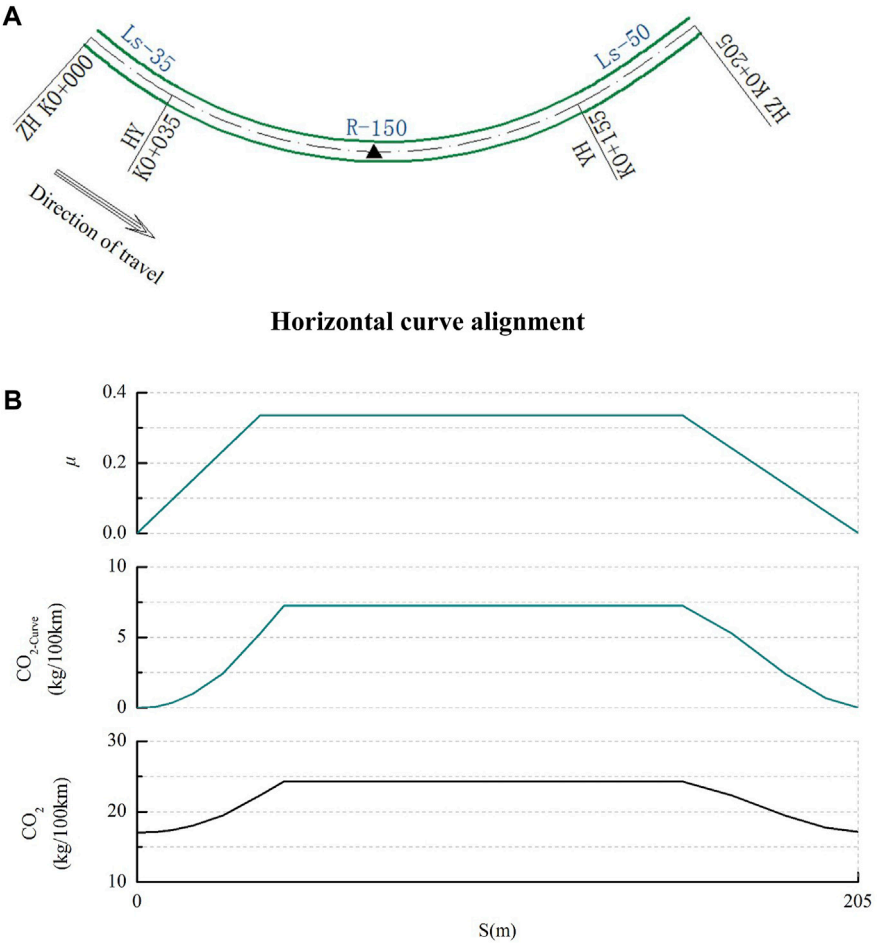

FIGURE 9
Vehicle carbon emission rates on horizontal curve sections. **(A)** geometric Design Specifications for Example Highway Horizontal Curves. **(B)** distribution of lateral force coefficients and vehicle carbon emission rates.

3.3 Validation of vehicle carbon emission models for flat curve road sections under variable speed conditions

The test data under normal driving conditions on the circular curve section of the automobile test track are shown in Figure 10. The results show that for the test passenger cars and trucks, the maximum relative errors between the predicted and measured values of carbon emissions are 10.65% and 10.04% respectively, indicating that the model can reflect the carbon emissions under real driving conditions.

To test the statistical significance of the theoretical model in variable speed conditions, the model was subjected to residual analysis and likelihood ratio tests. The Adj-R^2 of the model is 0.925. The Durbin-Warson statistic was 1.592. The two-sided asymptotic Sig of the chi-square test is 0.010, which is less than 0.05. The results of these statistical tests indicate that the carbon emission model can explain the measured data well.

For planar lines, the transition curve can be regarded as a circular curve with gradually changing curvature. The carbon emission of the transition curve road section is equivalent to that of the circular road section with continuously changing curvature. It can be inferred that the accuracy of the carbon emission prediction of the transition curve road section and the circular road section is comparable. Due to time and site size constraints, and to avoid redundancy in the test program, this manuscript does not validate the modeling of vehicle carbon emissions on transition curve road sections with variable speeds.

To represent the impact of curve driving resistance and speed change on carbon emissions, the carbon emissions profile of a passenger car under normal driving conditions in the circular curve with a radius of 150 m and 400 m respectively are shown as an example, as shown in Figure 11. Among them, $CO_{2\text{-Curve}}$ is used to visualize the effect of plane line shape on carbon emission, and $CO_{2\text{-Velocity}}$ indicates the effect of speed change on carbon emission, whose value is determined by the air resistance, rolling resistance, and inertial resistance work done by the vehicle in the process of driving at variable speed in the flat straight road. The position of the midpoint of the curve is indicated by the symbol "▲".

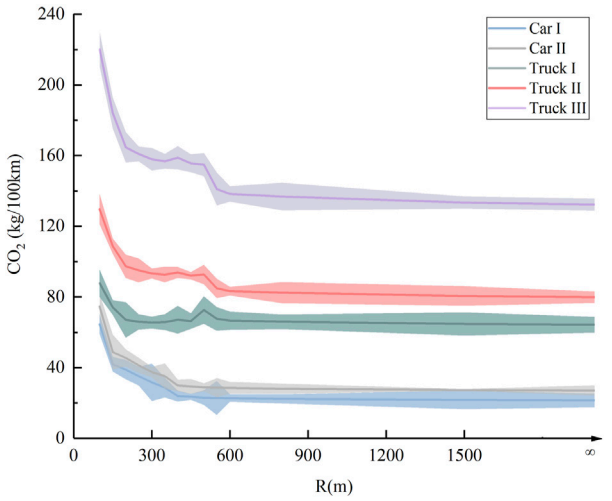

FIGURE 10
Normal driving test results of vehicles on circular curve section.

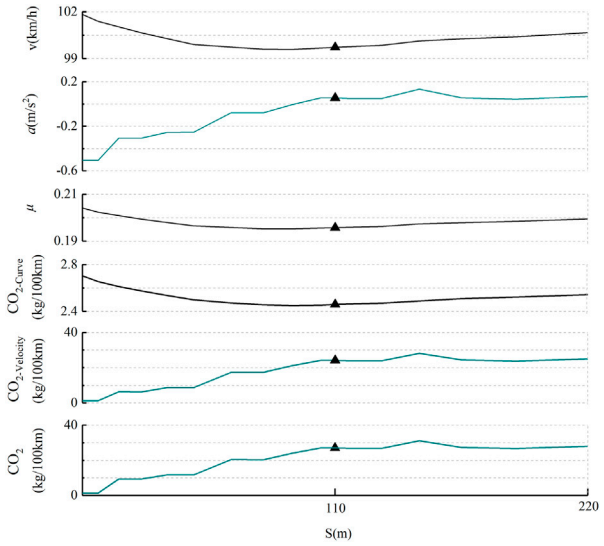

FIGURE 11
Carbon emissions under normal driving conditions on circular curve sections. **(A)** example of a circular curve with a radius of 150 meters. **(B)** the case of a circularl curve sections with a radius of 400 meters.

By analyzing the carbon emission curves in Figure 11, the following results can be obtained.

(1) In the first half of the circular curve with a radius of 150 m, the vehicle is traveling under braking and idling carbon emissions, which are illustrated by a dotted line in Figure 11A. The curve driving resistance is greater than the brake resistance and counteracts it, the vehicle has to overcome the remaining curve driving resistance, and the carbon emissions are at a low level, which is represented by a dotted line in Figure 11A. In the second half of the circular curve with a radius of 150 m, and in the whole length of the circular curve with a radius of 40 m, where the vehicle relies on engine-driven energy to drive, the trend of carbon emission and acceleration is same, and there is a high positive correlation between them.
(2) The smaller the radius, the more significant the degree of acceleration and deceleration, and the greater the magnitude of the change in carbon emissions.
(3) Under the above driving conditions, the speed fluctuations have a more significant effect on vehicle carbon emissions compared to the curve driving resistance.
(4) The trends of both vehicle turning carbon emissions and lateral force coefficients show a high degree of consistency.

Carbon emission tests were conducted on a circular curve section with consistent vehicle speeds to exclude the effect of speed variations on carbon emissions. The difference in carbon emissions when a vehicle is traveling at a constant speed on a curved and flat roadway, i.e., the incremental carbon emissions caused by the curve driving resistance. For trucks, this part of the carbon emission increment is caused by the curve driving resistance and suspension resistance. Based on the carbon emission model, the growth rate of carbon emission caused by vehicles turning at a constant speed can be predicted, see Figures 12, 13.

In Figures 12, 13, as the radius increases, the vehicle speed is gradually at a higher level, the lateral force coefficient gradually decreases, and the carbon emission decreases accordingly. Figure 12 shows that under the same road conditions, the growth rate of carbon emission caused by curve driving resistance is at different levels for passenger cars and trucks. According to the carbon emission theoretical model, the growth rate of a vehicle turning carbon emissions is determined by the geometric parameters of the curve (radius and superelevation) and the vehicle characteristics (including speed, load, tire characteristics, and tire number) and other factors. Passenger cars are commonly used for drivers' daily access, and the loads are all small. Trucks are usually used for freight transportation, and the load capacity is larger. Heavy-duty vehicles focus on driving safety when crossing the curve, the speed is at a lower level. These factors affect the curve driving resistance differently, causing different growth rates of vehicle carbon emissions.

The difference between the carbon emissions of the test vehicle driving normally and at a constant speed in the circular curve section is the increment of carbon emissions caused by speed fluctuations. Its growth rate is shown in Figure 14.

In Figure 14, for passenger cars and heavy-duty vehicles, the radius of the circular curve is less than 400 m and 550 m, respectively, the growth rate of carbon emission caused by acceleration and deceleration behavior increases dramatically with the decrease of radius. In Figure 14, the growth rate of carbon emission caused by acceleration and deceleration is very small, not more than 1%, when the radius of the curve is larger than 400 m and 550 m, respectively.

Based on the analysis of the velocity data in Figure 3, the following results can be derived. When the radius of a circular curve is greater than or equal to 400 m and 550 m, respectively, passenger cars and trucks tend to drive through the curved road at a stable speed, and the effect of horizontal curves on carbon emissions is mainly reflected by the curve driving resistance. When the radius is less than 400 m and 550 m, respectively, passenger cars and trucks float more significantly, and carbon

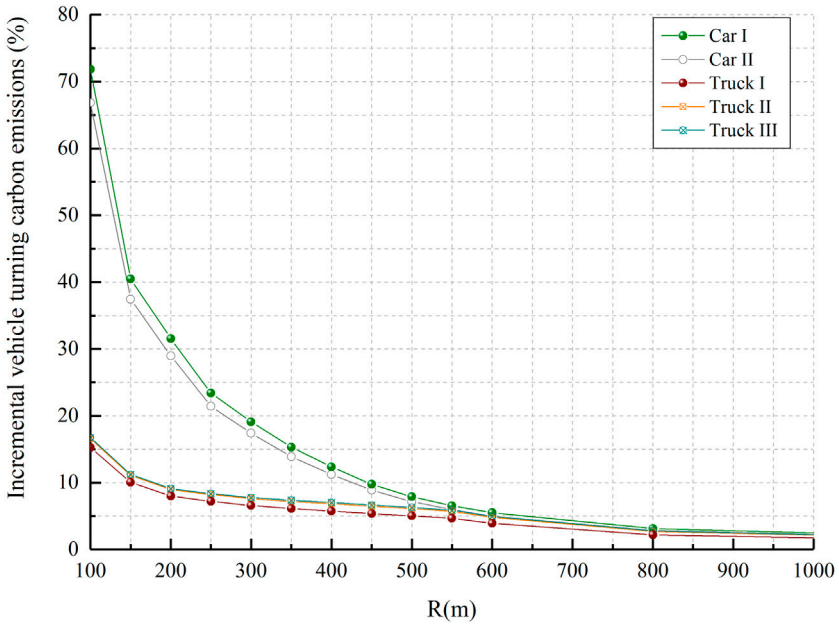

FIGURE 12
Incremental vehicle turning carbon emission.

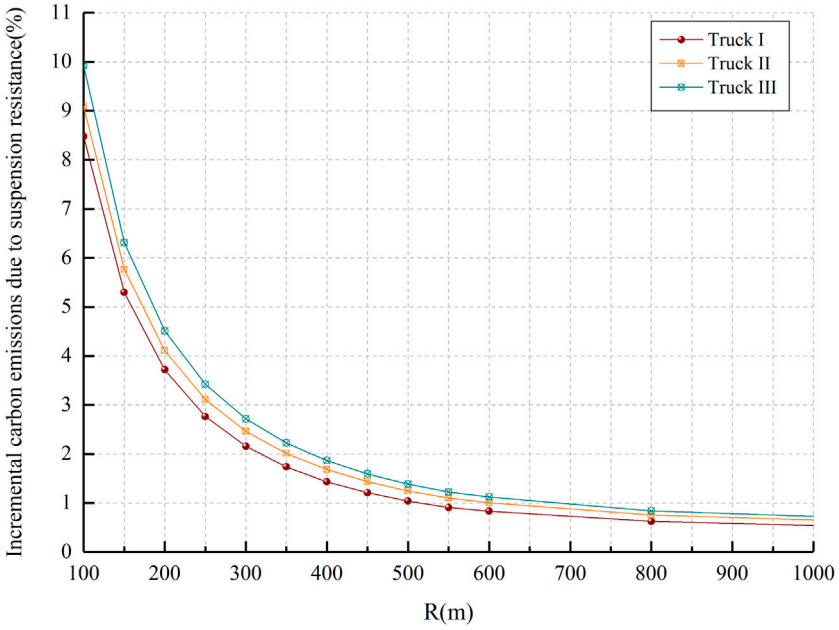

FIGURE 13
Incremental carbon emissions due to suspension resistance.

emissions are mainly affected by speed fluctuations, and carbon emissions increase sharply.

Unexpectedly, it was found that controlling the actual vehicle speed to be no greater than the operating speed at the midpoint of the curve and passing through the horizontal curve at a steady speed not only reduces the curve driving resistance, but also avoids additional carbon emissions caused by speed variations. The selection of the radius is closely related to the operating speed and superelevation. The design specification is often complied with in route design. Setting speed limits to adjust vehicle operating speeds when the route design parameters are constant is a practical guide to vehicle carbon emissions on constructed highways.

Based on the low-carbon theory, the maximum radius of the circular curve affecting the carbon emissions of passenger cars and

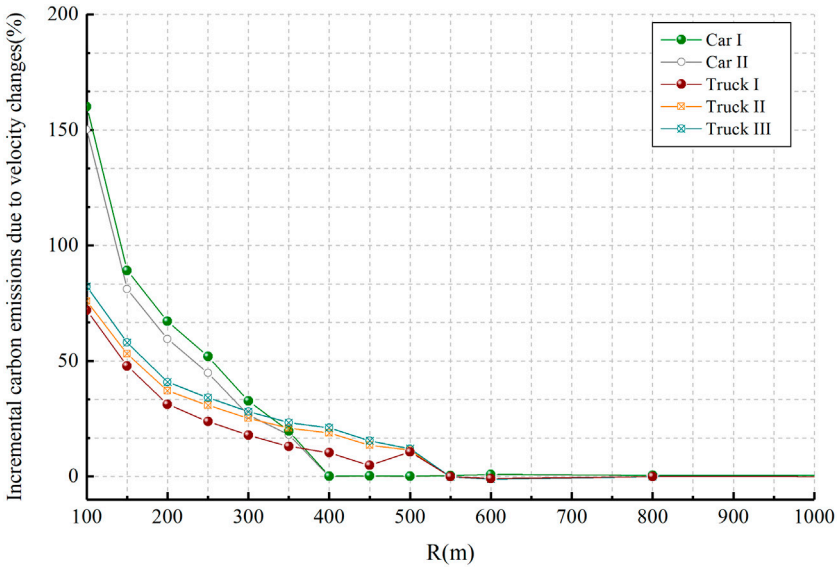

FIGURE 14
Incremental carbon emissions due to velocity changes.

trucks is 400 m and 550 m respectively, which can be used as a criterion to measure whether the design of horizontal curves is a basis for low-carbon and environmental protection. When the radius of the circular curve is smaller than this value, the carbon emission is mainly determined by the speed change, and it shows a sharp increase with the decrease of the radius. On the contrary, the incremental carbon emission of vehicles on curved road sections is mainly attributed to the effect of curve driving resistance.

4 Discussion

The Japan Road Association. (2004) conducted a field test on lateral force coefficients and fuel consumption, measured the growth rate of fuel consumption of small cars with different lateral force coefficients on the horizontal curved road section using the value of the lateral force coefficient as a control parameter. The speeds corresponding to different lateral force coefficients were not specified in the study. Considering that fuel consumption and carbon emissions are directly proportional, the growth rate of fuel consumption is equal to the growth rate of carbon emissions. The growth rate of carbon emissions due to lateral forces can be obtained by calculating the ratio of carbon emissions emitted by a vehicle traveling on a curved roadway to its emissions on a flat roadway. It can be viewed as the growth rate of carbon emissions due to curve-driving resistance. Based on the carbon emission model, the distribution range of the carbon emission growth profile can be predicted for different speeds and different lateral force coefficients. For the growth rate of carbon emissions, the measured results from the JRA against the model's predictions are detailed in Figure 15.

In Figure 15, the growth rate of carbon emissions is quadratically proportional to the lateral force coefficient under the same vehicle operating conditions. This proportionality has been described by the carbon emission prediction model. JRA used the measured statistical average speed to calculate the lateral force coefficient, weakening the relationship. The growth rate of carbon emission caused by the additional resistance of the curve shows a linear increasing trend. This supports the reliability of the carbon emission rules for vehicles on horizontal curve road sections proposed in this manuscript.

By comprehensively considering the direct and indirect effects of planar alignment on carbon emissions, this manuscript introduces the lateral force coefficient as the dependent variable and establishes a prediction model. In the model, the parameters that characterize the geometry of the horizontal curves that have an impact on carbon emissions are the radius of the circular curve, the superelevation, and the length of the transition curve. The larger the radius, the smaller the curve driving resistance and the lower the carbon emission. The setting of superelevation will reduce the lateral force coefficient, offset part of the centrifugal force, reduce the curve driving resistance, and thus reduce carbon emissions. Other research results can be summarized as follows.

1) The root cause of the increase in vehicle carbon emissions on horizontal curve sections is the curve driving resistance and speed fluctuations.
2) Under the free-flow driving condition of the actual highway, the maximum radius of the curve affecting the carbon emission of passenger cars and trucks is 400 m and 550 m, respectively. When the radius of the curve is smaller than the critical value, the carbon emission is mainly determined by the degree of acceleration and deceleration, and with the decrease of the radius, the carbon emission shows a sharp upward trend. On the other hand, the increase in carbon emission caused by speed fluctuations is very small, and the incremental carbon emissions is mainly attributed to the effect of the curve driving resistance.
3) In the process of low-carbon design of highways, by controlling the radius larger than the critical radius, the

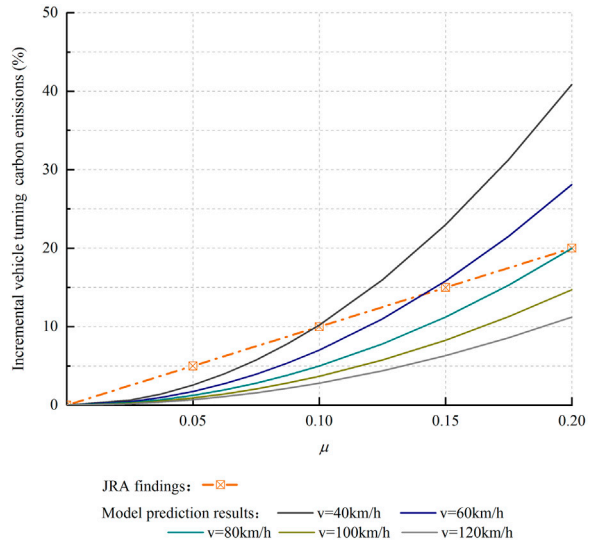

FIGURE 15
Growth rate of carbon emissions due to curve driving resistance to curves.

drastic increase of carbon emissions from curved traffic can be avoided.

4) In terms of low-carbon operation, the actual traveling speed of the vehicle is controlled to be no greater than the operating speed at the midpoint of the curve, and passing through the flat curve at a stable speed not only reduces the vehicle turning carbon emissions, but also avoids the additional carbon emissions caused by acceleration and deceleration.
5) The carbon emission rate of the uniform speed traveling on the horizontal curve sections shows a lateral segmental change. The carbon emission rate is a constant value in the circular curve section, and changes in the curve trend in the transition curve section. The longer the length of the transition curve, the more gentle the change of carbon emission rate.
6) When the vehicle relies on the driving energy from the engine to drive at variable speeds on horizontal curve sections, the carbon emission rate is the same as the change rules of acceleration.

The carbon emission model constructed in this manuscript is applies to the prediction of carbon emission under normal turning driving conditions, i.e., when the vehicle is in an accurate steering state with centrifugal acceleration of less than 0.4 g. In this case, the side deflection force is in the range of 0–2000 N and the side deflection angle is less than 3°(Mitschke and Wallentowitz, 2014). The model does not apply to the prediction of the vehicle in the state of understeer and oversteer.

5 Conclusion

In this study, a prediction model of vehicular carbon emissions on horizontal curve road sections is modeled, which can be realized to quantify the carbon emissions of traveling vehicles under different plane line conditions. The model characterizes the impact on carbon emissions in terms of the lateral force coefficient parameter regardless of the planar line shape. At the same time, a simplified test method is proposed to measure the carbon emissions of vehicles on different plane line conditions, i.e., by controlling the lateral force coefficient of the curved roadway as a dependent variable. Introducing the parameter of the transverse force coefficient can simplify the construction of the theoretical framework for the carbon emission of road vehicles under different planar geometries. At the same time, it can also reduce the implementation difficulty of the field test and shorten the test time and cost. The transverse force coefficient is determined by the radius of the circular curve, superelevation, and the length of the transition curve. Subsequent studies can be based on the model of this manuscript to further explore the degree of influence of each planar geometric linear indicator on carbon emission respectively, to put forward the suggested values of low carbon design for different planar linear indicators, and to realize the accurate and quantitative low carbon design of horizontal curve road sections.

Data availability statement

The original contributions presented in the study are included in the article/Supplementary Material, further inquiries can be directed to the corresponding authors.

Author contributions

YD: Conceptualization, Data curation, Formal Analysis, Funding acquisition, Methodology, Writing–original draft, Writing–review and editing. TL: Formal Analysis, Visualization, Writing–original draft. JX: Investigation, Supervision, Validation, Writing–review and editing.

Funding

The author(s) declare financial support was received for the research, authorship, and/or publication of this article. This research was funded by the Scientific Research Program of Shaanxi Provincial Education Department (Program No. 22JK0563), the Social Science Planning Fund of Xi'an City (23JX170), the Key Intelligent Database Research Project of Shaanxi Social Science Federation (2023ZD1100), the Natural Science Basic Research Plan in Shaanxi Province of China (2023-JC-QN-0261), the Qin Chuangyuan high-level innovation and entrepreneurship talent project (QCYRCXM-2022-242), the Social Science Foundation of Shaanxi Province of China (2023R361).

Conflict of interest

The authors declare that the research was conducted in the absence of any commercial or financial relationships that could be construed as a potential conflict of interest.

Publisher's note

References

Aashto, A. (2011). *Policy on geometric design of highways and streets*. 5th Edition. Washington, D. C. USA: American Association of State Highway and Transportation Officials, 231–240.

Ataei, S. M., Aghayan, I., Pouresmaeili, M. A., Babaie, M., and Hadadi, F. (2021). The emission factor adjustments of the passenger cars in multi-story car parks under drive modes. *Environ. Sci. Pollut. Res.* 29, 5105–5123. doi:10.1007/s11356-021-15960-6

Bonneson, J. A. (2000). *Superelevation distribution methods and transition designs NCHRP project 439*. Washington, D. C: Transportation Research Board.

Bonneson, J. A., and Pratt, M. P. (2009). Model for predicting speed along horizontal curves on two-lane highways. *Transp. Res. Rec.* 2092, 19–27. doi:10.3141/2092-03

Cruz, P., Echaveguren, T., and González, P. (2017). Estimación del potencial de rollover de vehículos pesados usando principios de confiabilidad. *Rev. Ing. Construccion* 32 (1), 5–14. doi:10.4067/s0718-50732017000100001

David, L., Ana, M. P., Alfredo, G., and García, A. (2018). Impact of horizontal geometric design of two-lane rural roads on vehicle CO_2 emissions. *Transp. Res. Part D, Transp. Environ.* 59, 46–57. doi:10.1016/j.trd.2017.12.020

Ding, F., and Jin, H. (2018). On the optimal speed profile for eco-driving on curved roads. *IEEE Trans. Intelligent Transp. Syst.* 19, 4000–4010. doi:10.1109/tits.2018.2795602

Dong, Y. P., Xu, J. L., and Gu, C. W. (2020). Modelling carbon emissions of diesel trucks on longitudinal slope sections in China. *PlosOne* 15 (6), e0234789. doi:10.1371/journal.pone.0234789

Dong, Y. P., Xu, J. L., Li, M. H., Jia, X., and Sun, C. (2019). Association of carbon emissions and circular curve in northwestern China. *Sustainability* 11 (4), 1156. doi:10.3390/su11041156

Dong, Y. P., Xu, J. L., and Ni, J. (2023). Carbon emission model of vehicles driving at fluctuating speed on highway. *Environ. Sci. Pollut. Res.* 30 (7), 18064–18077. doi:10.1007/s11356-022-23064-y

Faisal, A. (2005). Theoretical analysis for horizontal curves based on actual discomfort speed. *J. Transp. Eng.* 131 (11), 843–850. doi:10.1061/(asce)0733-947x(2005)131:11(843)

Fitzpatrick, K., Elefteriadou, L., Harwood, D. W., Collins, J. M., McFadden, J., Anderson, I. B., et al. (2000). Speed prediction for two-lane rural highways, drivers. Available at: https://www.fhwa.dot.gov/publications/research/safety/ihsdm/99171.pdf (accessed on November 30, 2023).

IPCC (Intergovernmental Panel on Climate Change) (2006). "Guidelines for national greenhouse gas inventories; prepared by the national greenhouse gas inventories program," in *IPCC-XLIX-9 – adoption and acceptance of 2019 refinement*. Editors H. S. Egglestone, L. Buendia, K. Miwa, T. Ngara, and K. Tanabe (Tsukuba, Japan: IGES).

Japan Road Association (2004). *Explanation and application of road structure ordinance*. Tokyo, Japan: Maruzen Publishing Co., Ltd.

Ko, M. (2015). Incorporating vehicle emissions models into the geometric highway design process. *Transp. Res. Rec. J. Transp. Res. Board* 2503, 1–9. doi:10.3141/2503-01

Lin, C. Y., Zhou, X. Y., Wu, D. Y., and Gong, B. W. (2019). Estimation of emissions at signalized intersections using an improved MOVES model with GPS data. *Int. J. Environ. Res. Public Health* 16, 3647. doi:10.3390/ijerph16193647

Mitschke, M., and Wallentowitz, H. (2014). *Dynamik der Kraftfahrzeuge*. 5nd Ed. Berlin: Springer Nature.

Moradi, E., and Miranda-moreno, L. (2020). Vehicular fuel consumption estimation using real-world measures through cascaded machine learning modeling. *Transp. Res. Part D* 88, 102576. doi:10.1016/j.trd.2020.102576

Pan, Y., Qiao, F., Tang, K., Chen, S., and Ukkusuri, S. V. (2020). Understanding and estimating the carbon dioxide emissions for urban buses at different road locations: a comparison between new-energy buses and conventional diesel buses. *Sci. Total Environ.* 703, 135533. doi:10.1016/j.scitotenv.2019.135533

Paolo, P. (2018). Influence of the general character of horizontal alignment on operating speed of two-lane rural roads. *Transp. Res. Rec.* 2075 (1), 16–23. doi:10.3141/2075-03

Peng, J., Chu, L., and Fwa, T. F. (2020). Determination of safe vehicle speeds on wet horizontal pavement curves. *Road Mater. Pavement Des.* 22 (11), 2641–2653. doi:10.1080/14680629.2020.1772350

Russo, F., Biancardo, S. A., and Busiello, M. (2016). Operating speed as A key factor in studying the driver behavior in a rural context. *Transport* 31 (2), 260–270. doi:10.3846/16484142.2016.1193054

Sil, G., Nama, S., Asce, S. M., and Maurya, A. K. (2019). Modeling 85th percentile speed using spatially evaluated free-flow vehicles for consistency-based geometric design. *J. Transp. Eng.* 146 (2), 1–12. doi:10.1061/jtepbs.0000286

Wang, X. M., Wang, X. S., Cai, B., and Liu, J. (2019). Combined alignment effects on deceleration and acceleration: a driving simulator study. *Transp. Res. Part C Emerg. Technol.* 104, 172–183. doi:10.1016/j.trc.2019.04.027

Wen, H., and Eric, T. D. (2010). Models of acceleration and deceleration rates on A complex two-lane rural highway results from a night time driving experiment. *Transp. Res.* 12, 397–408. doi:10.1016/j.trf.2010.06.005

Wong, J. Y. (2008). *Theory of ground vehicles*. 4th Edition. New York, USA: John Wiley& Sons, Ltd.

Xu, J. L., Dong, Y. P., and Yan, M. H. (2020). A model for estimating passenger-car carbon emissions that accounts for uphill, downhill and flat roads. *Sustainability* 12 (5), 2028. doi:10.3390/su12052028

Yin, Y., Wen, H., Sun, L., and Hou, W. (2020). Study on the influence of road geometry on vehicle lateral instability. *J. Adv. Transp.* 2020 (6), 1–15. doi:10.1155/2020/7943739

You, S. S., and Jeong, S. K. (2002). Controller design and analysis for automatic steering of passenger cars. *Mechatronics* 12 (3), 427–446. doi:10.1016/s0957-4158(01)00005-8

Zhang, L., Yu, L., Wang, Z., Zuo, L., and Song, J. (2016). All-wheel braking force allocation during a braking-in-turn maneuver for vehicles with the brake-by-wire system considering braking efficiency and stability. *IEEE Trans. Veh. Technol.* 65 (6), 4752–4767. doi:10.1109/TVT.2015.2473162

Zhang, X., Xu, J., Li, M., Li, Q., and Yang, L. (2019). Modeling impacts of highway circular curve elements on heavy-duty diesel trucks' CO_2 emissions. *Int. J. Environ. Res. Public Health* 16 (14), 2514. doi:10.3390/ijerph16142514

frontiers | Frontiers in Energy Research

TYPE Original Research
PUBLISHED 15 January 2024
DOI 10.3389/fenrg.2023.1346005

OPEN ACCESS

EDITED BY
Meng Jia,
Shandong University of Science and Technology, China

REVIEWED BY
Jia Sun,
Southeast University, China
Yingxin Hui,
Ningxia University, China

*CORRESPONDENCE
Lei Ma,
malei@roadmaint.com
Zongjun Pan,
panzongjun@roadmaint.com

RECEIVED 28 November 2023
ACCEPTED 20 December 2023
PUBLISHED 15 January 2024

CITATION
Ma L, Cao J, Pan Z, Guo L, Zhang H, Ma Y, Yang G and Wang H (2024), Use of condition-based valuation approach to evaluate the maintenance decision of pavement assets: a case study of Yunnan Province in China. *Front. Energy Res.* 11:1346005. doi: 10.3389/fenrg.2023.1346005

Use of condition-based valuation approach to evaluate the maintenance decision of pavement assets: a case study of Yunnan Province in China

Lei Ma*, Jiang Cao, Zongjun Pan*, Liming Guo, Hai Zhang, Yunqian Ma, Guang Yang and Haoyang Wang

The RoadMAinT Co., Ltd., Beijing, China

Pavements are critical components of highway assets, but accurately estimating their value can be challenging due to the lack of connection between valuation and long-term service performance degradation. To address this issue, the replacement cost and condition-based valuation methods were introduced using the Yunnan province highway in China as an example, which divided pavement into four performance states based on service stages. The rationality of maintenance decisions and the impact of preventive maintenance investment on life cycle assessments were also considered. The results indicate that there are issues of irrational allocation of maintenance funds of the highway in Yunnan province, and a higher proportion of preventive maintenance investment is required. Moreover, it is recommended to balance the maintenance funds for bridge and tunnel engineering in the following year, focusing on bridge engineering with a rapid decline in the newness rate. The implementation of preventive maintenance has a positive correlation with the replacement cost and newness rate of the road sections. Through comparison, it was found that the road surface renewal rate in 2019 was lower than that in 2018, and some highway management departments in certain regions need to adjust their preventive maintenance strategies. Overall, the condition-based pavement asset valuation method comprehensively considers each stage of pavement operation and can serve as an effective tool for evaluating pavement asset depreciation. This research finding can promote the sustainable development of road infrastructure.

KEYWORDS

highway assets, condition-based valuation method, pavement, maintenance strategy, newness rate, life cycle assessments

1 Introduction

Highway assets refer to the infrastructure assets that are formed through construction and are an essential part of government assets. Non-toll highway assets include the land used for highways, highways (including highway bridges, road tunnels, and road ferries, etc.), structures, traffic engineering, and roadside facilities (including traffic safety facilities, management facilities, service facilities, and green environmental protection facilities), as well as other assets that constitute an indispensable part of the normal use of the road. Due

to the increment in service life, highway assets inevitably face the issue of depreciation (Alshboul et al., 2021; Amin et al., 2022; Yuan et al., 2023). It is necessary to evaluate and calculate the value of non-toll highway assets combined with the actual situation of the transportation industry (Ivannikov and Dollery, 2020). Moreover, understanding the correlation between the dynamic changes in the value of non-toll highway assets and the level of road condition detection and maintenance can provide data support for asset management, financial management, budget management, and performance management, thereby enhancing the asset management level of highway infrastructure (Sun et al., 2017; Li and McNeil, 2021; Jiang et al., 2022).

Asset depreciation and valuation are generally recognized features in private sector accounting that are utilized to justify fund investment (Kuroki, 2022). The valuation of assets is crucial in various systems of worldwide asset conservancy since it converts the conditions of the infrastructure into financial terminology, like equity or public wealth. Road networks are critical infrastructure assets possessed and maintained by regional governments, and the valuation of highway assets has gained considerable attention in recent decades (Hwangbo et al., 2020). The world's leading economies have built up regulations or specifications for asset valuation to enhance asset management practices. For instance, the Government Accounting Standard Board (GASB) in the United States mandated regional authorities to report the value of the assets that they possess and provided representative valuation methods to select from through Statement No. 34 in 1999. The Institute of Public Works Engineering Australasia (IPWEA) in Australia collaborates with the Australasian Road Transport and Traffic Bureau to develop the Management Manual of International Infrastructure, which includes comprehensive guidelines and financial plans for the asset management of regional institutions. Similarly, the Chartered Institute of Public Finance and Accounting (CIPFA) designed a practice criterion for transportation infrastructure assets in Great Britain, offering references for allocating financial values to substantial assets. In China, administrative institutions are also required to conduct the enrolment and management of transportation infrastructure in alignment with specified standards.

Asset valuation is a crucial aspect of highway asset management, and numerous researches have been conducted to explore the potential for incorporating asset valuation into transport asset management plans. However, traditional valuation methods treat assets as homogeneous units and neglect valuation criteria reflecting asset users' and agencies' perspectives, such as asset service life and condition (Dojutrek et al., 2012). To address these limitations, a new methodology called elemental decomposition and multi-criteria (EDMC) has been developed (Dojutrek et al., 2014). This approach recognized that each element of transportation infrastructure assets may deteriorate at a different rate and conducted separate valuations of these elements, providing a more comprehensive and accurate valuation compared to traditional methods. Amekudzi-Kennedy et al. (Amekudzi-Kennedy et al., 2019) reviewed asset valuation methodologies with transportation applications and proposed innovative paths and future orientation to enhance existing capabilities in capturing an expanding notion of transportation infrastructure value. Hoang et al. (Hoang et al., 2020) proposed a comprehensive model integrating economic and utility concepts for bridge valuation. The specific performance measures in this model involve average annual daily traffic (AADT), safety, mobility, physical condition, and direct time savings. Lim et al. (Lim et al., 2019; Porras-Alvarado et al., 2015) employed utility theory and developed a productivity-based asset valuation method that reflects not only the actual conditions of the highway, but also its functionality and overall level of use.

Among the various highway assets, pavement is a vital component of highway infrastructure, and the valuation method employed can significantly influence asset value and decision-making outcomes, depending on the mathematical formulations and assumptions employed. Therefore, selecting an appropriate method to determine the value of existing infrastructure assets is crucial for highway asset management and maintenance decision-making. The replacement cost method is commonly used internationally to calculate the value of highway assets among the multiple methods (Sirirangsi et al., 2003; Lee and Lee, 2014; Sun et al., 2023). The key parameters include the total replacement cost and depreciation (substantive, economic, and functional). Substantive depreciation is related to asset performance and service levels and can be divided into three evaluation methods: straight-line method, S-shaped performance depreciation method, and condition-based depreciation method (Howe, 2004). The first two methods calculate depreciation based on service life, establishing a linear relationship between service life and depreciation. The condition-based depreciation method measures asset depreciation based on service level, using indicators such as pavement performance and capital input to indirectly consider the value of physical depreciation (Lombardi et al., 2021). Depreciation only occurs when asset performance falls below predetermined standards. When asset performance deteriorates significantly, there may also be situations of scrapping.

Regrettably, the current body of research concerning the valuation and assessment of pavement assets in highway infrastructure is scant. Furthermore, relating the degradation of pavement performance to the replacement costs at each stage is a formidable task since it necessitates identifying the appropriate maintenance strategy and the optimal allocation of the available budget for pavement throughout its lifecycle (Fwa and Farhan, 2012; Xian and Yuanshun, 2018; Santos et al., 2022). As a result, it is imperative to conduct condition-based valuation and assessment in tandem with engineering practices to furnish data to grasp the dynamic shifts of pavement assets and to provide decision-making recommendations for enhancing the maintenance level of highways.

2 Objective and scope

This study aims to establish a connection between the valuation of pavement assets and their performance degradation, through the utilization of the replacement cost and condition-based valuation approach. Using the Yunnan province highway in China as an example, pavements were divided into four stages according to their performance during use. The scheme for this research is detailed in Figure 1. The specific objectives are as follows:

1) Evaluate the rationality of maintenance strategies employed by the management department;

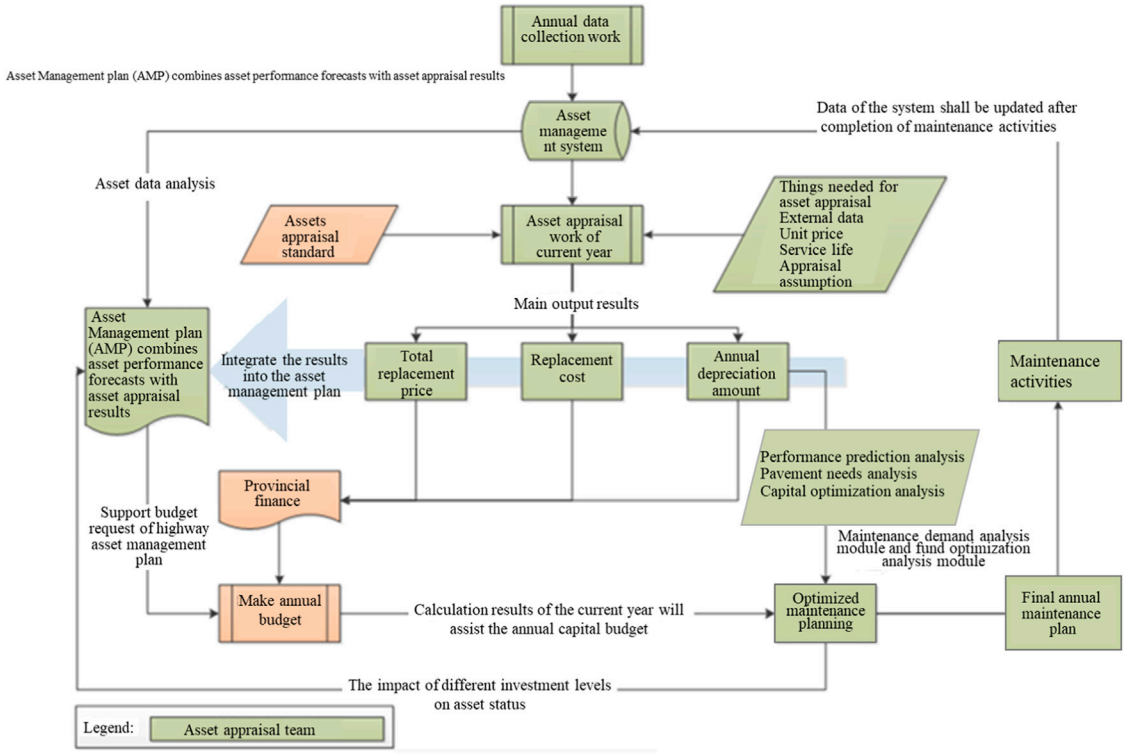

FIGURE 1
Scheme for this research.

2) Analyze the impact of preventive maintenance investment on pavement assets;
3) Provide suggestions for the maintenance strategies of highway assets under the jurisdiction of the Yunnan Provincial Highway Bureau.
4) Establish a correlation between changes in the value of transportation infrastructure and the annual work of management organizations through asset management systems, and establish performance evaluation indicators for internal management work.

3 Depreciation methodology and overall calculation method

3.1 Depreciation and replacement cost

3.1.1 Depreciation

Depreciation *D*) refers to the loss of asset value, including functional depreciation, economic depreciation, and substantive depreciation. Wherein:

Functional depreciation is the loss of asset value resulting from the relative obsolescence of asset function due to advancements in technology. In the calculation of full replacement price, functional depreciation is often not considered, as total replacement price is typically used.

Economic depreciation is the loss of asset value due to external factors such as idle assets, declining earnings, and changes in the broader economic environment. Non-toll roads, as "public infrastructure" generally occupy a dominant position in the overall road network and are typically not impacted by external factors such as political influences and macroeconomic policies. As a result, economic depreciation was not considered in the valuation of such assets as well.

Due to China's regulations, all provinces are required to monitor the technical condition of the national highway network every year. Highways with poor road surface technical conditions will be repaired in the same year, and there are rarely cases of roadbed damage due to severe road surface damage and long-term lack of repair. Through years of monitoring data investigation throughout the province, it has been found that the majority of highways use semi-rigid roadbeds, which meet industry standards for long-term performance and pavement structural strength, and meet functional requirements. Therefore, depreciation is not considered for the roadbeds in this asset evaluation. Substantive depreciation refers to the loss of value of assets caused by the degradation or deterioration of the physical properties of assets due to use and natural forces. To measure substantive depreciation, methods such as the service life method, observation method, and rehabilitation expense method are commonly employed. The pavement engineering-performance valuation method is a calculation method for highway engineering depreciation that considers the technical condition of highway assets and the influence of asset performance on value. This method is an advanced application of the rehabilitation expense method in the evaluation of highway engineering value. The basic principle of the pavement engineering-performance valuation method is to restore pavement performance to its optimal level, with substantive depreciation of pavement assets

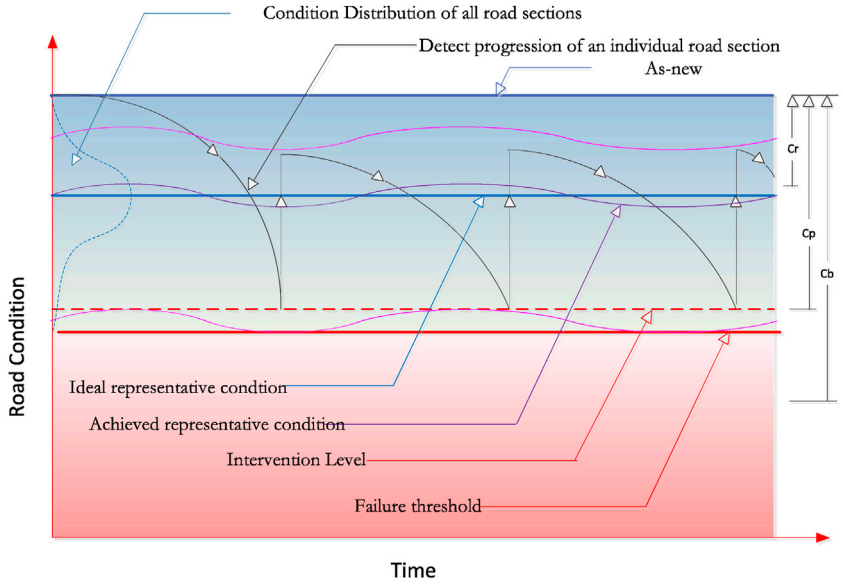

FIGURE 2
Composition of pavement engineering rehabilitation expense.

considered equal to the rehabilitation expense required to achieve this level (Snaith and Orr, 2006), as shown in Figure 2.

From Figure 2, it can be found that there are four types of working state according to the performance:

1) Best performance state: The status of new construction, reconstruction, and expansion.
2) Normal service condition: Pavement performance is at a normal service level.
3) Optimal maintenance time: This state is appropriate for implementing pavement repair measures when the road surface performance is lower than the intermediate maintenance standard and within the range of intervention level.
4) Structural rehabilitation state: Pavement performance is lower than the set heavy maintenance standard. The structural overhaul is necessary to restore its normal service level.

Based on the varying state of each pavement section of a highway network, the rehabilitation expense of the overall pavement can be calculated as follows:

a. For pavement sections in the highway network at the best performance state, the rehabilitation expense is zero.
b. For pavement sections in the network at normal service conditions, the level of pavement conditions tends to be higher in those sections in use. The rehabilitation expense of this pavement section is based on the level of the overall highway network. The proportion of the pavement repair cost with the optimal maintenance time is taken as the principle of pavement repair cost to calculate and can be represented by C_r.
c. In terms of pavement section at optimal maintenance time in the highway network, the required maintenance activities can be determined as per performance status to calculate the required maintenance engineering cost, which can be represented by C_p.
d. In terms of pavement section at structural rehabilitation state in the highway network, an overhaul or even an upgrade is required to restore its performance, the amount of capital required for optimal maintenance time tends to be bulky, and the cost of this part is expressed by C_b.

It can be concluded that the substantive depreciation of pavement engineering is equivalent to its rehabilitation expense, which is the sum of the costs for each of the four working states described above.

$$C = C_r + C_p + C_b \tag{1}$$

where C is the depreciation amount of pavement engineering, the cost of rehabilitating the pavement to best performance state; C_r is the rehabilitation expense required by the pavement at normal service conditions; C_p is the rehabilitation expense required by the pavement at optimal maintenance time; C_b is the rehabilitation expense required by the pavement at structural rehabilitation state.

(1) Calculation method of substantive depreciation at normal state

The rehabilitation expense for a certain proportion of pavement rehabilitation expense during optimal maintenance time can be used as the pavement's rehabilitation expense by comparing it to the overall road network level. The formula is as follows:

$$C_r = p \times U_p \times S_r \tag{2}$$

where p is the proportion of daily maintenance pavement section, which is set as a percentage. The value here is 33%, that

is, the proportion of the area requiring daily maintenance is 33%; U_p is the unit price of functional maintenance project; S_r is the total area of normal service road section.

(2) Calculation method of substantive depreciation at optimal maintenance time

A highway network with a high maintenance level tends to have relatively stable capital investment. The section area in the road network with the optimal maintenance time shall be a fixed proportion of the total area of the road network, according to which the required cost of maintenance activities can be determined. This part of the maintenance work cost is expressed as functional maintenance work cost.

The calculation formula is as follows:

$$C_p = \Sigma\left(U_p \times S_p\right) \tag{3}$$

where C_p is the functional maintenance work cost is the maintenance cost of functional maintenance of the road network; U_p is the state/city functional maintenance project unit price; S_p is the total area of road section at optimal maintenance time.

(3) Calculation method of substantive depreciation at structural repair state

In terms of road section at structural repair state in the highway network, an overhaul or even an upgrade is required to restore its performance. The cost of structural maintenance work for each section is the substantive depreciation of the section. The formula is as follows:

$$C_b = \Sigma\left(U_b \times S_b\right) \tag{4}$$

where C_b is the maintenance cost for structural rehabilitation of the road network; U_b is the structural maintenance project unit price of each state/city can be adjusted according to local conditions every year of each state/city by using relevant parameters; S_b is the total area of road section at structural repair ($PQI < 70$). The pavement quality index (*PQI*) is a comprehensive index used to evaluate pavement technical condition. It includes the corresponding sub-indexes: pavement damage condition index (*PCI*), pavement driving quality index (*RQI*), pavement rut depth index (*RDI*), pavement jumping index (*PBI*), pavement wear index (*PWI*), pavement skid resistance index (*SRI*), and pavement structural strength index (*PSSI*).

3.1.2 Total replacement price

Total replacement price (*TRP*) is a financial metric that represents the total cost of purchasing or constructing an asset that would perform identically to the one being evaluated under present conditions. It typically comprises two components: restoration and renewal replacement costs. Restoration replacement cost is the cost required to recover the expenditure incurred in the acquisition and construction of the top-performance road property at current prices, using the same materials, construction, or manufacturing standards, designs, formats, and techniques as those of the original route. Renewal replacement cost, on the other hand, refers to the cost of producing or building new roads with the same functionality at current prices by using top-performance materials and adhering to modern standards, designs, and formats. In this study, the renewal replacement cost is used. The formula for calculating the total replacement price is as follows:

$$TRP = Q \times U \tag{5}$$

where TRP is the total replacement price of assessed assets; Q is the number of projects of different types of assets (volume, length, etc.); U is the technical-economic indicator of the quantity (volume and length) per unit of projects of different types of assets.

3.1.3 Replacement cost

The replacement cost (*RC*) of non-toll highway assets is the asset value obtained by subtracting the real depreciation, functional depreciation, and economic depreciation of the asset from the total replacement price of the asset in its best performance state under current conditions (Deng et al., 2020; Junzhe et al., 2023). The basic formula for highway infrastructure replacement cost calculation is as follows:

$$RC = TRP - D \tag{6}$$

4 Case study of Yunnan Province in China

4.1 Measuring range

Our team has completed the public infrastructure including land used for highways, highway (including highway Bridges and culverts, highway tunnels, and highway ferries, etc.) and structures, traffic engineering and facilities along the road (including traffic safety facilities, management facilities, service facilities, green and environmental protection facilities) was measured. However, it does not include buildings, equipment and vehicles used for management and maintenance which are independent of public infrastructure and do not constitute an indispensable part of its usage.

4.2 Calculation object

The total highway infrastructure (non-toll roads) from 2018 to 2019 under the jurisdiction of The Highway Bureau of Yunnan Province was investigated, as summarized in Table 1.

5 Results and discussion

5.1 Overall analysis of replacement cost

A measurement model for replacement cost was employed to determine the total replacement price of all non-toll highway infrastructure assets in Yunnan Province (excluding the value of public land), which has a total management and maintenance mileage of 20, 873.658 km. The results showed that the total replacement price was RMB 350, 013, 510, 622, which was

TABLE 1 Basic information on highway infrastructure of Yunnan Province.

Name	Unit	National highway	Provincial highway	County highway	Total
as of 31 December 2018					
Class I highway	Kilometer	630.067	148.615	6.912	688.081
Class II highway		6811.300	3232.262	193.551	10237.113
Class III highway		2726.449	1480.026	346.447	4552.922
Class IV highway		1760.971	2628.969	407.211	4797.151
Substandard highway		62.159	183.678	90.855	336.692
Total		11893.433	7673.55	1044.976	20611.959
as of 31 December 2019					
Grade I highway	Kilometer	630.067	134.338	21.925	786.330
Grade II highway		7243.143	3281.010	277.638	10801.791
Grade III highway		2736.328	1337.197	622.998	4696.523
Grade IV highway		1415.045	2080.571	923.817	4419.433
Substandard highway		0	55.797	113.784	169.581
Total		12024.583	6888.913	1960.162	20873.658

TABLE 2 Summary of highway asset replacement cost in Yunnan Province.

Category	Total replacement price/RMB	Depreciation/RMB	Replacement cost/RMB	Newness rate/%
Pavement	56, 594, 974, 587	12, 725, 819, 356	43, 869, 155, 231	77.51
Subgrade	222, 539, 847, 264	0	222, 539, 847, 264	100.00
Culvert	6, 332, 053, 974	3, 160, 815, 369	3, 171, 238, 605	50.08
Bridge	36, 398, 007, 756	7, 940, 686, 522	28, 457, 321, 234	78.18
Tunnel	13, 011, 979, 802	2, 943, 863, 301	10, 068, 116, 501	77.38
Roadside facilities	15, 136, 647, 239	4, 957, 097, 705	10, 179, 549, 534	67.25
Total	350, 013, 510, 622	31, 728, 282, 253	318, 285, 228, 369	90.94

depreciated to RMB 31, 728, 282, 253, resulting in a replacement cost of RMB 318, 285, 228, 369, as presented in Table 2. The newness rates for various infrastructure components were also calculated, such as 77.51% for pavement engineering, 100% for subgrade engineering, 50.08% for culvert engineering, 78.18% for bridge engineering, 77.38% for tunnel engineering, 67.25% for roadside facilities, and 90.94% for the overall newness rate.

Furthermore, in comparison with 2018, the total mileage of Yunnan's overall highway infrastructure assets increased by 261.699 km at the end of 2019. Additionally, the total replacement price increased by RMB 5, 459, 649, 034, while the depreciation increased by RMB 5, 775, 520, 402. Consequently, the final replacement cost decreased by RMB 315, 871, 368.

From Figure 3, it indicates that as of 31 December 2019, the replacement cost of highway infrastructure reconstruction of Yunnan Province was RMB 318, 285, 228, 369, where pavement engineering accounts for 14%, subgrade accounts for 70%, culvert accounts for 1%, bridge accounts for 9%, tunnels accounts for 3%, and roadside facilities accounts for 3%. The replacement cost of subgrade engineering accounts for more than 60%, which is not depreciated in the calculation. In other types of assets, pavement engineering accounts for the largest proportion of highway assets, implying that pavement section is the main direction of maintenance fund investment.

In addition to subgrade engineering, it can be seen that the replacement cost of the pavement represents the largest share of highway assets at 46%, followed by bridge engineering at 30%, tunnel engineering at 10%, and facilities along the road at 11%. These findings suggest that the maintenance fund allocation to pavement engineering is a critical component of the overall maintenance fund, which aligns with the importance principle.

In terms of asset depreciation, it is noteworthy that pavement engineering experiences the most significant substantive depreciation, indicating that investment in pavement engineering constitutes the primary direction of maintenance fund allocation. With respect to pavement repair cost composition in Figure 4, major repair or structural rehabilitation cost constitutes approximately 16%, medium repair or periodic replacement cost constitutes

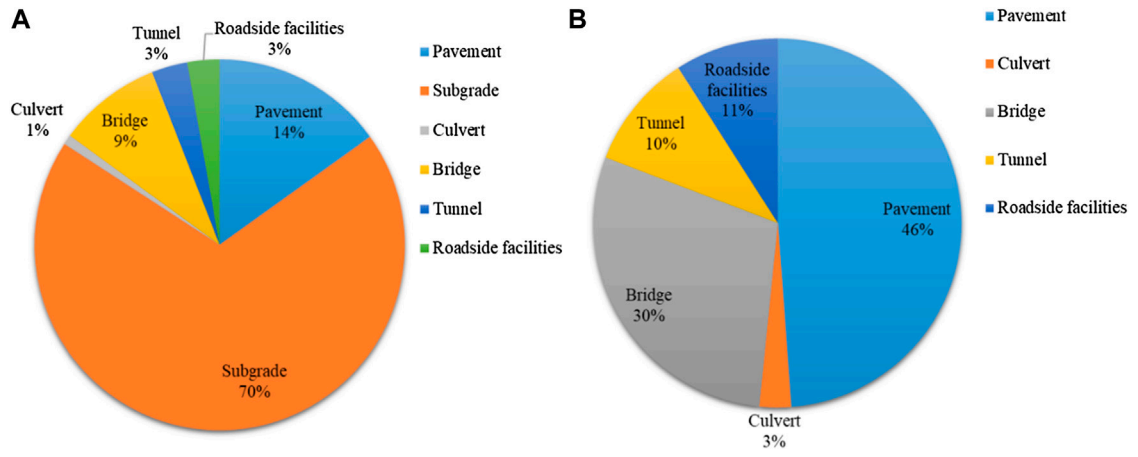

FIGURE 3
Proportions of each type of highway asset. **(A)** Include subgrade. **(B)** Exclude subgrade.

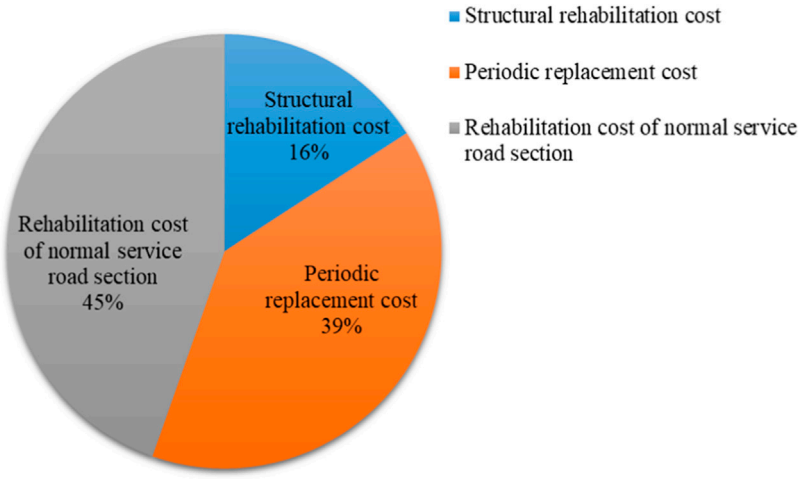

FIGURE 4
Cost composition of pavement rehabilitation.

around 39%, and normal service section repair cost accounts for about 45%. This breakdown better reflects the annual maintenance demand in terms of its scale and composition.

5.2 Benefit analysis of road network maintenance fund investment

5.2.1 Maintenance fund gap

Upon analyzing the newness rates of various types of assets in Figure 5, it is found that the newness rate of pavement engineering was 77.51% in 2019, indicating a slight decrease from 78.40% in 2018. This suggests that the newness rate of pavement assets declined by 0.89% during the study period. To estimate the maintenance fund gap, it is necessary to maintain the new rate in 2019 at the level of 2018 (78.40%), which would require an additional investment of RMB 503, 695, 274.

Similarly, the newness rate of culvert engineering decreased from 57.61% in 2018 to 50.08% in 2019, implying a 7.53% reduction in newness rate. To maintain the new rate in 2019 at the level of 2018, an additional investment of RMB 476, 803, 664 will be necessary.

In addition, the newness rate of bridge engineering was 78.18% in 2019 and 81.12% in 2018, indicating a newness rate decline of 2.94%. To maintain the new rate in 2019 at the level of 2018, an additional investment of RMB 1, 070, 101, 428 is required.

Moreover, the newness rate of tunnel assets increased from 68.72% in 2018 to 77.38% in 2019, with a newness rate increase of 8.66%. The value increment of tunnel assets estimated by the newness rate is RMB 1, 126, 837, 451.

Finally, the newness rate of roadside facilities was 67.25% in 2019, compared to 69.21% in 2018, with a newness rate decrease of 1.96%. To maintain the new rate in 2019 at the level of 2018 (69.21%), an additional investment of RMB 296, 678, 286 is required.

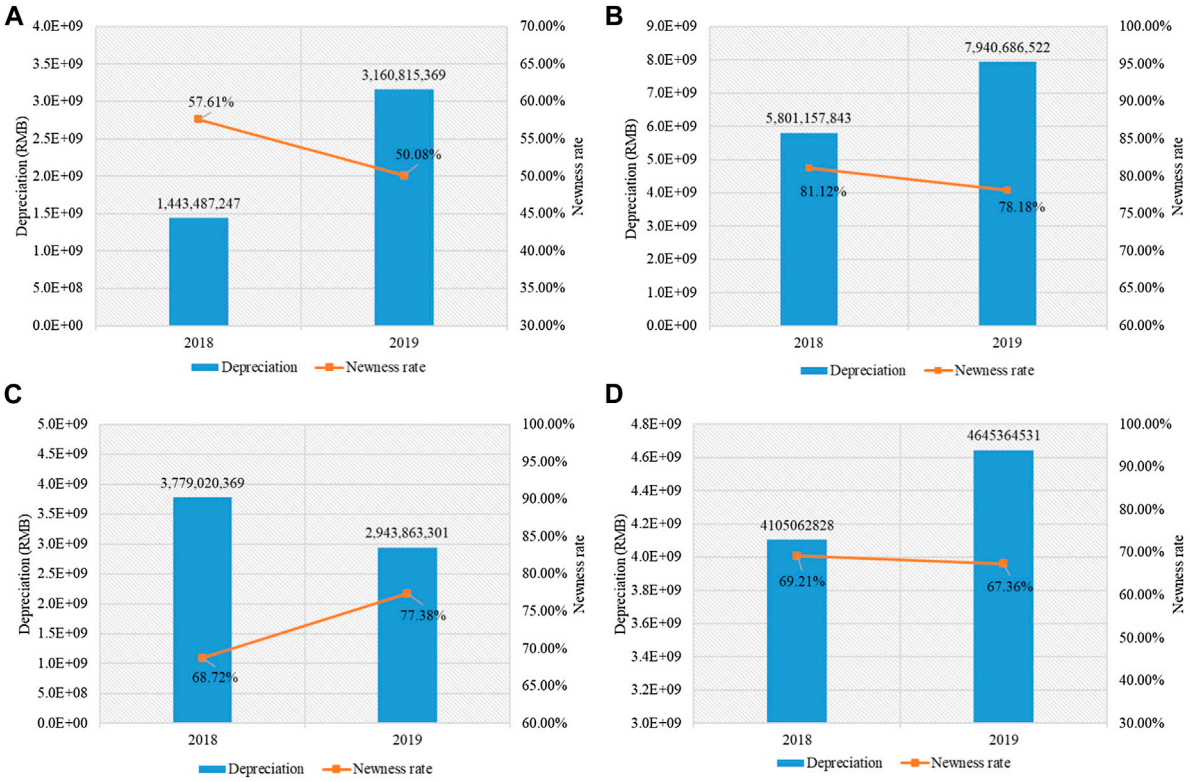

FIGURE 5
Depreciation and newness rate of various projects. **(A)** Culvert. **(B)** Bridge. **(C)** Tunnel. **(D)** Roadside facilities.

Based on the fund gap estimation of the newness rate of various projects, the total fund gap was RMB 2, 314, 162, 131 under the premise that the newness rate of overall projects in 2019 was kept the same as that in 2018. Bridge engineering was the part with the largest estimated fund gap, and tunnel engineering was the only type of engineering whose replacement rate had increased compared with that of the previous year. It is suggested that maintenance funds for bridge engineering and tunnel engineering should be balanced in the next year, focusing on bridge engineering with the rapid decline of the newness rate. It is worth noting that the newness rate of the tunnel has increased by 8.66% and it is not conducive to the rational allocation of funds to achieve the goal of maintaining the overall performance of the road network system in terms of value engineering. There may be excessive function phenomenon and the fund gap between bridge and tunnel projects can be solved by rational allocation of funds. The fund gap between pavement engineering and culvert engineering is second only to that of bridge engineering, indicating that new maintenance funds need to be injected into pavement engineering and culvert engineering. The number of road sections requiring overhaul increases sharply, and the pavement performance indexes of several sections decline dramatically. Therefore, the necessity and timeliness of maintenance fund investment are given higher priority than other types of projects.

5.2.2 Deployment of maintenance fund

After the maintenance fund is replenished in place, the fund should be allocated and used scientifically and rationally to maximize the use benefit of the fund according to the calculation results of the gap of the maintenance fund. For this purpose, the maintenance decision analysis was carried out with the pavement projects.

The comparison of pavement asset depreciation for the 2 years in Figure 6 shows that structural rehabilitation costs have increased exponentially in 2019 compared to 2018, while the periodic replacement costs, as well as the rehabilitation costs of the normal service section, are within the normal range of increase compared to 2018. The significant increase in structural rehabilitation costs corresponds to a decrease of 1.13 points in PQI (from 88.50 points to 87.37 points), which is attributed to the lag in the allocation of the normal service section rehabilitation costs from the maintenance costs. The majority of maintenance funds are taken up by structural rehabilitation and periodic replacement projects, while the total maintenance funds cannot support extensive structural rehabilitation and periodic replacement projects. As a result, the normal service section with the largest proportion cannot be funded for preventive maintenance and there is a decline in the overall performance of the road network.

Developing scientific maintenance strategies based on predetermined maintenance objectives can help maximize the benefits of maintenance funds. Through an analysis of the technical characteristics of Yunnan's road network, this paper proposes maintenance strategy recommendations for the highway assets under the jurisdiction of the Yunnan Provincial Highway Bureau:

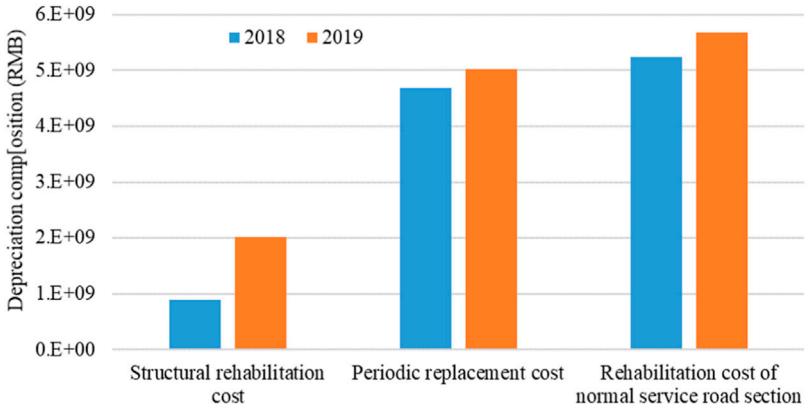

FIGURE 6
Depreciation composition of highway assets in 2018 and 2019.

1) Continue to implement rehabilitation and maintenance on the substandard roads in the road network until basic eliminating the substandard roads present in the network;
2) Combining with the current technical condition of the general road network, it is necessary to vigorously implement preventive maintenance and increase the proportion of preventive maintenance in maintenance projects to prevent the rapid deterioration of road conditions and achieve the goal of a virtuous cycle of the road network;
3) For road sections with a road condition level between preventive and rehabilitation maintenance, daily maintenance work should be strengthened, and road surface distresses should be treated in a timely manner to decelerate the rate of deterioration of road conditions. Rehabilitation and maintenance should be scheduled for the following year based on the road conditions.

5.3 Impact of preventive maintenance investment on pavement assets

Taking pavement engineering as an example, this paper conducted a specialized and detailed analysis of the impact of preventive maintenance investment on pavement assets for the Highway Administration as the analysis unit, by comparing the changes in replacement costs between 2018 and 2019.

As shown in Figure 7, the replacement cost (initial assessment) of pavement assets in 2018 was RMB 39, 292, 036, 245. the corresponding value had witnessed an increase of 11.65% and reached RMB 43, 869, 155, 231 in 2019. This is due to the growth of the construction engineering price index and the grade improvement of several road sections, resulting in a faster growth rate of the replacement cost than the depreciation of pavement assets. The newness rate of pavement engineering decreased from 78.40% in 2018 to 77.51% in 2019, which is attributed to the decrease of 1.13 points in the *PQI* score for the entire road network.

The detailed information on replacement cost and newness rate of each bureau is listed in Figure 8. It can be observed that in 2019, the newness rate of the pavement in Diqing and Nujiang showed an improvement, while in places such as Kunming, Wenshan, Xishuangbanna, Yuxi, and Zhaotong, there was a relatively significant decline in the newness rate of the pavement.

The preventive maintenance details of each highway Bureau are shown in Figure 9 below. In 2019, the Yunnan Provincial Highway Bureau implemented a total mileage of 1, 677 km of preventive maintenance, accounting for 8.03% of the total management and maintenance, with a total investment of RMB 112.49 million. Among them, Honghe Highway Bureau displayed the largest mileage of preventive maintenance with 223 km, while Nujiang Highway Bureau had the least mileage of preventive maintenance with 30 km. Honghe Highway Bureau also invested the most in preventive maintenance, with RMB 13.1 million, while Nujiang Highway Bureau invested the least with RMB 2.23 million.

Overall, the average cost of preventive maintenance per kilometer in 2019 was RMB 67, 078/km, as depicted in Figure 10. Among them, Qujing Highway Bureau had the highest investment in preventive maintenance per kilometer at RMB 114, 237/km, while Diqing Highway Bureau had the lowest investment at RMB 42,481/km. From the changes in replacement cost per kilometer in 2018 and 2019, the preventive maintenance investments have led to an increase in replacement cost per kilometer for 15 highway bureaus, including Baoshan, Chuxiong, Dali, Dehong, Diqing, Honghe, Kunming, Lijiang, Lincang, Nujiang, Pu'er, Qujing, Wenshan, Yuxi, and Zhaotong. Only Xishuangbanna Highway Bureau exhibited a slight decrease in replacement cost per kilometer.

Regarding the changes in the newness rate from 2018 to 2019, the preventive maintenance investment led to an increase for five highway bureaus, including Diqing, Lijiang, Lincang, Nujiang, and Qujing. However, the newness rates of the other 11 highway bureaus had decreased. This indicates that preventive maintenance investment has achieved better results for Diqing, Lijiang, Lincang, Nujiang, and Qujing Highway Bureaus. The high proportion of preventive maintenance mileage in certain cities has led to an increase in replacement cost per kilometer, indicating a positive correlation between preventive maintenance mileage and replacement cost per kilometer. The overall trend is shown in the Figs below.

Comparing the changes in replacement cost per kilometer and the proportion of preventive maintenance mileage in Figure 11A, it

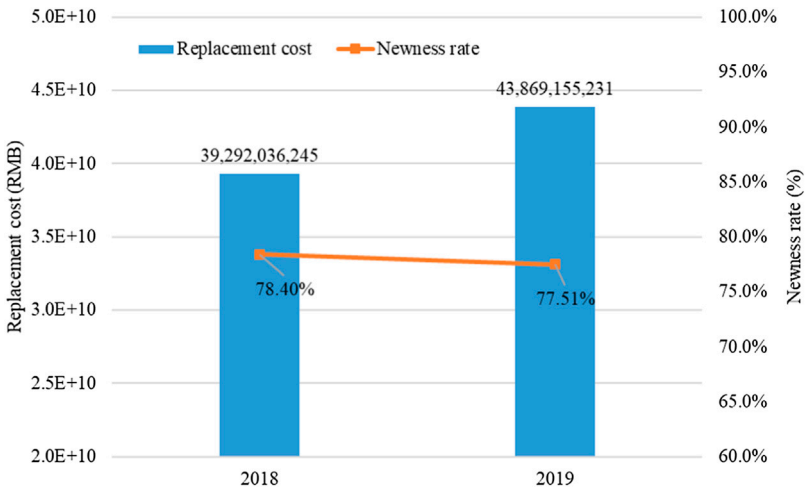

FIGURE 7
Replacement cost and newness rate of pavement engineering in 2018 and 2019.

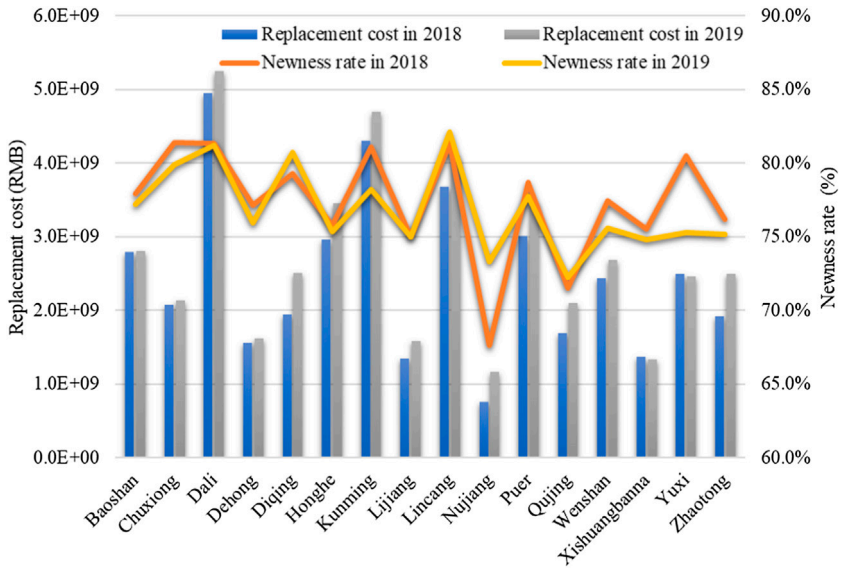

FIGURE 8
Replacement cost and newness rate of pavement asset in each bureau.

can be seen that Diqing Highway Bureau possesses the highest proportion of preventive maintenance mileage implemented, accounting for 11.75%. Its replacement cost per kilometer has also increased the most, reaching RMB 497, 013 per kilometer, indicating that the implementation of preventive maintenance has a positive correlation with the replacement cost of the road sections.

Comparing the proportion of preventive maintenance mileage and the changes in newness rate in Figure 11B, it can be seen that the implementation of preventive maintenance in Lijiang Highway Bureau, Qujing Highway Bureau, Nujiang Highway Bureau, Lincang Highway Bureau, and Diqing Highway Bureau has achieved an increase in newness rate. Among them, the increase in the newness rate of Nujiang Highway Bureau is the most significant, reaching 5.67%. Preventive maintenance has achieved the best effects in Nujiang. Whereas the newness rates of Kunming and Yuxi reduce uncharacteristically, implying the preventive maintenance plans may not be suitable, and the mileage proportion of periodic replacement and even structural rehabilitation should be increased.

6 Conclusion

In this study, a condition-based valuation method was introduced to establish the connection between the valuation of

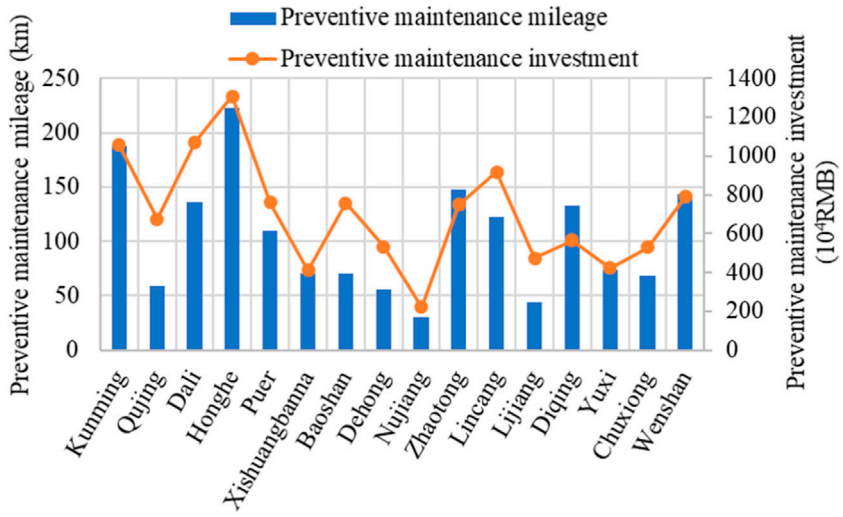

FIGURE 9
Preventive maintenance statistics for 2019 of Highway Bureau of Yunnan Province.

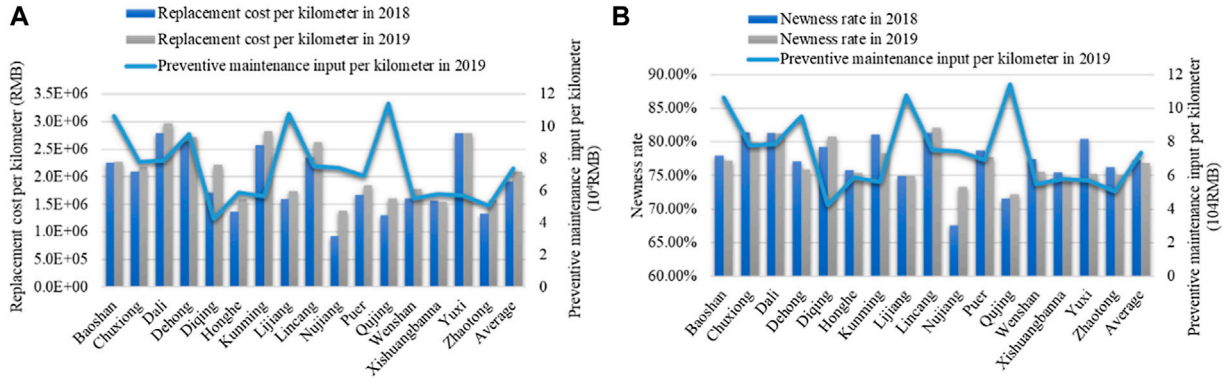

FIGURE 10
Relationship between replacement cost, newness rate, and preventive maintenance investment. **(A)** Replacement cost. **(B)** Newness rate.

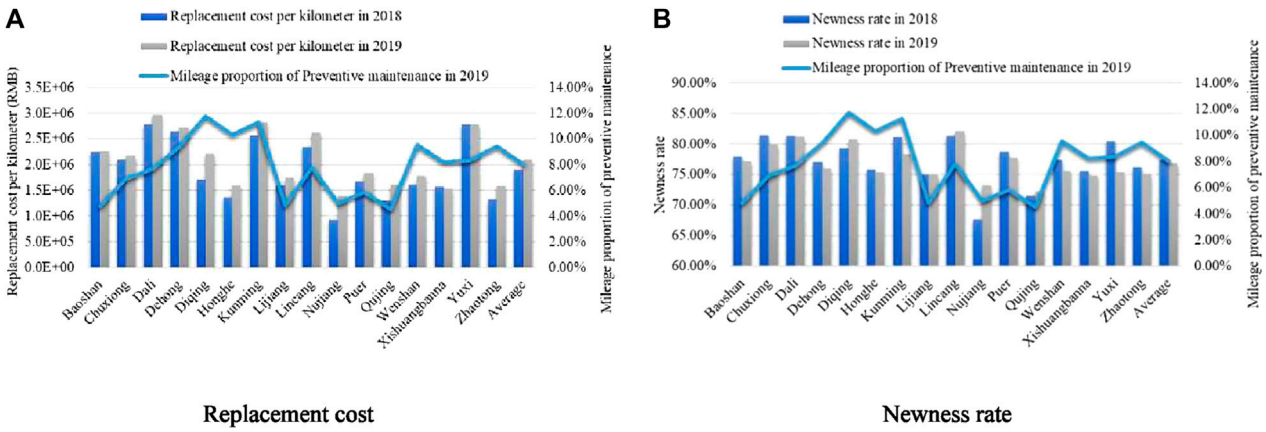

FIGURE 11
Relationship between replacement cost, newness rate, and mileage proportion of preventive maintenance. **(A)** Replacement cost. **(B)** Newness rate.

pavement assets and their performance degradation. Using the highway of Yunnan province in China as an example, pavements were divided into four performance states based on service stages. The rationality of maintenance decisions and the impact of preventive maintenance investment on pavement assets were also considered. Throughout the entire analysis, the following conclusions can be summarized.

1) The replacement cost and condition-based pavement asset valuation method comprehensively considers each stage of pavement operation and can serve as an effective tool for evaluating pavement asset depreciation.
2) There are issues of irrational allocation of maintenance funds for the highway in Yunnan province, and a higher proportion of preventive maintenance investment is required to maintain the newness rate of pavements.
3) It is recommended to balance the maintenance funds for bridge and tunnel engineering in the following years, focusing on bridge engineering with a rapid decline in the newness rate.
4) The implementation of preventive maintenance has a positive correlation with the replacement cost and newness rate of the road sections. The preventive maintenance strategies adopted by Lijiang, Qujing, Nujiang, Lincang, and Diqing Highway Bureaus are highly effective. However, other highway bureaus such as Kunming and Yuxi need to adjust their preventive maintenance strategies based on their actual highway technical conditions. In cases where preventive maintenance cannot restore pavement performance, functional or structural repair projects should be chosen.

Overall, the condition-based pavement asset valuation method allows highway management departments to utilize asset attributes, performance, and investment amounts to estimate future maintenance capital investments and improve highway asset management. It is worth noting that there are multiple factors that affect the replacement cost and newness rate of pavement engineering, such as traffic volume, investment in major and intermediate rehabilitation, natural conditions, and Implementation quality of maintenance engineering. This paper singly analyzed the impact of preventive maintenance. Further items are required to be included in the following investigations.

Data availability statement

The original contributions presented in the study are included in the article/Supplementary material, further inquiries can be directed to the corresponding authors.

Author contributions

LM: Conceptualization, Data curation, Investigation, Project administration, Writing–original draft, Writing–review and editing. JC: Conceptualization, Data curation, Writing–original draft. ZP: Data curation, Methodology, Project administration, Validation, Writing–original draft, Writing–review and editing. LG: Investigation, Methodology, Writing–original draft. HZ: Investigation, Writing–original draft, Writing–review and editing. YM: Conceptualization, Investigation, Methodology, Writing–original draft. GY: Investigation, Validation, Writing–review and editing. HW: Investigation, Methodology, Validation, Writing–review and editing.

Funding

The author(s) declare that no financial support was received for the research, authorship, and/or publication of this article.

Conflict of interest

Authors LM, JC, ZP, LG, HZ, YM, GY, and HW were employed by The RoadMAinT Co., Ltd.

Publisher's note

References

Alshboul, O., Shehadeh, A., and Hamedat, O. (2021). Development of integrated asset management model for highway facilities based on risk evaluation. Int. *J. Constr. Manag.*, 1–10. doi:10.1080/15623599.2021.1972204

Amekudzi-Kennedy, A., Labi, S., and Singh, P. (2019). Transportation asset valuation: pre-peri-and post-fourth industrial revolution. *Transp. Res. Rec.* 2673, 163–172. doi:10.1177/0361198119846470

Amin, M. A., Pan, S., and Zhang, Z. (2022). Pavement maintenance and rehabilitation budget allocation considering multiple objectives and multiple stakeholders. *Int. J. Pavement Eng.* 1-14. doi:10.1080/10298436.2022.2027941

Deng, J., Han, X., Pan, Z., Wang, J., Zhang, H., Geng, G., et al. (2020). "Research on physical depreciation methods of non-toll road assets," in CICTP 2020: Advanced Transportation Technologies and Development-Enhancing Connections - Proceedings of the 20th COTA International Conference of Transportation Professionals, 1011–1021.

Dojutrek, M. S., Makwana, P. A., and Labi., S. (2012). *A methodology for highway asset valuation in Indiana*. West Lafayette, Indiana: Publication FHWA/IN/JTRP-2012/31. Joint Transportation Research Program, Indiana Department of Transportation and Purdue University.

Dojutrek, M. S., Volovski, M., and Labi, S. (2014). Elemental decomposition and multicriteria method for valuing transportation infrastructure. *Transp. Res. Rec.* 2460, 137–145. doi:10.3141/2460-15

Fwa, T. F., and Farhan, J. (2012). Optimal multiasset maintenance budget allocation in highway asset management. *J. Transp. Eng.* 138, 1179–1187. doi:10.1061/(ASCE)TE.1943-5436.0000414

Hoang, T., Han, Z., and Zhang, Z. (2020). Integrating economic and utility concepts for a comprehensive bridge valuation model. *Transp. Res. Rec.* 2674, 26–37. doi:10.1177/0361198120926509

Howe, S. (2004). Condition-based depreciation - the engineering perspective. *Aust. Acc. Rev.* 14, 48–55. doi:10.1111/j.1835-2561.2004.tb00240.x

Hwangbo, W., Mohammadi, A., Amador-Jimenez, L., and Kachua, S. (2020). Value-based optimisation for cross-asset maintenance in a Canadian municipality. *Asset Manag.* 7, 86–94. doi:10.1680/jinam.18.00036

Ivannikov, I., and Dollery, B. (2020). Accounting problems in infrastructure asset valuation and depreciation in new south wales local government. *Aust. Acc. Rev.* 30, 105–115. doi:10.1111/auar.12275

Jiang, W., Yuan, D., Shan, J., Ye, W., Lu, H., and Sha, A. (2022). Experimental study of the performance of porous ultra-thin asphalt overlay. *Int. J. Pavement Eng.* 23 (6), 2049–2061. doi:10.1080/10298436.2020.1837826

Junzhe, W., Zhi, C., Ming, C., and Jie, Z. (2023). A study of condition based valuation method for pavement asset management. *CICTP* 2023, 12–19.

Kuroki, M. (2022). Impact of depreciation information on capital budgeting among local governments: a survey experiment. *Acc. Rev.* 32, 201–213. doi:10.1111/auar.12355

Lee, D.-Y., and Lee, M.-J. (2014). A study of the asset valuation method for efficient road facility maintenance. *J. Asian Archit. Build. Eng.* 13, 279–286. doi:10.3130/jaabe.13.279

Li, J. Q., and McNeil, S. (2021). Data envelopment analysis for highway asset investment assessment. *J. Traffic Transp. Eng.* 8, 117–128. doi:10.1016/j.jtte.2019.06.001

Lim, T., Porras-Alvarado, J. D., and Zhang, Z. (2019). Pricing of highway infrastructure for transportation asset management. *Built Environ. Proj. Asset Manag.* 9, 64–79. doi:10.1108/BEPAM-05-2018-0083

Lombardi, R., Schimperna, F., Smarra, M., and Sorrentino, M. (2021). Accounting for infrastructure assets in the public sector: the state of the art in academic research and international standards setting. *Public Money Manag.* 41, 203–212. doi:10.1080/09540962.2020.1840761

Porras-Alvarado, J. D., Peters, D., Han, Z., and Zhang, Z. (2015). Novel utility-based methodological framework for valuation of road infrastructure. *Transp. Res. Rec.* 2529, 37–45. doi:10.3141/2529-04

Santos, J., Torres-Machi, C., Morillas, S., and Cerezo, V. (2022). A fuzzy logic expert system for selecting optimal and sustainable life cycle maintenance and rehabilitation strategies for road pavements. *Int. J. Pavement Eng.* 23, 425–437. doi:10.1080/10298436.2020.1751161

Sirirangsi, P., Amekudzi, A., and Herabat, P. (2003). Capturing effects of maintenance practices in highway asset valuation: replacement-cost approach versus book-value method. *Transp. Res. Rec.* 1824, 57–65. doi:10.3141/1824-07

Snaith, M. S., and Orr, D. M. (2006). Condition-based capital valuation of a road network. *Proc. Proc. Institution Civ. Engineers-Municipal Eng. Thomas Telford Ltd* 159, 91–95. doi:10.1680/muen.2006.159.2.91

Sun, J., Luo, S., Wang, Y., Dong, Q., and Zhang, Z. (2023). Pre-treatment of steel slag and its applicability in asphalt mixtures for sustainable pavements. *Chem. Eng. J.* 476, 146802. doi:10.1016/j.cej.2023.146802

Sun, J., Park, K., and Lee, M. J. (2017). A multi-level asset management decision method considering the risk and value of bridges. *J. Asian Archit. Build. Eng.* 16, 163–170. doi:10.3130/jaabe.16.163

Xian-Xun, Y., and Yuanshun, L. (2018). Residual value risks of highway pavements in public–private partnerships. *J. Infrastruct. Syst.* 24, 4018020. doi:10.1061/(ASCE)IS.1943-555X.0000438

Yuan, D., Jiang, W., Sha, A., Xiao, J., Wu, W., and Wang, T. (2023). Technology method and functional characteristics of road thermoelectric generator system based on Seebeck effect. *Appl. Energy* 331, 120459. doi:10.1016/j.apenergy.2022.120459

frontiers | Frontiers in Energy Research

TYPE Original Research
PUBLISHED 25 January 2024
DOI 10.3389/fenrg.2024.1365532

OPEN ACCESS

EDITED BY
Meng Jia,
Shandong University of Science and Technology, China

REVIEWED BY
Chaoliang Fu,
RWTH Aachen University, Germany
Zhongnan Tian,
Design and Research Institute Co.,Ltd., China

*CORRESPONDENCE
Yufei Zhang,
zyufei@chd.edu.cn

RECEIVED 04 January 2024
ACCEPTED 15 January 2024
PUBLISHED 25 January 2024

CITATION
Liao Z, Zhang Y, Zhao X, Zhang Y, Liu M, Hong J and Cao H (2024), Comprehensive analysis of renewable hybrid energy systems in highway tunnels.
Front. Energy Res. 12:1365532.
doi: 10.3389/fenrg.2024.1365532

Comprehensive analysis of renewable hybrid energy systems in highway tunnels

Zhen Liao[1], Yufei Zhang[2]*, Xin Zhao[3], Yubiao Zhang[1], Manhu Liu[1], Jinlong Hong[2] and Hao Cao[3]

[1]Guangxi Communications Investment Group Corporation Ltd., Nanning, China, [2]Chang'an University, Xi'an, China, [3]Shaanxi Transportation Planning and Design Institute Co., Ltd., Shaanxi, China

In order to explore the feasibility of a renewable hybrid energy system in highway tunnels, a scenario-coupled construction method for a highway tunnel renewable hybrid energy system is proposed. Based on this method, a tunnel on a highway in southern China serves as an example, and a renewable hybrid energy system for the highway tunnel is constructed. Using HOMER, the hybrid energy system is simulated, optimized, and analyzed, studying the characteristics of the operation of the highway tunnel hybrid renewable energy system in an off-grid mode. The optimal configuration for the hybrid energy system is proposed. The research results indicate the feasibility of constructing a highway tunnel renewable hybrid energy system by utilizing natural resources within the road area (solar energy, wind energy). The hybrid renewable energy system for this tunnel can provide 1112392 kWh of electrical energy annually, with the lowest energy cost being $0.17/kW. Furthermore, the hybrid energy system can reduce greenhouse gas emissions, contributing to the sustainable development of the environment.

KEYWORDS

road engineering, hybrid energy, homer, optimization configuration, feasibility, sustainability

1 Introduction

With the continuous development of the economy, the technology of highway traffic infrastructure is constantly improving (Jiang et al., 2022; Sun et al., 2023a; Sun et al., 2023b; Wang et al., 2023; Wu et al., 2024). The mileage of highways is also increasing continuously, and a considerable amount of electricity is consumed by highways each year. The existing energy supply for highways primarily relies on urban power grids, The pavement structure of highways has complex construction techniques (Büchner et al., 2019; K; Shi et al., 2024; Renken et al., 2018; Walther et al., 2019). Due to the extensive linear characteristics of highways, the conventional power grid transportation cost is exceptionally high. Moreover, the high dependence of highways on the power grid poses a significant risk; in case of power grid failure, the electricity supply to highways cannot be guaranteed. To avoid such issues, this study considers utilizing renewable resources within the highway domain to construct a scenario-coupled highway renewable hybrid energy system, exploring the feasibility of applying renewable hybrid energy systems on highways.

The highway domain encompasses abundant renewable energy resources. In the context of researching renewable energy within the available area of the highway domain (Liu and Fei, 2021), proposed a road photovoltaic prediction model. This

model leverages remote sensing images and other geospatial information system (GIS) data to estimate the photovoltaic capacity of urban roads based on acquired urban characteristics (Ferri et al., 2022). evaluated the potential electricity generation of three different photovoltaic road materials and proposed a traffic shadow model (Duman and Guler, 2019). installed photovoltaic power generation equipment on both sides of the road, creating an off-grid system to supply power to road LED lighting devices. The study results indicated that the system is easy to maintain, installation is simple and fast, and it has a long lifespan (Rehman et al., 2020). introduced a method for assessing the solar potential of electric bus routes. The research findings suggest that installing solar panels on the roof of electric buses can offset approximately 8.5% of the power demand (Tian et al., 2020). utilized three-dimensional computational fluid dynamics (3D CFD) to numerically simulate wind turbines and turbine arrays on highways, investigating optimal rotor clearances (Sundaram et al., 2021). developed an off-grid vertical-axis wind turbine power generation system on highways, utilizing wind energy to power streetlights. Regarding road surface energy harvesting devices (Chen et al., 2021), proposed a road piezoelectric energy collection system, with research results indicating that the open-circuit voltage energy density can reach 15.37 J/(m.pass.lane) (Jiang et al., 2018). introduced a road thermoelectric generator system, where the module converts heat absorbed by asphalt surfaces into electrical energy, lowering the surface temperature. Experimental test results showed that the electrical output of a 300 mm × 300 mm × 100 mm asphalt surface can reach 0.564 V (Azam et al., 2021). designed a road energy harvesting device based on speed bumps. This device achieved a peak power of 11.99W and a peak voltage of 20.57V at a speed of 120 mm/s and a load of 150N (Yuan et al., 2023). proposed a road thermoelectric power generation system technology based on the Seebeck effect.

In the realm of technical research (Kotb et al., 2021), investigated the structure of the Wind/PV/Diesel/battery renewable hybrid energy system, considering factors such as load demand, storage costs, and interest rate varia

tions. Sensitivity analysis was conducted on the system. (Vendoti et al., 2021), studied the structure of the PV/Wind/Biomass/Biogas/Fuel Cell/battery renewable hybrid energy system under off-grid conditions, evaluating its economic and technical aspects (Das et al., 2021b). explored the PV/Diesel/Pump-hydro storage (PHS) renewable hybrid energy system, conducting sensitivity analysis on the system using variables such as solar radiation, diesel prices, PHS prices, and interest rates (Azerefegn et al., 2020). researched the structure of the Diesel/PV/battery hybrid energy system under grid-connected conditions and conducted sensitivity analysis on the system considering factors such as solar radiation, PV capital costs, grid electricity prices, load demand, fuel prices, and grid interruptions.

In terms of economic research, the primary focus is on the impact of two indicators: Net Present Cost (NPC) and Cost Of Energy (COE) (Das et al., 2021a). studied the PV/Wind/Diesel/Battery system under off-grid and grid-connected modes, finding that the cost of the PV/Diesel/PHS system combination is higher than that of the PV/Diesel/Battery hybrid system, with an energy cost of 0.34$/kWh (Cano et al., 2020). investigated the structure of the PV/Hydro Kinetic Turbines (HKT)/Battery renewable hybrid energy generation system, and the results indicated an energy cost of

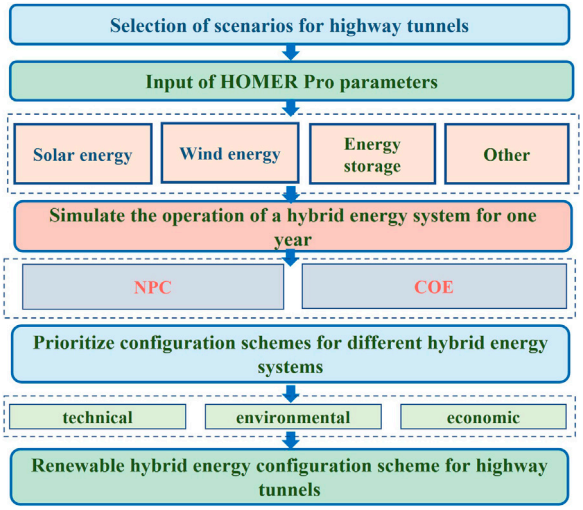

FIGURE 1
Flowchart of the Construction Method for the Highway Tunnel Renewable Hybrid Energy System.

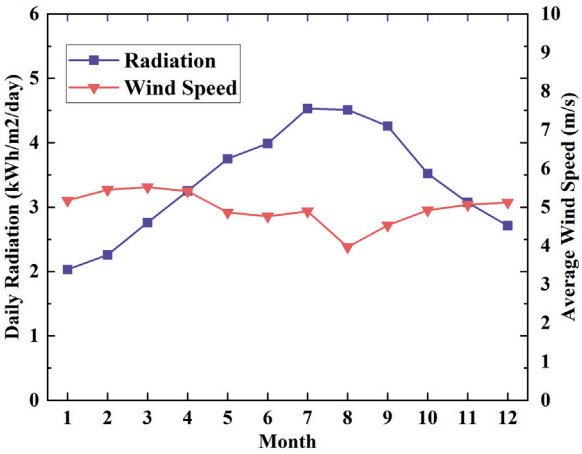

FIGURE 2
Solar Radiation and Wind Speed Data in the Case Area.

0.182$/kWh for the system (Li et al., 2020). examined the off-grid PV/Wind/Biomass hybrid renewable energy system, showing that the energy cost for this system is 0.182$/kWh (Coban et al., 2022). researched the structure of the Wind/Diesel/PV/battery grid-connected renewable hybrid energy system, revealing an energy cost of 0.182$/kWh for the system.

In summary, renewable hybrid energy systems have been widely applied in various fields, demonstrating good economic and technical feasibility. However, their application in the transportation sector is relatively limited. Therefore, this study considers the characteristics of highways, aiming to construct a scenario-coupled renewable hybrid energy system for highways. Using a tunnel on a highway in southern China as an example, the study analyzes the technical and economic feasibility of the highway's crucial energy nodes with a hybrid renewable energy system in off-grid mode.

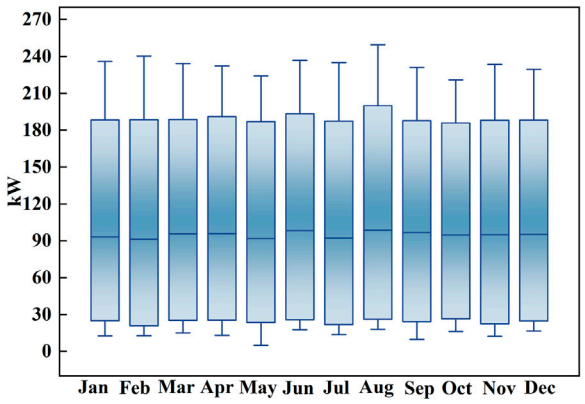

FIGURE 3
Distribution of Annual Electricity Consumption for Tunnel Main Loads.

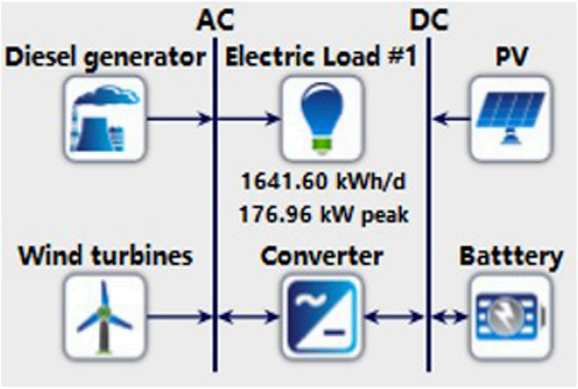

FIGURE 4
Schematic Diagram of the Tunnel Renewable Hybrid Energy System.

2 Tunnel renewable hybrid energy system construction method

The most widely used software in hybrid energy research is HOMER (developed by the U.S. National Renewable Energy Laboratory). It can simulate all possible combinations of hybrid energy systems based on inputs such as the distribution of annual electricity loads, resource data, technical and economic parameters of components, load data, and other project parameters. Following simulation optimization, different combinations are prioritized based on their cost, and a detailed technical and economic analysis is conducted for each system combination. This study primarily analyzes the utilization of renewable resources such as solar and wind energy in the areas where crucial energy nodes of highways are located. Through simulation optimization, hybrid energy solutions adaptable to highway scenarios are determined. The process flowchart of the construction method is shown in Figure 1.

Input for Multi-Scenario Coupled Highway Renewable Hybrid Energy System: The first step involves analyzing the renewable energy situation in the region where the highway is located, considering factors such as sunlight resources, wind resources, etc. The selection of renewable resources in the highway region is optimized, and data related to meteorology, economics, technology, electricity demand, etc., are collected. Meteorological data includes solar radiation, wind speed, and other relevant parameters.

Simulation and Optimization: Once the data input is complete, the system is simulated and optimized using HOMER. Under the condition of meeting the load demand, the system's operation is simulated for 1 year (8,760 h) to determine the feasibility of the hybrid energy solution. Optimization of the solution is based on the relevant cost parameters of each component in the renewable hybrid energy system. The optimization criterion is to minimize the Net Present Cost (NPC). After simulation and optimization, HOMER ranks different hybrid energy solutions based on the minimum NPC, providing a list of feasible solutions.

3 Case study

Case Location: The case study tunnel is located in the southern part of China at 24°43′12″N latitude and 109°48′56″E longitude.

Assessment of Utilizable Natural Resources: The case tunnel benefits from favorable wind and sunlight resources. Data on solar energy resources, wind speed, and other relevant parameters are sourced from NASA (National Aeronautics and Space Administration) (The period from July 1983 to June 2005.)and survey and design materials, as shown in Figure 2.

As indicated in Figure 2, solar radiation is higher in July and August each year, while it is lower in January and December. The maximum solar radiation is 4.5 kWh/m2/day, and the minimum solar radiation is 2.0 kWh/m2/day. The wind speed exhibits relatively stable variations throughout the year, with an average speed of 3 m/s.

Based on the assessment of utilizable resources mentioned above, this study considers constructing a scenario-coupled renewable hybrid energy system for the highway, utilizing the wind and sunlight resources in the region.

3.1 Load demand

Actual load data for this location can be obtained through design documents. The annual load of the main electrical equipment for this highway tunnel is depicted in Figure 3. The graph indicates that the energy consumption range of the tunnel is between 30 and 200 kW, and there is relatively small monthly variation in energy consumption, with a low fluctuation in the energy consumption curve.

3.2 Design of the renewable hybrid energy system

Based on the analysis of natural resources in the area where the highway tunnel is located, the consideration is given to utilizing the wind and solar resources of this region to construct a hybrid energy system. Due to the intermittent nature of solar and wind energy, the power generation of photovoltaic panels and wind turbines is

TABLE 1 Input parameters of hybrid energy system components.

Component name	Cost ($)	Replacement cost ($)	Operation and maintenance ($)	Model	Life
Pv (Li et al., 2020)	1,000/kW	950/kW	10/year	Peimar SG200M5	25years
Diesel generator (Askari and Ameri, 2012; Uwineza et al., 2021)	750/kW	750/kW	1.34 ($/op. hour)	Generic 500 kW Fixed Capacity Genset	30,000 (Hour)
Battery (El-houari et al., 2021)	1,650	1,650	15	H2500 ($LiFePO_4$)	12years
Wind (Sharma et al., 2022)	997	997	150	Generic30 kW	20years
Converter (Shiroudi et al., 2012; He et al., 2018)	300	300	0	SG100k3	15years

TABLE 2 Optimized design of microgrid proposed by HOMER.

Serial number	Configuration plan	PV (kW)	Wind (kW)	Diesel generator (kW)	Battery (kWh)
Case-A	PV- wind- Diesel generator - Battery	805	7	500	150
Case-B	PV- Diesel generator- Battery	1,283	—	500	188
Case-C	Wind - Diesel generator - Battery	—	20	500	261
Case-D	Diesel generator - Battery	—	—	500	73
Case-E	PV- Wind - Diesel generator	2,111	24	500	—
Case-F	Wind - Diesel generator	—	36	500	—
Case-G	PV - Diesel generator	3,120	—	500	—
Case-H	Diesel generator	—	—	500	—

unstable. Therefore, to ensure a stable power supply, the addition of a diesel generator as a backup power source is considered in the system. At the same time, batteries act as energy storage units to maintain a stable voltage at the load end, and a converter is used for current conversion between AC and DC modes. The schematic diagram of the highway renewable hybrid energy system is shown in Figure 4.

3.3 Parameters of the renewable hybrid energy system

To analyze the capacity, environmental impact, and economic aspects of the hybrid energy system in the case of the highway tunnel area using HOMER Pro software, it is necessary to input relevant parameters for renewable energy system components. The technical and economic parameters for the selected components in this study were obtained from published literature or manufacturers. The parameters are shown in Table 1.

4 Results and discussion

After simulation calculations using HOMER Pro software, the results include eight hybrid energy configuration scenarios. Analyzing the technical, economic, and environmental aspects of different system compositions, the optimal system configuration is selected based on comprehensive considerations.

4.1 Technical analysis

Using HOMER for optimization analysis, in this study, the hybrid energy system of the case tunnel was examined, with all configurations being a combination of solar photovoltaic components, batteries, and diesel generators. Cost of Energy (COE) and Net Present Cost (NPC) are important indicators for evaluating hybrid energy systems. Through optimization calculations and analysis using HOMER Pro software, the hybrid system with the minimum COE and NPC is determined, thereby establishing the feasibility of the hybrid energy system configuration. HOMER software simulated over 40,000 configurations of energy hybrid systems to meet load demands and assessed eight different scenarios technically and economically, as shown in Table 2.

The electricity generation results of the eight different hybrid energy system combinations simulated by HOMER are presented in Figures 5A–H, showing the percentage of electricity generated by each power generation device in each hybrid energy system. The electricity produced by each combination serves two main purposes: providing power for electrical loads and storing surplus electricity when the system's electricity generation exceeds load demand.

4.2 Economic analysis

In HOMER Pro, the economic viability of each hybrid system was also assessed. Table 3 reveals that the Net Present Cost (NPC)

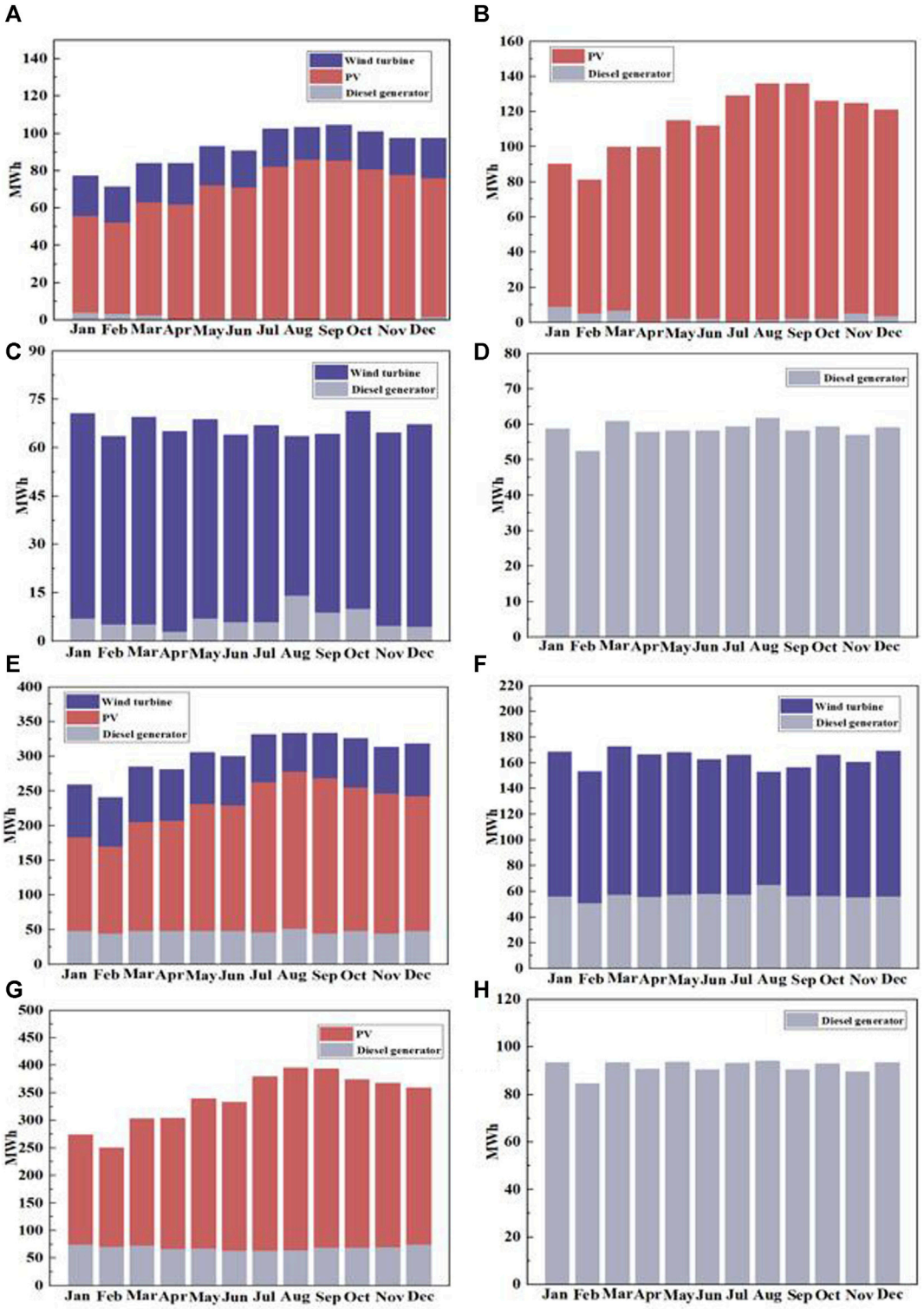

FIGURE 5
Power generation curve for each renewable hybrid energy system.

increases sequentially from case-A to case-H, with case-A having the minimum NPC value of $1,363,913, and case-H having the maximum NPC value of $7,986,208. From the perspective of energy cost, case-A has the lowest energy cost at $0.176/kWh.

4.3 Environmental analysis

HOMER Pro assessed the environmental impact of each hybrid energy system, and the results are presented in Table 4.

TABLE 3 Economic evaluation of each renewable hybrid energy option.

Serial number	NPC ($)	COE ($)	O&M ($)
Case-A	1363913	0.17	19184.67
Case-B	1522473	0.19	30963.81
Case-C	2070396	0.26	49105.64
Case-D	4358426	0.56	294335.8
Case-E	6101477	0.78	333560.1
Case-F	6329236	0.81	377294.1
Case-G	7426704	0.95	467025
Case-H	7986208	1.03	588760.3

The concept of penetration rate is defined as follows: the proportion of electricity demand served by the green energy generated throughout the year is called the Green Energy Penetration Rate (Renfrac). The calculation formula is given by Eq. 1:

$$Renfrac = \frac{P_{\text{ren}}}{L_{\text{served}}} \quad (1)$$

4.4 Determination of the optimal configuration

Based on the analysis of technical, economic, and environmental factors, case-A, case-B, and case-C are the top three ranked combination scenarios. Case-A's electricity is primarily generated by solar photovoltaic components, wind turbines, and batteries, making it the optimal combination with the best NPC, so Case-A is considered the best system configuration.

Table 5 shows the annual electricity generation of different renewable energy sources in the optimal combination. It can be observed that photovoltaic power generation contributes the most, accounting for 75.2%, while the contribution of diesel generators is the lowest, at 2.39%.

5 Conclusion

The paper focuses on the feasibility of constructing a hybrid energy system in the context of highway tunnels, particularly analyzing the potential for combining solar and wind energy within the highway tunnel environment. By leveraging the solar and wind resources available within the highway domain and considering the magnitude of the tunnel's electricity demand, an optimized calculation process identifies the optimal hybrid energy configuration. This proposed configuration aims to reduce carbon emissions from highway tunnels.

(1) The composition of the scenario-coupled renewable hybrid energy system for a highway tunnel needs to be determined based on the types of available energy scenarios in the region, including solar energy resources, wind resources, etc.
(2) Once the site selection and relevant energy conversion equipment parameters are determined, the Net Present Cost (NPC) and Cost of Energy (COE) serve as the primary indicators for evaluating the hybrid energy system. Simultaneously considering the emission of environmental pollutants from the hybrid energy system can assist decision-makers in selecting economically, environmentally friendly, and feasible renewable hybrid energy configuration schemes.

TABLE 4 Environmental impact assessment for each renewable hybrid energy option.

Serial number	CO_2(kg/yr)	CO(kg/yr)	HC(kg/yr)	PM(kg/yr)	SO_2(kg/yr)	NO_x (kg/yr)	Renfrac (%)
Case-A	20945	108	5.75	0.927	512	20.8	95.55
Case-B	36973	191	10.2	1.64	904	36.7	92.15
Case-C	68659	355	18.9	3.04	168	68.1	85.43
Case-D	477281	2,469	131	21.1	1,167	473	0
Case-E	456554	2,362	125	20.2	1,116	453	3.11
Case-F	539710	2,792	148	23.9	1,319	535	0
Case-G	650715	3,366	179	28.8	1,591	645	0
Case-H	867134	4,486	238	38.4	2,120	860	0

TABLE 5 Summary of annual power generation of different renewable energy sources.

Serial number	Assembly	Annual energy output (kWh/yr)	Percentage (%)
1	PV	836169	75.2
2	Diesel generator	26625	2.39
3	Wind turbines	249598	22.4
	total	1112392	100

(3) In this study, a highway tunnel in southern China was selected as a case. Through simulation and analysis from technical, economic, and environmental perspectives, the optimal renewable hybrid energy system configuration for this highway tunnel under the wind-solar scenario coupling was identified as PV-wind-Diesel generator-Battery. At this configuration, the system NPC and COE are $1,363,913 and $0.176/kWh, respectively. The annual emissions are as follows: 20,945 kg/year of CO_2, 108 kg/year of CO, and 512 kg/year of SO_2.

(4) Due to the influence of various uncertain variables on the renewable energy system for highways, future research can investigate the impact of uncertainties such as project lifecycle, interest rates, river flow rates, wind speeds, etc., on hybrid energy systems.

Data availability statement

The original contributions presented in the study are included in the article/Supplementary material, further inquiries can be directed to the corresponding author.

Author contributions

ZL: Formal Analysis, Funding acquisition, Resources, Writing–review and editing. YfZ: Methodology, Project administration, Writing–original draft, Writing–review and editing. XZ: Writing–review and editing. YbZ: Writing–review and editing. ML: Investigation, Writing–original draft. JH: Data curation, Writing–review and editing. HC: Investigation, Supervision, Writing–original draft.

Funding

The author(s) declare financial support was received for the research, authorship, and/or publication of this article. This study was sponsored by the National Key Research and Development Program of China (Grant No. 2021YFB1600200)、Guangxi Transportation Science and Technology Demonstration Project "Guilin-Zhongshan Highway Green Energy Self-consistent Supply and Efficient Utilization Key Technology Integration Application Research and Demonstration": 2023-0002 and Scientific Research Projects (21-53K, 21-36X) of Shaanxi Provincial Department of Transportation. The authors are grateful for the financial supports.

Conflict of interest

Authors ZL, YbZ, and ML were employed by Guangxi Communications Investment Group Corporation Ltd. Authors XZ and HC were employed by Shaanxi Transportation Planning and Design Institute Co., Ltd.

The remaining authors declare that the research was conducted in the absence of any commercial or financial relationships that could be construed as a potential conflict of interest.

Publisher's note

References

Askari, I. B., and Ameri, M. (2012). Techno-economic feasibility analysis of stand-alone renewable energy systems (PV/bat, wind/bat and hybrid PV/wind/bat) in kerman, Iran. *Energy Sources, Part B Econ. Plan. Policy* 7 (1), 45–60. doi:10.1080/15567240903330384

Azam, A., Ahmed, A., Hayat, N., Ali, S., Khan, A. S., Murtaza, G., et al. (2021). Design, fabrication, modelling and analyses of a movable speed bump-based mechanical energy harvester (MEH) for application on road. *Energy* 214, 118894. doi:10.1016/j.energy.2020.118894

Azerefegn, T. M., Bhandari, R., and Ramayya, A. V. (2020). Techno-economic analysis of grid-integrated PV/wind systems for electricity reliability enhancement in Ethiopian industrial park. *Sustain. CITIES Soc.* 53, 101915. doi:10.1016/j.scs.2019.101915

Büchner, J., Wistuba, M. P., Remmler, T., and Wang, D. (2019). On low temperature binder testing using DSR 4 mm geometry. *Mater. Struct.* 52 (6), 113. doi:10.1617/s11527-019-1412-3

Cano, A., Arevalo, P., and Jurado, F. (2020). Energy analysis and techno-economic assessment of a hybrid PV/HKT/BAT system using biomass gasifier: cuenca-Ecuador case study. *ENERGY* 202, 117727. doi:10.1016/j.energy.2020.117727

Chen, C., Xu, T.-B., Yazdani, A., and Sun, J.-Q. (2021). A high density piezoelectric energy harvesting device from highway traffic - system design and road test. *Appl. ENERGY* 299, 117331. doi:10.1016/j.apenergy.2021.117331

Coban, H. H., Rehman, A., and Mohamed, A. (2022). Technical and economical investigation of a centralized and decentralized hybrid renewable energy system in cadaado, Somalia. *PROCESSES* 10 (4), 667. doi:10.3390/pr10040667

Das, B. K., Alotaibi, M. A., Das, P., Islam, M. S., Das, S. K., and Hossain, M. A. (2021a). Feasibility and techno-economic analysis of stand-alone and grid-connected PV/Wind/Diesel/Batt hybrid energy system: a case study. *ENERGY STRATEGY Rev.* 37, 100673. doi:10.1016/j.esr.2021.100673

Das, B. K., Hasan, M., and Rashid, F. (2021b). Optimal sizing of a grid-independent PV/diesel/pump-hydro hybrid system: a case study in Bangladesh. *Sustain. ENERGY Technol. ASSESSMENTS* 44, 100997. doi:10.1016/j.seta.2021.100997

Duman, A. C., and Guler, O. (2019). Techno-economic analysis of off-grid photovoltaic LED road lighting systems: a case study for northern, central and southern regions of Turkey. *Build. Environ.* 156, 89–98. doi:10.1016/j.buildenv.2019.04.005

El-houari, H., Allouhi, A., Salameh, T., Kousksou, T., Jamil, A., and El Amrani, B. (2021). Energy, Economic, Environment (3E) analysis of WT-PV-Battery autonomous hybrid power plants in climatically varying regions. *Sustain. ENERGY Technol. ASSESSMENTS* 43, 100961. doi:10.1016/j.seta.2020.100961

Ferri, C., Ziar, H., Thien Tin, N., van Lint, H., Zeman, M., and Isabella, O. (2022). Mapping the photovoltaic potential of the roads including the effect of traffic. *Renew. ENERGY* 182, 427–442. doi:10.1016/j.renene.2021.09.116

He, L., Zhang, S., Chen, Y., Ren, L., and Li, J. (2018). Techno-economic potential of a renewable energy-based microgrid system for a sustainable large-scale residential community in Beijing, China. *Renew. Sustain. Energy Rev.* 93, 631–641. doi:10.1016/j.rser.2018.05.053

Jiang, W., Xiao, J., Yuan, D., Lu, H., Xu, S., and Huang, Y. (2018). Design and experiment of thermoelectric asphalt pavements with power-generation and temperature-reduction functions. *ENERGY Build.* 169, 39–47. doi:10.1016/j.enbuild.2018.03.049

Jiang, W., Yuan, D. D., Shan, J. H., Ye, W. L., Lu, H. H., and Sha, A. M. (2022). Experimental study of the performance of porous ultra-thin asphalt overlay. *Int. J. PAVEMENT Eng.* 23 (6), 2049–2061. doi:10.1080/10298436.2020.1837826

Kotb, K. M., Elkadeem, M. R., Khalil, A., Imam, S. M., Hamada, M. A., Sharshir, S. W., et al. (2021). A fuzzy decision-making model for optimal design of solar, wind, diesel-based RO desalination integrating flow-battery and pumped-hydro storage: case study in Baltim, Egypt. *ENERGY Convers. Manag.* 235, 113962. doi:10.1016/j.enconman.2021.113962

Li, J., Liu, P., and Li, Z. (2020). Optimal design and techno-economic analysis of a solar-wind-biomass off-grid hybrid power system for remote rural electrification: a case study of west China. *ENERGY* 208, 118387. doi:10.1016/j.energy.2020.118387

Liu, Z., and Fei, T. (2021). Road PV production estimation at city scale: a predictive model towards feasible assessing regional energy generation from solar roads. *J. Clean. Prod.* 321, 129010. doi:10.1016/j.jclepro.2021.129010

Rehman, N. U., Hijazi, M., and Uzair, M. (2020). Solar potential assessment of public bus routes for solar buses. *Renew. ENERGY* 156, 193–200. doi:10.1016/j.renene.2020.04.081

Renken, P., Büchler, S., Falchetto, A. C., Wang, D., and Wistuba, M. P. (2018). Warm mix asphalt-a German case study. *Asph. Paving Technol.* 87, 685–716. doi:10.12783/aapt2018/33821

Sharma, S., Sood, Y. R., Sharma, N. K., Bajaj, M., Zawbaa, H. M., Turky, R. A., et al. (2022). Modeling and sensitivity analysis of grid-connected hybrid green microgrid system. *AIN SHAMS Eng. J.* 13 (4), 101679. doi:10.1016/j.asej.2021.101679

Shi, K., Ma, F., Fu, Z., Song, R., Yuan, D., and Ogbon, A. W. (2024). Enhancing aged SBS-modified bitumen performance with unaged bitumen additives. *Constr. Build. Mater.* 412, 134768. doi:10.1016/j.conbuildmat.2023.134768

Shiroudi, A., Rashidi, R., Gharehpetian, G. B., Mousavifar, S. A., and Foroud, A. A. (2012). Case study: simulation and optimization of photovoltaic-wind-battery hybrid energy system in Taleghan-Iran using HOMER software. *J. Renew. Sustain. ENERGY* 4 (5), 053111. doi:10.1063/1.4754440

Sun, J., Huang, W., Lu, G. Y., Luo, S., and Li, Y. H. (2023a). Investigation of the performance and micro-evolution mechanism of low-content thermosetting epoxy asphalt binder towards sustainable highway and bridge decks paving. *J. Clean. Prod.* 384, 135588. doi:10.1016/j.jclepro.2022.135588

Sun, J., Luo, S., Wang, Y. Z., Dong, Q. F., and Zhang, Z. H. (2023b). Pre-treatment of steel slag and its applicability in asphalt mixtures for sustainable pavements. *Chem. Eng. J.* 476, 146802. doi:10.1016/j.cej.2023.146802

Sundaram, A., Almobasher, L., Al-Eid, M., Bazroon, M., and Abohasson, A. (2021). Implementation of a highway wind power generation using vertical axis wind turbine to automatically power a street lamp. *WIND Eng.* 45 (5), 1175–1192. doi:10.1177/0309524x20969421

Tian, W., Song, B., and Mao, Z. (2020). Numerical investigation of wind turbines and turbine arrays on highways. *Renew. ENERGY* 147, 384–398. doi:10.1016/j.renene.2019.08.123

Uwineza, L., Kim, H.-G., and Kim, C. K. (2021). Feasibility study of integrating the renewable energy system in Popova Island using the Monte Carlo model and HOMER. *ENERGY STRATEGY Rev.* 33, 100607. doi:10.1016/j.esr.2020.100607

Vendoti, S., Muralidhar, M., and Kiranmayi, R. (2021). Techno-economic analysis of off-grid solar/wind/biogas/biomass/fuel cell/battery system for electrification in a cluster of villages by HOMER software. *Environ. Dev. Sustain.* 23 (1), 351–372. doi:10.1007/s10668-019-00583-2

Walther, A., Bchler, S., Falchetto, A. C., Wang, D., Riccardi, C., and Wistuba, M. P. (2019). Experimental investigation on asphalt mixtures prepared with reclaimed asphalt pavement and rejuvenators based on the BTSV method. *ROAD Mater. PAVEMENT Des.* 20 (7), 1695–1708. doi:10.1080/14680629.2019.1594053

Wang, H. P., Airey, G. D., Leng, Z., and Lu, G. Y. (2023). Optimisation of the preparation procedure of crumb rubber modified bitumen with wax-based additives. *ROAD Mater. PAVEMENT Des.*, 1–12. doi:10.1080/14680629.2023.2191724

Wu, W., Cavalli, M. C., Jiang, W., and Kringos, N. (2024). Differing perspectives on the use of high-content SBS polymer-modified bitumen. *Constr. Build. Mater.* 411, 134433. doi:10.1016/j.conbuildmat.2023.134433

Yuan, D. D., Jiang, W., Sha, A. M., Xiao, J. J., Wu, W. J., and Wang, T. (2023). Technology method and functional characteristics of road thermoelectric generator system based on Seebeck effect. *Appl. ENERGY* 331, 120459. doi:10.1016/j.apenergy.2022.120459

frontiers | Frontiers in Energy Research

TYPE Original Research
PUBLISHED 02 February 2024
DOI 10.3389/fenrg.2024.1362957

OPEN ACCESS

EDITED BY
Dongdong Yuan,
Chang'an University, China

REVIEWED BY
Jinhuan Shan,
University of Leeds, United Kingdom
Fan Zhang,
Aalto University, Finland
Jiyu Xin,
Lehigh University, United States

*CORRESPONDENCE
Yufei Zhang,
zyufei@chd.edu.cn

RECEIVED 29 December 2023
ACCEPTED 19 January 2024
PUBLISHED 02 February 2024

CITATION
Wang G, Zhang Y, Tang W, Liao Z, Wang T, Zhang S and Zhao X (2024), Feasibility analysis of hybrid energy generation systems for desert highway service areas: a case study in northern Xinjiang, China.
Front. Energy Res. 12:1362957.
doi: 10.3389/fenrg.2024.1362957

Feasibility analysis of hybrid energy generation systems for desert highway service areas: a case study in northern Xinjiang, China

Guangtao Wang[1], Yufei Zhang[2]*, Wenbin Tang[1], Zhen Liao[1], Teng Wang[2], Shuo Zhang[2] and Xin Zhao[3]

[1]Guangxi Communications Investment Group Corporation Ltd., Nanning, China, [2]Chang'an University, Xi'an, China, [3]Shaanxi Transportation Planning and Design Institute Co, Ltd., Shaanxi, China

Highways consume a significant amount of electrical energy annually, especially in remote desert regions where the cost of electricity is high. This research explores the utilization of natural resources along desert highways to establish hybrid energy generation systems for service areas. Three service areas along the desert highway in northern Xinjiang, China, serve as case studies. To assess the feasibility of hybrid energy generation systems in these service areas, meteorological data for the three locations were obtained from the NASA platform. The HOMER Pro software was employed for technical, economic, and environmental analyses of the systems. The results indicate the feasibility of Photovoltaic (PV)/Wind/Battery hybrid energy systems in the Huanghuagou, Kelameili, and Wujiaqu service areas. The application of these hybrid energy generation systems across the three service areas could provide 3,349,557 kWh of electrical energy annually for the desert highway. Sensitivity analysis reveals that the Net Present Cost (NPC) and Cost of Energy (COE) values decrease with increasing radiation levels, while NPC shows an increasing trend with growing load demand, and COE exhibits a decreasing trend. Among the three regions, Wujiaqu demonstrates the highest economic viability, with a COE of $0.34/kWh and an NPC of $3,141,641/kWh. Furthermore, Wujiaqu exhibits the lowest environmental impact, with CO_2 emissions of 198,387 kg/yr, SO_2 emissions of 493 kg/yr, and NO_x emissions of 1,711 kg/yr.

KEYWORDS

road engineering, service area, hybrid energy, feasibility, economic, technical, environmental

1 Introduction

The development of highways significantly impacts a nation's economic growth. Highways consume a substantial amount of electrical energy annually, and typically, the power supply for highways is sourced from nearby cities to ensure reliable electricity. However, for highways located in remote areas, particularly desert highways, the cost of electricity transportation is prohibitively high. Addressing the power supply challenges for desert highways has become an urgent matter. Desert regions, where highways are often situated, possess immense potential for energy asset utilization. Exploring the renewable

natural resources such as wind and solar energy within the road corridor of desert highways could offer a strategic solution to alleviate the energy challenges faced by the transportation system. The electrification of infrastructure assets in desert highway areas holds significant promise for mitigating energy-related concerns in the transportation sector.

In recent years, the construction technology of highways has been continuously developing (Jiang et al., 2022; Sun et al., 2023a; Sun et al., 2023b; Wang et al., 2023; Shi et al., 2024), while new energy technologies are also constantly being updated and iterated. In the field of renewable energy utilization on expressways, (Zhang et al., 2022), assessed the photovoltaic road potential for electricity generation in Chinese highways. The research findings indicate that the installed capacity of Chinese highways is 700.85 GW, with the capability to generate 629.06 TWh. (Yuan et al., 2023). Research proposes a technology method for energy collection using temperature differences on highway road surfaces. (Kim et al., 2018). studied the establishment of site selection criteria for photovoltaic (PV) power generation projects on Korean national roads. They conducted a survey of spatial information data for unused roads, determining the feasibility of potential project locations selected using these criteria for future solar road projects. Jiang et al. (2024) proposed a multi indicator evaluation method based on Analytic Hierarchy Process (AHP) and Geographic Information System (GIS) to fully utilize solar energy resources along highways. (Ahmad et al., 2020) investigated the design method of roadside vertical axis wind turbine generators and conducted experimental validation. The results show that the equipment can be installed on one side of the road, providing clean and affordable energy for road lighting. It is evident that individual renewable energy sources such as wind power and photovoltaics have broad prospects for application in the transportation sector. However, the main drawback of utilizing a single renewable energy source is the intermittent nature of its use, significantly reducing the reliability of renewable energy systems. To enhance the reliability of power supply and reduce economic costs, this study considers combining renewable energy with batteries and diesel generators to create a Hybrid Renewable Energy System (HRES). This system aims to supply power to critical loads at important energy nodes on highways. Compared to a single renewable energy system, a hybrid energy system has advantages such as high reliability and low cost (Ribó-Pérez et al., 2021).

In terms of technical and economic analysis, (El-houari et al., 2021), conducted a simulation of technical, economic, and environmental analyses of hybrid renewable energy systems in 24 selected cities in Morocco. They demonstrated the social and economic benefits of promoting the use of hybrid energy systems in remote towns and villages on the African continent (Haghighat Mamaghani et al., 2016). employed Net Present Cost (NPC), initial capital cost, and Levelized Cost of Energy (COE) as economic indicators to analyze the technical and economic feasibility of hybrid energy systems in three small rural communities in Colombia. They proposed different configuration

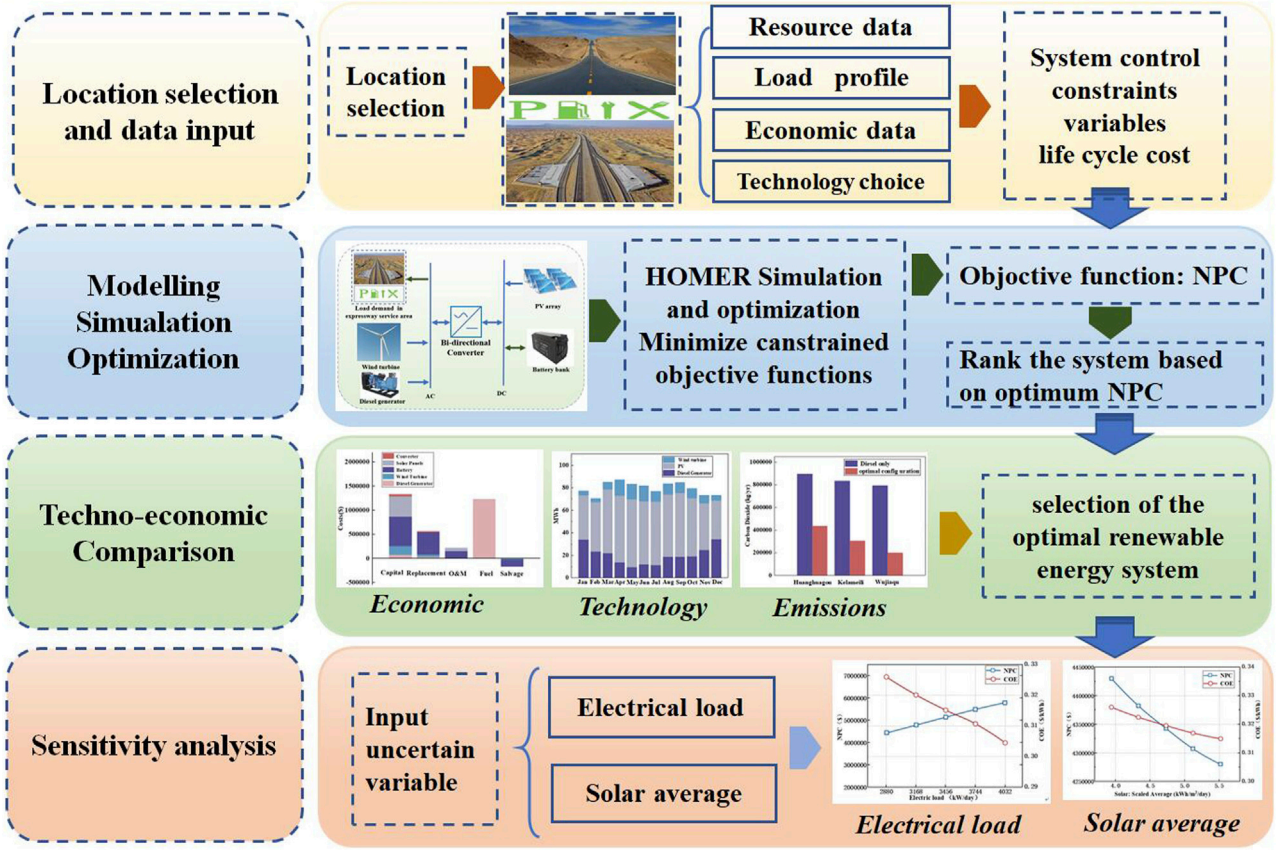

FIGURE 1
Construction method of mixed energy system in desert expressway service area.

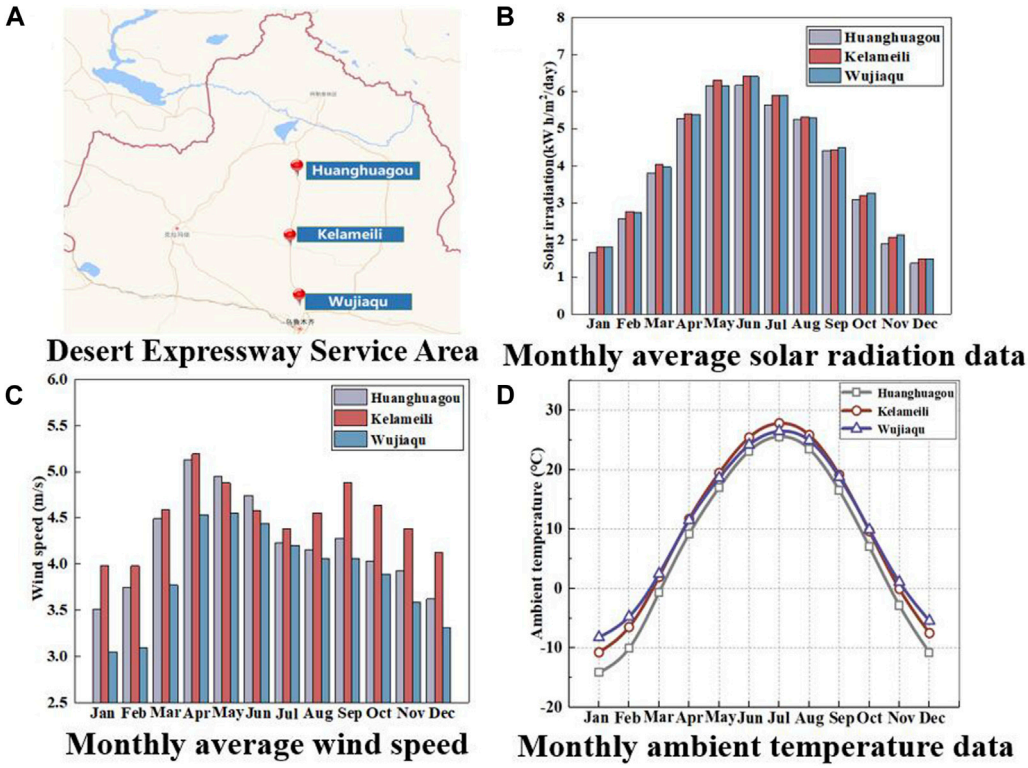

FIGURE 2
Meteorological resource data of service area location.

combinations of diesel generators, solar photovoltaic modules, and wind power equipment (Rezaei et al., 2021). and others studied off-grid hybrid renewable energy systems, analyzing the impact of changes in discount rates and inflation rates on system costs (Uwineza et al., 2021). conducted a feasibility analysis of mixed energy resources on Popova Island, studying the influence of discount rates and fuel costs on hybrid energy systems, providing references for decision-makers (Vendoti et al., 2020). and others utilized renewable resources in rural locations to find optimal configuration combinations that meet power loads, constructing a hybrid energy generation model. The research results indicate that a combination of photovoltaic, wind, biogas biomass, diesel generators, and batteries is an economical and reliable solution (Coban et al., 2022). performed a feasibility analysis of a wind and photovoltaic hybrid energy generation system in selected locations in Somalia, comparing off-grid and grid-connected modes.

During the construction process of highways, harmful gas emissions will be generated. Therefore, in the feasibility analysis stage of new energy construction, it is also necessary to analyze environmental emissions (Renken et al., 2018; Büchner et al., 2019; Walther et al., 2019; Wu et al., 2024). In terms of environmental impact, (Vergara-Zambrano et al., 2022), proposed a design method for a solar-biogas hybrid renewable energy system that can help reduce environmental pollutant emissions by 30%–80%. (Razmjoo et al., 2021). studied a hybrid power system composed of photovoltaics, wind, diesel generators, and batteries. The results indicate that the renewable rate of this hybrid system exceeds 72%, resulting in a reduction of over 2000 kg of CO_2 emissions per household annually. (El-houari et al., 2020). investigated a mixed energy system incorporating renewable sources such as solar, wind, and biomass, leading to an annual reduction of 26.48 tons of CO_2 emissions. (Das et al., 2021). researched a photovoltaic and wind energy hybrid system using different energy storage technologies, demonstrating that the hybrid energy system can reduce carbon dioxide emissions by 134,183.5 kg annually.

The focus of this study is to analyze the technical and economic feasibility of hybrid energy systems in service areas of desert highways, using three service areas along a desert highway in northern Xinjiang, China, as a case study. The study optimizes the best configuration of renewable energy for critical energy nodes in the road domain. In off-grid mode, using Net Present Cost (NPC) and Levelized Energy Cost (COE) as economic indicators, different system configuration parameters are optimized through simulation, analyzing the economics of service areas in different regions. Additionally, sensitivity analysis of hybrid energy systems in different regions is conducted, considering variables such as radiation intensity and the impact of load demand growth on the system.

2 Construction method of service area hybrid energy systems

2.1 Construction approach

The hybrid energy simulation software used in this study is HOMER Pro, designed by the National Renewable Energy Laboratory (NREL) in the United States. This simulation tool is

TABLE 1 Geographical and climatic data of selected areas on desert highways.

Name of the area	Longitude (°E)	Latitude (°N)	Altitude(m)	Scaled annual average (kwh/m²/day)	Scaled annual average (m/s)
Huanghuagou	87.55	46.53	576	3.94	4.23
Kelameili	87.40	45.25	479	4.09	4.51
Wujiaqu	87.57	44.22	460	4.08	3.87

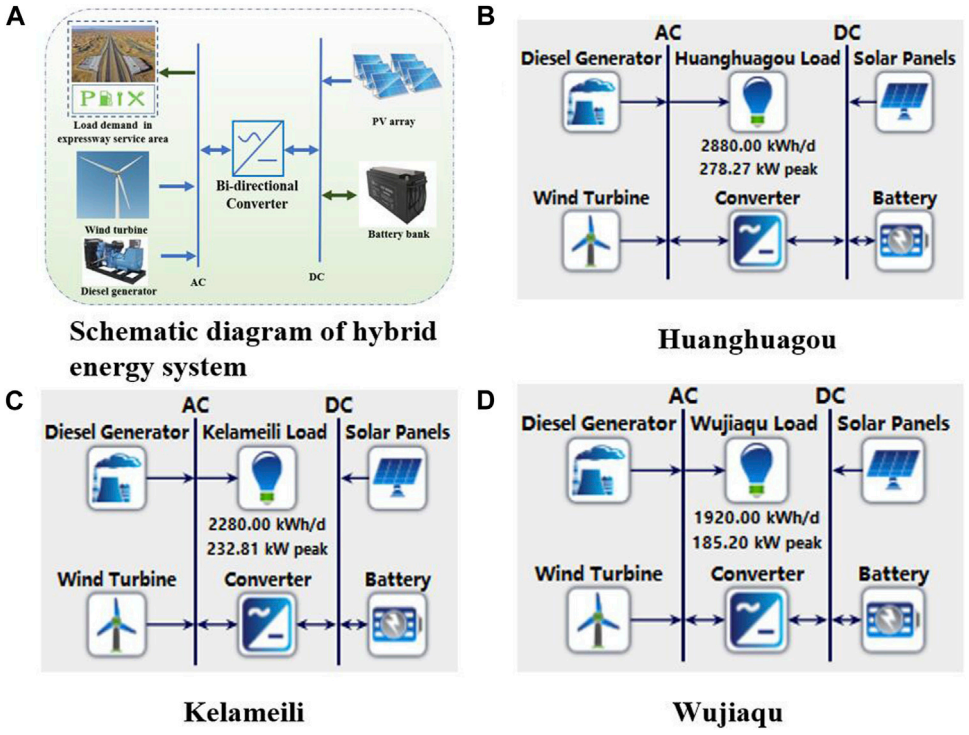

FIGURE 3
Mixed energy system in desert expressway service area.

TABLE 2 Comparison of main electricity load in service areas.

Name of the area	Surveillance system (kW)	Lamp (kW)	Average (kWh/day)
Huanghuagou	75	45	1920
Kelameili	50	45	1920
Wujiaqu	50	30	2,880

primarily utilized for optimizing hybrid power systems, conducting feasibility analyses, and performing technical, economic, and sensitivity analyses. Figure 1 illustrates the feasibility analysis process for the hybrid energy system in service areas along a desert highway.

Initially, the location of the desert service area where the hybrid energy system is to be constructed is selected. The available types of green energy in the region are analyzed, and meteorological data for the area, as well as technical and economic parameters for the selected green energy equipment, are obtained. Subsequently, through simulation and optimization calculations using HOMER Pro software, the best hybrid energy configuration is evaluated based on two crucial economic output parameters: Net Present Cost (NPC) and Levelized Cost of Energy (COE), considering environmental and technical factors. Finally, a sensitivity analysis of the hybrid energy system is conducted for uncertain variables.

The Net Present Cost (NPC) is a crucial economic parameter for assessing hybrid energy systems. The formula for calculating the total Net Present Cost is as follows (Jahangir et al., 2020; Sifakis et al., 2021; Al-Buraiki and Al-Sharafi, 2022; Ma et al., 2022b; Das et al., 2022):

TABLE 3 Input parameters of hybrid energy system components.

Component name	Cost ($)	Replacement cost ($)	Operation and maintenance ($)	Life
Pv module (Li et al., 2020)	1,000/KW	950/KW	10/year	25years
Diesel generator (Coban et al., 2022)	75000	75000	0.1 ($/op. hour)	4,000 (Hour)
Battery (Uwineza et al., 2021)	560	560	16.8	12years
Wind (Li et al., 2022)	13000	11000	50	20years
Converter Akhtari and Baneshi, (2019)	300	300	0	20years

TABLE 4 Summary of optimization results for huanghuagou.

System	PV/Wind/Diesel/Battery	PV/Diesel/Battery	Wind/Diesel/Battery	PV/Battery	Diesel only
COE ($/kWh)	0.32	0.33	0.37	0.89	0.42
NPC($/kWh)	4430135	4581608	5057828	12180140	5786267
Renewable fraction (%)	47	36.8	29.4	100	—
Pv capacity (kW)	331	465	—	4,453	—
Wind capacity	30	—	53	—	—
Diesel generator (kW)	440	440	440	—	440
Battery capacity (kWh)	607	575	304	6,460	—
Converter (kW)	161	175	135	459.5	—
Excess energy (kWh)	1323860	1333591	1254602	6413484	1153904

$$NPC\ (\$) = \frac{TAC}{CRF(q,n)} \tag{1}$$

Where TAC is the Total Annualized Cost (the sum of all the annualized costs for each system component), and CRF is the Capital Recovery Factor. The calculation formula is as follows (Ramesh and Saini, 2020; Ma et al., 2022a; Demirci et al., 2022):

$$CRF = \frac{q(1+q)^n}{(1+q)^n - 1} \tag{2}$$

Where n is the project's lifecycle in years, and q is the annual interest rate.

The Levelized Cost of Energy (COE) is the average cost of electricity produced by the hybrid energy system per kilowatt-hour. The calculation of COE involves dividing the annualized cost of electricity generation (total annualized cost minus the cost for servicing thermal loads) by the total electrical load served. The COE calculation formula is as follows (Toopshekan et al., 2020; Al-Najjar et al., 2022; Ang et al., 2022; Khan et al., 2022):

$$COE = \frac{TAC}{E_{AC} + E_{DC} + E_{def}} \tag{3}$$

Where TAC is the annualized cost of electricity generation; EAC, EDC, and Edef represent the total amounts of alternating current (AC), direct current (DC), and deferred load (kWh/year), respectively.

NPC and COE are used as evaluation indicators for hybrid energy systems. The smaller the NPC and COE, the better the economic efficiency of the hybrid energy system. The lower the investment cost of establishing hybrid energy, the greater the benefits obtained.

2.2 Location meteorological resource data

The selected desert highway in this study is located in the Gurbantünggüt Desert region of Xinjiang, China, with the highway overall running in a north-south direction. As illustrated in Figure 2A, the chosen service areas along the highway, from north to south, are Huanghuagou, Kelameili, and Wujiaqu. The geographical and climatic data for the selected region are presented in Table 1.

The solar radiation data used in this study are sourced from the NASA database (July 1983- June 2005). Figure 2B illustrates the monthly average solar radiation and clarity index data for the selected highway service areas. The solar radiation in the regions of Huanghuagou, Kelameili, and Wujiaqu ranges between 1.37 kWh/m2/d and 6.42 kWh/m2/d. The annual average solar radiation values for Huanghuagou, Kelameili, and Wujiaqu are 3.94, 4.09, and 4.08 kWh/m2/d. From the graph, it can be seen that solar radiation has larger data in May and June, while the radiation data in January and December is smaller. This is because in summer, the Sun is closer to the region, resulting in a significant increase in radiation.

The available annual average wind speeds within the study location are depicted in Figure 2C. The maximum wind speeds for Huanghuagou, Kelameili, and Wujiaqu occur in April at 5.19 m/s, while the minimum speeds are observed in January at 3.05 m/s. The

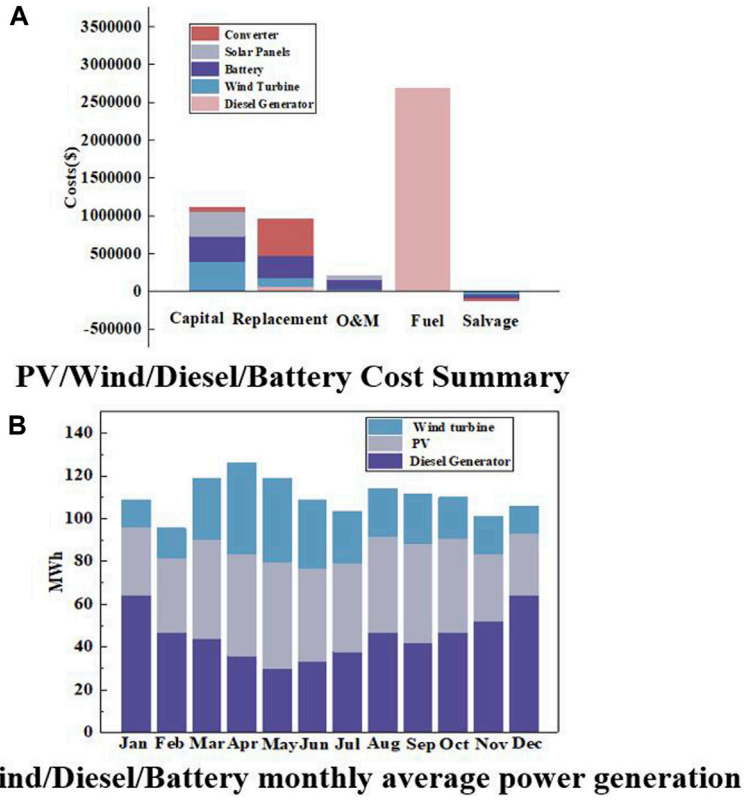

FIGURE 4
Technical and economic analysis of hybrid energy system in huahuanggou service area.

TABLE 5 Summary of kelameili optimization results.

System	PV/Wind/Diesel/Battery	PV/Diesel/Battery	Wind/Diesel/Battery	PV/Battery	Diesel only
COE ($/kWh)	0.34	0.34	0.42	0.80	0.50
NPC($/kWh)	3738790	3746409	4598883	8675314	5405541
Renewable fraction (%)	54	50	16.8	100	—
Pv capacity (kW)	427	432	—	—	—
Wind capacity (kW)	9	—	37	—	—
Diesel generator (kW)	440	440	440	—	440
Battery capacity (kWh)	1,069	1,063	151	4,608	—
Converter (kW)	153	160	98	247	—
Excess energy (kWh)	1066558	1050523	904588	5255743	1052992

annual average wind speeds for Huanghuagou, Kelameili, and Wujiaqu are 4.23, 4.51, and 3.87 m/s, respectively. Kelameili experiences the highest annual average wind speeds from January to April and July to December, while Huanghuagou peaks from June to July. Wujiaqu consistently maintains lower average wind speeds than the other regions. Altitude information affects the magnitude of wind speed, and it is also an important parameter in hybrid energy simulation analysis. Therefore, when obtaining data, it is also necessary to collect altitude information of the area where it is located.

Environmental temperature data significantly impact the actual output power of PV modules. The monthly average environmental temperature data for the three service areas are illustrated in Figure 2D. The highest temperature in Huanghuagou is 25.57°C in July, with a minimum of −14.13°C in January. Kelameili experiences a maximum temperature of 27.81°C in July, with a minimum of −10.07°C in January. Wujiaqu reaches a maximum temperature of 26.46°C in July, with a minimum of −8.19°C in January.

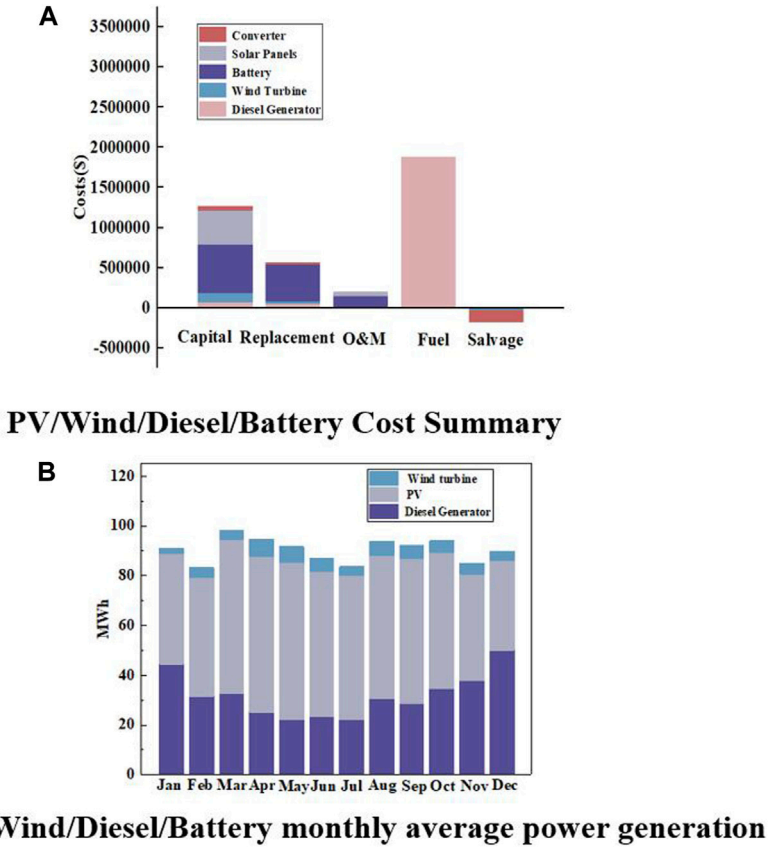

FIGURE 5
Technical and economic analysis of the hybrid energy system in kelameili service area.

TABLE 6 Summary of wujiaqu optimization results.

System	PV/Wind/Diesel/Battery	PV/Diesel/Battery	Wind/Diesel/Battery	PV/Battery	Diesel only
COE ($/kWh)	0.34	0.35	0.43	0.83	0.56
NPC($/kWh)	3141641	3183166	3923007	7574182	5146344
Renewable fraction (%)	65	60	24	100	—
Pv capacity (kW)	422	469	—	3,408	—
Wind capacity (kW)	14	—	40	—	—
Diesel generator (kW)	440	440	440	—	440
Battery capacity (kWh)	1,090	1,112	307	3,651	—
Converter (kW)	139	132	96	272	—
Excess energy (kWh)	959139	960086	820624	4938917	984292

2.3 System design and modeling

The desert highway service area hybrid energy system is comprised of PV modules, wind turbines, diesel engines, and batteries. Photovoltaic components and batteries are connected to the DC bus, while diesel generators and wind turbines are connected to the AC bus. The electrical load for highway use is connected to the AC bus, and bidirectional converters facilitate the connection between the DC and AC buses, as shown in Figure 3A.

Based on the design data for the desert highway, the annual energy demand for Huanghuagou, Kelameili, and Wujiaqu in 2022 was obtained, and the power consumption was assessed. Based on the collected load data, combined with the time of energy consumption in different service areas and the power of energy consuming equipment, the corresponding energy consumption loads for different areas can be calculated. According to the collected load data, the daily average power consumption for Huanghuagou, Kelameili, and Wujiaqu service

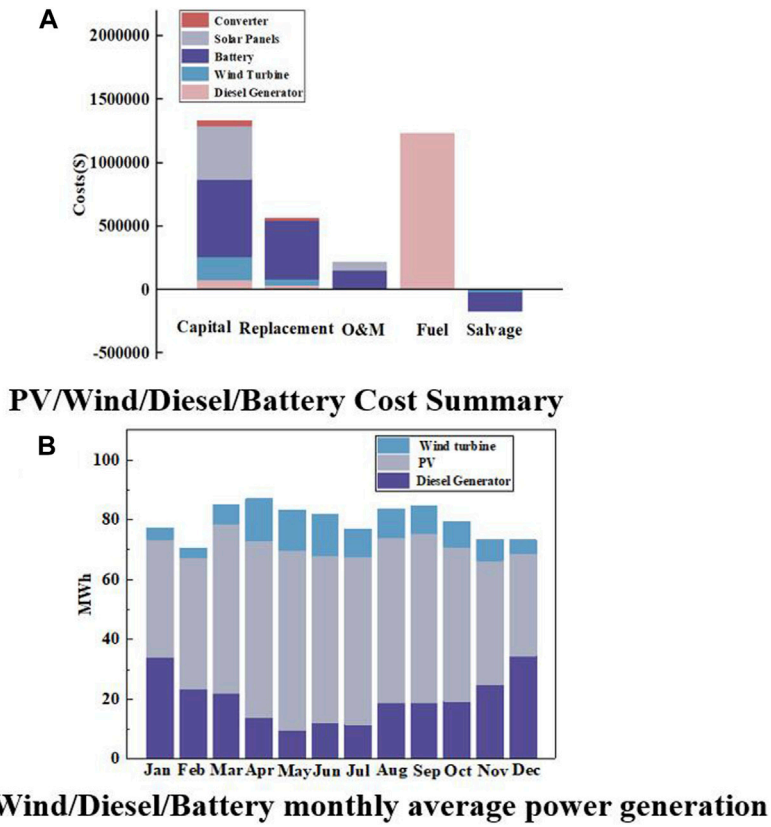

FIGURE 6
Technical and economic analysis of the hybrid energy system in wujiaqu service area.

areas is 10.5, 10.5, and 5.79 MWh, respectively. The main reason for the different load data in different regions is that there is inconsistency in the number of electrical equipment used in different areas. Compared to Huanghuagou and Kela Meili, Wujiaqu has the smallest electrical equipment. We obtained these data through design documents. The service area is a critical energy node for the highway, encompassing a mix of small industrial buildings for refueling, charging, monitoring, communication, business (including supermarkets and public restrooms), and residential purposes. Among various load types, monitoring and lighting are essential loads for the daily operation of the service area. Therefore, this study considers monitoring and lighting as important loads, intending to harness natural resources within the road domain to provide green energy for these loads, constructing a hybrid energy system. The daily average power consumption for monitoring and lighting in Huanghuagou, Kelameili, and Wujiaqu service areas is 1920, 1920, and 2,880 kWh, respectively, as shown in Table 2.

In the HOMER Pro software, input relevant data for the Huanghuagou, Kelameili, and Wujiaqu highway service areas to conduct an analysis of the hybrid energy system's capacity, environmental impact, and economic considerations. The hybrid energy system diagrams for the three service areas are depicted in Figures 3B–D, respectively.

Photovoltaic Modules: The final power generated by solar photovoltaics is influenced by various factors such as solar irradiance, characteristics of the photovoltaic cells (e.g., conversion efficiency, placement of photovoltaic panels, and derating factors), and the temperature of the photovoltaic cells. The equation used to calculate the output of a photovoltaic array is as follows (Oko. et al., 2012):

TABLE 7 Optimal mixed energy environmental emissions for huanghuagou, kelameili, and wujiaqu.

	Carbon Dioxide (kg/yr)	Carbon Monoxide (kg/yr)	Unburned Hydrocarbons (kg/yr)	Particulate Matter (kg/yr)	Sulfur Dioxide (kg/yr)	Nitrogen Oxides (kg/yr)
Huanghuagou	434502	642	4.94	14.8	1,080	3,748
Kelameili	305045	451	3.47	10.4	758	2,631
Wujiaqu	198387	293	2.25	6.76	493	1711

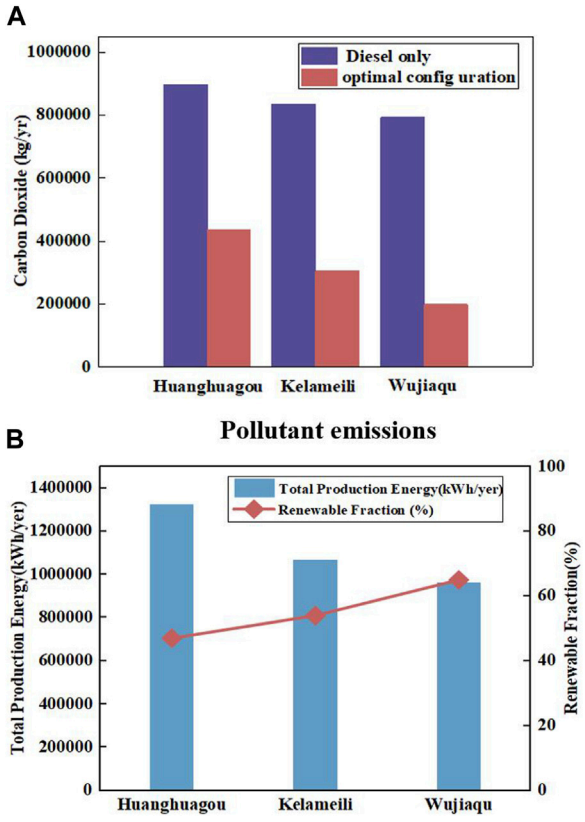

FIGURE 7
CO_2 emissions from hybrid energy systems and diesel generator only systems.

$$P_{PV} = \frac{\bar{R}_T}{\bar{R}_{T,STC}}\left[d_{PV}Y_{PV}\left(1+\alpha_{PV}\left(T_C - T_{C,STC}\right)\right)\right] \quad (4)$$

Where RT is the solar radiation incident on the site's photovoltaic array (kW/m2); RT, STC is the solar irradiance at Standard Test Conditions (STC) (1 kW/m2); dPV is the derating factor for PV (%); YPV is the rated capacity of the photovoltaic array; αPV is the power temperature coefficient, 0.44 (%/°C), for the selected photovoltaic modules; TC is the temperature of the photovoltaic cells in °C; TC, STC is the temperature of the photovoltaic cells at STC (25°C).

Wind Components: Wind turbines can convert kinetic energy into electrical energy. The electricity generated by a wind power system depends on factors such as air density, wind direction, site height, nearby topography, site temperature, and other elements. An arc is used to simulate the wind turbine. The power curve is a graph illustrating the relationship between energy output and wind speed at a specific hub height. The power output of a wind turbine under standard temperature and pressure conditions is expressed as (Sharma et al., 2022):

$$PoWer_{WT,STP} = \frac{1}{2}\rho_a A U_{\text{hub}}^3 \quad (5)$$

$$U_{\text{hub}} = U_{an}\left(\frac{Z_{\text{hub}}}{Z_{an}}\right)^{\chi_p} \quad (6)$$

TABLE 8 Load variables.

Location	Load demand				
Huanghuagou	2,880.00	3,168	3,456	3,744	4,032
Kelameili	2,280	2,508	2,736	2,964	3,192
Wujiaqu	1920	2,112	2,304	2,496	2,688

TABLE 9 Light radiation variables.

Location	Solar radiation				
Huanghuagou	3.94	4.33	4.72	5.12	5.51
Kelameili	4.1	4.51	4.92	5.33	5.74
Wujiaqu	4.09	4.49	4.90	5.31	5.72

Where p_a is the air density at standard pressure and temperature (1.225 kg/m³), A is the cross-sectional area of the wind flow (m²), U_{hub} is the wind speed at the hub height of the wind turbine (m/s), U_{an} is the wind speed at the anemometer height (m/s), Z_{hub} is the hub height of the wind turbine (m), Z_{an} is the anemometer height (m), vp is the power-law exponent, q is the actual air density (kg/m³). This equation represents the output power equation of the wind turbine at standard pressure and temperature. The actual performance of the wind turbine is expressed as:

$$PoWer_{\text{WT}} = \left(\frac{\rho}{\rho_a}\right) \times PoWer_{\text{WT,STP}} \quad (7)$$

Battery Components: As the hybrid energy system constructed in this study operates as an off-grid model, it is necessary to store excess electricity when the system's capacity exceeds demand or when the energy load requirements decrease. Additionally, when the power generated by the hybrid energy system does not meet the demand for load electricity, energy storage batteries are essential. The battery selected for this study is a lithium iron phosphate battery, which uses lithium iron phosphate (LiFePO4) as the positive electrode material and carbon as the negative electrode material in a lithium-ion battery. Lithium iron phosphate batteries have advantages such as high operating voltage, large energy density, long cycle life, good safety performance, low self-discharge rate, and no memory effect (Ramli et al., 2018). The battery capacity is calculated based on the load electricity demand and the number of autonomous days, as follows:

$$N_{\text{Batt}} = \frac{E_{\text{L}} n_{\text{d}}}{V_{inv} V_b D_{\text{d}}} \quad (8)$$

Where n_d represents the autonomous days. E_L: Daily load electricity demand. V_b: Battery efficiency (90%). V_{inv}: Inverter efficiency (95%). D_d: Battery discharge depth (80%).

Diesel Generator: In this study, a diesel generator is utilized as a backup for renewable electricity output to meet power demands, with a minimum capacity of 25%. The fuel cost is set at 0.88$/L, and the estimated diesel maintenance oil cost is 1.34$/L/HG. The fuel

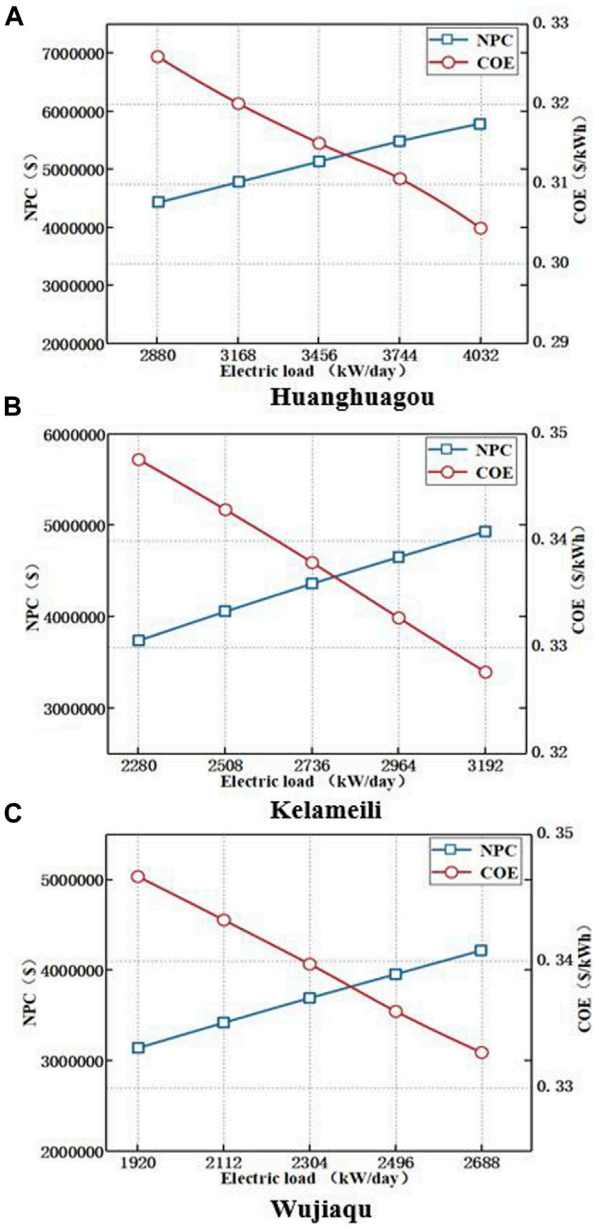

FIGURE 8
The impact of changes in load demand on NPC and COE.

consumption rate F (t) is defined by the formula (Askari and Ameri, 2012):

$$F(\tau) = F_0 P_{\text{rate\_gen}} + F_1 P_{\text{gen}}(\tau) \quad (9)$$

In the equation: *F(t)*: Fuel consumption rate of the diesel generator. F_o: Intercept coefficient. F_1:Slope of the fuel curve. $P_{rate\ gen}$: Rated output power of the diesel generator. $P_{gen}(t)$: Active output power of the diesel generator.

Converters: Converters are integrated into the microgrid system, where the DC component is used for AC loads and *vice versa*. Converters can be inverters (converting DC to AC), rectifiers (converting AC to DC), or a combination of both. In this study, the SG100k3 inverter is employed. Both the inverter and rectifier have an efficiency of 95%. It is assumed that the inverter can operate simultaneously with the AC generator, and the rated capacity of the rectifier relative to the inverter is 100% (He et al., 2018).

The primary input parameters for the components of the hybrid energy system are detailed in Table 3.

3 Results and discussion

3.1 Technical and economic analysis

This study analyzes the electricity generation potential of independent hybrid energy systems at three different locations—Huanghuagou, Kelameili, and Wujiaqu—along the desert highway based on cost-benefit and environmental indicators. Evaluation is conducted based on parameters such as COE, NPC, photovoltaic capacity, wind turbine electricity generation, diesel generator electricity generation, battery capacity, bidirectional converter capacity, excess energy production, and renewable energy penetration rate. The findings for the three distinct locations along the desert highway are summarized as follows.

(1) Huanghuagou

Optimization results for various system configurations at Huanghuagou service area are presented in Table 4. According to the optimization outcomes, the hybrid energy system composed of PV/Wind/Diesel/Battery has the lowest COE and NPC, amounting to 0.32$/kWh and 4430135$, respectively. This system requires 331 kW of photovoltaic modules, 30 wind turbines, 440 kW diesel generators, 607 kWh of battery storage, and a 161 kW bidirectional converter. The cost summary of different components in the PV/Wind/Diesel/Battery hybrid energy system at Huanghuagou service area is depicted in Figure 4A. The wind turbine component incurs the highest investment cost, followed by the battery and photovoltaic components. Additionally, fuel costs contribute significantly to the overall expenses.

The monthly average electricity generation profile for the PV/Wind/Diesel/Battery hybrid energy system at Huanghuagou service area is illustrated in Figure 4B. During the summer, photovoltaic generation dominates the energy supply, while in winter, due to reduced sunlight hours, diesel generators become the primary energy source.

(2) Kelameili

Optimization results for various system configurations at Kelameili service area are presented in Table 5. According to the optimization outcomes, the hybrid energy system composed of PV/Wind/Diesel/Battery has the lowest COE and NPC, amounting to 0.34$/kWh and 3738790$, respectively. This system requires 427 kW of photovoltaic modules, 9 wind turbines, 440 kW diesel generators, 1,069 kWh of battery storage, and a 153 kW bidirectional converter. The cost summary of different components in the PV/Wind/Diesel/Battery hybrid energy system at Kelameili service area is depicted in Figure 5A. The battery component incurs the highest investment cost, followed by photovoltaic modules and wind turbine components. Additionally, fuel costs contribute significantly to the overall expenses.

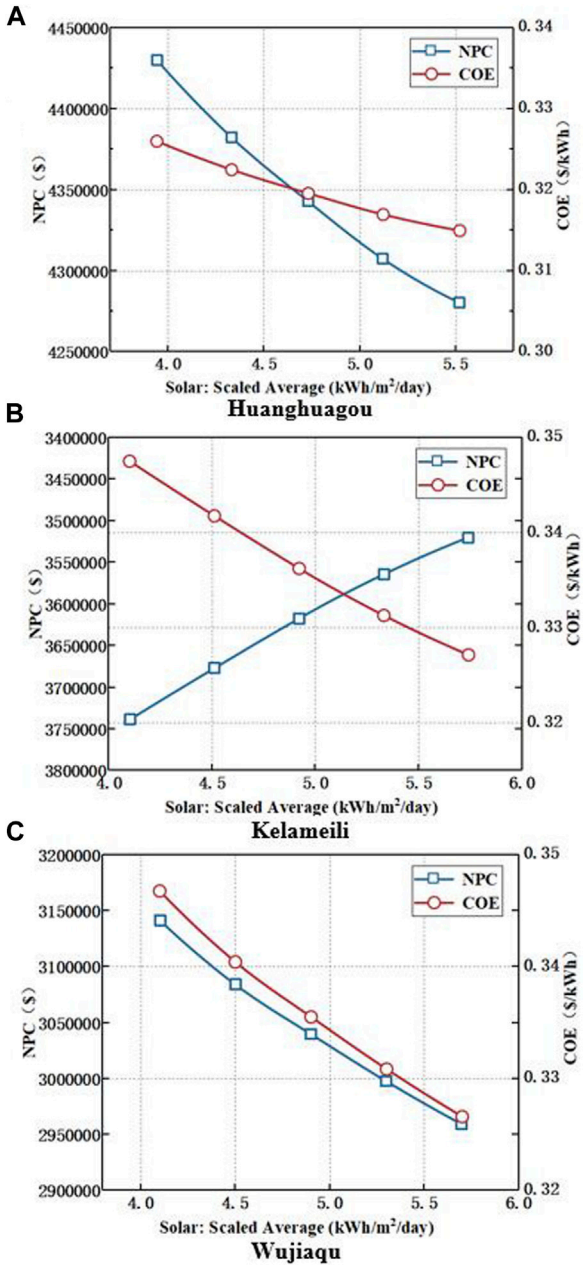

FIGURE 9
Effects of changes in radiation intensity on NPC and COE.

The monthly average electricity generation profile for the PV/Wind/Diesel/Battery hybrid energy system at Kelameili service area is illustrated in Figure 5B. As depicted, photovoltaic generation is the main energy source during the summer, while in winter, due to reduced sunlight hours, diesel generators contribute the primary energy supply.

(3) Wujiaqu

Optimization results for various system configurations at Wujiaqu service area are presented in Table 6. According to the optimization outcomes, the hybrid energy system composed of PV/Wind/Diesel/Battery has the lowest COE and NPC, amounting to 0.34$/kWh and 3141641$, respectively. This system requires 422 kW of photovoltaic modules, 14 wind turbines, 440 kW diesel generators, 1,090 kWh of battery storage, and a 139 kW bidirectional converter. The cost summary of different components in the PV/Wind/Diesel/Battery hybrid energy system at Wujiaqu service area is depicted in Figure 6A. The battery component incurs the highest investment cost, followed by photovoltaic modules and wind turbine components. Additionally, fuel costs contribute significantly to the overall expenses.

The monthly average electricity generation profile for the PV/Wind/Diesel/Battery hybrid energy system at Wujiaqu service area is shown in Figure 6B. As depicted, photovoltaic generation is the main energy source during the summer, while in winter, due to reduced sunlight hours, diesel generators contribute the primary energy supply.

Through the above analysis, it can be found that the three case areas have different COE and NPC after optimized configuration simulation. The main reason is that different areas have different solar and wind energy resources, and there are differences in energy demand among different areas.

3.2 Environmental analysis

The emissions of pollutants in hybrid energy systems primarily depend on the fuel consumption of diesel generators. Table 7 presents a comparison of different types of pollutants emitted annually at Huanghuagou, Kelameili, and Wujiaqu highway service areas.

The comparison of CO_2 emissions for optimal hybrid energy systems and diesel-only systems at Huanghuagou, Kelameili, and Wujiaqu locations is illustrated in Figure 7A. In comparison to other regions, Huanghuagou exhibits higher CO_2 emissions, generating approximately 896,305 kg of carbon dioxide annually with the diesel-only power system, whereas the optimal hybrid energy system produces 425,862 kg of carbon dioxide. Conversely, Wujiaqu demonstrates lower CO_2 emissions, with the diesel-only system producing around 792,513 kg of carbon dioxide annually, and the optimal hybrid energy system generating 198,387 kg of carbon dioxide. The renewable energy penetration rates and electricity generation from different hybrid energy systems in various regions are depicted in Figure 7B. Wujiaqu service area has the highest renewable energy penetration rate at 65%, while Huanghuagou service area has a lower rate at 47%. Examining the electricity generation, Huanghuagou has a higher annual output, while Wujiaqu has a lower annual output. Permeability can reflect the proportion of green energy in hybrid energy. The higher the penetration rate, the more environmentally friendly the system is and the less impact it has on the environment. Therefore, in the process of hybrid energy configuration, it is necessary to pursue a higher penetration rate.

3.3 Sensitivity analysis

The sensitivity analysis reveals the impact of specific variables on the optimal system type, NPC, COE, and emissions. This study investigates the influence of load growth and solar radiation intensity as variables. Considering a 10% growth in load demand,

the load variables for Huanghuagou, Kelameili, and Wujiaqu are presented in Table 8. Based on the 2.2 load data and considering a 10% increase rate, calculate the data for four load increases.

Taking into account a 10% increase in solar radiation variables, the radiation variables for Huanghuagou, Kelameili, and Wujiaqu are outlined in Table 9. Based on the 2.2 radiation data and considering a 10% increase rate, calculate the data for four radiation increases.

Figure 8 illustrates the sensitivity analysis results of the optimal hybrid energy systems to changes in load demand. The NPC values for all locations increase with the growth in load demand, while the COE values decrease with the increasing load demand.

Figure 9 depicts the sensitivity analysis results of the increase in solar radiation on NPC and COE. The NPC and COE values for all locations decrease with the rise in radiation intensity.

4 Conclusion

This In this paper, a technical, economic, and environmental analysis of the hybrid energy generation systems in three service areas of a desert highway was conducted. The main conclusions are as follows:

i. Proposed the process and method of constructing a hybrid energy system for the Desert Expressway service area using HOMER Pro software. Using NPC and COE as control indicators, combined with environmental impact assessment, configure a hybrid energy scheme.
ii. The technical and economic analysis of the Huanghuagou, Kelameili, and Wujiaqu service areas of the Desert Expressway indicates that the PV/Wind/Diesel/Battery combination is the lowest-cost configuration for the hybrid energy system, and this combination is feasible in all three regions.
iii. Looking at the annual average electricity generation of the hybrid energy systems, the Huanghuagou system has a higher annual average electricity generation, producing 1,323,860 kWh. In contrast, the Wujiaqu system has a lower annual average electricity generation, producing 959,139 kWh. According to the analysis results, it can be seen that among the three service areas, the average annual CO_2 emissions in Huanghuagou are relatively high at 434502 kg/yr, SO_2 emissions are 1,080 kg/yr, and NO_x emissions are 3,748 kg/yr. The average annual CO_2 emissions in Wujiaqu are 198387 kg/yr, SO_2 emissions are 493 kg/yr, and NO_x emissions are 1711 kg/yr.
iv. Examining environmental pollutant emissions, the primary pollutant in the hybrid energy systems is carbon dioxide (CO_2). Therefore, reducing CO_2 emissions is a key focus of current air pollution control efforts. The analysis results indicate that among the three service areas, Huanghuagou has the highest annual average CO_2 emissions at 434,502 kg/yr, while Wujiaqu has the lowest at 198,387 kg/yr.
v. Sensitivity analysis results indicate that the Net Present Cost (NPC) of all three service areas' hybrid energy systems increases with an increase in load demand, while the Cost of Energy (COE) decreases with an increase in load demand. Both NPC and COE values for the hybrid energy systems in all three service areas decrease with an increase in radiation values

This study, through the analysis of the technical, economic, and environmental impacts of the hybrid energy systems in three service areas of the Desert Expressway, demonstrates the power generation potential of independent hybrid energy systems for service areas along the desert highway. The optimal hybrid energy configurations for each service area are established, providing an economically and operationally efficient solution for the hybrid energy systems. This enhances the energy independence of highways in desert regions and promotes the sustainable development of highway energy. The feasibility analysis presented in this study can serve as an application guide for the design and implementation of hybrid energy generation at critical energy nodes such as service areas along desert highways.

Data availability statement

The original contributions presented in the study are included in the article/Supplementary material, further inquiries can be directed to the corresponding author.

Author contributions

GW: Formal Analysis, Funding acquisition, Resources, Writing–review and editing. YZ: Methodology, Project administration, Writing–original draft, Writing–review and editing. WT: Writing–review and editing. ZL: Writing–review and editing. TW: Investigation, Writing–original draft. SZ: Data curation, Writing–review and editing. XZ: Investigation, Supervision, Writing–original draft.

Funding

The author(s) declare financial support was received for the research, authorship, and/or publication of this article. This study was sponsored by the National Key Research and Development Program of China (Grant No. 2021YFB1600200)、Guangxi Transportation Science and Technology Demonstration Project "Guilin-Zhongshan Highway Green Energy Self-consistent Supply and Efficient Utilization Key Technology Integration Application Research and Demonstration": 2023-0002 and Scientific Research Projects (21–53K, 21-36X) of Shaanxi Provincial Department of Transportation. The authors are grateful for the financial supports.

Conflict of interest

Authors GW, WT, and ZL were employed by Guangxi Communications Investment Group Corporation Ltd. Author XZ

was employed by Shaanxi Transportation Planning and Design Institute Co, Ltd.

The remaining authors declare that the research was conducted in the absence of any commercial or financial relationships that could be construed as a potential conflict of interest.

The handling editor DY declared a past collaboration with authors YZ, TW, SZ at the time of the review.

Publisher's note

References

Ahmad, A., Loya, A., Ali, M., Iqbal, A., Baig, F. M., and Afzal, A. M. (2020). Roadside vertical Axis wind turbine (VAWT): an effective evolutionary design for Australian highway commuters with minimum dynamic stall. *Engineering* 12 (09), 601–616. doi:10.4236/eng.2020.129042

Akhtari, M. R., and Baneshi, M. (2019). Techno-economic assessment and optimization of a hybrid renewable co-supply of electricity, heat and hydrogen system to enhance performance by recovering excess electricity for a large energy consumer. *Energy Convers. Manag.* 188, 131–141. doi:10.1016/j.enconman.2019.03.067

Al-Buraiki, A. S., and Al-Sharafi, A. (2022). Hydrogen production via using excess electric energy of an off-grid hybrid solar/wind system based on a novel performance indicator. *Energy Convers. Manag.* 254, 115270. doi:10.1016/j.enconman.2022.115270

Al-Najjar, H., El-Khozondar, H. J., Pfeifer, C., and Al Afif, R. (2022). Hybrid grid-tie electrification analysis of bio-shared renewable energy systems for domestic application. *Sustain. Cities Soc.* 77, 103538. doi:10.1016/j.scs.2021.103538

Ang, Y. Q., Polly, A., Kulkarni, A., Chambi, G. B., Hernandez, M., and Haji, M. N. (2022). Multi-objective optimization of hybrid renewable energy systems with urban building energy modeling for a prototypical coastal community. *Renew. Energy* 201, 72–84. doi:10.1016/j.renene.2022.09.126

Askari, I. B., and Ameri, M. (2012). Techno-economic feasibility analysis of stand-alone renewable energy systems (PV/bat, Wind/bat and Hybrid PV/wind/bat) in Kerman, Iran. Energy Sour. Part B: econ. *Plan. Policy* 7, 45–60. doi:10.1080/15567240903330384

Büchner, J., Wistuba, M. P., Remmler, T., and Wang, D. (2019). On low temperature binder testing using DSR 4 mm geometry. *Mater. Struct.* 52 (6), 113. doi:10.1617/s11527-019-1412-3

Coban, H. H., Rehman, A., and Mohamed, A. (2022). Technical and economical investigation of a centralized and decentralized hybrid renewable energy system in cadaado, Somalia. *Processes* 10 (4), 667. doi:10.3390/pr10040667

Das, B. K., Hasan, M., and Das, P. (2021). Impact of storage technologies, temporal resolution, and PV tracking on stand-alone hybrid renewable energy for an Australian remote area application. *Renew. Energy* 173, 362–380. doi:10.1016/j.renene.2021.03.131

Das, P., Das, B. K., Rahman, M., and Hassan, R. (2022). Evaluating the prospect of utilizing excess energy and creating employments from a hybrid energy system meeting electricity and freshwater demands using multi-objective evolutionary algorithms. *Energy* 238, 121860. doi:10.1016/j.energy.2021.121860

Demirci, A., Akar, O., and Ozturk, Z. (2022). Technical-environmental-economic evaluation of biomass-based hybrid power system with energy storage for rural electrification. *Renew. Energy* 195, 1202–1217. doi:10.1016/j.renene.2022.06.097

El-houari, H., Allouhi, A., Rehman, S., Buker, M. S., Kousksou, T., Jamil, A., et al. (2020). Feasibility evaluation of a hybrid renewable power generation system for sustainable electricity supply in a Moroccan remote site. *J. Clean. Prod.* 277, 123534. doi:10.1016/j.jclepro.2020.123534

El-houari, H., Allouhi, A., Salameh, T., Kousksou, T., Jamil, A., and El Amrani, B. (2021). Energy, Economic, Environment (3E) analysis of WT-PV-Battery autonomous hybrid power plants in climatically varying regions. *Sustain. Energy Technol. Assessments* 43, 100961. doi:10.1016/j.seta.2020.100961

Haghighat Mamaghani, A., Avella Escandon, S. A., Najafi, B., Shirazi, A., and Rinaldi, F. (2016). Techno-economic feasibility of photovoltaic, wind, diesel and hybrid electrification systems for off-grid rural electrification in Colombia. *Renew. Energy* 97, 293–305. doi:10.1016/j.renene.2016.05.086

He, L., Zhang, S., Chen, Y., Ren, L., and Li, J. (2018). Techno-economic potential of a renewable energy-based microgrid system for a sustainable large-scale residential community in Beijing, China. *Renew. Sustain. Energy Rev.* 93, 631–641. doi:10.1016/j.rser.2018.05.053

Jahangir, M. H., Shahsavari, A., and Vaziri Rad, M. A. (2020). Feasibility study of a zero emission PV/Wind turbine/Wave energy converter hybrid system for stand-alone power supply: a case study. *J. Clean. Prod.* 262, 121250. doi:10.1016/j.jclepro.2020.121250

Jiang, W., Yuan, D. D., Shan, J. H., Ye, W. L., Lu, H. H., and Sha, A. M. (2022). Experimental study of the performance of porous ultra-thin asphalt overlay. *Int. J. PAVEMENT Eng.* 23 (6), 2049–2061. doi:10.1080/10298436.2020.1837826

Jiang, W., Zhang, S., Wang, T., Zhang, Y., Sha, A., Xiao, J., et al. (2024). Evaluation method for the availability of solar energy resources in road areas before route corridor planning. *Appl. Energy* 356, 122260. doi:10.1016/j.apenergy.2023.122260

Khan, F. A., Pal, N., Saeed, S. H., and Yadav, A. (2022). Techno-economic and feasibility assessment of standalone solar Photovoltaic/Wind hybrid energy system for various storage techniques and different rural locations in India. *Energy Convers. Manag.* 270, 116217. doi:10.1016/j.enconman.2022.116217

Kim, S., Lee, Y., and Moon, H.-R. (2018). Siting criteria and feasibility analysis for PV power generation projects using road facilities. *Renew. Sustain. Energy Rev.* 81, 3061–3069. doi:10.1016/j.rser.2017.08.067

Li, J., Liu, P., and Li, Z. (2020). Optimal design and techno-economic analysis of a solar-wind-biomass off-grid hybrid power system for remote rural electrification: a case study of west China. *Energy* 208, 118387. doi:10.1016/j.energy.2020.118387

Li, J., Liu, P., and Li, Z. (2022). Optimal design of a hybrid renewable energy system with grid connection and comparison of techno-economic performances with an off-grid system: a case study of West China. *Comput. Chem. Eng.* 159, 107657. doi:10.1016/j.compchemeng.2022.107657

Ma, Q., Huang, X., Wang, F., Xu, C., Babaei, R., and Ahmadian, H. (2022a). Optimal sizing and feasibility analysis of grid-isolated renewable hybrid microgrids: effects of energy management controllers. *Energy* 240, 122503. doi:10.1016/j.energy.2021.122503

Ma, X., Zhang, T., Xie, Y., and Tan, Q. (2022b). A simulation-assessment-optimization approach towards energy self-sufficiency and carbon reduction in regional-scale sewage systems. *Resour. Conservation Recycl.* 187, 106595. doi:10.1016/j.resconrec.2022.106595

Oko, C., Eo, D., Omunakwe, N.F., and Anthony Nnamdi, Ezemerihe (2012). Design and economic analysis of a photovoltaic system-a case study. *Int. J. Renew. Energy Dev.* 1 (3), 65–73. doi:10.14710/ijred.1.3.65-73

Ramesh, M., and Saini, R. P. (2020). Dispatch strategies based performance analysis of a hybrid renewable energy system for a remote rural area in India. *J. Clean. Prod.* 259, 120697. doi:10.1016/j.jclepro.2020.120697

Ramli, M. A. M., Bouchekara, H. R. E. H., and Alghamdi, A. S. (2018). Optimal sizing of PV/wind/diesel hybrid microgrid system using multi-objective self-adaptive differential evolution algorithm. *Renew. Energy* 121, 400–411. doi:10.1016/j.renene.2018.01.058

Razmjoo, A., Gakenia Kaigutha, L., Vaziri Rad, M. A., Marzband, M., Davarpanah, A., and Denai, M. (2021). A Technical analysis investigating energy sustainability utilizing reliable renewable energy sources to reduce CO_2 emissions in a high potential area. *Renew. Energy* 164, 46–57. doi:10.1016/j.renene.2020.09.042

Renken, P., Büchler, S., Falchetto, A. C., Wang, D., and Wistuba, M. P. (2018). Warm mix asphalt-a German case study. *Asph. Paving Technol.* 87, 685–716. doi:10.12783/aapt2018/33821

Rezaei, M., Dampage, U., Das, B. K., Nasif, O., Borowski, P. F., and Mohamed, M. A. (2021). Investigating the impact of economic uncertainty on optimal sizing of grid-independent hybrid renewable energy systems. *Processes* 9 (8), 1468. doi:10.3390/pr9081468

Ribó-Pérez, D., Herraiz-Cañete, Á., Alfonso-Solar, D., Vargas-Salgado, C., and Gómez-Navarro, T. (2021). Modelling biomass gasifiers in hybrid renewable energy microgrids; a complete procedure for enabling gasifiers simulation in HOMER. *Renew. Energy* 174, 501–512. doi:10.1016/j.renene.2021.04.083

Sharma, S., Sood, Y. R., Sharma, N. K., Bajaj, M., Zawbaa, H. M., Turky, R. A., et al. (2022). Modeling and sensitivity analysis of grid-connected hybrid green microgrid system. *Ain Shams Eng. J.* 13 (4), 101679. doi:10.1016/j.asej.2021.101679

Shi, K., Ma, F., Fu, Z., Song, R., Yuan, D., and Ogbon, A. W. (2024). Enhancing aged SBS-modified bitumen performance with unaged bitumen additives. *Constr. Build. Mater.* 412, 134768. doi:10.1016/j.conbuildmat.2023.134768

Sifakis, N., Konidakis, S., and Tsoutsos, T. (2021). Hybrid renewable energy system optimum design and smart dispatch for nearly Zero Energy Ports. *J. Clean. Prod.* 310, 127397. doi:10.1016/j.jclepro.2021.127397

Sun, J., Huang, W., Lu, G. Y., Luo, S., and Li, Y. H. (2023a). Investigation of the performance and micro-evolution mechanism of low-content thermosetting epoxy asphalt binder towards sustainable highway and bridge decks paving. *J. Clean. Prod.* 384, 135588. doi:10.1016/j.jclepro.2022.135588

Sun, J., Luo, S., Wang, Y. Z., Dong, Q. F., and Zhang, Z. H. (2023b). Pre-treatment of steel slag and its applicability in asphalt mixtures for sustainable pavements. *Chem. Eng. J.* 476, 146802. doi:10.1016/j.cej.2023.146802

Toopshekan, A., Yousefi, H., and Astaraei, F. R. (2020). Technical, economic, and performance analysis of a hybrid energy system using a novel dispatch strategy. *Energy* 213, 118850. doi:10.1016/j.energy.2020.118850

Uwineza, L., Kim, H.-G., and Kim, C. K. (2021). Feasibility study of integrating the renewable energy system in Popova Island using the Monte Carlo model and HOMER. *Energy Strategy Rev.* 33, 100607. doi:10.1016/j.esr.2020.100607

Vendoti, S., Muralidhar, M., and Kiranmayi, R. (2020). Techno-economic analysis of off-grid solar/wind/biogas/biomass/fuel cell/battery system for electrification in a cluster of villages by HOMER software. *Environ. Dev. Sustain.* 23 (1), 351–372. doi:10.1007/s10668-019-00583-2

Vergara-Zambrano, J., Kracht, W., and Díaz-Alvarado, F. A. (2022). Integration of renewable energy into the copper mining industry: a multi-objective approach. *J. Clean. Prod.* 372, 133419. doi:10.1016/j.jclepro.2022.133419

Walther, A., Bchler, S., Falchetto, A. C., Wang, D., Riccardi, C., and Wistuba, M. P. (2019). Experimental investigation on asphalt mixtures prepared with reclaimed asphalt pavement and rejuvenators based on the BTSV method. *ROAD Mater. PAVEMENT Des.* 20 (7), 1695–1708. doi:10.1080/14680629.2019.1594053

Wang, H. P., Airey, G. D., Leng, Z., and Lu, G. Y. (2023). Optimisation of the preparation procedure of crumb rubber modified bitumen with wax-based additives. *ROAD Mater. PAVEMENT Des.*, 1–12. doi:10.1080/14680629.2023.2191724

Wu, W., Cavalli, M. C., Jiang, W., and Kringos, N. (2024). Differing perspectives on the use of high-content SBS polymer-modified bitumen. *Constr. Build. Mater.* 411, 134433. doi:10.1016/j.conbuildmat.2023.134433

Yuan, D. D., Jiang, W., Sha, A. M., Xiao, J. J., Wu, W. J., and Wang, T. (2023). Technology method and functional characteristics of road thermoelectric generator system based on Seebeck effect. *Appl. ENERGY* 331, 120459. doi:10.1016/j.apenergy.2022.120459

Zhang, K., Chen, M., Yang, Y., Zhong, T., Zhu, R., Zhang, F., et al. (2022). Quantifying the photovoltaic potential of highways in China. *Appl. Energy* 324, 119600. doi:10.1016/j.apenergy.2022.119600

frontiers | Frontiers in Energy Research

TYPE Original Research
PUBLISHED 16 February 2024
DOI 10.3389/fenrg.2024.1375653

OPEN ACCESS

EDITED BY
Meng Jia,
Shandong University of Science and Technology, China

REVIEWED BY
Ziming Liu,
Tongji University, China
Xinli Gan,
Guizhou Institute of Technology, China

*CORRESPONDENCE
Jiefu Bi,
bijiefu@chd.edu.cn

RECEIVED 24 January 2024
ACCEPTED 05 February 2024
PUBLISHED 16 February 2024

CITATION
Bi J and Zhang Q (2024), A comprehensive evaluation of asphalt concrete modified with ACP based on improved AHP and radar chart method.
Front. Energy Res. 12:1375653.
doi: 10.3389/fenrg.2024.1375653

A comprehensive evaluation of asphalt concrete modified with ACP based on improved AHP and radar chart method

Jiefu Bi[1]* and Qing Zhang[2,3,4]

[1]School of Highway, Chang'an University, Xi'an, China, [2]Henan Key Laboratory of High-Grade Highway Detection and Maintenance Technology, Xinxiang, China, [3]National Engineering Research Center of Highway Maintenance Equipment, Xinxiang, China, [4]Key Laboratory of Green Chemical Media and Reactions, Ministry of Education, Collaborative Innovation Center of Henan Province for Fine Chemicals Green Manufacturing, School of Chemistry and Chemical Engineering, Henan Normal University, Xinxiang, China

Microwave heating, as an efficient and environmentally friendly heating technology, is used in solving rapid deicing issues of asphalt pavement. In this study, activated carbon powder (ACP) was adopted to partly replace mineral powder and improve the microwave heating efficiency of asphalt concrete. Some tests of key indexes about deicing, microwave heating, asphalt concrete and asphalt mastic were conducted in laboratory. In order to comprehensively compare and analyze the performance of asphalt concrete at different replacements and recommend the best type of asphalt concrete with laboratory data, an advanced data processing and mathematical model was established based on improved Analytic Hierarchy Process (AHP) and radar chart method. The results show that the f_i representing the comprehensive performance of each type of asphalt concrete can be ranked as $f_6>f_5>f_4>f_3>f_2>f_1$. Therefore, it can be easily recommended that the type of asphalt concrete that meets the expected requirements is that with 100% ACP replacement amount. Additionally, the established model has proved feasible and effective through the application of this research. Finally, this research's process and results can provide a new idea and reference for resolution of similar problems in the future.

KEYWORDS

asphalt concrete, deicing, microwave heating, improved AHP, radar chart method

1 Introduction

1.1 Background

Compared with traditional deicing methods, microwave heating provides significant convenience and considerable saving in cost (Mou and Li, 2003). It exploits the energy carried by microwave and turned into heat to melt the ice on the surface of the pavement. Opinions have been pointed out that aggregates (especially sieve size from 4.75 to 9.5 mm) account for most in microwave heating and determine the heating efficiency (Guo et al., 2020; Trigos et al., 2020). However, due to the conventional material used in asphalt mixture, the microwave heating efficiency (MHE) has not reached the satisfactory researchers expect (Osborne and Hutcheson, 1989). In recent years, much attention has been paid to search

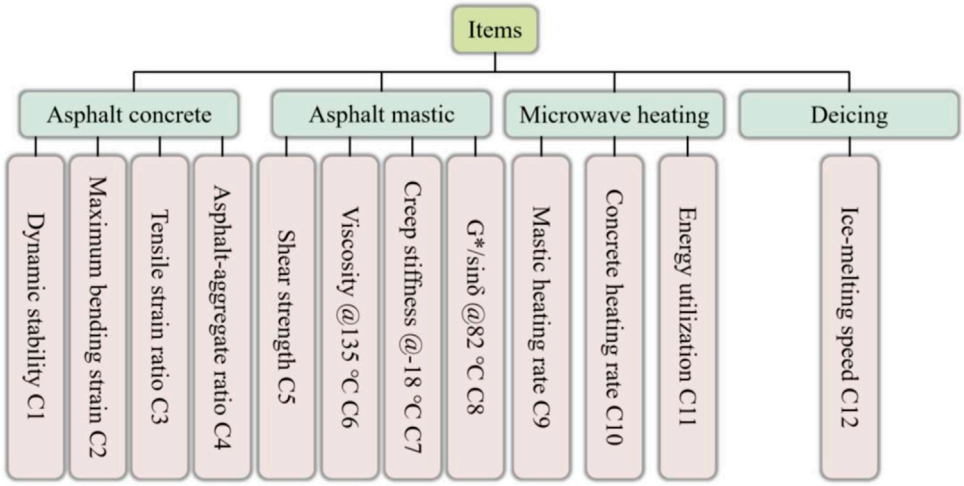

FIGURE 1
The selected indexes system.

TABLE 1 Test data of evaluation index.

Type index	C1/ times/mm	C2/ με	C3/ %	C4/ %	C5/ KPa	C6/ Pa·s	C7/ MPa	C8/ KPa	C9/ °C/s	C10/ °C/s	C1/ %	C12/ g/s
0% (P1)	887	2700	89.4	4.71	96.87	1.05	654	0.402	0.238	0.430	40	0.246
20% (P2)	978	2800	80.3	4.79	102.5	1.068	697	0.410	0.256	0.487	45	0.299
40% (P3)	1061	3000	77.1	4.87	117.68	1.083	699	0.430	0.432	0.509	48	0.434
60% (P4)	1187	3300	76.0	4.95	126.48	1.345	715	0.447	0.478	0.710	63	0.459
80% (P5)	1231	3500	75.2	5.03	328.23	1.415	718	0.462	0.674	0.750	69	0.518
100% (P6)	1358	3750	75.0	5.13	351.1	1.58	738	0.493	0.720	0.838	79	0.607

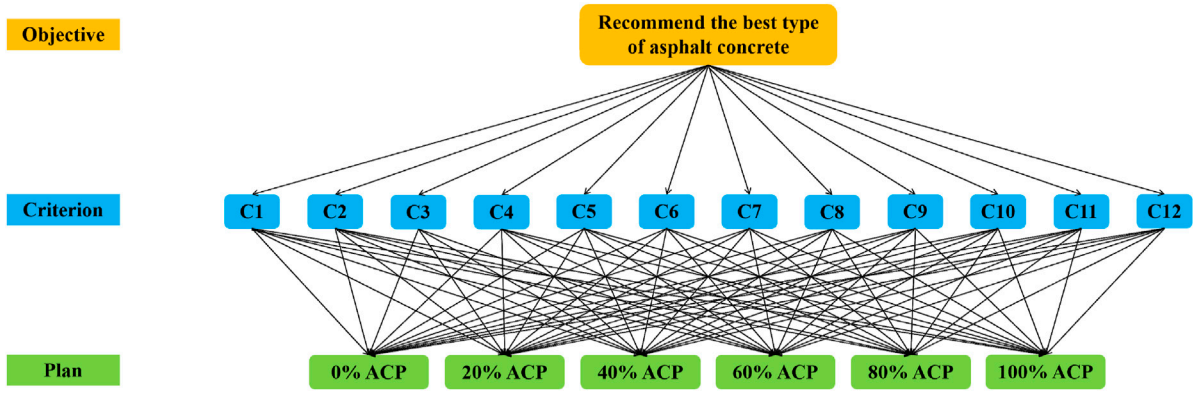

FIGURE 2
The hierarchical analysis model.

proper microwave absorbing materials. For instance, Wang et al. (2016) compared the MHE of asphalt containing magnetite aggregates with that containing general basalt aggregates, finding out MHE of the former is 6.15 times of the latter. Wang et al. (2019a) get the similar result and put forward that MHA reduces heating uniformity and MHE can be influenced by ambient temperature. Jahanbakhsh, et al. (2018) found out that carbon black (CB) can enhance the conductivity and sensitivity to microwave radiation and

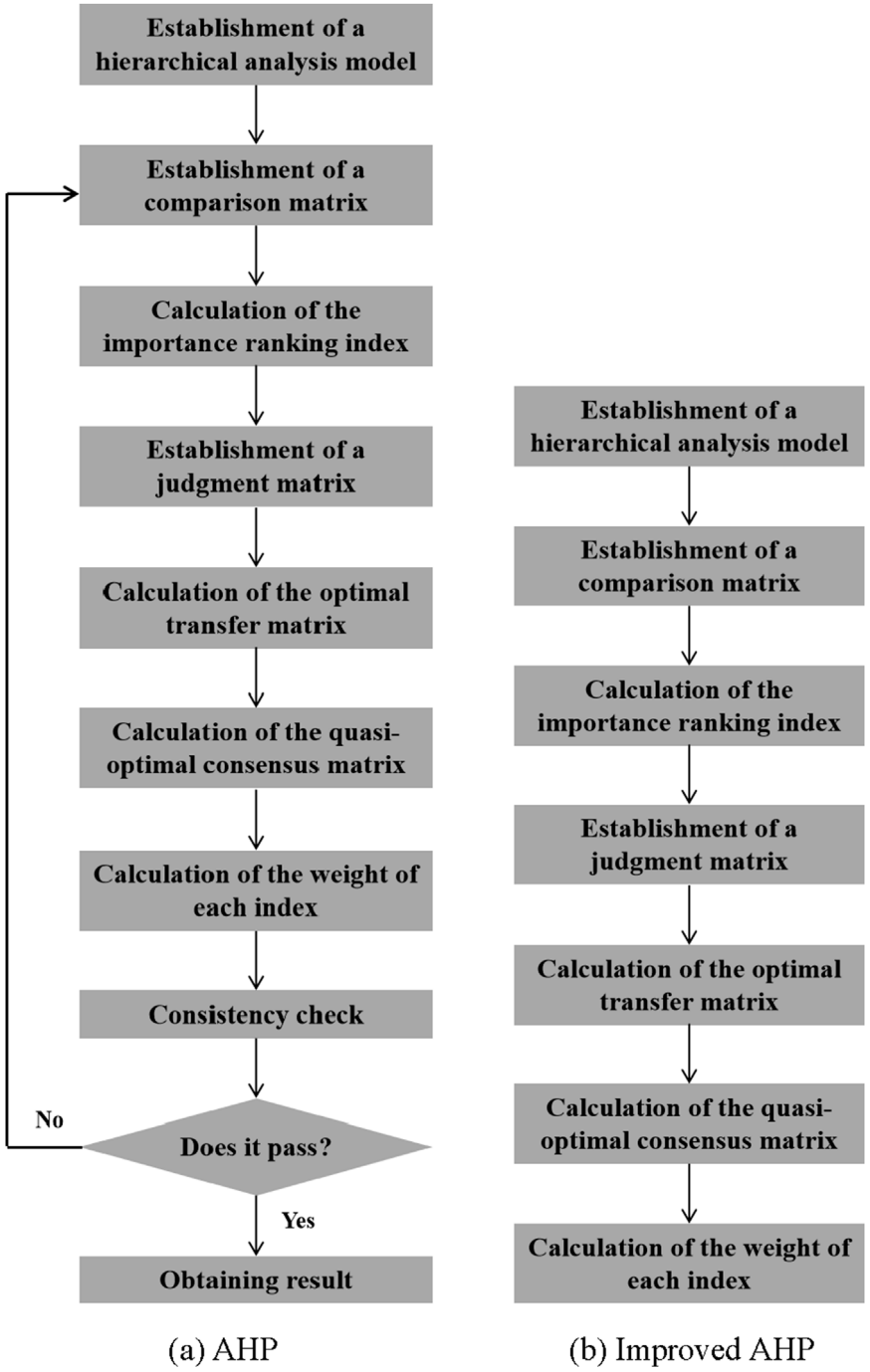

FIGURE 3
The processing flow AHP and improved AHP.

TABLE 2 Establishment method of comparison matrix.

Value meaning	Scale
The *i*th factor is more important than the *j*th factor	2
The *i*th factor is as important as the *j*th factor	1
The *i*th factor is not as important as the *j*th factor	0

CB modified asphalt mixture showed higher MHE than those of limestone and siliceous mixture. Gao et al. (2019) utilized steel wool fiber and assessed the heating uniformity and sustainability of the asphalt mixture under −5 and −10°C and offered an optimal content. Ding et al. (2020) conducted a microwave heating test to establish the effectiveness of a ferric aluminum mixture (Al_2O_3:Fe_3O_4 = 1:1) and hydroxy iron powder in enhancing microwave deicing

TABLE 3 Comparison matrix.

Index	C1	C2	C3	C4	C5	C6	C7	C8	C9	C10	C11	C12
C1	1	1	1	1	2	2	2	2	2	2	2	0
C2	1	1	1	1	2	2	2	2	2	2	2	0
C3	1	1	1	1	2	2	2	2	2	2	2	0
C4	1	1	1	1	2	2	2	2	2	2	2	0
C5	0	0	0	0	1	1	1	1	0	0	0	0
C6	0	0	0	0	1	1	1	1	0	0	0	0
C7	0	0	0	0	1	1	1	1	0	0	0	0
C8	0	0	0	0	1	1	1	1	0	0	0	0
C9	0	0	0	0	2	2	2	2	1	1	1	0
C10	0	0	0	0	2	2	2	2	1	1	1	0
C11	0	0	0	0	2	2	2	2	1	1	1	0
C12	2	2	2	2	2	2	2	2	2	2	2	1

TABLE 4 Judgment matrix.

Index	C1	C2	C3	C4	C5	C6	C7	C8	C9	C10	C11	C12
C1	1	1	1	1	9/2	9/2	9/2	9/2	11/4	11/4	11/4	4/9
C2	1	1	1	1	9/2	9/2	9/2	9/2	11/4	11/4	11/4	4/9
C3	1	1	1	1	9/2	9/2	9/2	9/2	11/4	11/4	11/4	4/9
C4	1	1	1	1	9/2	9/2	9/2	9/2	11/4	11/4	11/4	4/9
C5	2/9	2/9	2/9	2/9	1	1	1	1	3/8	3/8	3/8	1/6
C6	2/9	2/9	2/9	2/9	1	1	1	1	3/8	3/8	3/8	1/6
C7	2/9	2/9	2/9	2/9	1	1	1	1	3/8	3/8	3/8	1/6
C8	2/9	2/9	2/9	2/9	1	1	1	1	3/8	3/8	3/8	1/6
C9	3/8	3/8	3/8	3/8	11/4	11/4	11/4	11/4	1	1	1	1/4
C10	3/8	3/8	3/8	3/8	11/4	11/4	11/4	11/4	1	1	1	1/4
C11	3/8	3/8	3/8	3/8	11/4	11/4	11/4	11/4	1	1	1	1/4
C12	9/4	9/4	9/4	9/4	23/4	23/4	23/4	23/4	4/1	4/1	4/1	1

sensitivity.Yıldız and Atakan, (2020) evaluated the possibility of fly ash in enhancing the microwave heating performance, which shows positive impact as a result. Liu et al. (2019b) and Wang et al. (2019b) used active carbon powder (ACP) as filler and described the ice-melting characteristic by infrared thermography and melting speed while examine the mechanical performance of the mixture simultaneously, which showed improvement in rutting and fatigue resistance and microwave absorbing capacity. Liu and Sun, (2024) proved that ACP replacement of mineral powder can improve the thermal stability of asphalt mixture. In order to quantificationally compare the microwave performance, researchers have also brought out key parameters including the surface temperature, heat distribution, deicing time and thermal diffusion to judge the microwave deicing performances of all the additives (Guo, et al., 2020).

Activated carbon powder (ACP) is a material in black with developed pore structure and large specific surface area, thus it is equipped with its good adsorption performance, chemical and physical stability. In view of its unique microcrystalline and chemical structure, researchers have applied ACP to asphalt mixture in order to improve its performances and other functional demand. In mechanical performances, Bostancioğlu and Oruc, (2015) used ACP and furan resin as additives and discovered increase in Marshall stability and quotient by 9% and 25% respectively. Seyrek et al. (2020) further found that the addition of ACP makes contribution to high- and low-temperature performance and resistance against fatigue cracking as well as permanent deformation. Liu and Wang, (2019a) substituted mineral powder by ACP to modify asphalt mastic, which showed significant improvement in shear strength viscosity and low-

TABLE 5 Optimal transfer matrix.

Index	C1	C2	C3	C4	C5	C6	C7	C8	C9	C10	C11	C12
C1	0	0	0	0	0.6891	0.6891	0.6891	0.6891	0.3484	0.3484	0.3484	−0.2229
C2	0	0	0	0	0.6891	0.6891	0.6891	0.6891	0.3484	0.3484	0.3484	−0.2229
C3	0	0	0	0	0.6891	0.6891	0.6891	0.6891	0.3484	0.3484	0.3484	−0.2229
C4	0	0	0	0	0.6891	0.6891	0.6891	0.6891	0.3484	0.3484	0.3484	−0.2229
C5	−0.6891	−0.6891	−0.6891	−0.6891	0	0	0	0	−0.3407	−0.3407	−0.3407	−0.9120
C6	−0.6891	−0.6891	−0.6891	−0.6891	0	0	0	0	−0.3407	−0.3407	−0.3407	−0.9120
C7	−0.6891	−0.6891	−0.6891	−0.6891	0	0	0	0	−0.3407	−0.3407	−0.3407	−0.9120
C8	−0.6891	−0.6891	−0.6891	−0.6891	0	0	0	0	−0.3407	−0.3407	−0.3407	−0.9120
C9	−0.3484	−0.3484	−0.3484	−0.3484	0.3407	0.3407	0.3407	0.3407	0	0	0	−0.5713
C10	−0.3484	−0.3484	−0.3484	−0.3484	0.3407	0.3407	0.3407	0.3407	0	0	0	−0.5713
C11	−0.3484	−0.3484	−0.3484	−0.3484	0.3407	0.3407	0.3407	0.3407	0	0	0	−0.5713
C12	0.2229	0.2229	0.2229	0.2229	0.9120	0.9120	0.9120	0.9120	0.5713	0.5713	0.5713	0

TABLE 6 Quasi-optimum consistent matrix.

Index	C1	C2	C3	C4	C5	C6	C7	C8	C9	C10	C11	C12
C1	1	1	1	1	4.8876	4.8876	4.8876	4.8876	2.2305	2.2305	2.2305	0.5985
C2	1	1	1	1	4.8876	4.8876	4.8876	4.8876	2.2305	2.2305	2.2305	0.5985
C3	1	1	1	1	4.8876	4.8876	4.8876	4.8876	2.2305	2.2305	2.2305	0.5985
C4	1	1	1	1	4.8876	4.8876	4.8876	4.8876	2.2305	2.2305	2.2305	0.5985
C5	0.2046	0.2046	0.2046	0.2046	1	1	1	1	0.4563	0.4563	0.4563	0.1225
C6	0.2046	0.2046	0.2046	0.2046	1	1	1	1	0.4563	0.4563	0.4563	0.1225
C7	0.2046	0.2046	0.2046	0.2046	1	1	1	1	0.4563	0.4563	0.4563	0.1225
C8	0.2046	0.2046	0.2046	0.2046	1	1	1	1	0.4563	0.4563	0.4563	0.1225
C9	0.4483	0.4483	0.4483	0.4483	2.1913	2.1913	2.1913	2.1913	1	1	1	0.2683
C10	0.4483	0.4483	0.4483	0.4483	2.1913	2.1913	2.1913	2.1913	1	1	1	0.2683
C11	0.4483	0.4483	0.4483	0.4483	2.1913	2.1913	2.1913	2.1913	1	1	1	0.2683
C12	1.6707	1.6707	1.6707	1.6707	8.1660	8.1660	8.1660	8.1660	3.7265	3.7265	3.7265	1

TABLE 7 Weights of all indexes.

Index	C1	C2	C3	C4	C5	C6	C7	C8	C9	C10	C11	C12
Weights	0.1276	0.1276	0.1276	0.1276	0.0261	0.0261	0.0261	0.0261	0.0572	0.0572	0.0572	0.2133

TABLE 8 The included angles between the index axes in the radar chart.

Index	α_1	α_2	α_3	α_4	α_5	α_6	α_7	α_8	α_9	α_{10}	α_{11}	α_{12}
Angle/o	45.936	45.936	45.936	45.936	9.396	9.396	9.396	9.396	20.592	20.592	20.592	76.788

temperature rheological property. Thanks to ACP's porous structure, environment functions become possible. Hu et al. (2019) noted that the addition of ACP not only enhanced filtration effectiveness but also lowered the pH of runoff and increased the rate of pollution removal. Lei et al. (2020) adopted ACP to modify TiO_2 by which the spectral response range is

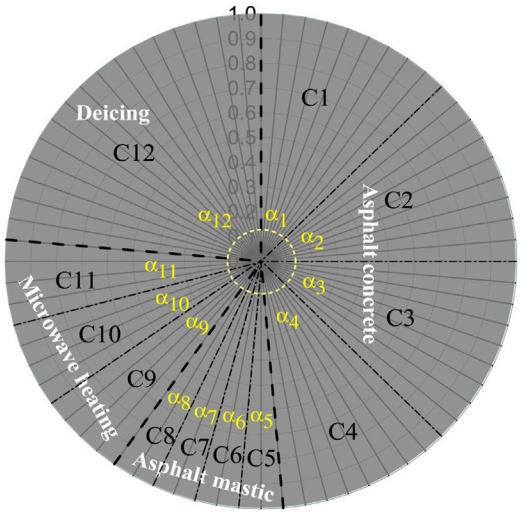

FIGURE 4
Radar chart considering weight value.

extended and dispersion performance enhanced. Xiao et al. (2017) verified the high porosity and large internal surface in ACP and used it to reduce volatile organic compounds (VOCs) the pavement produces. Moreover, Karimi et al. (2018) took advantage of ACP's microwave adsorption ability and use it as binder-based conductive addictive, which showed potential in crack-healing performance under microwave. Kavussi et al. (2020) evaluated the microwave heating properties of ACP and pointed out its feasibility in microwave healing. As mentioned above, ACP shows a huge potential in road engineering.

Based on above literature review and analysis, the idea which ACP was used in asphalt concrete to improve its microwave heating capable is feasible. Therefore, many related tests were conducted in laboratory and a lot of data was obtained. In order to qualitatively and quantitatively analyze and compare the comprehensive performance of all types of asphalt concrete considering all test results of indexes, Analytic Hierarchy Process (AHP) and radar chart method are used to complete this work. AHP was first brought forward in the 1980 by Saaty to assist in solving complex decision problems by capturing both subjective and objective evaluation measures (Saaty, 1980). Since it is simplicity and of great flexibility, AHP has been studied extensively and utilized in nearly every application related to multiple criteria decision-making (MCDM) problem (Ho and Ma, 2018). It provides a concise and useful method for decision making in a complex system composed of many interrelated and restrictive factors (Ishizaka and Labib, 2011). AHP contains four main steps: stratification, weights comparison, weights calculation and verification of consistency (Shin et al., 2020). Stratification leads to the formation of a hierarchy, which comprises a decision goal, decision criteria, and alternatives. Then, elements at each level are compared based on the assumption of inter-independent and the weight matrix is structured. Consistency verification is conducted to prevent the mistake made subjectively by decision-makers and to ensure the optimal outcome (Darko et al., 2018). Moreover, radar chart method originated in Japan as a useful graphical display method for multivariate data and has been used in several fields (Bianchin et al., 2018). Compared with traditional mathematical analysis method, radar chart projects the indicator status of the evaluation object onto a two-dimensional plane, therefore offering an intuitive visualization under various indicators and quantitative evaluation via combination of numerical proportions (Chen et al., 2010; Wang et al., 2017). The basic shape of a radar chart generally contains 3 concentric circles and necessary indicators dividing the circle by fan shapes. The smallest circle represents the lowest level, which is 1/2 of the average, while the middle circle corresponds to the average level, and the largest circle denotes the advanced level. Furthermore, each sector is subdivided into sub-indicators.Corresponding index values of subfactors are marked and the adjacent points are connected with lines to form a radar chart. Before forming a radar chart, optimal combination of indicators should be determined in order to prevent the impact on evaluation indexes such as area and perimeter caused by the change in the order of indicators (Liu et al., 2008; Kalonia et al., 2013).

In this study, ACP was used to partly replace mineral powder to improve deicing efficiency of asphalt concrete under microwave heating. In the laboratory, the twelve key indexes of these different types of asphalt concrete were studied and a large amount of data was obtained. Under the premise of considering the weight of each index, it is very difficult to compare and analyze the comprehensive performance of these different types of asphalt concrete. In order to solve this problem, the improved AHP was used to determine the weight of each index, and then the radar chart method was used to qualitatively and quantitatively analyze the comprehensive performance of different types of asphalt concrete. After these calculations and analyses, a best type of asphalt concrete that meets the expected requirements is recommended. Finally, the

TABLE 9 Data after being standardized.

Type index	C1	C2	C3	C4	C5	C6	C7	C8	C9	C10	C11	C12
P1	0.6532	0.7200	1.0000	0.9181	0.2759	0.6646	0.8862	0.8154	0.3306	0.5131	0.5063	0.4053
P2	0.7202	0.7467	0.8982	0.9337	0.2919	0.6759	0.9444	0.8316	0.3556	0.5811	0.5696	0.4926
P3	0.7813	0.8000	0.8624	0.9493	0.3352	0.6854	0.9472	0.8722	0.6000	0.6074	0.6076	0.7150
P4	0.8741	0.8800	0.8501	0.9649	0.3602	0.8512	0.9688	0.9067	0.6639	0.8473	0.7975	0.7562
P5	0.9065	0.9333	0.8412	0.9805	0.9349	0.8956	0.9729	0.9371	0.9361	0.8950	0.8734	0.8534
P6	1.0000	1.0000	0.8389	1.0000	1.0000	1.0000	1.0000	1.0000	1.0000	1.0000	1.0000	1.0000

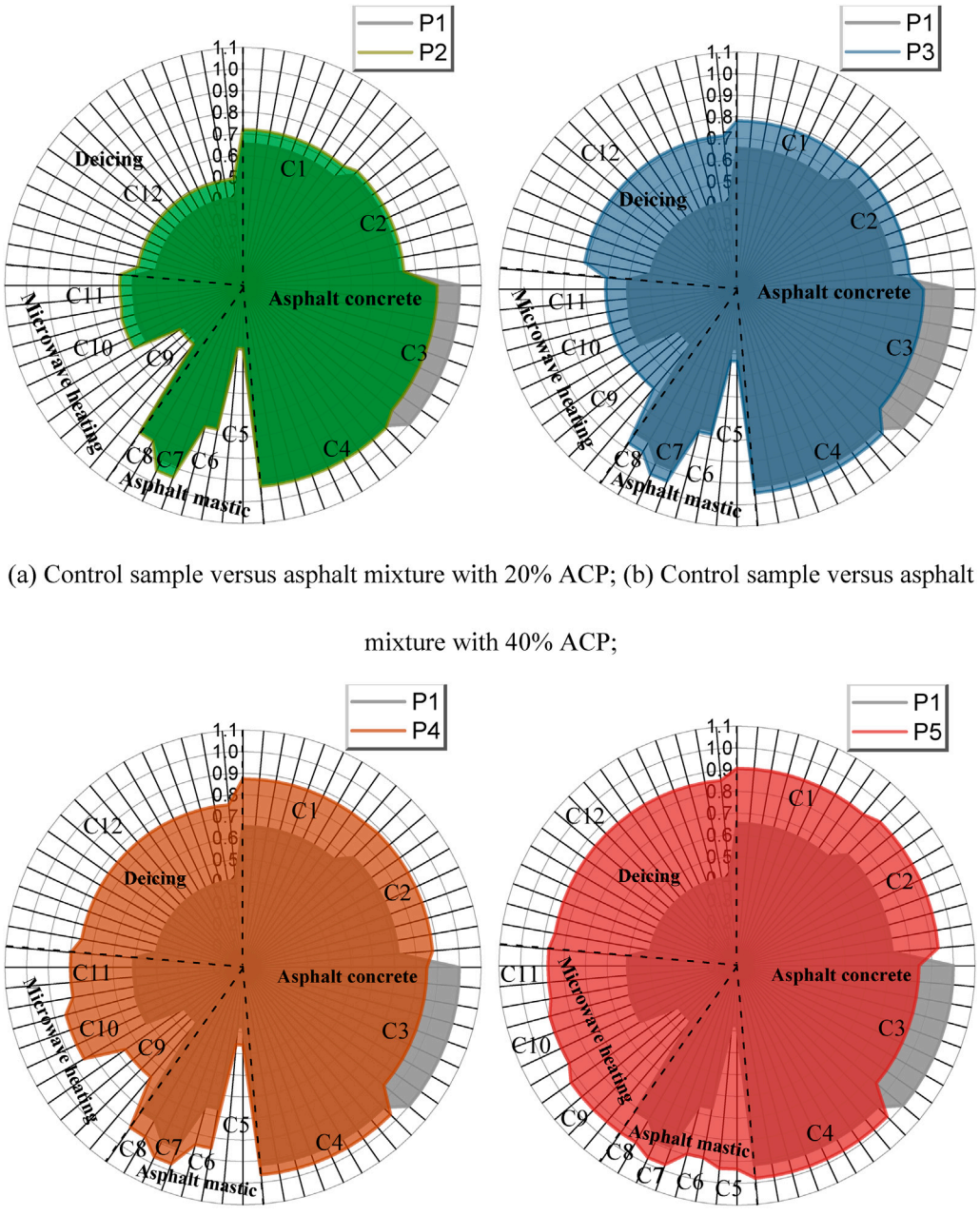

(a) Control sample versus asphalt mixture with 20% ACP; (b) Control sample versus asphalt mixture with 40% ACP;

(c) Control sample versus asphalt mixture with 60% ACP; (d) Control sample versus asphalt mixture with 80% ACP;

FIGURE 5
(Continued).

process and results of this research can provide a new idea and reference for solving similar problems in the future.

1.2 Objective of this research

Based on the above literature review and discussion, the main objectives of this research are summarized as the following two points:

1) A model that can comprehensively compare and analyze the performance of different types of asphalt concrete will be established under the condition of considering multiple indexes.
2) This established model will be applied to analyze different types of ACP modified asphalt concrete, and finally the best type of asphalt concrete that meets the expected requirements will be recommended.

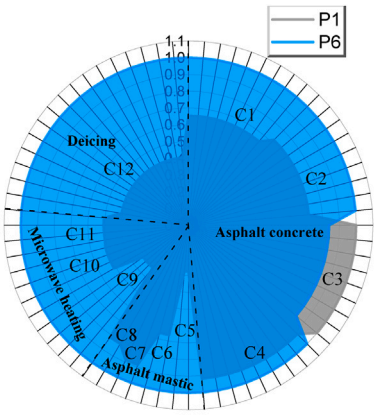

(e) Control sample versus asphalt mixture with 100% ACP.

FIGURE 5
(Continued). The radar charts for six types of asphalt mixture.

TABLE 10 The calculation results of f_i.

f_i	f_1	f_2	f_3	f_4	f_5	f_6
Calculation results	0.6849	0.7103	0.7840	0.8494	0.9199	0.9992

2 Information of the evaluated object

2.1 Introduction of the evaluated object

In this study, ACP was used to partially replace mineral powder (0%, 20%, 40%, 60%, 80%, and 100% replacement of volume of mineral powder) to achieve efficient deicing of asphalt concrete under microwave radiation. To know whether this idea is feasible, these six types of asphalt concrete should be prepared and then comprehensively evaluated. Finally, the final conclusion can be drawn. These six asphalt concretes are all prepared in the laboratory using the Marshall design method in accordance with Chinese standards (Chinese Standard, 2011). Some special measures in preparing process can refer to the related requirements in references Liu et al. (2019b) and Wang et al. (2019a).

2.2 Selection of evaluation index

The selected evaluation indicators mainly include four categories. They are asphalt mastic, asphalt concrete, microwave heating and deicing. Asphalt mastic is an important part of asphalt concrete, and it plays a very important role in asphalt concrete. Its composition and structure determine the high-temperature deformation resistance and low-temperature cracking resistance of asphalt concrete (Liu et al., 2008; Wang et al., 2019a). More importantly, in this study, ACP is used to partially replace mineral powder, so the impact of this on asphalt mastic has to be considered. Additionally, the engineering performance of asphalt concrete must be considered under any circumstances. Chen, (2023) found several relationships with the performance of asphalt mixtures. Liu and Sun, (2024) found that high temperature elasticity of asphalt was enhanced by adding ACP and asphalt mastic interaction ability were strongly enhanced when replacing part of filler with ACP. If in order to achieve a certain purpose, the engineering performance of asphalt concrete cannot meet the requirements of its use, then any effort is futile. It is the ultimate goal of this research to improve the microwave heating capacity of asphalt concrete and finally achieve the goal of efficient deicing. Therefore, these two categories cannot be ignored.

Based on the above discussion, after the four aspects are determined, some specific key evaluation indexes in each aspect are selected for subsequent related experiments. These selected specific indexes are summarized in Figure 1. These indexes are divided into four categories which are deicing, microwave heating, asphalt mastic and asphalt concrete, respectively. The ranking of their importance is $I_{deicing} > I_{asphalt\ concrete} > I_{microwave\ heating} > I_{asphalt\ mastic}$.

2.3 Collection of evaluated data

After the evaluation index and test plan are determined, relevant experiments need to be carried out to obtain the laboratory test data of each evaluation index. Eight of the twelve index tests (C1, C2, C3, C4, C4, C6, C7, and C8) were carried out in accordance with the requirements of the Chinese standard (Chinese Standard, 2011), and the remaining four (C9, C10, C11, and C12) were carried out in accordance with the requirements described in these three references (Liu and Wang, 2019a; Liu et al., 2019b; Wang et al., 2019b). By many and orderly laboratory experiments, many expected data have been obtained, as shown in Table 1. These data will be used and processed in subsequent research.

3 Methodology and data pre-processing

3.1 Analytic hierarchy process of improvement

The Analytic Hierarchy Process (AHP) treats the object of study as a system and makes decisions using a process of decomposition, comparative judgment, and synthesis. It has become an important tool for system analysis, developed after the methods of mechanistic and statistical analysis. The essence of the system's approach is to not sever the impact of various factors on the outcome. In AHP, the weighting of each level directly or indirectly affects the outcome, and the impact of each factor at every level on the outcome is quantified, making it very clear and precise. This method is particularly useful for evaluating systems with unstructured characteristics, as well as for multi-objective, multi-criteria, and multi-period system evaluations.When the number of selected indicators is large, it is necessary to improve AHP, and the specific methods are as follows.

1) Establishment of a hierarchical analysis model

Our aim in this study is to recommend the best type of asphalt concrete that meets expectations. Therefore, the best type of asphalt concrete is of course the objective layer in the AHP. The twelve selected key indexes are used as the criterion layer in the model.

Finally, the six types of asphalt concrete are the plan layer in the model. The hierarchical analysis model constructed according to this idea is shown in Figure 2.

2) Comparison matrix

The traditional AHP judgment matrix is established by the nine-scale method. In the practical establishment process, the subjective factors of experts dominate, which will bias the evaluation results. In addition, when the matrix consistency check is performed, if the judgment matrix is not consistent, the main function of the AHP scheme's optimal ranking will be destroyed. Therefore, it must be restructured and calculated until it is passed, and the amount of calculation is large and the accuracy is not high (Ho and Ma, 2018). The improved AHP adopts the three-scale method, which makes it easy for experts to make relatively important comparisons between the two factors without the need for consistency testing. Moreover, this method can also greatly reduce the number of iterations, improve the convergence speed, and meet the requirement of calculation accuracy (Kong et al., 2013). Their calculation processes are shown in Figures 3A, B respectively.

The specific description of the three-scale method is shown in Table 2. Comparison matrix ($\boldsymbol{A}=(A_{ij})_{m\times n}$) according to the method in Table 2 can be easily established. The comparison matrix form of $\boldsymbol{A}$ is shown in Eq. 1.

$$A = \begin{bmatrix} a_{11} & a_{12} & \cdots & a_{1n} \\ a_{21} & a_{22} & \cdots & a_{2n} \\ \cdots & \cdots & & \cdots \\ a_{m1} & a_{m2} & \cdots & a_{mn} \end{bmatrix} \tag{1}$$

3) Calculation of the importance ranking index

The importance ranking index (r_i and r_j) is used to calculate the judgment matrix. r_i and r_j are calculated according to Eq. 2 and Eq. 3, respectively.

$$r_i = \sum_{j=1}^{n} a_{ij} \tag{2}$$

$$r_j = \sum_{i=1}^{m} a_{ij} \tag{3}$$

4) Judgment matrix

The judgment matrix ($\boldsymbol{B}$) is calculated according to Eq. 4.

$$b_{ij} = \begin{cases} \dfrac{r_i - r_j}{r_{\max} - r_{\min}} \times (k_m - 1) + 1 & r_i \geq \text{or} = r_j \\ \left[\dfrac{|r_i - r_j|}{r_{\max} - r_{\min}} \times (k_m - 1) + 1 \right]^{-1} & r_i \leq r_j \end{cases} \tag{4}$$

The parameter k_m in Eq. 4 is calculated according Eq. 5.

$$k_m = \frac{r_{\max}}{r_{\min}} \tag{5}$$

5) The optimal transfer matrix of the judgment matrix

The optimal transfer matrix $\boldsymbol{C}$ of the judgment matrix $\boldsymbol{B}$ is calculated according to Eq. 6.

$$c_{ij} = \frac{1}{n} \sum_{k=1}^{n} \left(\lg \frac{b_{ik}}{b_{jk}} \right) \tag{6}$$

6) Calculation of the quasi-optimum consistent matrix of the judgment matrix

Eq. 7 is the calculation method of the quasi-optimum consistent matrix $\boldsymbol{D}$ of the judgment matrix $\boldsymbol{B}$.

$$d_{ij} = 10^{c_{ij}} \tag{7}$$

7) Calculation of the weight of each index

The eigenvector corresponding to the largest eigenvalue of matrix $\boldsymbol{D}$ is calculated, and then they are standardized. Finally, the weight value (W_j) of each index is obtained.

8) Calculation of the included angle of the index axis

Finally, the included angles between the index axes can be calculated by applying the weights calculated in the previous step in combination with Eq. 8.

$$\alpha_j = 360^{\circ} \times W_j \tag{8}$$

3.2 Radar chart method

3.2.1 Standardized processing of evaluation index data

Usually there are both absolute and relative quantitative indicators in the comprehensive evaluation (CE) system. The absolute quantity index is a physical quantity related to the dimension. Generally speaking, different indicators have different units, and the same indicator often does not have the same value in different units. This often results in several orders of magnitude difference in values between the indicators. When the magnitude and speed of the change of each index value are close, the relative index can be used for comprehensive evaluation. Therefore, in this case, the data can be processed without dimension according to Eq. 9. If the magnitude and speed of the change of each index value are very different, the data can be standardized according to Eqs 10–12. According to the characteristic of the data obtained in this study, the application of Eq. 9 can complete the standardization of these data. In addition, the indexes selected in this study are all positive indexes, so all data can be standardized according to the same formula.

$$E_{pq} = \begin{cases} \dfrac{e_{pq}}{\max e_{pq}} \text{ (Positive index)} \\ \dfrac{e_0}{|e_{pq} - e_0| + e_0} \text{ (Fixed index)} \\ 1 - \dfrac{e_{pq}}{\max e_{pq}} \text{ (Reverse index)} \end{cases} \tag{9}$$

$$y_p^q = \frac{x_p^q - E(x_p)}{\sigma(x_p)} \tag{10}$$

$$E(x_p) \approx \frac{1}{n}\sum_q x_p^q \tag{11}$$

$$\sigma(x_i) \approx \sqrt{\frac{1}{n}\sum_q \left(x_p^q - E(x_p)\right)^2} \tag{12}$$

After the standardization is completed, all the data can be displayed in the radar chart. But the comprehensive performance of each asphalt mixture can only be roughly seen from the radar chart, their ranking must be obtained by calculating area and perimeter of the radar chart. Eq. 13 is the characteristic vector including the area and perimeter of the radar chart.

$$U_p = [S_p, L_p] \tag{13}$$

where U_p represents the characteristic vector of the pth object; S_p represents the area of the radar chart; L_p represents the perimeter of the radar chart. Their calculation method is shown in Eq. 14.

$$\begin{cases} S_p = \sum_{q=1}^{n} \pi a_{pq}^2 \cdot \frac{\alpha_q}{360} = \sum_{q=1}^{n} \pi a_{pq}^2 \cdot W_q \\ L_p = \sum_{q=1}^{n} 2\pi a_{pq} \cdot \frac{\alpha_q}{360} = \sum_{q=1}^{n} 2\pi a_{ij} \cdot W_q \end{cases} \tag{14}$$

Evaluation vector (Z_p) is defined as Eq. 15.

$$Z_p = [z_{p1}, z_{p2}] \tag{15}$$

where z_{p1} is the relative area of evaluation indicator; z_{p2} is the relative perimeter of evaluation indicator. Their calculation method is shown in Eq. 16.

$$\begin{cases} z_{p1} = \frac{S_p}{\max S_p} \\ z_{p2} = \frac{L_p}{2\sqrt{\pi S_p}} \end{cases} \tag{16}$$

The final evaluation result is calculated according to Eq. 17. The larger the value is, the better the performance of the evaluated object is.

$$f_p = \sqrt{z_{p1} \times z_{p2}} \tag{17}$$

4 Results and discussion

4.1 Calculation results of each index weight based on improved analytic hierarchy process

Since the matrix established in this study is difficult to be processed by manual calculation, the following calculation results are all calculated with the help of Matlab® software. The Supplementary Appendix is the original calculation procedure.

1) Comparison matrix

Comparison matrix ($\boldsymbol{A}=(A_{ij})_{m\times n}$) according to the method in Table 2 can be easily established. The results are shown in Table 3.

2) Judgment matrix

According to Eq. 4, the judgment matrix ($\boldsymbol{B}$) is calculated and their calculation results are summarized in Table 4.

3) The optimal transfer matrix

According to Eq. 6, the optimal transfer matrix $\boldsymbol{C}$ of the judgment matrix $\boldsymbol{B}$ is calculated and the results are shown in Table 5.

4) The quasi-optimum consistent matrix

The quasi-optimum consistent matrix $\boldsymbol{D}$ of matrix $\boldsymbol{B}$ can be calculated by Eq. 7, and the calculation results are shown in Table 6.

5) Calculation of the weight of each index

Complete the calculation according to the aforementioned method and obtain the calculation results. They are all summarized in Table 7.

6) Calculation of the included angle of the index axis

When the weight of each index is determined, the angle between the indexes in the radar chart can be calculated according to Eq. 8. The calculation results of the included angle of the index axis are shown in Table 8. Based on these angles, a radar chart that considers the weights of all indexes can be drawn, as shown in Figure 4 can intuitively show the proportion of importance that each indicator occupies in the whole part. Radar charts provide an intuitive display of multi-dimensional data sets, allowing for the identification of similar values among variables and the detection of outliers. They are particularly effective for highlighting which variables score high or low within a dataset, showcasing performance and strengths. These charts are especially suitable for presenting multiple key features of a dataset, or for comparing these features against standard values. Generally, radar charts are applicable for comparing multiple data entries across various dimensions.This is mainly due to the calculation of the weights of all indicators using the improved AHP. However, such work still only stays at the level of qualitative analysis and cannot reach the level of quantitative analysis. This is difficult to accept for scientific research. Simultaneously, the best type of asphalt concrete type cannot be recommended based on these results. Therefore, follow-up work will be continued to make up for this deficiency.

4.2 Analysis of radar chart results

The laboratory test data in Table 1 is standardized by Eq. 9. These standardized results are shown in Table 9.

From the calculation results in Table 9 and included angles between the index axes, the radar chart shown in Figure 5 can be

drawn. The comprehensive performances of the six types of asphalt concrete are drawn on five radar charts. This is to allow a clear comparison between the control group and the five modified asphalt concretes. First of all, it can be seen intuitively and clearly from Figure 5 that the comprehensive performances of the five modified asphalt concretes is all better than that of the control group. Additionally, from the observation and comparison of these five radar charts, it is found that when the replacement amount of ACP reaches 80%, the index C5 has increased significantly. Index C5 represents the shear strength of asphalt mastic. Such results indicate that 80% or more of the replacement amount of ACP is very effective for improving the shear strength of asphalt mastic. Index C3 is also very special, and it represents the moisture sensitivity of asphalt concrete. Figure 5 shows that the moisture sensitivity of the control group is the lowest, and the moisture sensitivity of asphalt concrete increases slightly with the increase of the ACP replacement amount. The performance of other indexes of modified asphalt concrete is better than those of the control group and with the increase in the amount of ACP replacement, the performances of modified asphalt concrete are getting better and better. However, all these comparisons and analyses only stay at the level of qualitative analysis. Such results are far from meeting the requirements of a scientific research. Therefore, in the next step we will focus on making this research reach the level of quantitative analysis.

In order to get the exact ranking of all types of asphalt mixture, the results of Z_p are calculated according to Eqs 13–16. The results are as follow:

$Z_1 = [z_{11}, z_{12}] = [0.4971, 0.9438]$; $Z_2 = [z_{21}, z_{22}] = [0.5238, 0.9633]$;$Z_3 = [z_{31}, z_{32}] = [0.6235, 0.9857]$; $Z_4 = [z_{41}, z_{42}] = [0.7279, 0.9911]$;$Z_5 = [z_{51}, z_{52}] = [0.8475, 0.9985]$; $Z_6 = [z_{61}, z_{62}] = [0.1000, 0.9983]$.

According to the results of Z_i, f_i can be easily calculated according to Eq. 17. The calculation results are summarized in Table 10.

From Table 10, it can be concluded that the ranking of f_i is $f_6 \succ f_5 \succ f_4 \succ f_3 \succ f_2 \succ f_1$. From the perspective of comprehensive performance, the larger the replacement amount of ACP is, the better the performance of asphalt concrete is. The comprehensive performance of the asphalt concrete with 100% ACP replacement amount was about 46% higher than that of the control group. The comprehensive performance of asphalt concrete with the least 20% ACP replacement amount is also about 4% higher than that of the control group. Certainly, such conclusions are based on the evaluation system and evaluation model of this research. This is not a fixed conclusion. Readers can modify this model according to their focus and perspective, and they may get different conclusions. This also reflects that the purpose and original intention of this research is to find and establish a flexible and hierarchical evaluation system for the comprehensive performance of asphalt concrete. Such an evaluation system can reduce the influence of human factors on conclusions and is more objective, convenient and scientific.

5 Summary

In this study, ACP was used to partly replace mineral powder to improve deicing efficiency of asphalt concrete under microwave heating. In the laboratory, the twelve key indexes of these different types of asphalt concrete were studied and a large amount of data was obtained. Under the premise of only considering the weight of each index, it is very difficult to compare and analyze the comprehensive performance of these different types of asphalt concrete. In order to solve this problem, the improved AHP was used to determine the weight of each index, and then the radar chart method was used to qualitatively and quantitatively analyze the comprehensive performance of different types of asphalt concrete. The conclusions obtained are as follows:

- From the calculation results of the model, the rank of f_i representing the comprehensive performance of each type of asphalt concrete can be obtained as $f_6 > f_5 > f_4 > f_3 > f_2 > f_1$. Based on this result, it can be easily recommended that the type of asphalt concrete that meets the expected requirements is an asphalt concrete with 100% ACP replacement amount.
- The established comprehensive comparison and analysis model of different types of asphalt concrete performance has proved feasible and effective through the application of this research. However, the object of this article is specific, and the factors considered are relatively targeted.This research process and results can provide a new idea and reference for resolution of similar problems in the future.

Data availability statement

The raw data supporting the conclusion of this article will be made available by the authors, without undue reservation.

Author contributions

JB: Conceptualization, Data curation, Formal Analysis, Funding acquisition, Investigation, Methodology, Software, Writing–original draft, Writing–review and editing, Supervision. QZ: Project administration, Resources, Supervision, Validation, Visualization, Writing–original draft, Writing–review and editing, Methodology.

Funding

The author(s) declare that no financial support was received for the research, authorship, and/or publication of this article.

Acknowledgments

The authors thank the Chang'an university for providing materials and friendly environment to conduct this research study.

Conflict of interest

The authors declare that the research was conducted in the absence of any commercial or financial relationships that could be construed as a potential conflict of interest.

Publisher's note

All claims expressed in this article are solely those of the authors and do not necessarily represent those of their affiliated organizations, or those of the publisher, the editors and the reviewers. Any product that may be evaluated in this article, or claim that may be made by its manufacturer, is not guaranteed or endorsed by the publisher.

Supplementary material

The Supplementary Material for this article can be found online at: https://www.frontiersin.org/articles/10.3389/fenrg.2024.1375653/full#supplementary-material

References

Bianchin, M., Külkamp-Guerreiro, I., Oliveira, C., Contri, R. V., Guterres, S. S., and Pohlmann, A. R. (2015). Radar charts based on particle sizing as an approach to establish the fingerprints of polymeric nanoparticles in aqueous formulations. *J. Drug Deliv. Sci. Technol.* 30, 180–189. doi:10.1016/j.jddst.2015.10.015

Bostancioğlu, M., and Oruç, Ş. (2015). Effect of activated carbon and furan resin on asphalt mixture performance. *Road Mater. Pavement Des.* 17 (2), 512–525. doi:10.1080/14680629.2015.1092465

Chen, B., Dong, F., Yu, X., Zheng, C., Guo, Y., and Zu, Y. (2023). Research on evaluation method of asphalt mixture workability based on minimum mixing energy consumption. *Constr. Build. Mater.* 389 (2023), 131760. doi:10.1016/j.conbuildmat.2023.131760

Chen, Y., Chen, X., Li, Z., and Lin, Y. (2010). Method of radar chart comprehensive evaluation with uniqueness feature. *Trans. Beijing Inst. Technology* 30 (12), 1409–1412.

Chinese Standard (2011). *Standard test method of bitumen and bituminous mixture for highway engineering in China*. JTG E20-2011. Beijing, China: General Administration of Quality Supervision, Inspection and Quarantine of the People' s Republic of China.

Darko, A., Chan, A., Ameyaw, E., Owusu, E. K., Pärn, E., and Edwards, D. J. (2018). Review of application of analytic hierarchy process (AHP) in construction. *Int. J. Constr. Manag.* 19 (5), 436–452. doi:10.1080/15623599.2018.1452098

Ding, L., Wang, X., Cui, X., Zhang, M., and Chen, B. (2020). Development and performance research of new sensitive materials for microwave deicing pavement at different frequencies. *Cold Regions ence Technol.* 181, 103176. doi:10.1016/j.coldregions.2020.103176

Gao, J., Guo, H., Wang, X., Wang, P., Wei, Y., Wang, Z., et al. (2019). Microwave deicing for asphalt mixture containing steel wool fibers. *J. Clean. Prod.* 206, 1110–1122. doi:10.1016/j.jclepro.2018.09.223

Guo, H., Wang, Z., Huo, J., Wang, X., Liu, Z., and Li, G. (2020). Microwave heating improvement of asphalt mixtures through optimizing layer thickness of magnetite and limestone aggregates. *J. Clean. Prod.* 273, 123090. doi:10.1016/j.jclepro.2020.123090

Ho, W., and Ma, X. (2018). The state-of-the-art integrations and applications of the analytic hierarchy process. *Eur. J. Operational Res.* 267, 399–414. doi:10.1016/j.ejor.2017.09.007

Hu, X., Dai, K., and Pan, P. (2019). Investigation of engineering properties and filtration characteristics of porous asphalt concrete containing activated carbon. *J. Clean. Prod.* 209, 1484–1493. doi:10.1016/j.jclepro.2018.11.115

Ishizaka, A., and Labib, A. (2011). Review of the main developments in the analytic hierarchy process. *Expert Syst. Appl.* 38, 14336–14345. doi:10.1016/j.eswa.2011.04.143

Jahanbakhsh, H., Karimi, M., Jahangiri, B., and Nejad, F. M. (2018). Induction heating and healing of carbon black modified asphalt concrete under microwave radiation. *Constr. Build. Mater.* 174, 656–666. doi:10.1016/j.conbuildmat.2018.04.002

Kalonia, C., Kumru, O., Kim, J., Middaugh, C. R., and Volkin, D. B. (2013). Radar chart array analysis to visualize effects of formulation variables on IgG1 particle formation as measured by multiple analytical techniques. *J. Pharm. Sci.* 102, 4256–4267. doi:10.1002/jps.23738

Karimi, M., Jahanbakhsh, H., Jahangiri, B., and Moghadas Nejad, F. (2018). Induced heating-healing characterization of activated carbon modified asphalt concrete under microwave radiation. *Constr. Build. Mater.* 178, 254–271. doi:10.1016/j.conbuildmat.2018.05.012

Kavussi, A., Karimi, M., and Dehaghi, E. (2020). Effect of moisture and freeze-thaw damage on microwave healing of asphalt mixes. *Constr. Build. Mater.* 254, 119268. doi:10.1016/j.conbuildmat.2020.119268

Kong, Y., Chen, J., Zhang, J., Ren, X., and Ma, L. (2013). Application of three-scale ahp method in nuclear emergency decision making. *Math. Pract. Underst.* 43 (9), 109–114.

Lei, J., Zheng, N., Luo, F., and He, Y. (2020). Purification of automobile exhaust gas by activated carbon supported Fe^{3+} modified nano-TiO_2 and its application on asphalt pavement. *Road Mater. Pavement Des.* 1, 2424–2440. doi:10.1080/14680629.2020.1763831

Liu, H., Liu, A., and Zhang, B. (2008). A fuzzy comprehensive evaluation method of maintenance quality based on improved radar chart. *Isecs Int. Colloquium Comput. Commun. Control, Manag.* doi:10.1109/CCCM.2008.208

Liu, Z., and Wang, Y. (2019a). Laboratory research on asphalt mastic modified with activated carbon powder: rheology, microstructure and adhesion. *Road Mater. Pavement Des.* 1, 1424–1441. doi:10.1080/14680629.2019.1691043

Liu, Z., Xu, Y., Wang, Y., and Luo, S. (2019b). Engineering properties and microwave heating induced ice-melting performance of asphalt mixture with activated carbon powder filler. *Constr. Build. Mater.* 197, 50–62. doi:10.1016/j.conbuildmat.2018.11.094

Liu, Z. M., and Sun, L. J. (2024). "Rheological behavior evaluation of activated carbon powder modified asphalt," in *Advances in functional pavements* (Boca Raton, Florida, United States: CRC Press), 106–110.

Mou, Q., and Li, X. (2003). Applications of microwave heating technology. *Physics* 33 (6), 438–442.

Osborne, T., and Hutcheson, W., 1989, Asphalt compounds and method for asphalt reconditioning using microwave radiation.

Saaty, T. L. (1980). *The analytical hierarchy process: planning, priority setting, resource allocation*. New York: McGraw-Hill.

Seyrek, E., Yalçin, E., Yilmaz, M., Vural Kök, B., and Arslanoğlu, H. (2020). Effect of activated carbon obtained from vinasse and marc on the rheological and mechanical characteristics of the bitumen binders and hot mix asphalts. *Constr. Build. Mater.* 240, 117921. doi:10.1016/j.conbuildmat.2019.117921

Shin, E., Kim, E., Lee, J., and Kang, J. K. (2020). Assessment of the engineering conditions of small dams using the analytical hierarchy process. *Iran. J. ence Technol. Trans. Civ. Eng.* 2020, 1297–1305. doi:10.1007/s40996-020-00456-z

Trigos, L., Gallego, J., and Escavy, J. (2020). Heating potential of aggregates in asphalt mixtures exposed to microwaves radiation. *Constr. Build. Mater.* 230, 117035–117112. doi:10.1016/j.conbuildmat.2019.117035

Wang, S., Hou, L., Lee, J., and B.u., X. (2017). Evaluating wheel loader operating conditions based on radar chart. *Automation Constr.* 84, 42–49. doi:10.1016/j.autcon.2017.08.020

Wang, Y., Liu, Z., and Hao, P. (2019a). Investigation on mechanical and microwave heating characteristics of asphalt mastic using activated carbon powder as electro-magnetic absorbing materials. *Constr. Build. Mater.* 202, 692–703. doi:10.1016/j.conbuildmat.2019.01.050

Wang, Z., He, Z., Wang, Z., and Ning, M. (2019b). Microwave deicing of functional pavement using sintered magnetically separated fly ash as microwave-heating aggregate. *J. Mater. Civ. Eng.* 31 (7), 04019127. doi:10.1061/(asce)mt.1943-5533.0002771

Wang, Z., Wang, H., An, D., Ai, T., and Zhao, P. (2016). Laboratory investigation on deicing characteristics of asphalt mixtures using magnetite aggregate as microwave-absorbing materials. *Constr. Build. Mater.* 124, 589–597. doi:10.1016/j.conbuildmat.2016.07.137

Xiao, Y., Wan, M., Jenkins, K., Wu, S. P., and Cui, P. Q. (2017). Using activated carbon to reduce the volatile organic compounds from bituminous materials. *J. Mater. Civ. Eng.* 29 (10), 04017166. doi:10.1061/(asce)mt.1943-5533.0002024

Yıldız, K., and Atakan, M. (2020). Improving microwave healing characteristic of asphalt concrete by usingfly ash as a filler. *Constr. Build. Material* 262, 120448. doi:10.1016/j.conbuildmat.2020.120448

Frontiers in
Energy Research

Advances and innovation in sustainable, reliable and affordable energy

Explores sustainable and environmental developments in energy. It focuses on technological advances supporting Sustainable Development Goal 7: access to affordable, reliable, sustainable and modern energy for all.

Discover the latest Research Topics

See more →

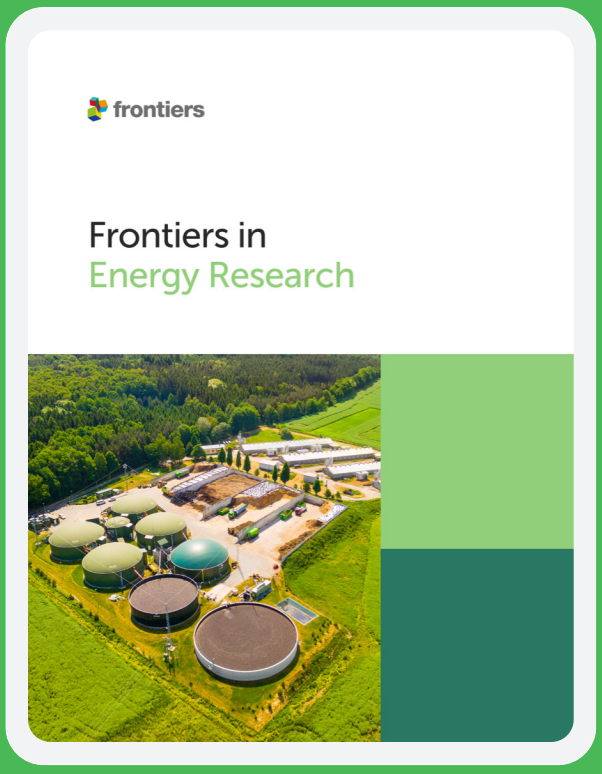

Frontiers

Avenue du Tribunal-Fédéral 34
1005 Lausanne, Switzerland
frontiersin.org

Contact us

+41 (0)21 510 17 00
frontiersin.org/about/contact